



Universitat Autònoma de Barcelona

**ADVERTIMENT.** L'accés als continguts d'aquesta tesi queda condicionat a l'acceptació de les condicions d'ús establertes per la següent llicència Creative Commons:  [http://cat.creativecommons.org/?page\\_id=184](http://cat.creativecommons.org/?page_id=184)

**ADVERTENCIA.** El acceso a los contenidos de esta tesis queda condicionado a la aceptación de las condiciones de uso establecidas por la siguiente licencia Creative Commons:  <http://es.creativecommons.org/blog/licencias/>

**WARNING.** The access to the contents of this doctoral thesis it is limited to the acceptance of the use conditions set by the following Creative Commons license:  <https://creativecommons.org/licenses/?lang=en>



Universitat Autònoma  
de Barcelona

# Molecular modelling of Quatsome nanovesicles

Sílvia Illa Tuset

PhD Thesis  
PhD program in Material Science

Supervised by:

Dr. Jordi Faraudo

Prof. Swapan K. Pati

Tutor:

Dr. Juan Camacho

Physics department  
Science faculty

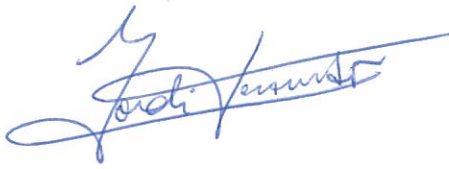
2018



Report submitted for the achievement of the Doctor degree in  
Material Science by:

Sílvia Illa Tuset

Checked and accepted:



Dr. Jordi Faraudo



Prof. Swapan K. Pati



जवाहरलाल नेहरु उन्नत वैज्ञानिक अनुसंधान केंद्र  
JAWAHARLAL NEHRU CENTRE FOR ADVANCED SCIENTIFIC RESEARCH  
जक्कर बेंगलूर/JAKKUR, BANGALORE- 560 064.

Bellaterra, December 2018



# Preamble

This PhD Thesis has been performed in the framework of the Marie Skłodowska-Curie Action ITN "Nano2Fun". Many results included in this Thesis were obtained thanks to a collaborative effort of several partners of the Nano2Fun network and researchers belonging to other institutions.



# Abstract

This thesis is devoted to the theoretical and computational study at atomistic and molecular scales of the properties of novel organic nanoparticles called “Quatsomes” (vesicles made by mixing CTAB cationic surfactant and cholesterol) as well as the interactions of Quatsomes with different types of fluorescent molecules. The methodology employed is computational molecular modelling. It includes modelling of the interactions between molecules at different scales and resolutions (DFT electronic structure calculations, atomistic molecular mechanics force fields and coarse-grain molecular mechanics force fields) and molecular dynamics simulations at atomistic and coarse-grain molecular resolutions. Most of the results have observable consequences that have been confirmed experimentally.

The thesis is divided into an Introduction to the topic (with a brief explanation of the main experimental results and the main theoretical concepts), a chapter describing in detail the methods to be employed in the thesis, four chapters containing new results and a chapter with conclusions and perspectives.

The results of the thesis are presented in two parts. The first part (Chapters 3 and 4) contains the results concerning the simulations and calculations of structure and properties of the Quatsome vesicle from atomistic and coarse-grain molecular simulations. The second part (Chapters 5 and 6) contains the simulation study of the interaction of Quatsome vesicles with different types of dyes.

The atomistic simulation results presented in Chapter 3 provide a detailed characterization of the properties of the Quatsome bilayer. The molecular organization of the components across the bilayer (positioning, orientation and diffusion of the component molecules)



was studied as well as mechanical properties such as bending modulus and area expansion modulus. The effect of temperature and added salt was also analyzed. Remarkably, it was found that the orientation of the molecules has a spontaneous symmetry breaking between the two leaflets of the bilayer and states with different orientations coexist, a theoretical prediction that has been tested experimentally.

In Chapter 4 two coarse-grain Martini-type parametrizations of a force field for CTAB surfactant (one for explicit solvent and one for implicit solvent simulations) was developed and successfully tested against atomistic simulations. The model was further employed to perform simulations of full Quatsome vesicles. These simulations revealed that the Quatsome vesicle is made of planar faces linked by curved defects, a kind of vesicle organization never found before. These predictions were confirmed by experimental Cryo-TEM images.

Chapters 5 and 6 start by developing (from DFT) CHARMM compatible atomistic force fields for simulation of different dyes (fluorescein in Chapter 4 and DiD and DiI in Chapter 5). These force fields were employed in molecular dynamics simulations of the interactions of these dyes with Quatsomes. The results demonstrate that despite the hydrophilic fluorescein dye interacts strongly with Quatsome (via electrostatic interactions), the adsorption of the dye competes with the more favorable formation of soluble molecular clusters. Hence, a more suitable approach is to employ hydrophobic dyes such as DiI and DiD. The simulations reported in the thesis show that these dyes are integrated in the bilayer without deforming or altering the Quatsome and without aggregating inside the Quatsome bilayer, thus providing suitable alternatives for developing fluorescent vesicles.

The conclusions and perspectives section shows that the thesis not only present many new results but also has many possible future perspectives in different directions: vesicles with resonant energy transfer, conceptual aspects regarding the spontaneous self-assembly of vesicles, possibility of replacing the components by other different bilayer components. All these options have been initially explored and all of them are very promising.

*It is invaluable to have a friend who shares your interests and helps you stay motivated.*

Maryam Mirzakhani

## Acknowledgments

Gratitude is one of the most powerful human emotions, because it not only enables us to appreciate what we already have, but also helps to attract new things into our lives.

First of all, I would like to thank Swapan K. Pati, from the JNCASR. To be hosted in that institution for two years was a big challenge for me, so I appreciate him very much for his help and support. To the TSU department where I belonged, a big thank you for being my family there; Shubhajit, Abhiroop, Arkamita, Swastika, Ashvini, Dibyajyoti and Bothra, and finally Anusooya Pati for being the "ma'am" of us all. To my friend Sergio, for all the coffee breaks together in the amazing campus in the middle of the wilderness. Finally to Prof. Prakash, for helping me with all the doubts and solving problems with MD



simulations. Dhanyavaad!

I would like to thank to the Nano2fun family and the Marie Curie Initial Training Network (ITN) program funded by the European Commission through the FP7-Marie Curie Actions. From Bengaluru to Barcelona, passing by Bordeaux, Hannover and Parma, I had the chance to meet and share science with really talented people, and learn from them along the way. To Sergio, Antonio, Davide, Domna, Laura, Paolo, Valentina, Luca, Slava... for all the good times we spend together during the meetings. Specially thanks to Antonio for not only helping me with my thesis work, but also for becoming a friend during this journey.



El meu treball de tesi no hagués estat possible sense la col·laboració i pertànyer al grup Nanomol. Primer de tot agrair a la Dra. Nora Ventosa, per confiar amb mi i haver-me donat l'oportunitat de marxar (a l'Índia) però també de tornar (a l'ICMAB). Per fer-me partícip dels seminaris i reunions internes del grup que tant m'han ajudat en el desenvolupament de la tesi i com no, per haver pogut gaudir de la gran família que és Nanomol, tant a nivell científic com personal. Gràcies als Profs. Jaume i Cun per donar-me l'oportunitat d'aprendre dintre el seu grup d'investigació. A persones clau, com Antonio, Guillem, Lidia F, Mariana i Josep pel seu interès i suport en meu treball, per totes les discussions i suggeriments. Gràcies! En l'àmbit personal, vull donar les gràcies a tots els companys de Nanomol. És increïble pensar en tota la gent que he pogut conèixer i amb la que he pogut compartir aquests dos últims

anys de tesi. Gent de molta qualitat que fa que l'ambient de treball sigui immillorable. Trobaré a faltar moments com aquests: cafès a primera hora del matí, Josep; el suport mental per escriure la tesi i el suport físic per l'escalada i el running, Adri; tot el que m'has fet riure i treballar amb tu, Guillem; el dia a dia al despatx i les nostres converses, Francesc; els cafes davant del mapa del món, Joffre; los holas y las mini-conversaciones con María en la 3a planta, així com tots els dinars a las 13h, plans i celebracions amb la Lúdia B, Paula, Inés, Toni, Carles, David, Ramon, Òscar, Judit, Simona, Albert, Miquel, Solène, Nathaly, Carla, Teresa, Mario, Jose, Àngel, Marc, Edu, Javi...



Per altra banda, al llarg de la meua tesi he tingut l'oportunitat de col·laborar en diferents grups d'investigació. On one hand, I would like to thank Prof. Anna Painelli, Dra. Cristina Sissa and Dra. Francesca Terenziani for hosting me in Università di Parma for 3 months. Per altra banda, a la Dra. Marina I. Giannotti i Dra. Berta Gumí-Audenis (IBEC) i Dra. Imma Ratera (ICMAB) pel treball mixte tan "xulo" que ens ha quedat. No sempre es té l'oportunitat de publicar un article amb una bona amiga. Por último, al Dr. Enrique Chacón (ICMM) por el intercambio de emails y ayuda para calcular las propiedades elásticas de nuestro sistema.

Aprofito també per agrair a les meves amigues i amics, els que han pogut estar més a prop però també aquells que han estat tot i estar lluny. Els que em coneixen de sempre i coneixen tot el meu esforç en primera persona per haver arribat fins aquí, però també tots aquells que he anat coneixent duran aquests anys de tesi i que m'han ajudat a continuar.

A tots ells; Berta, Mireia, Oriol, Anna, Ferran, Josep, Adriana i Sara, gràcies en especial! També a la meva família; papa, mama, Glòria i Niels i avis, per tot el que heu fet per ser qui sóc i estar on vull.

Tesi honetako abentura handienetako bat zu ezagutzea izan da, eta azken hiru urte hauek zurekin partekatzea. Urte horietako bakoitza oso berezia eta ezberdina izan da. Eskerrik asko, eskerrik asko eta eskerrik asko nire lan zientifikoan engaiatzeagatik, *.tex* guztiak irakurriz eta zuzenketak eta gomendioak eginez. Maite zaitut.

A vosaltres us volia deixar pel final. Quiero empezar por Yamila, para mi has sido una fuente de energía, buenos momentos e inspiración. Gracias y te deseo lo mejor por que te lo mereces. David, el mejor compañero de trabajo que se puede tener. Gracias por tu ayuda constante, resolver mis dudas, ayudarme con mi trabajo y por el paper juntos que tenemos. Me siento muy afortunada por haberte tenido tan cerca en esta última etapa de la tesis. I Jordi... la persona més clau i important d'aquest període per mi. Gràcies per ser un referent a qui seguir. He après molt de totes les nostres converses, no només científiques sinó també personals. Gràcies per venir a la Índia a donar-me suport i una empenta a la tesi i pel treball constant aquí a l'ICMAB. Penso sincerament que el món de l'acadèmia aniria molt, molt, molt millor si hi hagués més gent que fes i desfés com tu.



Dear past, I'm grateful for your lessons. Dear future, I'm ready for you!!

# Contents

<b>1</b>	<b>Introduction</b>	<b>1</b>
1.1	Vesicles as nanostructured system . . . . .	3
1.1.1	Conditions for vesicle formation . . . . .	5
1.2	Quatsome; a unique Cationic Vesicle made of CTAB and Cholesterol . . . . .	10
1.3	Organization of the thesis and Objectives . . . . .	15
<b>2</b>	<b>Methods: Molecular Modelling</b>	<b>21</b>
2.1	Molecular Modelling: Density Functional Theory . . . . .	24
2.2	Molecular Modelling: Force Field All Atomic Molecular Dynamics (MM-MD)	26
2.2.1	Atomistic Structure . . . . .	28
2.2.2	Modeling Atomic Interactions . . . . .	28
	Force Field Functions . . . . .	30
	CHARMM Parametrization Philosophy . . . . .	33
	Parametrization Procedure for New Compounds . . . . .	34
2.2.3	MD Simulation Method . . . . .	34
	Numerical Integration of the Newtonian Equation of Motion . . . . .	35
	Boundary Conditions . . . . .	37
	Solvent Models for CHARMM . . . . .	38
	Thermodynamic Ensembles . . . . .	39
2.3	Molecular Modelling: Coarse-Grained Molecular Dynamics . . . . .	42
2.3.1	MARTINI Model . . . . .	43

2.3.2	Explicit and Implicit Solvent . . . . .	46
2.4	Analysis of Results . . . . .	47
3	Atomistic simulations of a Quatsome bilayer . . . . .	57
3.1	Full analysis of Quatsome bilayer at 25 °C . . . . .	58
3.1.1	Description of the all-atomic MD simulation . . . . .	58
3.1.2	Molecular organization . . . . .	60
3.1.3	Organization of counterions . . . . .	62
3.1.4	Diffusion coefficient study . . . . .	66
3.1.5	Orientation of Quatsome components . . . . .	68
3.1.6	Elastic properties . . . . .	71
	Bending rigidity . . . . .	71
	Area expansion modulus and effect of tension . . . . .	73
3.2	Effect of Temperature . . . . .	76
3.3	Effect of addition of salt . . . . .	80
4	CG Simulations: Loosing detail to gain insight . . . . .	89
4.1	Martini Models of Cholesterol and CTAB . . . . .	90
4.2	Martini MD Simulations of CTAB . . . . .	93
4.2.1	Interface simulations . . . . .	94
4.2.2	Single Micelle simulations . . . . .	98
4.2.3	Simulation of the self-assembly of many micelles . . . . .	102
4.3	Martini MD simulations of 1:1 CTAB:Chol; Quatsome Vesicle . . . . .	106
4.3.1	Vesicle Build-up . . . . .	107
4.3.2	Simulations' results . . . . .	108
5	Quatsomes with hydrophilic dyes . . . . .	115
5.1	Model and Force Field for Fluorescein dianion . . . . .	119
5.2	Molecular Dynamics Simulation of Fluorescein in water . . . . .	123
5.3	Fluorescein in Quatsome bilayer . . . . .	127

5.4	Analysis of experimental results . . . . .	133
6	Quatsomes with hydrophobic dyes	141
6.1	Model and Force Field of carbocyanine dyes . . . . .	143
6.2	Molecular Dynamics simulations of carbocyanine dyes . . . . .	145
6.2.1	Simulations about the starting position . . . . .	146
6.2.2	Single dye (Dil or DiD) at Quatsome bilayer . . . . .	149
6.2.3	Dye-Dye interaction . . . . .	155
	Simulations with two identical dyes: Dil-Dil and DiD-DiD . . . . .	156
	Simulation with Dil-DiD dyes . . . . .	158
6.2.4	Experimental results . . . . .	161
7	Conclusions and Perspectives	170
7.1	General Conclusions . . . . .	170
7.2	Perspectives and ongoing work . . . . .	172
7.2.1	Self-assembly of Quatsome vesicle . . . . .	173
7.3	Changing the surfactant: MKC . . . . .	177
7.4	Changing the sterol: Cholesterol with a vinyl sulphone group . . . . .	181
Appendix A	Annex	187
A.1	Chapter 2 Annex: Methods . . . . .	188
A.1.1	Preparation of the Quatsomes by the DELOS-SUSP method . . . . .	188
A.1.2	Description of the equipment . . . . .	188
A.2	Chapter 3 Annex: Characterization of the QS bilayer . . . . .	190
A.2.1	MD simulation of DPPC/Chol bilayer . . . . .	190
A.2.2	Computational details of the all MD simulation performed . . . . .	191
A.2.3	Further details of the effect of T and added salt on the characteriza- tion of the QS bilayer . . . . .	193
References		





*I didn't want to just know names of things. I remember really wanting to know how it all worked.*

Elizabeth Blackburn

# 1

## Introduction

In 1998, the Nobel Prize in Chemistry was awarded jointly to Walter Kohn for his development of the density-functional theory and John A. Pople for his development of computational methods in quantum chemistry. This was the first time in history that the prize was given to a work that contained molecular modelling computer simulations. In 2013, three pioneers of computational biophysics and structural biology, Martin Karplus, Arieh Warshel, and Michael Levitt, were awarded the Nobel Prize in Chemistry, for the development of multiscale methods for complex systems. They were recognized for their development and application of methods to simulate the behavior of molecules at various

scales, from simple molecules to proteins.

These milestones could be seen as the dawn of a new era for chemistry, the era of experiments based on computer simulations. On one hand, these molecular modelling simulations have some advantages versus the traditional experimental method. For instance, the increase in spatial resolution, which informs about the exact molecular conformation of building blocks providing a more complete picture of any system, or the decrease in the cost of experiments. On the other hand, simulations also hold advantages versus the purely theoretical approach. For example, they provide much more visually appealing information, facilitating the interpretation of theoretical models, which can be unwieldy and fragile (especially when they are large). However, **simulations (as a new method), are not intended to substitute any of the other two approaches, but to complement both of them, acting as a bridge between them, enlarging or even completing the picture of the reality that chemistry provides.**

One of the fields where simulation methods have had a bigger impact is that of the investigation of biomolecules<sup>34</sup>, and this, at the same time, has brought a remarkable progress in several fields. The simulation of biological systems<sup>22</sup> is one of the best examples. That progress has brought understanding of biological phenomena and the relationships in those systems, to a field that had before a lack of scientific accuracy and mathematical/phenomenological tractability. Methods to study biological systems require considering a big amount of parameters, all of them critical for the functioning, making the study of those systems and their mechanisms really complex. Molecular modelling methodology attempts to eliminate the natural variability of a biological system so that differences in behavior can be more clearly identified. Development of modern computers has paralleled the need for quantitative understanding of complex biological problems, and it has accelerated the development of most modeling studies, to create a model that is simple yet retains the essential physical and biological attributes<sup>21</sup>.

Within the field of biomolecules, a particular case of especial relevance is that of vesicles, which are introduced and explained in the next section.

## 1.1 VESICLES AS NANOSTRUCTURED SYSTEMS

Vesicles are spherical objects enclosing a liquid compartment (lumen), with a diameter ranging from 20 nm to a few thousand of nanometers, separated from its surroundings by at least one thin membrane consisting of a bilayer (unilamellar) or several layers (multilamellar) of amphiphilic molecules<sup>30</sup> (see Figure 1.1). They can be classified by their size, being the focus of this work those called SUVs (small unilamellar vesicles, size < 200 nm and single bilayer). For a more detailed information see ref<sup>41</sup>.

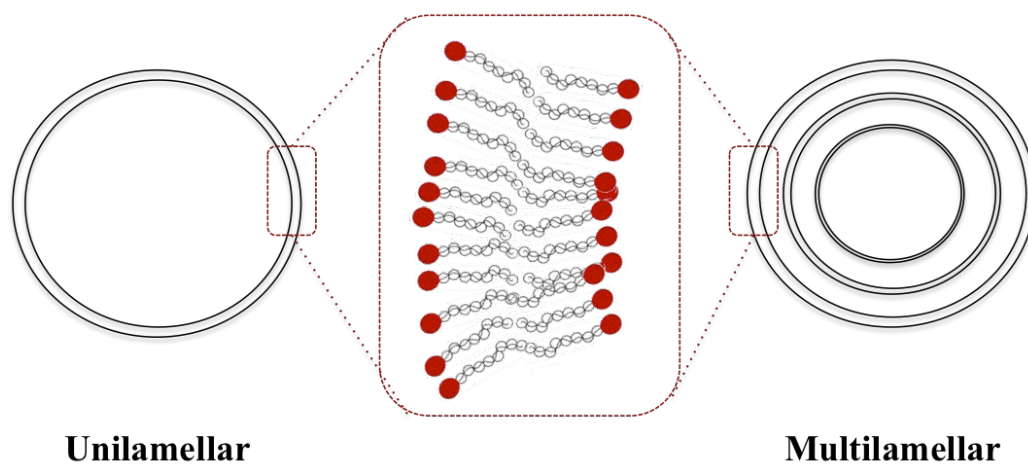


**Figure 1.1:** Schematic representation of some possible vesicular structures.

Vesicles are formed by amphiphilic molecules. The term relates to the fact that all amphiphilic molecules consist of at least two parts, one which is soluble in a solvent (the lyophilic part) and one which is insoluble (the lyophobic part). When the solvent is water, one usually talks about the hydrophilic and hydrophobic parts, respectively.

Vesicles can be formed by amphiphilic molecules such as surfactants or/and phospholipids, but may also be prepared from macromolecular analogues, this is, amphiphilic block

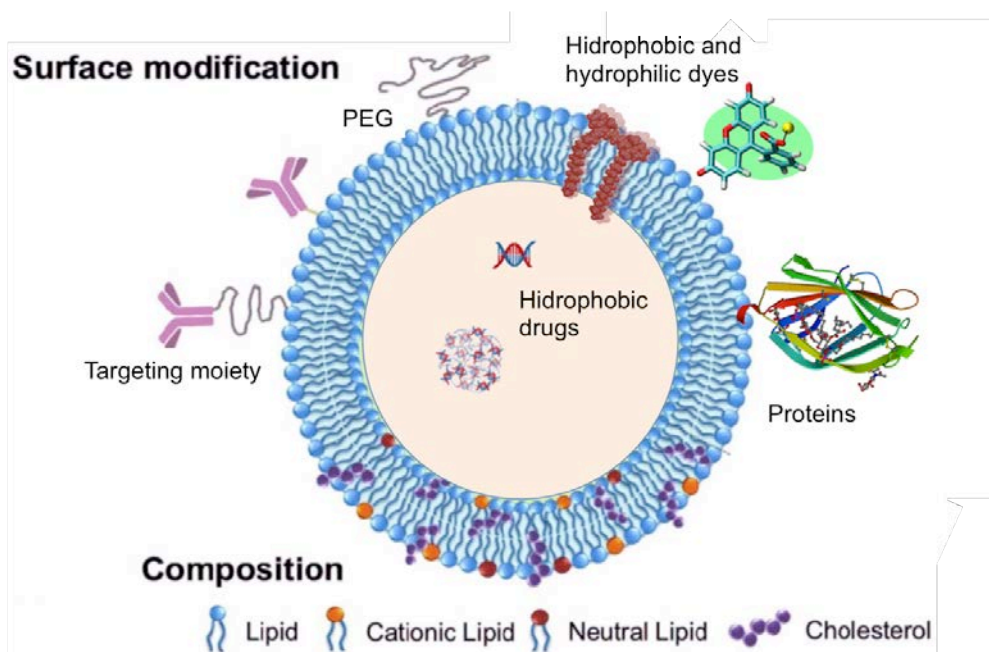


Figure 1.2: Schematic representation of the different types of vesicle drug delivery systems. Vesicles consist of a bilayer that can be composed of cationic, anionic, or neutral phospholipids, as well as surfactants, which enclose an aqueous core. Both the bilayer and the aqueous space can incorporate hydrophobic or hydrophilic compounds, respectively.

copolymers ("polymersomes")<sup>14</sup>.

On one hand, those formed by phospholipids are known as lipid vesicles or liposomes, which usually have anionic character. On the other hand, the ones formed by surfactants can be either cationic or anionic vesicles. Besides, vesicles formed by the combination of a lipid and a surfactant exist. One example of those are niosomes, whose main amphiphilic component is a non-ionic surfactant that forms a bilayer upon the addition of cholesterol (e.g., dicetyl phosphate)<sup>42</sup>. Another example are cationic vesicles, that can be formed by cationic lipids. Among all, cationic vesicles have some advantages over vesicles formed by phospholipids or non-ionic surfactants, as they are simple and quick to formulate, and are constituted by readily available ingredients that are chemically stable against oxidative degradation<sup>45</sup>.

Vesicles can play a major role in modeling biological membranes, transport and targeting of active agents<sup>41</sup>. In recent years, vesicles have become the vehicle of choice in drug

delivery<sup>10,43</sup>, (see an illustrative scheme in Figure 1.2). Vesicular drug delivery reduces the cost of therapy by improved bioavailability of medication, especially in the case of poorly soluble drugs. They can incorporate both hydrophilic and hydrophobic drugs, delaying drug elimination of rapidly metabolizable drugs, and work as sustained release systems. Thus, based on that, many technological innovations have arisen from the applications of vesicle system in order to solve the problems of drug insolubility, instability, and rapid degradation. Furthermore, lipid vesicles have been found to be of value in immunology, membrane biology, diagnostic techniques, and most recently, genetic engineering<sup>32</sup>.

Finally, a word must be said about the significant role of small molecules in vesicle formation and stabilization. Incorporation of certain components into natural or artificial membranes can stabilize and rigidify the membrane bilayers of the vesicles. Cholesterol, for instance, has proven to influence the membrane organization, affecting the membrane permeability to ions, the compressibility of the bilayers, and the diffusion of oxygen<sup>39</sup>. Cholesterol, incorporated into liposomes for example, plays an important role in biomedical applications. Its ability to modulate the physico-chemical properties of lipid bilayers has been employed to stabilize liposomes for their application in drug delivery or analytical science<sup>9</sup>. Considering mixed system for vesicle formation could give rise to a new sort of important, emerging class of self-assembled vesicular systems<sup>7</sup>.

### 1.1.1 CONDITIONS FOR VESICLE FORMATION

Amphiphilic molecules dispersed in a solvent can form a large variety of aggregates of very different morphologies and sizes<sup>25</sup>. Depending on amphiphile(s) concentration, temperature and solvent properties, the amphiphiles can either be dissolved in solution or form monolayer aggregates like micelles (spherical or cylindrical) or assemble into bilayers. Examples of bilayer aggregates are planar lamellae, closed hollow spheres (vesicles) and bi-continuous (sponge like) mesophases. A complete review of all the possible amphiphile phases can be found in reference<sup>25,30</sup>.

Vesiculation in an aqueous solution is considered a spontaneous process driven by minimization of free energy, as, given a planar patch of membrane, the nonpolar hydrophobic part repels the contact with polar water molecules. When this driving force is sufficiently high to overcome the corresponding bending resistance of the planar membrane, the curving of the patch into a sphere becomes possible, bringing the formation of a vesicle of minimal size<sup>2,18</sup>.

Two common ways to induce spontaneous vesiculation are the thermodynamic vesicle formation approach and the kinetic vesicle formation approach, leading to equilibrium and non-equilibrium structures respectively. On one hand, in the thermodynamic case, a closed vesicle (or a curved surface in general) requires the existence of asymmetry between the inner and external membrane layers. The easiest and most common way to induce spontaneous vesiculation is that of mixing two different amphiphiles<sup>38,44</sup>. As an example of this, mixing cationic and anionic amphiphiles facilitates the bilayer asymmetry by introducing the additional degree of freedom of the bilayer composition<sup>40</sup>. Figure 1.3 shows an exam-

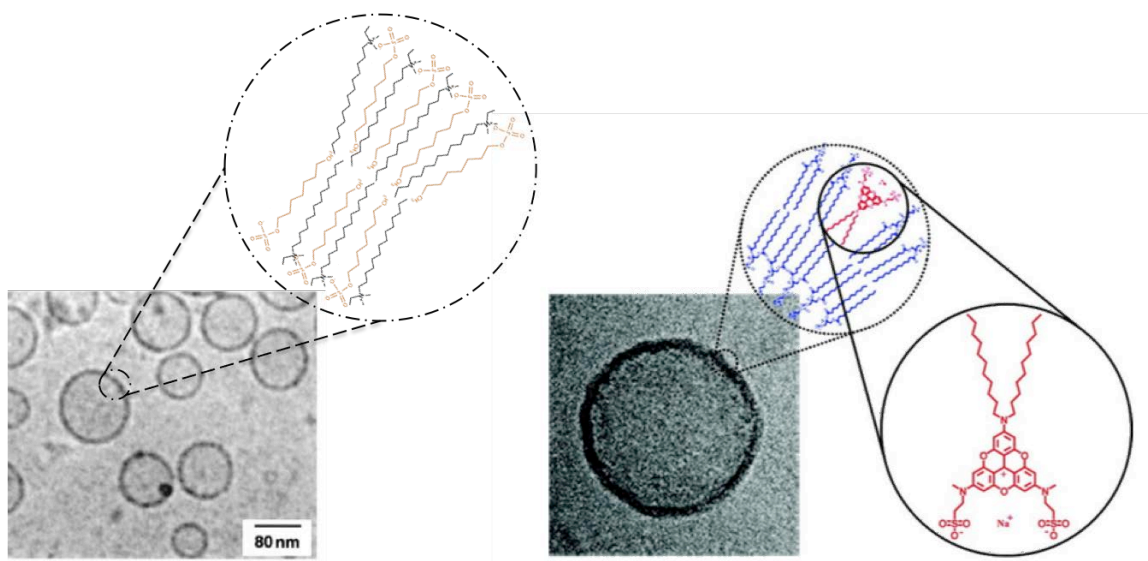


**Figure 1.3:** On the left panel, cryo-TEM image of CTAB/SOS (molecules zoomed are coloured in black and orange, respectively) system showing equilibrium spontaneous unilamellar<sup>20</sup> vesicles. On the right panel, cryo-TEM image of DMPC/DLA (molecules zoomed are colored in blue and red, respectively) forming highly stable unilamellar vesicles<sup>37</sup> with spontaneous curvature induced by bilayer asymmetry.

ple of CTAB/SOS (cationic and anionic surfactants, respectively) that form equilibrium unilamellar vesicles spontaneously. Nevertheless, other factors that can induce asymmetry between the layers exist. An example is the case of DMPC/DSA lipid based system, in which one of the components induces the curvature due to its different structure (see Figure 1.3). On the other hand, in the kinetic case, spontaneous vesiculation occurs due to initial aggregation, that happens often on a very fast time scale ( $10^{-6}$  -  $10^{-1}$  s). While this initial aggregation is very fast, once vesicles are formed they can continue to evolve over longer time scales (up to weeks or months). This suggests that this type of spontaneous vesiculation leads to out of equilibrium, kinetically controlled, meta-stable structures. The kinetics of spontaneous vesicle formation has been traditionally less studied. However, a review on the kinetics of morphological changes in 2003<sup>15</sup> boosted the research in the topic, and since then more studies were published, covering both experiments and modelling (see an example in work<sup>23</sup>). Decanoate vesicles are an example of kinetic vesiculation<sup>28</sup>.

Another key concept is the one introduced by Israelachvili et al.<sup>19</sup> in 1976, the concept of molecular packing parameter. It uses some simple geometrical considerations to explain the ability of a given amphiphile to pack into very small spherical micelles or conversely to assemble into lamellar phase bilayers. The idea is that an amphiphilic molecule can be described by a single dimensionless parameter  $p$  that combines the volume of the hydrophobic portion of the surfactant molecule,  $v$ , the length of the hydrocarbon chains,  $l$ , and the effective area per head group,  $a$ . These three quantities can be combined in a single dimensionless quantity known as the packing parameter,  $p$ , defined as

$$p = \frac{v}{la}, \quad (1.1)$$

Different values of the packing parameter  $p$  correspond to different self-assembled supramolecular structures. As it can be seen in Figure 1.4, ranges for the packing parameter that correspond to different supramolecular shapes are defined, from micelles to vesicles and inverted micelles. At the same time, by the definition of the formula 1.1, the packing



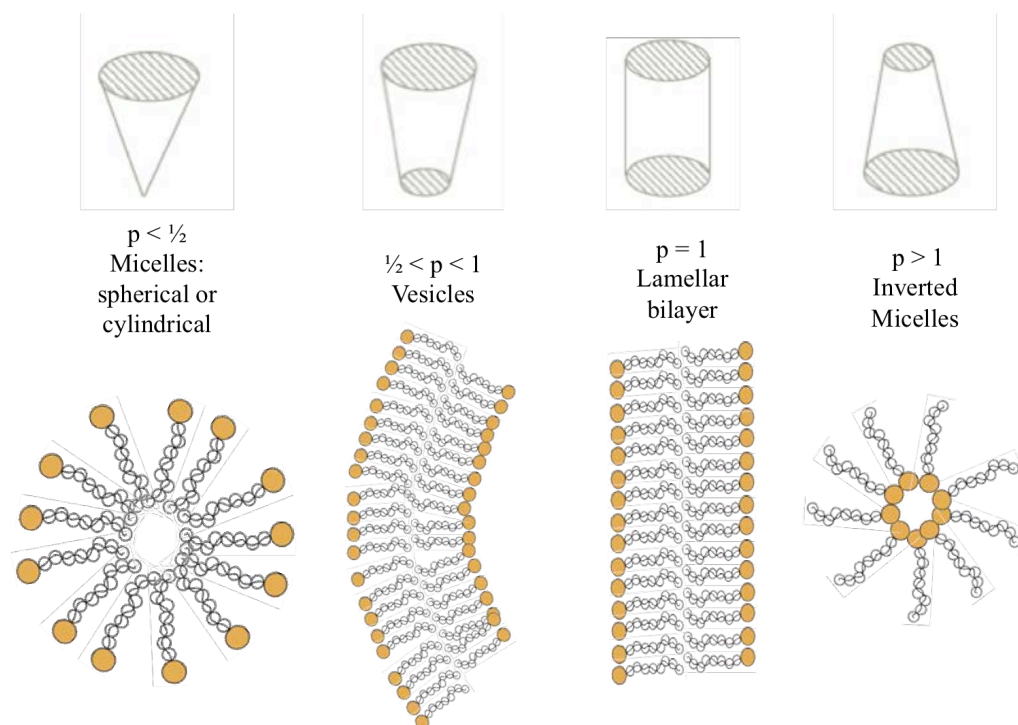


**Figure 1.4:** Different packing parameter values are related to different molecular shapes with their corresponding supramolecular assemblies. Figure partly taken from ref. <sup>17</sup>.

parameter depends on the molecular geometry, defined by  $v$ ,  $l$  and  $a$ . The volume  $v$  and the tail length  $l$  are fixed but the effective area per head group  $a$ , might be affected by temperature or ionic forces, for example. Thus, the form giving the minimum free energy for the parameter  $a$  determines the optimal aggregate. The simplest ones are spherical and cylindrical micelles and bilayers, which are characterized by certain values of the packing parameter as shown in Table 1.1.

**Table 1.1:** Packing parameter values describing the supramolecular assembly and the correspondence molecular shape of the volume occupied by an amphiphilic molecule.

Supramolecular assembly	Packing parameter	Molecular shape
Spherical micelles	$< 1/3$	cone
Cylindrical micelles	$1/3 < p < 1/2$	truncated cone
Vesicles	$1/2 < p < 1$	truncated cone
Planar bilayer	$\sim 1$	cylinder
Inverted micelles	$> 1$	inverted truncated cone

The hydrophobic interaction, as well as the effective molecule conformation, determines the tail volume and length. Branched and double-tailed surfactants, for example, show a much bigger tail volume and hence are more prone to pack into bilayer-based structures, like vesicles or lamellae, rather than into micelles<sup>19,40</sup>.

Based on the explained packing parameter concept, in 1991, Safran et al.<sup>33</sup> performed a study considering two amphiphilic molecules which separately do not form spontaneously vesicles, but other structures like micelles, in aqueous media. They saw that their non-ideal mixing gave rise to a packing parameter that corresponded to the formation of vesicular nanostructures (see Table 1.1). This enabled a new way of vesicle formation by following an indirect strategy: stirring the directionality of the spontaneous assembly by the adequate choice or design of the precursor molecule structures<sup>31</sup>. Following this strategy, it is possible to mimic cases where vesiculation is spontaneous from the thermodynamic perspective. As an example, we have the case employing anionic (sodium dodecyl sulphate) and cationic (dodecylammonium chloride) surfactants, which form cationic vesicles<sup>5</sup>. These two components have a fixed volume and area per head group, it is easy to compute the packing parameter, and it is known that such packing parameter gives rise to the formation of vesicles. Then, it is possible to substitute one or both of the original components for other(s) that maintain the same packing parameter value (mimicking), and the spontaneous formation of vesicles is ensured.

Despite all the research done considering all the vesicular systems, undoubtedly, liposomes are still the most widely used as supramolecular assemblies for nanomedicine, due to their great versatility in size, composition, surface characteristics and capacity for integrating and encapsulating bioactive molecules. Moreover, they are well recognized as pharmaceutical carriers because of their biocompatibility, biodegradability and low toxicity<sup>36,16</sup>. Nevertheless, one of the major problems limiting the widespread use of liposomes is their poor stability, both physical (colloidal), this is, the tendency for aggregation or fusion of vesicles to form larger and heterogeneous particles, and chemical, i.e., hydrolysis of ester

groups and oxidation of unsaturated chains<sup>1</sup>.

The need for alternative vesicular systems with enhanced properties compared to those of liposomes and their current alternatives (such as cationic vesicles) has led to the design of alternative nanovesicles. In particular, cationic vesicles are good candidates due to their capacity to interact with biomolecules. Two examples of this are vesicles (made of mixed cationic lipids) interacting with DNA<sup>4</sup>, or vesicles (made of surfactants like quaternary nitrogen moiety) acting as bactericides<sup>27</sup>.

## 1.2 QUATSOME; A UNIQUE CATIONIC VESICLE MADE OF CTAB AND CHOLESTEROL

As shown in the previous section, a possible route for vesicle formation is mixing two components that, despite individually they may not self-assemble into vesicles, they do so when interacting together. In recent years, a new nanovesicle system has been developed at

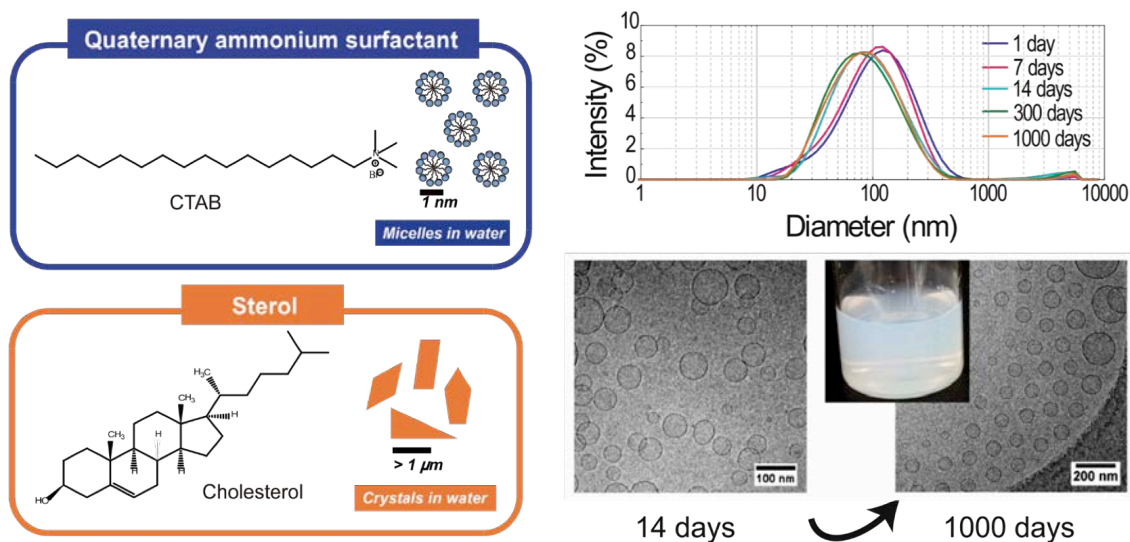


Figure 1.5: CTAB quaternary ammonium surfactant, and cholesterol sterol chemical structures. Dynamic light scattering (DLS) measurements and cryo-TEM images showing the stability of the Quatsome system. DLS measurements and cryo-TEM images are kindly provided by Nanomol group (ICMAB-CSIC).

ICMAB and proven very promising following this approach: the Quatsome or QS, composed of quaternary ammonium surfactants and sterols (Figure 1.5). Those components separated form micelles and crystals respectively, but the adequate mixing of them results in the formation of small unilamellar bilayer vesicles of less than 100 nm in diameter<sup>12</sup>.

This system is stable for periods as long as several years, its morphology does not change upon rising temperature or dilution, and it shows outstanding vesicle-to-vesicle homogeneity regarding size, lamellarity, and membrane supramolecular organization<sup>8,11</sup> (see Figure 1.5). Quatsome system fulfills the structural and physico-chemical requirements to be a potential encapsulation platform for site-specific delivery of both hydrophilic and hydrophobic molecules<sup>6,24</sup>. Many functionalizations can be implemented simultaneously in Quatsomes, either by covalent attachment to sterol-like molecules or by electrostatic interaction with the cationic ammonium head of surfactant units, or by hydrophobic interaction with the bilayer. The QS system is being actively employed for developing new applications, for instance for enhancing specific bioactivity of proteins and protecting them against premature degradation in topical pharmaceutical formulations<sup>7</sup>, or for the topical delivery of the recombinant human epidermal growth factor (rh-EGF) to treat complex wounds<sup>35</sup>, or for acting as fluorescent probe for bioimaging applications<sup>3</sup>. In particular, this last case will

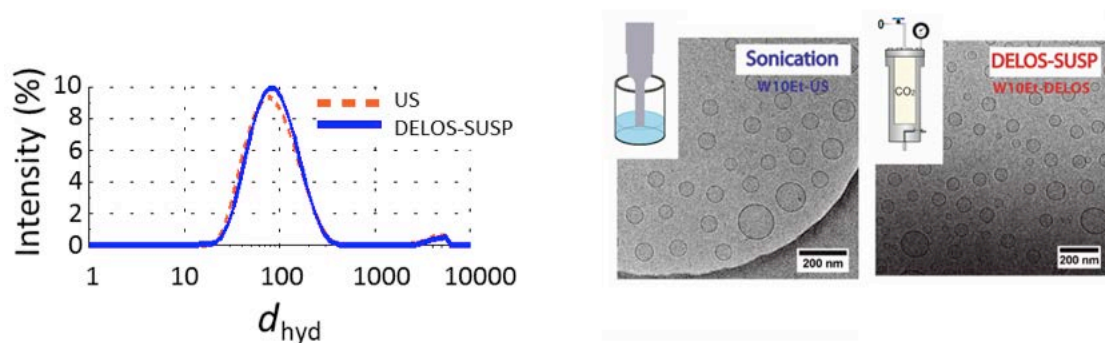
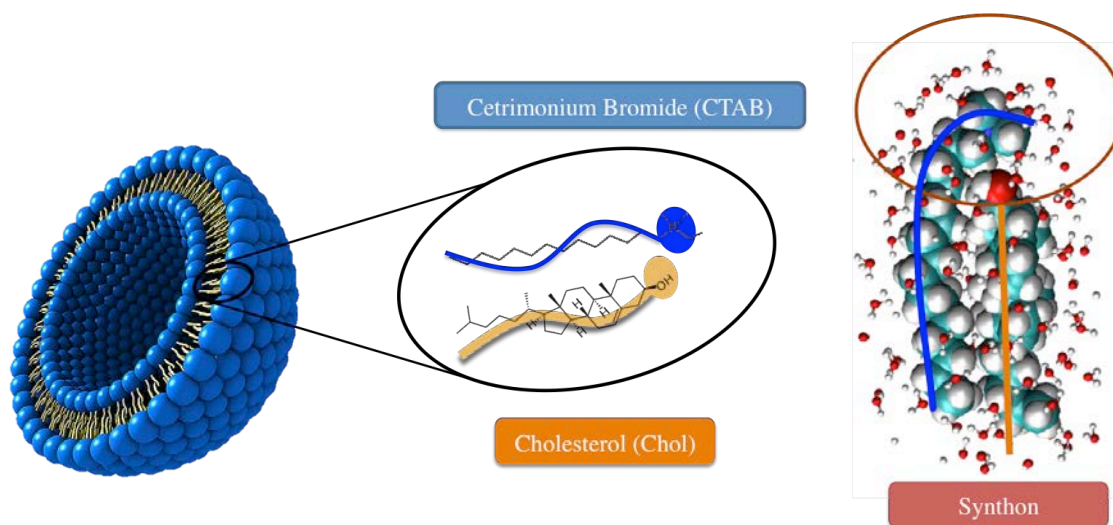


Figure 1.6: Quatsome characteristics of formation path. Left: Light intensity weighted distribution of hydrodynamic diameters  $d_{hyd}$  obtained by DLS, showing largely overlapping size distributions for Quatsomes obtained with ultra-sounds (US) and DELOS-SUSP. Right: cryo-TEM images showing small unilamellar vesicles. Experimental results are provided by Nanomol group (ICMAB-CSIC).

be analyzed in depth in one of the chapters of this thesis.

Quatsomes can be obtained following different preparation routes, resulting in practically identical characteristics<sup>8</sup>. It has been found that size distributions, vesicle morphology and  $\zeta$ -potential are practically identical when Quatsomes are prepared using ultrasounds (US) or the depressurization of a CO<sub>2</sub>-expanded liquid (DELOS-SUSP) (see Figure 1.6). A full description of the methods are also given in the Annex, Figure A.1. In both cases small unilamellar vesicles are obtained, with a  $\zeta$ -potential of  $\sim 100$  mV.

At this point it is worth briefly introducing the components of the Quatsome vesicle; CTAB surfactant and cholesterol. On the one hand, the surfactant  $[\text{N}(\text{CH}_3)_3]^+\text{Br}^-$  known as CTAB (cetyltrimethylammonium bromide), is a quaternary ammonium cationic surfactant, which has a bromide anion as counterion. It is used in many commercial products such as hair conditioning products or antiseptic chemicals. As shown in Figure 1.5, CTAB in water self-assembles in micelles with a cmc of  $\approx 0.9$  mM at 25 °C<sup>26,29</sup>. On the other hand, cholesterol, C<sub>27</sub>H<sub>46</sub>O, is a sterol (a combination steroid and alcohol) and a lipid found in the cell membranes of all body tissues. Cholesterol in water forms crystals due to its insolubility (see Figure 1.5).



**Figure 1.7:** Schematic illustration of the Quatsome vesicle with the Chol/CTAB bimolecular amphiphile components. Snapshot of the synthon made of 1 CTAB and 1 Chol from an all-atomic MD trajectory of this thesis, surrounded by water molecules.

In the work by Ferrer-Tasies et al.<sup>12,13</sup>, the Quatsome system made of a 1:1 mixture of CTAB and cholesterol molecules, was described in detail for the first time. In addition, the first all-atomic molecular dynamics (MD) simulations about the Quatsome were carried out. It was predicted that the synergy between the cetyltrimethyl ammonium ( $\text{CTA}^+$ ) of CTAB and Chol molecules would make them self-assemble into bimolecular amphiphiles, called synthons (see Figure 1.7). It was also predicted that this would lead to the formation of a bilayer, and thereafter, of a vesicle. This was confirmed by the results of the simulations, and the experimental results.

MD simulations were of great importance to understand fundamental concepts of the Quatsome in general, and of the synthon in particular: as a definition, a synthon is found when a CTAB molecule and a cholesterol molecule form an entity with a strong hydrophobic interaction, with a value of free energy ( $\Delta G = -4.7$  kcal/mol) large enough to consider this a noncovalent molecular association (see Figure 1.8). This free energy gives a unique supramolecular synthon, providing a new building block unit for complex structure formation (see snapshot of Figure 1.7 and 1.8). The equilibrium state obtained in the simulations corresponds to an association of the cholesterol molecule with the hydrocarbon chain of the

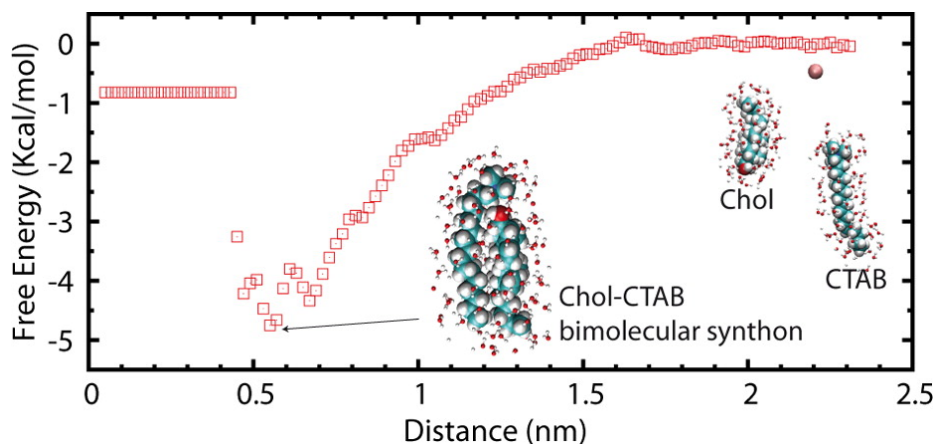


Figure 1.8: Evolution of the Gibbs free energy of interaction between a single CTAB and a single cholesterol molecule in water as a function of the intermolecular distance. A snapshot from MD simulations, showing on the right, the initial state of the simulation, and on the left, the structure of the Chol/CTAB supramolecular synthon at the free-energy minimum state. This Figure is reproduced from ref.<sup>12</sup> with permission from American Chemistry Society.

surfactant. The mismatch in size between the two molecular entities and the rigidity of the cholesterol molecule produces a deformation of the polar ammonium headgroup of the surfactant around the polar oxygen group of cholesterol, as it can be observed also in Figure 1.7. Moreover, the cholesterol has a very low solubility in water, so it tends to interact with CTAB in order to reduce the contact with water<sup>12</sup>.

Also, the packing parameter of the CTAB-Chol synthon can be estimated, approximating the length ( $l$ ) of the hydrocarbon tail by that of the cholesterol molecule (1.73 nm), and computing the volume ( $v$ ) by the sum of both ( $0.54 + 0.40 = 0.94 \text{ nm}^3$ ). The value of the area per head group was taken as equal to the value for pure CTAB ( $a = 0.64 \text{ nm}^2$ ), since the headgroup of the synthon coincides with that of the CTAB surfactant (see the simulation snapshot in Figure 1.7). Using these values, it was obtained a value of  $p = 0.85$ , which is consistent with the packing parameter value for vesicle formation (see Table 1.1).

All these previous results show that this synthon, made of the association of the cationic surfactant and sterol, becomes an effective amphiphilic self-assembled object with a hydrophilic head and two long hydrophobic alkyl tails. The geometric characteristics of the synthon are very similar to those of phospholipids that form bilayers (for its hydrophobic and hydrophilic parts).

So far, these novel QS nanostructures have proven to be very interesting in terms of their physico-chemical properties and their applicability. Since their were first obtained, wide range of experimental work have been done in the Nanomol group at ICMAB with the aim of giving a promising applicability such as fuctionalizing with dyes or proteins. Thus, to be able to do a rational design of the Quatsome system and modifications for future applications, it is a must to deeply understand its structure and interactions at a molecular scale.

Molecular modeling is a mature science ready to be used by the chemist, and not just the theoretical chemist. Desktop computers are now fast enough to do meaningful calculations. The positive experience of how valuable the information given by MD simulations was with

the Quatsome case justifies the strategy followed in this thesis, i.e., to study this system using precisely MD simulations. Besides, although the experimental work about this system has advanced prominently, the simulation work has remained unexplored, reinforcing the motivation for the present thesis.

### 1.3 ORGANIZATION OF THE THESIS AND OBJECTIVES

The main goal of this thesis is to study in detail the Quatsome vesicular system, that is a unique system with outstanding physical and chemical properties. We believe that the good properties that the Quatsome has shown so far deserve the effort of acquiring a deep molecular understanding. In fact, this understanding is required for the Quatsome to attain its full potential, when it comes to applicability. The thesis is divided in three parts: In part I, the systems and methods are introduced. In part II, the Quatsome system is studied with MD simulations. In part III, we study the interaction of QS with dyes. The work ends with conclusions and perspectives. The objectives of each part are as follows:

**PART I:** The goal is to provide an introduction of the work, contextualizing it and showing the state of the art, in **Chapter 1**, and to describe in detail the methods and tools employed, in **Chapter 2**.

**PART II: Molecular dynamics simulations of the Quatsome system:** The main goal of this first part of the thesis is to develop knowledge of the structure and dynamics of the Quatsome system at the atomic and molecular level. The technique employed will be molecular dynamics (MD) simulations, at different resolution scales.

- **Chapter 3:** The objective is to obtain a -detailed, all-atomic analysis of the Quatsome bilayer: the molecular structure and organization, the effect of temperature or the interaction of ions, the elastic properties, etc.



- **Chapter 4:** The ambitious but clear goal is to obtain a molecular picture of the full Quatsome vesicle by using coarse-grain MD simulations, in order to study it at the molecular level.

**PART III: Interaction of Quatsome system with dyes:** The main objective of the second part of the thesis is to explore the possibilities of functionalizing the Quatsome, using it as a mean for nanostructuring several dye molecules of different nature in aqueous media.

- **Chapter 5:** The main goal here is to understand the mechanism of interaction of water-soluble dyes, like fluorescein, over the Quatsome surface. A secondary but still important objective is to properly model the dye, for obtaining reliable results.
- **Chapter 6:** The goal is to explore other alternatives for decorating the Quatsome bilayer, in particular using an hydrophobic family of dyes, the carbocyanines.

# References

- [1] Akbarzadeh, A., Rezaei-Sadabady, R., Davaran, S., Joo, S. W., Zarghami, N., Hanifehpour, Y., Samiei, M., Kouhi, M., & Nejati-Koshki, K. (2013). Liposome: classification, preparation, and applications. *Nanoscale Research Letters*, 8(1), 102+.
- [2] Antonietti, M. & Förster, S. (2003). Vesicles and Liposomes: A Self-Assembly Principle Beyond Lipids. *Advanced Materials*, 15(16), 1323–1333.
- [3] Ardizzone, A. (2017). *New fluorescent nanovesicles, by self-assembly of organic fluorophores, sterols and surfactants, as probes for bioimaging*. PhD thesis, Institut de Ciència de Materials de Barcelona (ICMAB-CSIC).
- [4] Barreleiro, P. C. A., Olofsson, G., & Alexandridis, P. (2000). Interaction of DNA with Cationic Vesicles: A Calorimetric Study. *The Journal of Physical Chemistry B*, 104(32), 7795–7802.
- [5] Bergström, M. & Eriksson, J. C. (1996). The Energetics of Forming Equilibrated Bilayer Vesicles. *Langmuir*, 12(3), 624–635.
- [6] Cabrera, I., Elizondo, E., Esteban, O., Corchero, J. L., Melgarejo, M., Pulido, D., Córdoba, A., Moreno, E., Unzueta, U., Vazquez, E., Abasolo, I., Schwartz, S., Villaverde, A., Albericio, F., Royo, M., García-Parajo, M. F., Ventosa, N., & Veciana, J. (2013). Multifunctional Nanovesicle-Bioactive Conjugates Prepared by a One-Step Scalable Method Using CO<sub>2</sub>-Expanded Solvents. *Nano Letters*, 13(8), 3766–3774.
- [7] Cano-Sarabia, M., Angelova, A., Ventosa, N., Lesieur, S., & Veciana, J. (2010). Cholesterol induced CTAB micelle-to-vesicle phase transitions. *Journal of Colloid and Interface Science*, 350(1), 10–15.
- [8] Cano-Sarabia, M., Ventosa, N., Sala, S., Patiño, C., Arranz, R., & Veciana, J. (2008). Preparation of Uniform Rich Cholesterol Unilamellar Nanovesicles Using CO<sub>2</sub>-Expanded Solvents. *Langmuir*, 24(6), 2433–2437.
- [9] Cevc, G. & Richardsen, H. (1999). Lipid vesicles and membrane fusion. *Advanced Drug Delivery Reviews*, 38(3), 207–232.
- [10] Ciobanu, M., Heurtault, B., Schultz, P., Ruhlmann, C., Muller, C. D., & Frisch, B. (2007). Layersome: Development and optimization of stable liposomes as drug delivery system. *International Journal of Pharmaceutics*, 344(1-2), 154–157.

- [11] Elizondo, E., Larsen, J., Hatzakis, N. S., Cabrera, I., Bjørnholm, T., Veciana, J., Stamou, D., & Ventosa, N. (2012). Influence of the Preparation Route on the Supramolecular Organization of Lipids in a Vesicular System. *Journal of the American Chemical Society*, 134(4), 1918–1921.
- [12] Ferrer-Tasies, L., Moreno-Calvo, E., Cano-Sarabia, M., Aguilera-Arzo, M., Angelova, A., Lesieur, S., Ricart, S., Faraudo, J., Ventosa, N., & Veciana, J. (2013). Quatsomes: Vesicles Formed by Self-Assembly of Sterols and Quaternary Ammonium Surfactants. *Langmuir*, 29(22), 6519–6528.
- [13] Ferrer-Tasies, L. P. (2016). *Cholesterol and Compressed CO<sub>2</sub>: a Smart Molecular Building Block and Advantageous Solvent to Prepare Stable Self-assembled Colloidal Nanostructures*. PhD thesis, ICMAB-CSIC, UAB, Bellaterra.
- [14] Förster, S. & Borchert, K. (2002). *Polymer Vesicles*, chapter 6. John Wiley & Sons, Inc.: Hoboken, NJ, USA.
- [15] Gradzielski, M. (2003). Kinetics of morphological changes in surfactant systems. *Current Opinion in Colloid & Interface Science*, 8(4-5), 337–345.
- [16] Grimaldi, N., Andrade, F., Segovia, N., Ferrer-Tasies, L., Sala, S., Veciana, J., & Ventosa, N. (2016). Lipid-based nanovesicles for nanomedicine. *Chemical Society Reviews*, 45(23), 6520–6545.
- [17] Guida, V. (2010). Thermodynamics and kinetics of vesicles formation processes. *Advances in Colloid and Interface Science*, 161(1-2), 77–88.
- [18] Huang, C., Quinn, D., Sadovskiy, Y., Suresh, S., & Hsia, K. J. (2017). Formation and size distribution of self-assembled vesicles. *Proceedings of the National Academy of Sciences*, 114(11), 2910–2915.
- [19] Israelachvili, J. N., Mitchell, D. J., & Ninham, B. W. (1976). Theory of self-assembly of hydrocarbon amphiphiles into micelles and bilayers. *Journal of the Chemical Society, Faraday Transactions 2*, 72(0), 1525–1568.
- [20] Jung, H. T., Coldren, B., Zasadzinski, J. A., Iampietro, D. J., & Kaler, E. W. (2001). The origins of stability of spontaneous vesicles. *Proceedings of the National Academy of Sciences*, 98(4), 1353–1357.
- [21] Kaazempur-Mofrad, M. R., Bathe, M., Karcher, H., Younis, H. F., Seong, H. C., Shim, E. B., Chan, R. C., Hinton, D. P., Isasi, A. G., Upadhyaya, A., Powers, M. J., Griffith, L. G., & Kamm, R. D. (2003). Role of simulation in understanding biological systems. *Computers & Structures*, 81(8-11), 715–726.
- [22] Karplus, M. & McCammon, J. A. (2002). Molecular dynamics simulations of biomolecules. *Nature Structural Biology*, 9(9), 646–652.
- [23] Leng, J., Egelhaaf, S. U., & Cates, M. E. (2003). Kinetics of the Micelle-to-Vesicle Transition: Aqueous Lecithin-Bile Salt Mixtures. *Biophysical Journal*, 85(3), 1624–1646.

- 
- [24] Liu, X., Ardizzone, A., Sui, B., Anzola, M., Ventosa, N., Liu, T., Veciana, J., & Belfield, K. D. (2017). Fluorenyl-Loaded Quatsome Nanostructured Fluorescent Probes. *ACS Omega*, 2(8), 4112–4122.
- [25] Lyon, L. A. (2001). *Handbook of Applied Surface and Colloid Chemistry*, volume 124. John Wiley & Sons.
- [26] Magnus Bergström, L. (2016). Second CMC in surfactant micellar systems. *Current Opinion in Colloid & Interface Science*, 22, 46–50.
- [27] Martins, L. M. S., Mamizuka, E. M., & Carmona-Ribeiro, A. M. (1997). Cationic Vesicles as Bactericides. *Langmuir*, 13(21), 5583–5587.
- [28] Morigaki, K., Walde, P., Misran, M., & Robinson, B. H. (2003). Thermodynamic and kinetic stability. Properties of micelles and vesicles formed by the decanoic acid/decanoate system. *Colloids and Surfaces A: Physicochemical and Engineering Aspects*, 213(1), 37–44.
- [29] Moulik, S. P., Haque, M., Jana, P. K., & Das, A. R. (1996). Micellar Properties of Cationic Surfactants in Pure and Mixed States. *The Journal of Physical Chemistry*, 100(2), 701–708.
- [30] Ninham, B. W. & Nostro, P. (2010). *Molecular forces and self-assembly: in colloid, nano sciences and biology*. Cambridge University Press.
- [31] Packwood, D. M., Han, P., & Hitosugi, T. (2017). Chemical and entropic control on the molecular self-assembly process. *Nature Communications*, 8, 14463+.
- [32] Park, J. W., Hong, K., Kirpotin, D. B., Papahadjopoulos, D., & Benz, C. C. (1997). *Immunoliposomes for Cancer Treatment*, volume 40, (pp. 399–435). Elsevier.
- [33] Safran, S. A., Pincus, P., & Andelman, D. (1990). Theory of Spontaneous Vesicle Formation in Surfactant Mixtures. *Science*, 248(4953), 354–356.
- [34] Sansom, C. E. & Smith, C. A. (1998). Computer applications in the biomolecular sciences. Part 1: molecular modelling. *Biochemical Education*, 26(2), 103–110.
- [35] Santana, H., Ventosa, L., Martinez, E., Berlanga, J., Cabrera, I., & Veciana, J. (2012). Vesicles comprising epidermal growth factor and compositions. *Patent WO2014/019555*.
- [36] Sawant, R. R. & Torchilin, V. P. (2010). Liposomes as 'smart' pharmaceutical nanocarriers. *Soft Matter*, 6(17), 4026+.
- [37] Shi, D., Sfintes, G., Laursen, B. W., & Simonsen, J. B. (2012). Fluorescent and Highly Stable Unimodal DMPC Based Unilamellar Vesicles Formed by Spontaneous Curvature. *Langmuir*, 28(23), 8608–8615.
- [38] Shioi, A. & Hatton, T. A. (2002). Model for Formation and Growth of Vesicles in Mixed Anionic/Cationic (SOS/CTAB) Surfactant Systems. *Langmuir*, 18(20), 7341–7348.

- [39] Sulkowski, W. W., Pentak, D., Nowak, K., & Sulowska, A. (2005). The influence of temperature, cholesterol content and pH on liposome stability. *Journal of Molecular Structure*, 744-747, 737–747.
- [40] Svenson, S. (2004). Controlling surfactant self-assembly. *Current Opinion in Colloid & Interface Science*, 9(3-4), 201–212.
- [41] Talegaonkar, S., Mishra, P. R., Khar, R. K., & Biju, S. S. (2006). Vesicular systems: An overview. *Indian Journal of Pharmaceutical Sciences*, 68(2), 141+.
- [42] ten Cate, M. G. J., Crego-Calama, M., & Reinhoudt, D. N. (2004). Formation of a Hydrogen-Bonded Receptor Assembly in Niosomal Membranes. *Journal of the American Chemical Society*, 126(35), 10840–10841.
- [43] Tonigold, M., Simon, J., Estupiñán, D., Kokkinopoulou, M., Reinholz, J., Kintzel, U., Kaltbeitzel, A., Renz, P., Domogalla, M. P., Steinbrink, K., Lieberwirth, I., Crespy, D., Landfester, K., & Mailänder, V. (2018). Pre-adsorption of antibodies enables targeting of nanocarriers despite a biomolecular corona. *Nature Nanotechnology*, 13(9), 862–869.
- [44] Šegota, S. & Težak, D. (2006). Spontaneous formation of vesicles. *Advances in Colloid and Interface Science*, 121(1-3), 51–75.
- [45] Wiesman, Z., Dom, N., Sharvit, E., Grinberg, S., Linder, C., Heldman, E., & Zaccai, M. (2007). Novel cationic vesicle platform derived from vernonia oil for efficient delivery of DNA through plant cuticle membranes. *Journal of Biotechnology*, 130(1), 85–94.

*Know how to learn. Then want to learn.*

Katherine Johnson

# 2

## Methods: Molecular Modelling

The most extensively employed tools in this thesis are molecular modelling techniques. These tools have relevance enough in this work to constitute an end by themselves. For this reason, we dedicate the present chapter to them. As a general description, molecular modeling techniques compute the motion of atoms and explore configurations or compute the potential energy of a molecule given its molecular geometry. Firstly, there are two main techniques to evaluate the energy of the molecules and their configurations during the simulation; molecular mechanics (MM), or quantum mechanics (QM). Afterwards, once the energies are known, it is possible to calculate their movement (for instance via the

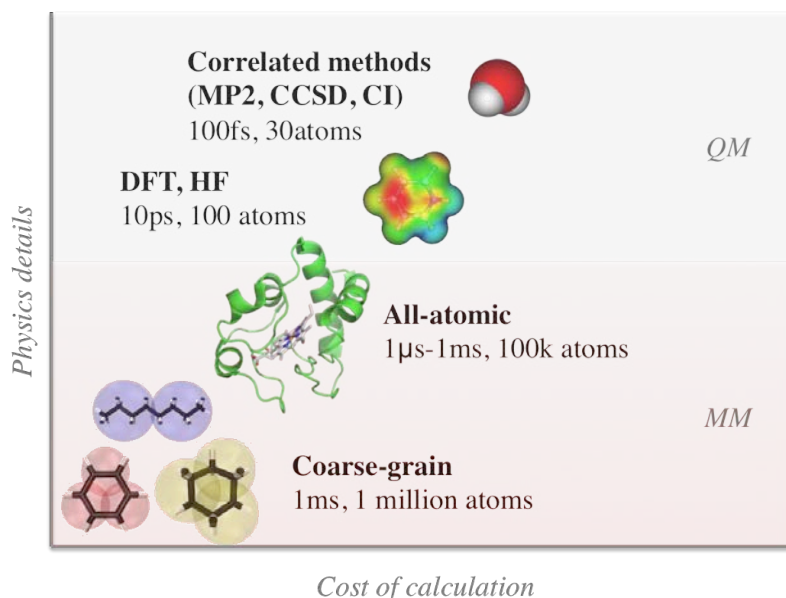


**Figure 2.1: General scheme classifying molecular modelling methods for the calculation of forces and energies in MD simulations within its physics details and cost of calculation.**

molecular dynamics (MD) method) or their thermodynamic behaviour (for instance via the Monte Carlo (MC) method). The differences between methods are mainly about the trade-offs made between computational cost and accuracy (see Figure 2.1).

The main concept in **Molecular Dynamics (MD)** method is to solve numerically the equations of motion of an atomistic model of a system. It implies developing an atomic model of the whole system, which may include a large number of atoms. It computes the equilibrium and transport properties of a classical many-body system. In this context, the word classical means that the nuclear motion of the constituent particles obeys the laws of classical mechanics<sup>16</sup>, albeit their interactions forces have quantum energies. A detailed description will be given in the following section.

**Monte Carlo (MC)** method is based on the generation of stochastic trajectories within a given statistical mechanical ensemble. Typical choices include the canonical (NVT) and isothermal–isobaric (NPT) ensembles. Any viable Monte Carlo procedure must sample the Boltzmann distribution and uphold the principle of detailed balance (microscopic reversibility). Thus, new configurations are rejected or accepted depending on a given probabilistic

criterion<sup>35</sup>. Provided that the sampling procedure is ergodic<sup>7</sup> (i.e. every point in configuration space is accessible from any other point), Monte Carlo sampling can be coupled with statistical mechanics to obtain the equilibrium thermodynamic properties of a system. As an example, MC methods have been often exploited for conformation calculations on proteins<sup>24</sup>.

MD and MC simulations require methods to calculate the energies. Those are the MM and QM methods described below:

**Molecular mechanics (MM)** methods are based on classical mechanics. MM methods are computationally very cheap and can be applied to systems as large as millions of atoms. They employ force fields comprised of parameter sets and specific functional forms to model the molecular potential energy as the interactions between pairs of atoms. In MD simulations, they model molecular behaviour over time. Two broad areas of study that give rise to two approaches that employ MM methods can be defined: in the context of electronic structure calculations, the use of hybrid quantum mechanics-molecular mechanics (QM:MM) approach, and in the context of classical Newtonian mechanics, the use of molecular dynamics (MD).

**Quantum mechanics (QM)** methods base their computations solely on the laws of their name, predominantly the Schrödinger equation (Equation 2.1). There are many different methods for the calculation of electronic structure. For example, semi-empirical calculations are relatively inexpensive and provide reasonable qualitative descriptions of molecular systems and fairly accurate quantitative predictions of energies and structures for systems where good parameter sets exists. In contrast, density functional theory (DFT) computations are more expensive but provide high quality quantitative predictions for a broad range of systems; they are not limited to any specific set of elements, class of system or chemical environment.

$$H\psi(\vec{r}, \vec{R}) = E\psi(\vec{r}, \vec{R}) \quad (2.1)$$

In this thesis we have used molecular dynamics (MD) simulations and different methods



from both MM and QM approaches to describe the molecular energies such as DFT from QM, and all-atomic and coarse-grain force fields from MM. All these methods have been employed for simulating different complex problems, for example, DFT method has been employed to parametrize MM force fields for MD simulations. At the same time, within MD, two modalities have been employed, all-atomic (AA) simulations and coarse-grain (CG) simulations. DFT has been employed for the geometry optimization of new models, those developed in this work. MD has been used for simulating the trajectories of the analyzed systems. As it can be seen, the simulator is continuously confronted with questions concerning the choice of techniques, because a bewildering variety of computational tools is available. We believe that, to make a rational choice, a good understanding of the physics behind each technique is essential. Accordingly, a detailed explanation of the principles underlying every employed method will be provided.

## 2.1 MOLECULAR MODELLING: DENSITY FUNCTIONAL THEORY

Density Functional Theory (DFT) can be defined as an electron correlation method that can lead to highly accurate values of the energies of atomic and molecular systems. However, this accuracy comes at a significant computational cost, limiting the application of these methods to relatively small molecules. If we want to answer questions that can only be addressed by modeling large number of atoms, another approach needs to be taken.

DFT provides this alternative<sup>20,29</sup>. The rudiments of this theory are originated from the Thomas-Fermi-Dirac model of the 1920s and from Slater's work in the 1950s. The Hohenberg-Kohn theorem, which proves the existence of a unique functional that determines the ground state energy and density of a system, was published in 1964<sup>20</sup>. But, it was not until the 1990s that DFT became widely used. Although the theory itself is quite precise, its implementation has not been so. Researchers continue to work to refine and improve the models, and each year many new density functional approximations (DFAs) are offered to the computational chemistry community.

The basic premise behind DFT is that the energy and associated properties of any system containing electrons are calculable from the probability distribution that is the total electron density,  $\varrho(\vec{r})$ . Using an orbital basis set, this quantity can be easily obtained as:

$$\varrho(\vec{r}_g) = \sum_i^{\text{occupied}} \varphi_i^2(\vec{r}_g) \quad (2.2)$$

Here the position vector,  $\vec{r}_g$ , represents all space coordinates for the system as defined by a grid  $g$ . The probability of observing an electron in the volume element at  $\vec{r}_g$  is  $\varrho \vec{r}_g$ . While it may be intuitively useful to picture the volume surrounding a molecule as divided into a three-dimensional rectangular grid of small cubic elements, the grids typically used in calculations employ spherical and radial coordinates centered on each atom.

Although it generally produces much more accurate results, typical DFT implementations use much of the same computational infrastructure as the Hartree-Fock method, which accounts for its speed and efficiency. In its "pure" form, DFT uses the following expression for the energy as a functional of the density:

$$E_{DFT}[\varrho(\vec{r})] = T[\varrho(\vec{r})] + V_{NE} + J[\varrho(\vec{r})] + E_{XC}[\varrho(\vec{r})] \quad (2.3)$$

The first three terms come from the Hartree-Fock theory<sup>19,14</sup>. The final term is known as the *exchange-correlation term*. It models the parts of the electron-electron interactions that are neglected by Hartree-Fock theory.

Those include exchange and correlation interactions. Unlike the coulombic repulsions, which are evaluated using integrals involving basis functions, this new quantity is evaluated by summing over a grid of points, with each volume element multiplied by a weighting factor,  $w_g$ . This technique was suggested by Kohn and Sham in 1965<sup>29</sup>. The additional work required scales more or less the same as a Hartree-Fock calculation, allowing DFT models to study a wide range of systems, including ones with very large number of atoms.

Unfortunately, the exact specification of  $E_{XC}$  is not known. Its form has been postulated

from the equations describing a uniform electron gas, from the exact solution of the hydrogen atom, by parametrization with experiments, and in other fashions, giving rise to a multitude of density functional approximations (DFAs). The more relevant functionals are: the local density approximation (LDA)<sup>40</sup>, the generalised gradients approximation (GGA)<sup>4</sup>, hybrid functionals<sup>8</sup>. Furthermore, once the choice of the exchange-correlation energy functional is made, the accuracy of any quantum calculation will depend on the basis set choice. There are two main categories of basis set<sup>44</sup>: the Slater-type Orbitals (STO) and the Gaussian-type Orbitals (GTO).

In this thesis we will employ DFT to obtain equilibrium molecular structures, charge distributions and molecular conformational energies. Mainly in Chapters 5 and 6.

## 2.2 MOLECULAR MODELLING: FORCE FIELD ALL-ATOMIC MOLECULAR DYNAMICS (MM-MD)

MD has become a popular and successful methodology to investigate the behavior of molecular systems at an atomistic and molecular scale, because it provides structural information at temporal and spatial resolutions much finer than those achieved by most experimental techniques. Two methods within the MD approach are all-atomic (AA) and coarse-grain (CG) methods. The first one is explained in this section, and the second one in the next.

The use of all-atomic MD simulations to study a molecular system requires three main steps as represented in Figure 2.2. The first step is about the design of the molecular atomistic structure and the environment, based on their chemistry. The second one is about the interaction models between atoms, which corresponds to the physical-chemistry part. This consists in studying the atomistic interactions inside the molecule or with another molecules in a well-defined thermodynamic system. And finally, the last step is about the methods simulating the motion of atoms based on physics. Once having all this information it is possible to make relevant predictions. This three steps are summarized in the following scheme (Figure 2.2).

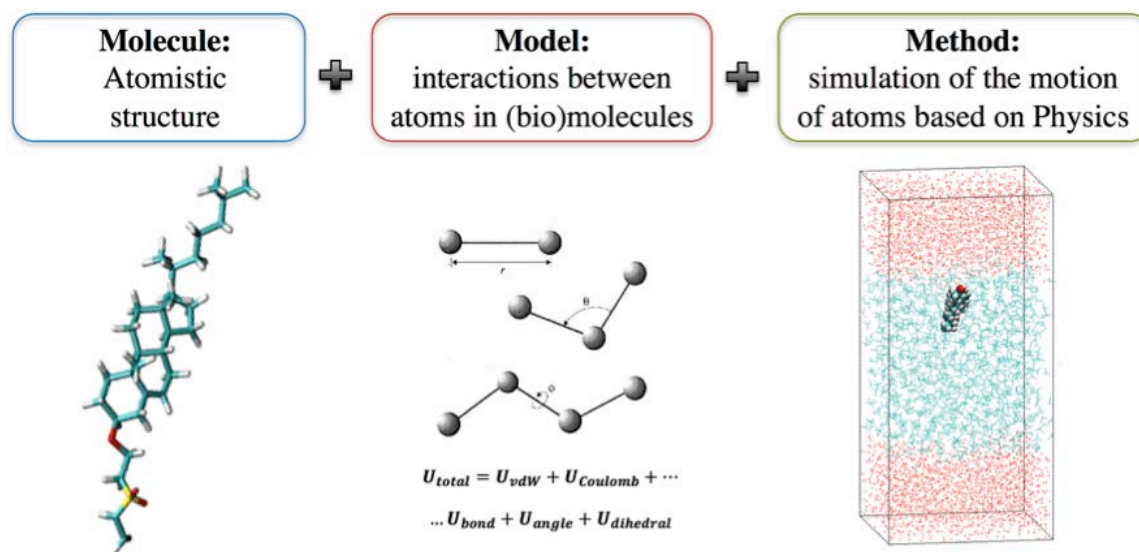


Figure 2.2: General scheme of the different parts of the all-atom MD simulations methodology.

For the last step, different algorithms have been designed to integrate numerically the equations of motion. Also, many programs and computational tools are readily available for performing MD simulations such as LAMMPS<sup>42</sup>, GROMACS<sup>5</sup>, NAMD<sup>41</sup>, DL\_POCY<sup>48</sup> and many others. In this thesis, we will employ mostly NAMD code for AA-MD simulations but also GROMACS for CG-MD simulations. On one hand, NAMD (Nanoscale Molecular Dynamics), can be defined as a parallel molecular dynamics code designed for high performance simulation of large biomolecular systems. NAMD employs the prioritized message-driven execution capabilities of the Charm<sup>++</sup>/Converse parallel runtime system, allowing excellent parallel scaling on both massively parallel supercomputers and commodity workstation clusters. The source code is distributed under the University of Illinois/NCSA Open Source License ([www.ks.uiuc.edu/Research/namd/](http://www.ks.uiuc.edu/Research/namd/)) to allow scientists total freedom of use and modification of code. On the other hand, GROMACS is a versatile package to perform molecular dynamics with hundreds to millions of particles. It is primarily designed for biochemical molecules like proteins, lipids and nucleic acids that have a lot of complicated bonded interactions, but since GROMACS is extremely fast at calculating the non-bonded interactions it is also used on non-biological systems, e.g. polymers. It also has

excellent CUDA-based GPU acceleration capabilities. GROMACS is also a free software, available under the GNU Lesser General Public License.

### 2.2.1 ATOMISTIC STRUCTURE

The first stage of conducting any MD simulation is the assignment of the initial spatial coordinates of the system. In computational modelling there are different file formats to describe the atomistic structure of the molecules. Some of the most used and standardized are on one hand the protein data bank (*.pdb*) file format, where all the atom coordinates in x, y and z are described (and optionally the atomic connectivity), and on the other hand protein structure (*.psf*) file format, where one obtains all the general information about the structure of the molecule, e.g. how atoms are bonded (covalent bonds, angles and dihedrals) and the charge distribution of the molecule. Originally, these file formats were generated for helping to define proteins, but nowadays they are used for all types of molecules. The atomic coordinates of both *.pdb* and *.psf* files are obtained experimentally by X-Ray spectrometry and nuclear magnetic resonance spectroscopy (NMR), and can be usually downloaded from computational repositories like Protein Data Bank<sup>6</sup> for biomolecules or HIC-Up<sup>28</sup> for mainly non-bio ones. For more complex molecular geometries, that cannot be found in those repositories, there are a number of different software packages to generate initial configurations such as GaussView<sup>10</sup> or Insane<sup>56</sup>. In this thesis, the first one has been used for generating initial configurations for organic dyes, and the second one for phospholipid or Quatsome bilayers.

### 2.2.2 MODELING ATOMIC INTERACTIONS

Once having the atomic positions and the molecular structure, the next step is to find out the inter or intra-molecular interactions between atoms (see Figure 2.2). They can be calculated either by QM or *ab-initio*-MD method, or by MM-MD method. The first one calculates the potential energy surface at a quantum level in each step. The computational

effort is huge (see Figure 2.1) and thus, it is used only in small systems and time scales (until few ps). The MM-MD method calculates the instantaneous force on each atom as a gradient of a prescribed interatomic potential function. In this work we will employ MM-MD, which is the only possible chance given the time and length scales that we will consider. This information is collected in the force field, which provides pre-defined classical potential functions that describe the interactions between atoms and/or molecules covering a broad range of elements and systems. They mainly reproduce molecules' properties as well as the properties of the solvent.

Efforts have been made in order to create standardized molecular force field repositories. Several force fields have been optimized so that the modelled molecule reproduces experimental data for small organic molecules, both synthetic and biological. Among these force fields are OPLS<sup>26</sup>, CHARMM<sup>51</sup>, UFF<sup>43</sup>, AMBER<sup>54</sup>, MARTINI<sup>31</sup>. In this work, the CHARMM force field has been used to describe interactions in all of the all-atomic MD simulations, whereas the MARTINI force field has been used for the coarse-grained MD simulations.

The CHARMM force field files are contained in its repository, the CHARMM GENeral Force Field (CGenFF)<sup>52</sup>. CGenFF is an organic force field repository explicitly aimed at simulating drug-like molecules in a biological environment. Other repository options like GAFF (General AMBER Force Field)<sup>54</sup> exist, although the principles underlying all of them, the modelling of the interactions between all atoms, is the same for all.

Nevertheless, sometimes the information is not available or is not precise enough in those general repositories, for some complex molecules or systems. Thus, sometimes the main challenge is to create a force field for specific systems of interest in order to cover the vast chemical space of the organic molecules. To attain this, a systematic optimization protocol must be followed, which is detailed in the following subsections.

## FORCE FIELD FUNCTIONS

To develop a new force field file, this is, to model the interactions for all atoms of a system, one assumes that every atom experiences a force specified by a model force field accounting for the interaction of that atom with the rest of the system. Today, such model force fields present a good compromise between accuracy and computational efficiency. Then, the total potential energy of a molecular system can be expressed as follows by two contributions:

$$U_{total} = U_{non\_bonded} + U_{bonded}, \quad (2.4)$$

The first term amounts for the interactions between non-bonded atom pairs, whereas the second term corresponds to bonded ones. For deeper details the following sources can be checked<sup>23,34</sup>.

- **Intermolecular or non-bonded interactions**, describe the interactions not related to chemical bonds. The first term of the Equation 2.5 is known as Lennard-Jones or van der Waals potential and the second one is Coulomb's force and describes the energy of interaction between charges:

$$U_{non-bonded} = U_{LJ}(r_{ij}) + U_{Coulomb} = 4\epsilon_{ij} \left[ \left( \frac{\sigma_{ij}^{12}}{r_{ij}} - \frac{\sigma_{ij}^6}{r_{ij}} \right) \right] + \frac{q_1 q_2}{4\pi \epsilon_0 r_{ij}}, \quad (2.5)$$

where  $\epsilon_{ij}$  and  $\sigma_{ij}$  denote the characteristic interaction energy and distance respectively for particles  $i$  and  $j$ ,  $q_i$  and  $q_j$  are the charges of particles  $i$  and  $j$  respectively, and  $\epsilon_0$  denotes the permittivity of free space. Both the Lennard-Jones and Coulombic interactions depends on the distance  $\mathbf{r}_{ij}$ .

The Lennard-Jones potential (Figure 2.3) has two exponents; the 12-potential increases the energy as the atoms get closer (preventing the collapse of atoms) while 6-potential decreases the energy and models an attractive force that exists between any neutral atoms, in other words, it is the short-range repulsion due to the Pauli

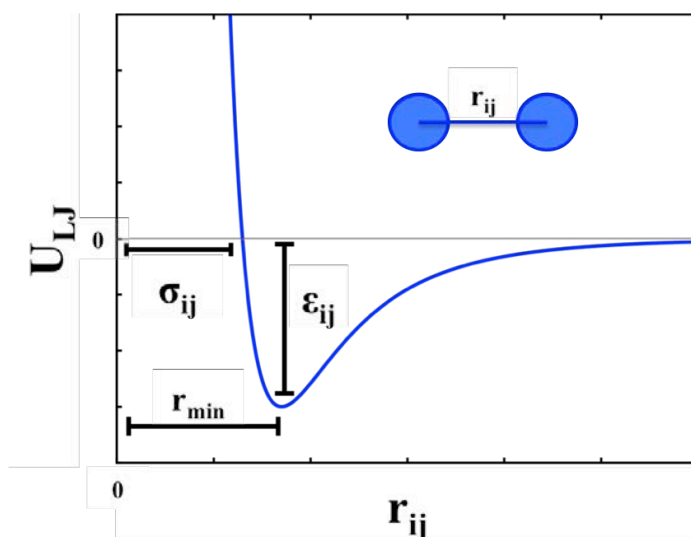


Figure 2.3: A graph showing functional form of the Lennard-Jones potential.

exclusion principle<sup>11</sup>. As this van der Waals interaction exists between every non-bonded pair of atoms in the system, computing the long-range interaction is unfeasible. For this reason it is spatially truncated in NAMD, at a user-specified cutoff distance, normally at  $2.5\sigma$  ( $\sim 10-12$  Å).

As in the Van der Waals case, the electrostatic interactions happen between every non-bonded pair of atoms. With periodic boundary conditions, as it is the case in NAMD, the computation of such interaction requires the particle-mesh Ewald method (PME), which is based in Ewald sum. This sum describes the long-range electrostatic interactions for a spatially limited system with periodic boundary conditions (for more details see Ewald sums at p. 292 in ref.<sup>16</sup>), and the PME is a fast numerical method for computing the Ewald sum, involving a grid scheme, interpolation basis functions and the Fast Fourier Transform<sup>41</sup>.

- **Intramolecular or bonded interactions**, describe the interactions between atoms of the same molecule. In Equation 2.6, *bonds* corresponds to each covalent bond in the system, *angles* refers to the angle between each pair of covalent bonds sharing a single atom at the vertex, and *dihedral* describes atom pairs separated by exactly



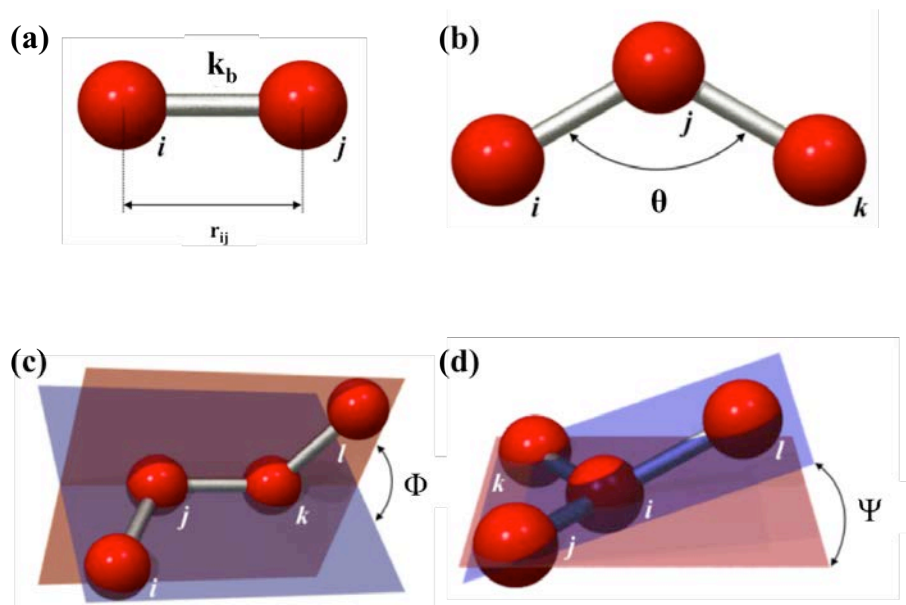


Figure 2.4: Schematic diagrams illustrating the various contributions to the bonded potential energy: a) bonds, b) angles, c) dihedrals and d) improper angles.

three covalent bonds with the central bond subject to a torsion angle (see Figure 2.4).

The total bonded contributions to the potential energy are given by the expression:

$$U_{\text{Bonded}} = \sum_{\text{bonds}} \frac{k_b}{2} (l - l_0)^2 + \sum_{\text{angles}} \frac{k_{\vartheta}}{2} (\vartheta - \vartheta_0)^2 + \sum_{\text{dihedrals}} \frac{k_{\varphi}}{2} (1 + \cos(n\varphi - \varphi_0))^2 + \sum_{\text{impropers}} \frac{k_{\psi}}{2} (\psi - \psi_0)^2 + \sum_{\text{Urey-Bradley}} \frac{k_u}{2} (u_{1,3} - u_{1,3}^0)^2, \quad (2.6)$$

where the force constants  $k_b$ ,  $k_{\vartheta}$ ,  $k_{\varphi}$ , indicate the amount of energy required to stretch or compress a chemical bond, angle or dihedral. Nowadays, quantum mechanical methods like DFT provide accurate values for bond, angle and dihedral parameters.  $n$  corresponds to the multiplicity and  $\varphi_0$  is the phase factor which determines the location of the minima in the potential. Finally, improper angles are imposed on some molecules to preserve geometry or chirality of atoms in a molecule, i.e. to maintain the planarity of aromatic rings in a fluorescein molecule.

## CHARMM PARAMETRIZATION PHILOSOPHY

As mentioned, CHARMM GENeral Force Field (CGenFF)<sup>52</sup> has been designed to cover the majority of atom types in many chemical applications. In principle, its parametrization for a new molecule is done as follows. It is based in identifying compounds whose force field is available from a validated parametrization from experimental data or DFT calculations and that are chemically similar to the compound of interest. These available compounds are then used as the starting point to create an initial topology; information from the available compounds in CGenFF should be used to select the appropriate atom types and initial estimates of the partial atomic charges<sup>57</sup>.

Firstly, the functional groups of the molecule of interest such as acids, amines, and alkyl moieties are assigned available parameters from CGenFF. Next, taking advantage of the modular nature of the distribution of charges in CHARMM, the charges are distributed among the atoms, preserving the total integer charge of the molecule. In the case of adding functional groups to an existing molecule, typically the addition of the available parameters of the appended functional group suffices for having a force field that is ready to use, without the need of further action. At this point it is worth noting that the partial atomic charges in CHARMM are obtained as initial estimates by analogy, or alternatively, taken from DFT at molecular level MP2/6-31G(d) Merz-Kollman charges.

However, in some cases new parameters may be required, often when more complex functional groups or linkers are added. Then, it will be necessary to assign wildcards or add explicit parameters. This situation (the need of new parameters) is identified by the presence of warnings in the built output force field file. Usually, these warnings are in the form of "penalty scores" associated with the partial charges and parameters. When that occurs, the new parameters need to be found by means of QM calculations, and the whole system must be validated. Penalties between 10 and 50 indicate that some basic validation is recommended; penalties higher than 50 are usually associated with parameters or charges that need additional optimization<sup>51</sup>.

## PARAMETRIZATION PROCEDURE FOR NEW COMPOUNDS

When working with a new compound, there will usually be a number of parameters that need to be validated and optimized. As explained in the previous subsection, once initial guesses are assigned to the new parameters, the user should test those parameters to determine if optimization is required.

*Geometry Optimization:* The way the total energy (the sum of the electronic and nuclear repulsion energies) of a molecular system varies with a small change in its structure is described by its potential energy surface (PES), which mathematically links the molecular structure and the resultant energy. We used QM calculations (see section 2.1) by means of Gaussian09 software for optimization of the molecular structure as well as the energy and other related properties. The structural changes that the molecule undergoes in the course of optimization can be visualized in GaussView<sup>10</sup>. In our case, we are interested in obtaining an energy minimum. A condition for obtaining a satisfactory value is that frequencies related to the second derivative of the energy have a 0 imaginary part.

For more details, in Chapter 5 there is an example of the parametrization procedure for a new compound, the case of fluorescein molecule. In that chapter we explain how we partition the molecule into fragments, identify model compounds and derive parameters by analogy, assemble molecules and construct molecular topology file, perform energy minimization and identify potential issues, identify and optimize any missing internal parameter and validate the new model using experimental data<sup>57</sup>.

## 2.2.3 MD SIMULATION METHOD

Summarizing, once an initial set of coordinates has been generated (section 2.2.1), energy minimization is performed to bring the system to a minimum of the potential energy landscape (section 2.2.2). Several numerical methods can be employed to accomplish the minimization, in this case being our choice the steepest descent algorithm<sup>1</sup>. Moreover, initial velocities are assigned a random value taken from a Maxwell-Boltzmann distribution.

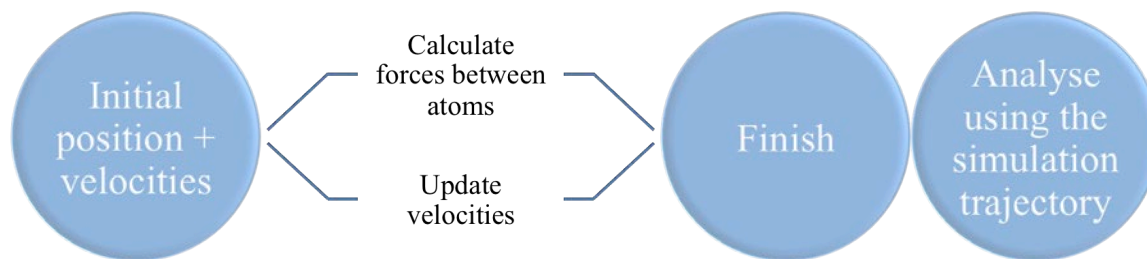


**Figure 2.5: Scheme of the MD simulation method.**

Interactions between the atoms, i.e. the interatomic forces, can be calculated based on various methods, ranging from density functional theory (DFT) to classical potentials. These forces determine the acceleration of the atoms and allow to propagate the positions and velocities across the simulation time, to the next discretized time step. Repeating this procedure yields a series of snapshots, describing the trajectory of the system in phase space, which can be analyzed to extract the desired properties (see scheme in Figure 2.5).

## NUMERICAL INTEGRATION OF THE NEWTONIAN EQUATION OF MOTION

All-atomic molecular dynamics simulations are a technique for computing the equilibrium and transport properties of a classical many-body system. In this context, the word classical refers to the fact that the MD method is based in solving numerically the Newton's equations of motion (classical mechanics)

$$F_i = m_i a_i; a_i = \frac{dv_i}{dt}; v_i = \frac{dr_i}{dt}, \quad (2.7)$$

for the interacting particles of the system (atoms or molecule) that we want to simulate. In all-atomic MD simulations, atoms are considered as classical entities, obeying Newton's Laws of motion. Electrons are not considered in classical MD. This method is an excellent approximation for a wide range of soft matter systems despite it has some limitations.

Different algorithms have been designed to integrate numerically the equations of mo-

tion. The most commonly used time integration algorithm is probably the so-called Verlet algorithm<sup>18</sup>. The basic idea is to write two third-order Taylor expansions for the positions of the atoms, one forward and one backward in time. A problem with this version of the Verlet algorithm is that velocities are not directly calculated. A better implementation of the same basic algorithm is the so-called velocity Verlet<sup>47</sup> scheme, where positions, velocities and accelerations are computed at time  $(t+\delta t)$ . The Velocity-Verlet algorithm obtains recursively the position and velocity at the next time step  $(r_{n+1}, v_{n+1})$  from the current one  $(r_n, v_n)$ , assuming that the force  $F_n = F(r_n)$  is computed. In the following equations this algorithm is shown (where  $m_m$  is the mass):

$$\textit{half-kick}; r_i(t + \delta t) = r_i + v_i(t)\delta t + \frac{1}{2}a_i(t)\delta t^2 \quad (2.8)$$

$$\textit{drift}; v_i\left(t + \frac{\delta t}{2}\right) = v_i(t) + a_i(t)\frac{\delta t}{2} \quad (2.9)$$

$$\textit{computer-force}; a_i(t + \delta t) = -\frac{1}{m_i}\nabla V(r(t + \delta t)) \quad (2.10)$$

$$\textit{half-kick}; v_i(t + \delta t) = v_i\left(t + \frac{\delta t}{2}\right) + a_i(t + \delta t)\frac{\delta t}{2} \quad (2.11)$$

The algorithm is composed by four steps as show above. The main point, however, is that being in an initial position and velocity  $(r_n, v_n)$ , and wanting to calculate the next position  $(r_{n+1})$ , an intermediate velocity called half-kick is calculated with the Equation 2.8. This new velocity  $(v_{n+1/2})$ , Equation 2.9, will be different from the initial one  $(v_n)$  and the final one  $(v_{n+1})$ . Then, the final velocity  $(v_{n+1})$  can be calculated (Equation 2.11) and used to compute the final position  $(r_{n+1})$ . This is commonly achieved via numerical integration by discretizing the time into small intervals called the time step ( $\delta t$  or  $\Delta t$ ). The time step defines the resolution of the numerical integration, thus, it will exist a trade off between choosing a time step sufficiently small to capture vibrations of atoms or sufficiently large to be computationally efficient. In the all-atomic simulations performed in this thesis a timestep of 2 fs is employed, as molecules selected in this framework are flexible and the

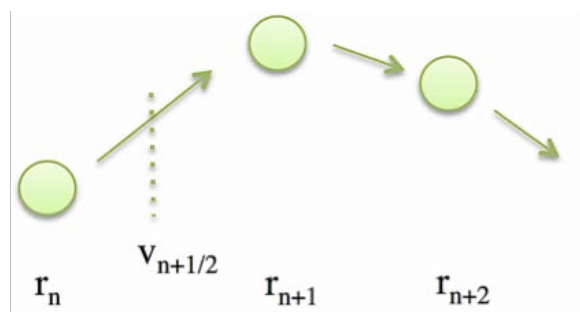


Figure 2.6: Graphic scheme of the Verlet-Velocity trajectory.

bonds are rigid, which means that the only limitation will be the lack of vibration of the atoms.

The Velocity-Verlet is an efficient algorithm that gives accurate results with few equations, with short time of calculation. More detailed discussion of more complex algorithms and their limitations can be found in chapter 4 of textbook by Frenkel and Smit<sup>16</sup>.

## BOUNDARY CONDITIONS

This section verses about boundary conditions, which are a fundamental computational concept for any efficient simulation program. The description of the concept and a discussion about it follows.

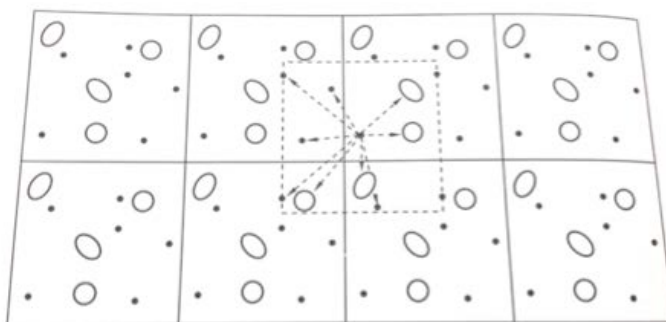


Figure 2.7: Schematic representation of periodic boundary conditions. Figure reproduced from ref.<sup>16</sup>.

The movement of atoms with a simulation program is confined to a simulation box with finite volume. A problem arises when atoms reach the boundary of the box. Without

boundary conditions, this situation would entail alterations of the system due to interactions with the walls. This is avoided by considering that equal boxes (for the case of periodic boundary conditions) are placed around the box of interest, in all directions. In this way, a particle interacts with the rest of the particles in its box but also with all the particles in the infinitely many periodic boxes. To simulate bulk properties, this boundary conditions mimicking an infinite bulk are necessary. This can be seen in Figure 2.7. Note that different choices of boundary conditions exist, leading to different behavior of the system. In this work, we employ the periodic boundary conditions.

## SOLVENT MODELS FOR CHARMM

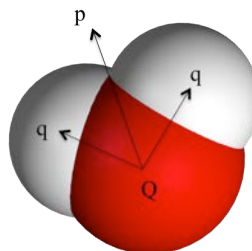
CHARMM force field is designed to be employed in condensed phase simulations, hence the necessity of having a model for the solvent of the system to be simulated. Major efforts have been done to develop models of water; for reviews of the development of water models, see<sup>39,27</sup> or the website<sup>9</sup> in which most of the water models available in literature are listed and compared. Below the models used in this work are presented.

The water model used in this work can be described as rigid, non-polarizable. This type of model has a long working trajectory over the last forty years. There are several models of this category, like the TIP3P, TIP4P, TIP5P, SPC/E and TIP4P/2005. Thus, although no model reproduces all the properties, some models perform better than others. It is clear that there are limitations for rigid non-polarizable models. In the reference<sup>53</sup>, 17 properties of water are discussed, including vapour and solid phases. Those are taken into account to evaluate the performance of a water model.

Rigid, non-polarizable models can be typically classified into three different families, namely, models with three interaction sites, models with four interaction sites and models with five interaction sites. Regardless of the number of sites, it is always the case that a single Lennard-Jones interaction site is located on the position of the oxygen atom. The main difference between three, four and five sites models is the way in which the partial

charges are distributed within the molecule. Common models with three interaction sites are TIP3P and SPC/E. In these models, a partial positive charge is placed on each of the hydrogen atoms.

**Table 2.1:** Table describes the LJ parameters and the charge of each atom of the water molecule of TIP3 model.



Atom	$\epsilon$ (kcal/mol)	$\sigma$ (Å)	$q$ (e)
<b>O</b>	0.152	3.536	-0.834
<b>H</b>	0.046	0.449	-0.417

The model TIP3P was proposed by Jorgensen et al. in 1983<sup>25</sup>. The two parameters of the Lennard-Jones (LJ) interaction (see Table 2.1) were chosen to reproduce the density of water at room temperature and pressure and the vaporization enthalpy at room temperature. The TIP3P version used in CHARMM which includes LJ centres on the hydrogen atoms is probably the most popular model of water especially because it is quite often used to describe water interactions in systems including biological molecules (i.e., proteins or nucleic acids) and also because of its simplicity and high computational efficiency. The standard parametrization of atomic charges in CHARMM for most molecules is done in presence of TIP3P water. For all these reasons, it is the one select for this work.

## THERMODYNAMIC ENSEMBLES

In classical statistical mechanics, the description of a many-body system is based on the concepts of statistical ensembles. According to the external conditions we can distinguish three fundamental ensembles: (i) the microcanonical (NVE) ensemble describing a perfectly isolated system, (ii) the canonical (NVT) ensemble describing a system exchanging energy with a heat bath of a given fixed temperature, and (iii) the grand canonical ( $\mu$ VT) ensemble



describing a system which can exchange both energy and particles with a reservoir at a given fixed temperature and chemical potential. In absence of external forces the Molecular Dynamics simulations describe a perfectly isolated system and provides an exact description of the microcanonical partition function. The total energy is conserved for a fixed number of particles and the volume (NVE). In this ensemble, the temperature and the pressure are not control variables but rather they are obtained as output of the simulation. Temperature (T) and pressure (P) are obtained as follows. The temperature T is related with kinetic energy of the atoms from the Equipartition Theorem<sup>16</sup>:

$$K_b T = \frac{2E_k}{N_f}, \quad (2.12)$$

where  $k_b$  is the Boltzmann constant,  $E_k$  corresponds to the total kinetic energy equal to  $(mv_i^2)/2$  of the system, and  $N_f$  corresponds to the number of degrees of freedom ( $3N - 3$  for a system of N particles with fixed total momentum). The pressure, P, is obtained from the Virial Theorem<sup>16</sup>:

$$P = \rho K_b T + \frac{1}{\delta V} \left( \sum_{i < j} \vec{r}_{ij} \vec{F}(\vec{r}_{ij}) \right) \quad (2.13)$$

where d is the dimensionality of the system usually equal to 3, and  $F(\mathbf{r}_{ij})$  is the force between particles  $i$  and  $j$  at a distance  $r_{ij}$ . The first term of the Equation 2.13 corresponds to the ideal gas pressure whereas the second term (virial term) is based on the interactions. In general, such perfectly isolated system does not occur in material science, because one prefers to control temperature and pressure, and therefore the system is open to the external environment and will thermalize. In this case, other ensembles such as NVT or NPT are employed.

The canonical partition function NVT is defined as a mechanical system, which is in thermal equilibrium with a heat bath. In this case the energy of the system varies because there is an exchange of energy (in the form of heat) with the thermostat at a certain temperature T. We can simulate this phenomenon by implementing external forces that

simulate the thermostat or the energy exchange with the thermostat. This is done by applying an external non conservative force, which is a function of atom velocities (in the same way as  $T$  is related to the atomic velocities, see Equation 2.12). If  $E_k$  is that high that the temperature is raising, it will be applied a friction force over all the atoms that will imply a decrease of the  $E_k$  and thus of  $T$ . Conversely, if  $E_k$  is too low the algorithm applies a external force increasing atomic velocities. There are different algorithms that achieve this objective. In particular, NAMD uses the Langevin Thermostat<sup>41</sup>.

$$M\dot{v} = F(r) - \gamma v + \sqrt{\frac{2\gamma K_b T}{M}} R(t) \quad (2.14)$$

where  $v$  is the velocity at each atom,  $F$  is the force over each atom,  $r$  is the position,  $\gamma$  is the friction coefficient,  $K_B$  is the Boltzmann constant,  $T$  is the temperature, and  $R(t)$  is a univariate Gaussian random process. The coupling to the reservoir is modelled by adding the fluctuating (the  $R(t)$  term) and dissipative ( $\gamma v$  term) forces to the Newtonian equations of motion (compare Equation 2.7 and 2.14).

If we work at constant pressure, the system is working in contact with a barostat, thus the ensemble will be isobaric-isothermal (NPT). This statistical mechanical ensemble proposes a modified set of equations of motion including an external force due to the piston (barostat). In this case, if the pressure of the system is above the targeted pressure the algorithm will increase the volume and viceversa, applying an external force. Different algorithms exist, and in particular, NAMD uses the Langevin-piston method<sup>12</sup>.

In relation with the previous paragraph, it exists another ensemble used in simulation, which is a variation of the  $N\gamma P_z T$  thermodynamic ensemble. This variation regulates the total pressure of the system in one direction (axis  $z$  perpendicular to the membrane or the interface). Its application is appropriate when having an interface, and the goal is to achieve a superficial tension  $\gamma$ . In the particular case of bilayers, one assumes that the surface tension or lateral pressure of a symmetric bilayer<sup>49</sup> in the resting state is zero, and that lateral pressure within each monolayer manifests itself directly only in the lateral

compressibility, when the membrane is subject to a lateral stress<sup>33</sup>.

### 2.3 MOLECULAR MODELLING: COARSE-GRAINED MOLECULAR DYNAMICS

In this section, we leave behind the all-atomic (AA) framework and explain the other framework that has been employed in this thesis for MD simulations, i.e., coarse-grain (CG).

In order to push the limits of reachable temporal and spatial scales of biomolecular systems' simulations with respect to AA standards, coarse-grained (CG) models can be utilized. Coarse-grain method is based on lowering the resolution of the system's model. This is achieved by grouping atoms into the so-called CG beads or pseudo-atoms. The level of coarse-graining depends on the number of atoms represented by one CG bead. Thus, the higher the number of atoms per bead, the lower the model resolution and the number of degrees of freedom of the system. Note that this CG beads interact with one another with more computationally efficient potentials than the atoms of the AA method<sup>34</sup>. The combination of this method with the continuous improvement of computer hardware and the recently-acquired ability of most common MD software packages (such as NAMD and GROMACS) to run efficiently on large numbers of computing nodes including GPUs, alleviates some of the problems that AA simulations face when dealing with the orders of magnitude (of system size and time scale) required for the study of phenomena like self-assembly or growth of aggregates<sup>15</sup>.

Many CG models have been proposed over the years. Two examples of successful CG models are Martini<sup>31</sup> and CMM-CG<sup>46</sup>, which are implemented in current molecular dynamics (MD) software. Not all CG models are created equally, and care must be taken when preparing the system and choosing the method of coarse-graining. There are three distinct approaches for coarse-graining a system: energy-based<sup>31,36</sup>, force-matching<sup>3</sup>, and structure-based methods<sup>37</sup>. In energy-based CG, the interaction potentials of the CG beads are derived and parameterized such that the free energies or energies of the all-atom (AA)

system are reproduced. In the force-matching method, the sum of the atomistic forces are mapped onto the corresponding CG beads. Lastly, the structure-based CG method relies on reproducing interactions obtained from atomistic simulations, often in the form of radial distribution functions.

Not only these methods provide the explained advantages in computational aspects, but also at a conceptual level, as in some cases the interpretation of the results require the time and length scales that are reachable by coarse-grain.<sup>38,32</sup> With respect to this thesis, this method has brought significant innovation, as the system that we analyze had not been simulated in this manner before. This has allowed us to experience at first hand all the mentioned benefits. In addition, it has meant also a methodological innovation for the group where this thesis is developed, as it had been barely used before. All these reasons constitute the motivation for the use of CG and in particular the MARTINI model, that is explained in the next section.

### 2.3.1 MARTINI MODEL

Among the available CG models, the Martini model<sup>30,32</sup>, is gaining increasing popularity due to its efficiency. The Martini model is based on a building block principle; uses a four-to-one mapping scheme; on average four heavy atoms are represented by one interaction site or bead. Those groups of atoms are replaced by a single bead which interacts with other beads with an effective interaction designed to maintain the chemical specificity<sup>32,31</sup>. A repository of many molecules such as lipids, ions, surfactants, etc. where this mapping has been applied is available at the site of the developers of Martini. Examples of this can be seen in Figure 2.8. Nevertheless, one can carry on the mentioned mapping for molecules that are not available in the repository by following the building block principle, an example of that being explained for the case of the CTAB molecule in chapter 4 of the present thesis.

This model has been employed mostly in simulations of properties of lipid membranes and proteins in membranes<sup>32</sup>. Recent works also employ the Martini model to simulate sys-

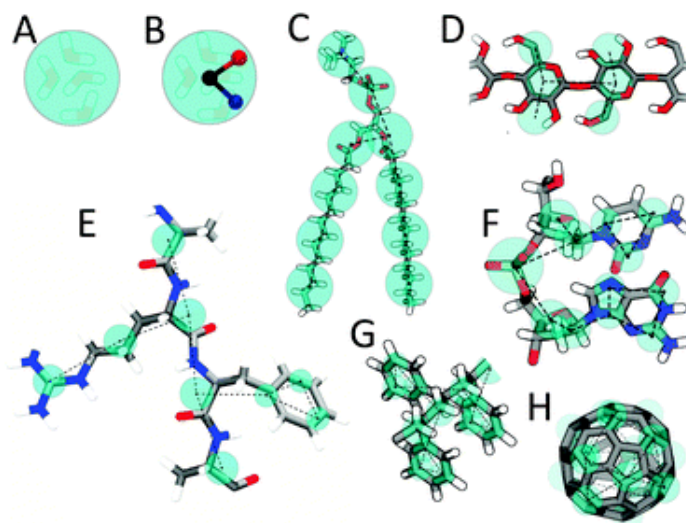


Figure 2.8: Martini mapping examples of selected molecules: (A) Standard water particle representing four water molecules, (B) Polarizable water molecule with embedded charges, (C) DMPC lipid, (D) Polysaccharide fragment, (E) Peptide, (F) DNA fragment, (G) Polystyrene fragment, (H) Fullerene molecule. In all cases Martini CG beads are shown as cyan transparent beads overlaying the atomistic structure. This Figure is reproduced from ref.<sup>32</sup> with permission from The Royal Society of Chemistry.

tems involving diverse surfactants such as anionic SDS micelles<sup>55</sup>, zwitterionic poly(ethylene oxide) surfactant micelles<sup>55</sup>, the effect of salt in micelles<sup>45</sup> and lipid self-assembled nanoparticles capped with zwitterionic surfactants<sup>13</sup>. MARTINI model was originally parameterized to study lipid bilayers and is mainly implemented in the MD program GROMACS<sup>5</sup>, but also NAMD<sup>41</sup>. Since the implementation of MARTINI is simpler in GROMACS than in NAMD, we have employed this program in most of our CG-MD simulations. Moreover, GROMACS comes with a large selection of flexible tools for trajectory analysis.

A more detailed explanation of the working principle based in a four-to-one mapping<sup>32</sup>. The model maps 4 or 5 heavy atoms (C,N,O) and their associated hydrogen atoms to a single bead, although some specific cases (e.g. molecules with rings) require treatment with higher resolution. In the Martini model, there are four generic types of beads (Q = charged, P = polar, N = non-polar and C = apolar) and, within each main type, subtypes are distinguished by a letter denoting the hydrogen bonding capabilities (d = donor, a = acceptor, da = both, and 0 = none) or by numbers indicating the degree of polarity (1 to 5). Standard masses of each bead is assigned to 72 amu. The use of standard masses yields

a more computationally efficient model, but may lead to underrepresented dynamics of the system<sup>31</sup>. For this reason, masses can be manually adjusted for beads. A good example is the case of the cholesterol Martini model<sup>22</sup> in which some of the bead masses are 45 amu.

In the MARTINI model, non-bonded interactions are described by a shifted Lennard-Jones (LJ) 12-6 potential of the form:

$$U_{LJ}(r) = 4\epsilon_{ij} \left[ \left( \frac{\sigma_{ij}}{r} \right)^{12} - \left( \frac{\sigma_{ij}}{r} \right)^6 \right] \quad (2.15)$$

where  $\epsilon_{ij}$  is the strength of the interaction between two beads, and  $\sigma_{ij}$  represents the smallest distance between two beads. The effective size of  $\sigma_{ij}=0.47$  nm is assumed for each bead except the specialized classes for antifreeze particles and ring structures.

The interactions in this model are divided in 10 levels. The interaction strength values  $\epsilon$  of each interaction level are reported in<sup>31</sup>. The level I interaction models strong polar interactions as in bulk water, levels II and III model more volatile liquids such as ethanol or acetone, level IV models the non-polar interactions in aliphatic chains, and levels V–VIII are used to mimic various degrees of hydrophobic repulsion between polar and non-polar phases. Level IX finally describes the interaction between charged particles and a very apolar medium.

Charged particles in the Martini force field bear a full charge  $q_{ij}$  which interacts via a shifted Coulombic potential of the form:

$$U_{el}(r) = \frac{q_i q_j}{4\pi \epsilon_0 \epsilon_r r} \quad (2.16)$$

with a field value of the relative dielectric constant,  $\epsilon_r=15$ . Note that the Coulomb interaction is computed with a fixed dielectric constant and a cut off with a reaction field mimicking the effect of a homogeneous dielectric environment beyond the cutoff radius, including the effect of ionic strength<sup>50</sup>. None Ewald summation neither PME methods are employed with MARTINI.

Bonded interactions between CG beads are described by a weak harmonic potential:

$$V_{bond}(R) = \frac{1}{2}K_{bond}(R - R_{bond})^2 \tag{2.17}$$

where the equilibrium bond distance is held at  $R_{bond} = \sigma_{ij} = 0.47$  nm, and the force constant is given by  $K_{bond}=1250$  kJ mol<sup>-1</sup> nm<sup>-2</sup> for all beads. Chain stiffness is achieved through a weak harmonic potential for the angles:

$$V_{angle}(\mathcal{D}) = \frac{1}{2}K_{angle}(\cos(\mathcal{D}) - \cos(\mathcal{D}_o))^2 \tag{2.18}$$

where values for  $\mathcal{D}_o = \sim 180$  and  $\sim 120$  for aliphatic chains and trans-unsaturated bond and cis-double bond respectively. And  $K_{angle} = 25$  and  $45$  kJ · mol<sup>-1</sup> · nm<sup>-2</sup> for aliphatic chains and trans-unsaturated bond and cis-double bond respectively. For ring particles in the Martini model, an improper dihedral angle potential is used to prevent out-of-plane distortions of more complicated geometries:

$$V_{id}(\mathcal{D}) = K_{id}(\cos(\mathcal{D}) - \cos(\mathcal{D}_{id}))^2 \tag{2.19}$$

Simplified potentials for the interaction sites (beads) provide a reduction in the degrees of freedom, which enables the use of longer time steps for the integration of Newton’s equations of motion. Traditional values for  $\mathcal{D}t$  in AA molecular dynamics fall in the range of 0.5-2.0 fs, while with the Martini force field it is suggested to use a time step of 40-50 fs, although sometimes a smaller time step is required for stability (20-30 fs).

### 2.3.2 EXPLICIT AND IMPLICIT SOLVENT

For water molecules, we have employed the standard Martini CG water model<sup>32</sup>. The complexity of liquid water (with substantial anisotropic hydrogen bonding interactions) cannot be simulated by a single bead. For this reason, the CG model of water is composed

of a mixture of  $P_4$  spherical beads and special AF (anti-freezing) beads. One  $P_4$  bead corresponds to 4 water molecules and the number of AF beads is one for each ten  $P_4$  beads. The highly interacting  $P_4$  beads, when let alone, tend to form isotropic crystals at room temperature, which are disrupted by the AF beads. With this mixture of two beads one obtains a highly interacting liquid at room temperature which resembles water. More details on the Martini water model can be found in ref.<sup>32</sup> and ref.<sup>31</sup>.

In the case of Martini implicit solvent simulations, we employed the recently developed Dry Martini force field<sup>2</sup>. In Dry Martini, one considers the same bead types as in standard Martini except for water, which is not included explicitly. The equations for the force field are the same as in standard Martini but the strength of the interactions is modified to take into account the fact that water is considered implicitly<sup>2</sup>. Therefore, the same model of CTAB with the same bead definitions developed for standard Martini (Figure 2.8) can be used for Dry Martini without any modification, except for the values of the parameters of the interactions.

## 2.4 ANALYSIS OF RESULTS

Up to this point we have extensively explained all the methods and techniques related to the computation of the simulations. However, an equally important tool in this thesis are the methods related to the visualization and analysis of results. In this section, we introduce and explain those.

**Visualization (snapshots and movies):** We employed the Visual Molecular Dynamics (VMD) program<sup>21</sup> for displaying molecules containing any number of atoms. User-defined atom selections can be displayed in any of the standard molecular representations. Besides, the program reads data files using an extensible plugin system, and supports Babel plugin, for conversion of other formats. Three analysis features of this program are highlighted, for their relevance in this thesis. Firstly, this program allows the visualization of dynamic molecular data, not only for NAMD but for other simulation packages like Gromacs



or Amber. The data can be used to animate the molecule or to plot variation over time in molecular properties such as angles, dihedrals, interatomic distances, or energies over time. Secondly, molecular analysis can be done, such as computing the center of mass of sets of atoms. Finally, and very relevantly in this thesis, VMD uses the freely available Python and Tcl scripting languages for processing text commands. This allows to write and load tailor-made scripts for analysis, like computing the diffusion coefficient. The explanation for the employed tailor-made scripts in this thesis is given in each corresponding chapter. However, it is worth introducing here two extensively-used analysis scripts, due to their presence across the whole work. Those are the density profile and the radial distribution function.

**Density Profile:** A simple but very informative structural function is the density profile. It is computed by dividing a length, area or volume in differential parts and counting the number of atoms per part. In particular, the density profile tool<sup>17</sup> is a software package that computes one-dimensional density profiles of molecular systems. It's script is written in Tcl and is platform-independent; it will therefore work on any of the platforms supported by the VMD system. The algorithm represents the mass density profile along the z-axis in this case, with a granularity of  $\Delta z$ . It can compute the density (atoms), mass (dalton),

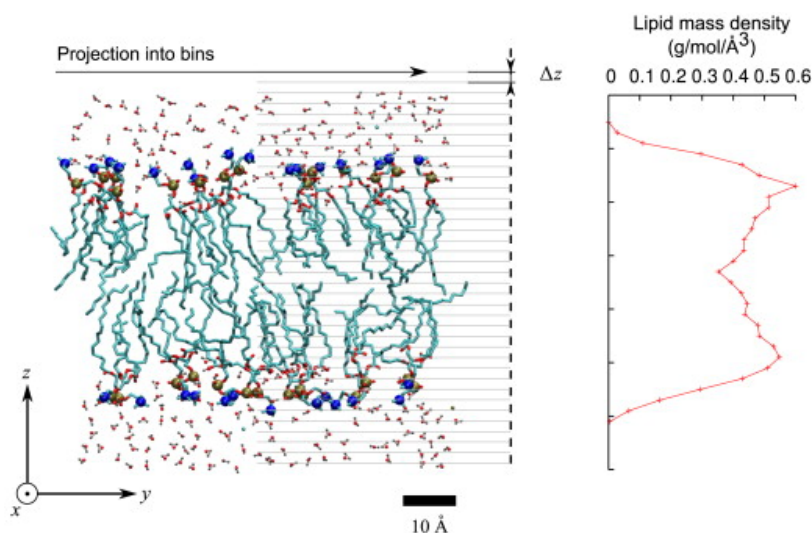


Figure 2.9: Example taken from ref. <sup>17</sup> of the computation of the mass density profile of a lipid bilayer.

charge (elementary charges) or electronic density, and its value is taken from different atomic attributes (see Figure 2.9).

Like many algorithms, one of the limitations is that the algorithm considers point-like atoms instead of volumetric distributions; the tool would therefore be inappropriate to compute the density of isolated atoms with sub-Å resolution (a setup generally outside the scope of MD).

**Radial distribution function:** In statistical mechanics, the radial distribution function, (or pair correlation function)  $g(r)$ , describes how density varies as a function of distance from a reference particle (see Figure 2.10). Conceptually, it is the ratio between the average number density  $\rho(r)$  at a distance  $r$  from any given atom (for simplicity it is assumed that all atoms are identical), and the density at a distance  $r$  from an atom in an ideal gas (that has the same overall density). In a simulation, it is straightforward to measure  $g(r)$ : it is simply computed as the distribution of distances between all particles of the system. By construction,  $g(r)$  is equal to 1 in an ideal gas, and any deviation from that value reflects correlations between the particles due to the intermolecular interactions<sup>16</sup>. This general theme is depicted in Figure 2.10, where the blue particle is our reference particle, and red particles are those which are within the circular shell, dotted in grey.

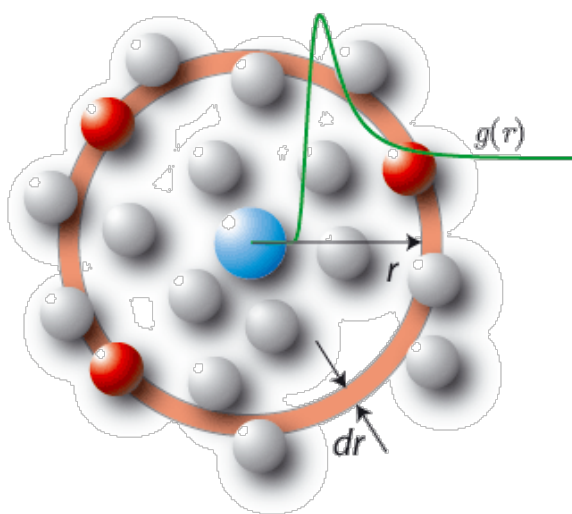


Figure 2.10: Schematic plot of a typical radial distribution function and the corresponding atomic structure.



# References

- [1] Armijo, L. (1966). Minimization of functions having Lipschitz continuous first partial derivatives. *Pacific Journal of Mathematics*, 16(1), 1–3.
- [2] Arnarez, C., Uusitalo, J. J., Masman, M. F., Ingólfsson, H. I., de Jong, D. H., Melo, M. N., Periole, X., de Vries, A. H., & Marrink, S. J. (2014). Dry Martini, a Coarse-Grained Force Field for Lipid Membrane Simulations with Implicit Solvent. *Journal of Chemical Theory and Computation*, 11(1), 260–275.
- [3] Ayton, G. S. & Voth, G. A. (2007). Multiscale simulation of transmembrane proteins. *Journal of Structural Biology*, 157(3), 570–578.
- [4] Becke, A. D. (1988). Density-functional exchange-energy approximation with correct asymptotic behavior. *Physical Review A*, 38(6), 3098–3100.
- [5] Berendsen, H. J. C., van der Spoel, D., & van Drunen, R. (1995). GROMACS: A message-passing parallel molecular dynamics implementation. *Computer Physics Communications*, 91(1-3), 43–56.
- [6] Berman, H. M. (2000). The Protein Data Bank. *Nucleic Acids Research*, 28(1), 235–242.
- [7] Birkhoff, G. D. (1942). What is the Ergodic Theorem? *The American Mathematical Monthly*, 49(4), 222–226.
- [8] Chai, J.-D. & Head-Gordon, M. (2008). Long-range corrected hybrid density functionals with damped atom–atom dispersion corrections. *Physical Chemistry Chemical Physics*, 10(44), 6615–6620.
- [9] Chaplin, M. (2000). Water Models [http://www1.lsbu.ac.uk/water/water\\_models.html](http://www1.lsbu.ac.uk/water/water_models.html).
- [10] Dennington, R., Keith, T. A., & Millam, J. M. (2016). GaussView, Version 6.
- [11] Fan, J. D. & Malozovsky, Y. M. (2013). Pauli exclusion principle. *International Journal of Modern Physics B*, 27(15), 1362024+.
- [12] Feller, S. E., Zhang, Y., Pastor, R. W., & Brooks, B. R. (1995). Constant pressure molecular dynamics simulation: The Langevin piston method. *The Journal of Chemical Physics*, 103(11), 4613–4621.
- [13] Fernandez-Luengo, X., Camacho, J., & Faraudo, J. (2017). Computer Simulations of Lipid Nanoparticles. *Nanomaterials*, 7(12), 461+.

- [14] Fock, V. (1930). Nherungsmethode zur Lsung des quantenmechanischen Mehrkrperproblems. *Zeitschrift fur Physik*, 61(1-2), 126–148.
- [15] Frederix, P. W. J. M., Patmanidis, I., & Marrink, S. J. (2018). Molecular simulations of self-assembling bio-inspired supramolecular systems and their connection to experiments. *Chemical Society Reviews*, 47(10), 3470–3489.
- [16] Frenkel, D. & Smit, B. (2001). *Understanding Molecular Simulation*. Orlando, FL, USA: Academic Press, Inc., 2nd edition.
- [17] Giorgino, T. (2014). Computing 1-D atomic densities in macromolecular simulations: The density profile tool for VMD. *Computer Physics Communications*, 185(1), 317–322.
- [18] Grubmüller, H., Heller, H., Windemuth, A., & Schulten, K. (1991). Generalized Verlet Algorithm for Efficient Molecular Dynamics Simulations with Long-range Interactions. *Molecular Simulation*, 6(1-3), 121–142.
- [19] Hartree, D. R. (2008). The Wave Mechanics of an Atom with a Non-Coulomb Central Field. Part I. Theory and Methods. *Mathematical Proceedings of the Cambridge Philosophical Society*, 24(01), 89–110.
- [20] Hohenberg, P. & Kohn, W. (1964). Inhomogeneous Electron Gas. *Physical Review*, 136(3B), B864–B871.
- [21] Humphrey, W., Dalke, A., & Schulten, K. (1996). VMD: Visual molecular dynamics. *Journal of Molecular Graphics*, 14(1), 33–38.
- [22] Illa-Tuset, S., Malaspina, D. C., & Faraudo, J. (2018). Coarse-grained molecular dynamics simulation of the interface behaviour and self-assembly of CTAB cationic surfactants. *Physical Chemistry Chemical Physics*, 20(41), 26422–26430.
- [23] Jensen, J. H. (2010). *Molecular Modeling Basics*. Boca Raton: Taylor & Francis Group.
- [24] Jones, D. (1998). *THREADER: protein sequence threading by double dynamic programming*, volume 32, (pp. 285–311). Elsevier.
- [25] Jorgensen, W. L., Chandrasekhar, J., Madura, J. D., Impey, R. W., & Klein, M. L. (1983). Comparison of simple potential functions for simulating liquid water. *The Journal of Chemical Physics*, 79(2), 926–935.
- [26] Jorgensen, W. L., Maxwell, D. S., & Tirado-Rives, J. (1996). Development and Testing of the OPLS All-Atom Force Field on Conformational Energetics and Properties of Organic Liquids. *Journal of the American Chemical Society*, 118(45), 11225–11236.
- [27] Jorgensen, W. L. & Tirado-Rives, J. (2005). Potential energy functions for atomic-level simulations of water and organic and biomolecular systems. *Proceedings of the National Academy of Sciences*, 102(19), 6665–6670.

- 
- [28] Kleywegt, G. J. & IUCr (2007). Crystallographic refinement of ligand complexes. *Acta Crystallographica Section D: Biological Crystallography*, 63(1), 94–100.
- [29] Kohn, W. & Sham, L. J. (1965). Self-Consistent Equations Including Exchange and Correlation Effects. *Physical Review*, 140(4A), A1133–A1138.
- [30] Marrink, S. J., de Vries, A. H., & Mark, A. E. (2004). Coarse Grained Model for Semiquantitative Lipid Simulations. *The Journal of Physical Chemistry B*, 108(2), 750–760.
- [31] Marrink, S. J., Risselada, H. J., Yefimov, S., Tieleman, D. P., & de Vries, A. H. (2007). The MARTINI Force Field: Coarse Grained Model for Biomolecular Simulations. *The Journal of Physical Chemistry B*, 111(27), 7812–7824.
- [32] Marrink, S. J. & Tieleman, D. P. (2013). Perspective on the Martini model. *Chemical Society Reviews*, 42(16), 6801–6822.
- [33] Marsh, D. (1996). Lateral pressure in membranes. *Biochimica et Biophysica Acta (BBA) - Reviews on Biomembranes*, 1286(3), 183–223.
- [34] Merchant, B. A. & Madura, J. D. (2011). *A Review of Coarse-Grained Molecular Dynamics Techniques to Access Extended Spatial and Temporal Scales in Biomolecular Simulations*, volume 7, (pp. 67–87). Elsevier.
- [35] Metropolis, N., Rosenbluth, A. W., Rosenbluth, M. N., Teller, A. H., & Teller, E. (1953). Equation of State Calculations by Fast Computing Machines. *The Journal of Chemical Physics*, 21(6), 1087–1092.
- [36] Monticelli, L., Kandasamy, S. K., Periole, X., Larson, R. G., Tieleman, D. P., & Marrink, S.-J. (2008). The MARTINI Coarse-Grained Force Field: Extension to Proteins. *J. Chem. Theory Comput.*, 4(5), 819–834.
- [37] Müller-Plathe, F. (2002). Coarse-Graining in Polymer Simulation: From the Atomistic to the Mesoscopic Scale and Back. *ChemPhysChem*, 3(9), 754–769.
- [38] Noid, W. G. (2013). Perspective: Coarse-grained models for biomolecular systems. *The Journal of Chemical Physics*, 139(9), 090901+.
- [39] Ouyang, J. F. & Bettens, R. P. A. (2015). Modelling Water: A Lifetime Enigma. *CHIMIA International Journal for Chemistry*, 69(3), 104–111.
- [40] Perdew, J. P. & Yue, W. (1986). Accurate and simple density functional for the electronic exchange energy: Generalized gradient approximation. *Physical Review B*, 33(12), 8800–8802.
- [41] Phillips, J. C., Braun, R., Wang, W., Gumbart, J., Tajkhorshid, E., Villa, E., Chipot, C., Skeel, R. D., Kalé, L., & Schulten, K. (2005). Scalable molecular dynamics with NAMD. *Journal of Computational Chemistry*, 26(16), 1781–1802.

- [42] Plimpton, S. (1995). Fast Parallel Algorithms for Short-Range Molecular Dynamics. *Journal of Computational Physics*, 117(1), 1–19.
- [43] Rappe, A. K., Casewit, C. J., Colwell, K. S., Goddard, W. A., & Skiff, W. M. (1992). UFF, a full periodic table force field for molecular mechanics and molecular dynamics simulations. *Journal of the American Chemical Society*, 114(25), 10024–10035.
- [44] Rosenberg, B. J. & Shavitt, I. (1975). Abinitio SCF and CI studies on the ground state of the water molecule. I. Comparison of CGTO and STO basis sets near the Hartree–Fock limit. *The Journal of Chemical Physics*, 63(5), 2162–2174.
- [45] Sangwai, A. V. & Sureshkumar, R. (2011). Coarse-Grained Molecular Dynamics Simulations of the Sphere to Rod Transition in Surfactant Micelles. *Langmuir*, 27(11), 6628–6638.
- [46] Shinoda, W., DeVane, R., & Klein, M. L. (2007). Multi-property fitting and parameterization of a coarse grained model for aqueous surfactants. *Molecular Simulation*, 33(1-2), 27–36.
- [47] Spreiter, Q. & Walter, M. (1999). Classical Molecular Dynamics Simulation with the Velocity Verlet Algorithm at Strong External Magnetic Fields. *Journal of Computational Physics*, 152(1), 102–119.
- [48] Todorov, I. T., Smith, W., Trachenko, K., & Dove, M. T. (2006). DL\_POLY\_3: new dimensions in molecular dynamics simulations via massive parallelism. *Journal of Materials Chemistry*, 16(20), 1911+.
- [49] Traïkia, M., Warschawski, D. E., Lambert, O., Rigaud, J.-L., & Devaux, P. F. (2002). Asymmetrical Membranes and Surface Tension. *Biophysical Journal*, 83(3), 1443–1454.
- [50] Van Der Spoel, D., Lindahl, E., Hess, B., Groenhof, G., Mark, A. E., & Berendsen, H. J. C. (2005). GROMACS: Fast, flexible, and free. *Journal of Computational Chemistry*, 26(16), 1701–1718.
- [51] Vanommeslaeghe, K., Hatcher, E., Acharya, C., Kundu, S., Zhong, S., Shim, J., Darian, E., Guvench, O., Lopes, P., Vorobyov, I., & Mackerell, A. D. (2009). CHARMM general force field: A force field for drug-like molecules compatible with the CHARMM all-atom additive biological force fields. *Journal of Computational Chemistry*, 31(4), NA.
- [52] Vanommeslaeghe, K., Raman, E. P., & MacKerell, A. D. (2012). Automation of the CHARMM General Force Field (CGenFF) II: Assignment of Bonded Parameters and Partial Atomic Charges. *Journal of Chemical Information and Modeling*, 52(12), 3155–3168.
- [53] Vega, C. & Abascal, J. L. F. (2011). Simulating water with rigid non-polarizable models: a general perspective. *Physical Chemistry Chemical Physics*, 13(44), 19663–19688.

- [54] Wang, J., Wolf, R. M., Caldwell, J. W., Kollman, P. A., & Case, D. A. (2004). Development and testing of a general amber force field. *Journal of Computational Chemistry*, 25(9), 1157–1174.
- [55] Wang, S. & Larson, R. G. (2015). Coarse-Grained Molecular Dynamics Simulation of Self-Assembly and Surface Adsorption of Ionic Surfactants Using an Implicit Water Model. *Langmuir*, 31(4), 1262–1271.
- [56] Wassenaar, T. A., Ingólfsson, H. I., Böckmann, R. A., Tieleman, D. P., & Marrink, S. J. (2015). Computational Lipidomics with insane : A Versatile Tool for Generating Custom Membranes for Molecular Simulations. *Journal of Chemical Theory and Computation*, 11(5), 2144–2155.
- [57] Zhu, X., Lopes, P. E. M., & MacKerell, A. D. (2012). Recent developments and applications of the CHARMM force fields. *Wiley Interdisciplinary Reviews: Computational Molecular Science*, 2(1), 167–185.





*For a research worker the unforgotten moments of his life are those rare ones which come after years of plodding work, when the veil over nature's secret seems suddenly to lift and when what was dark and chaotic appears in a clear and beautiful light and pattern.*

Gerty Cori

# 3

## Atomistic simulations of a Quatsome bilayer

This first chapter within Part II contains a detailed analysis, based in simulation methods, of the structure and mechanical properties of the Quatsome bilayer. This constitutes the motivation of this chapter, and to some extent the baseline of this thesis. Note that a planar patch of the bilayer will be considered for this task, employing atomistic simulations, which is the method that provides the maximum resolution at the nanoscale.

In other works, molecular dynamics (MD) simulations have been employed to show

the synergy between the (CTA<sup>+</sup>) of CTAB and cholesterol molecules that makes them self-assemble into bimolecular amphiphiles (synthon) and then into bilayers, with a similar structure of those formed by double-tailed unimolecular amphiphiles, like phospholipids<sup>11</sup>. Nevertheless, the aim of this chapter is to go further, simulating the bilayer in a wide variety of conditions, like the presence of an external tension or a change in the temperature, in order to obtain a detailed characterization of the bilayer.

In that sense, a first simulation will be carried out, that will constitute the baseline of the analysis work. In it, physico-chemical properties such as the molecular organization with atomistic detail, orientation of the Quatsome components, interaction of ions and mechanical properties will be analyzed, in order to understand the QS system. From that point on, several situations that can affect the structure will be simulated and studied, for instance the ion penetration in the bilayer<sup>20</sup>.

### 3.1 FULL ANALYSIS OF QUATSOME BILAYER AT 25°C

This section is the main part of this chapter, as it contains the all-atomic MD simulations of the Quatsome bilayer at 25 °C, which is the temperature of experimental interest. This is the main characterization of the bilayer. A note regarding the analyzed properties and parameters: molecular organization and orientation of the counterions are properties that are considered independent of time, and its analysis is averaged over a time period; on the contrary, diffusion, orientation of components and elastic properties are dependent with time, and they are analyzed along a certain time span.

#### 3.1.1 DESCRIPTION OF THE ALL-ATOMIC MD SIMULATION

To study the structural characteristics of the Quatsome bilayer in water we used the all-atomic MD simulation described in Table 3.1 and represented in Figure 3.1. This simulation (S1) allows us to deeply study the Quatsome system, but also the behaviour of its components individually; CTAB and cholesterol, that can be seen in Figure 3.1.

Table 3.1: Composition of the systems considered in the MD simulations, including total number of atoms, numbers of water, components' molecules and counterions, the simulation time and the equilibrated box size.

	Atoms (total)	molec. water/CTA <sup>+</sup> /Chol/Br <sup>-</sup>	Sim time	Box Size
S1	23727	5443/54/54/54	107 ns	226.5 nm <sup>3</sup>

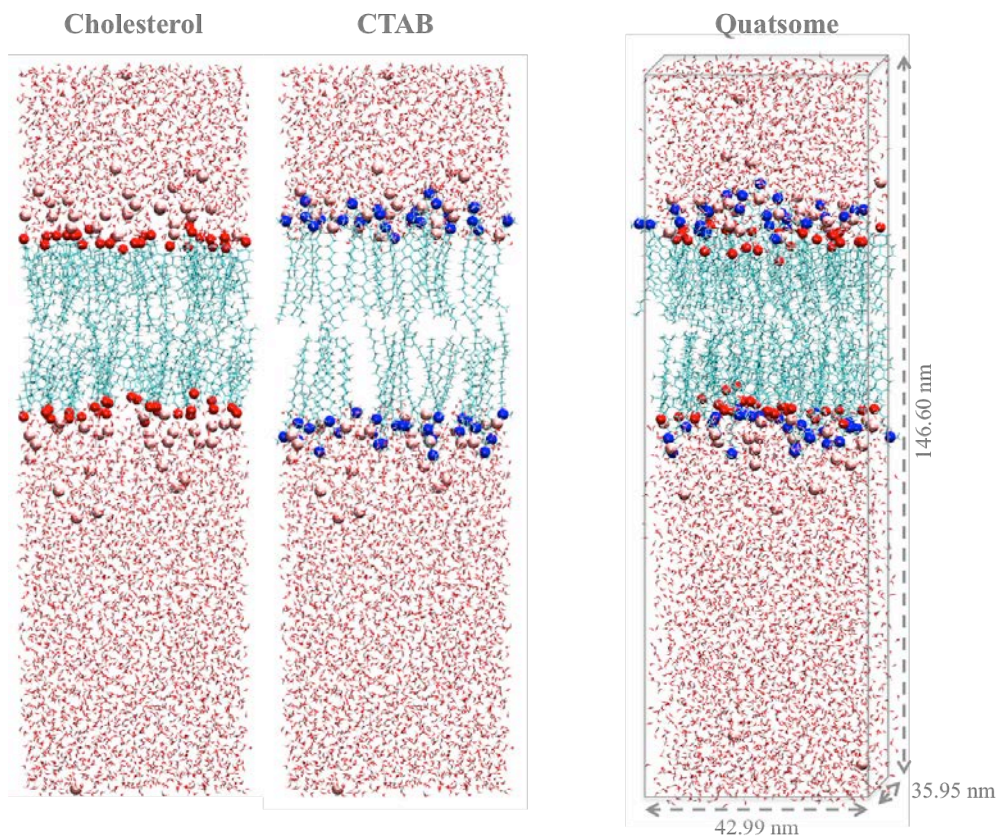


Figure 3.1: Snapshot of S1 simulation. On the left, snapshots of each of the components. Oxygen atoms of the cholesterol molecules (red spheres) and nitrogen atoms of the CTAB surfactants (blue spheres) have been highlighted. On the right, we show the simulation box where the Quatsome system is shown, indicating the size of the box in each spatial direction.

The employed force field and all the technical details of the simulation are the same as in the previously published work<sup>11</sup> with the only difference that the simulation was extended for an additional time of 107 ns using the NAMD 2.11 software<sup>23</sup>. The simulations were performed using the NPT $\gamma$  ensemble maintaining the QS bilayer at 25 °C, 1 atm of pressure and zero tension to mimic a vesicle bilayer (see Table 3.1). The simulated system (QS)

consists of two leaflets of 27 CTA<sup>+</sup> and 27 Chol molecules each, and 54 Br<sup>-</sup> ions immersed in 5443 TIP3P water molecules. As observed in Figure 3.1, there is an excess of water in the system in order to regulate the pressure. The equilibrium area of the bilayer is  $\sim 15.7$  nm<sup>2</sup>.

### 3.1.2 MOLECULAR ORGANIZATION

The first performed analysis is about the molecular organization, a time-averaged property. Figure 3.2 shows a bilayer that resembles the structure of those formed by double-tailed unimolecular amphiphiles and shows outstanding stability with time. The result from the S1 simulation was an atomistic structure of the Quatsome bilayer, a mixture containing equal numbers of CTAB and cholesterol molecules in water, forming a planar bilayer as illustrated in Figure 3.2. In the simulations we obtained a homogeneous bilayer in which cholesterol molecules are incorporated in the hydrophobic region of the bilayer (avoiding contact with water) and surfactant molecules are deformed in a way similar to that described in the introduction chapter (see Figure 3.2 where red spheres (Chol) are more hidden into the membrane than blue ones (CTA<sup>+</sup>)).

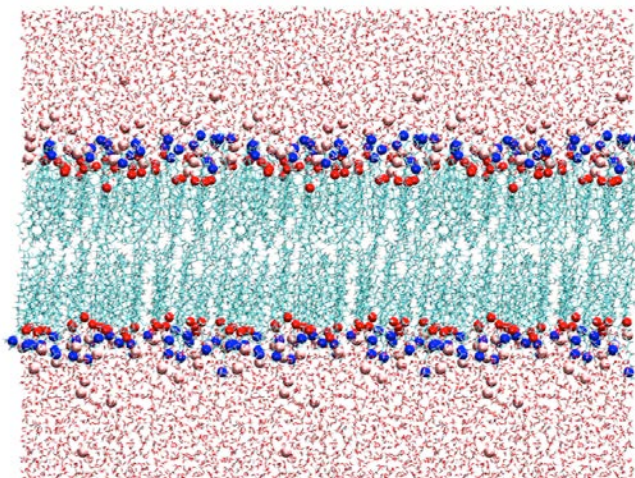


**Figure 3.2:** Snapshot of the Quatsome bilayer in water. It focuses on the bilayer area which is replicated thanks to the boundary conditions applied. Blue spheres representing the nitrogen atoms of the CTAB molecules limit the surface-water interface of the membrane. Pink spheres represent the bromide counterions.

A more quantitative description of the bilayer structure is given by the atomic density profile, shown in Figure 3.3. The headgroup and chain distribution of the CTAB across the bilayer has the typical shape observed in a two-chain phospholipid bilayer<sup>33,10</sup>, as the atomic distribution of carbon atoms from the surfactant tails has a small density depletion in the center (see for example reference<sup>33</sup>, Figure 2).

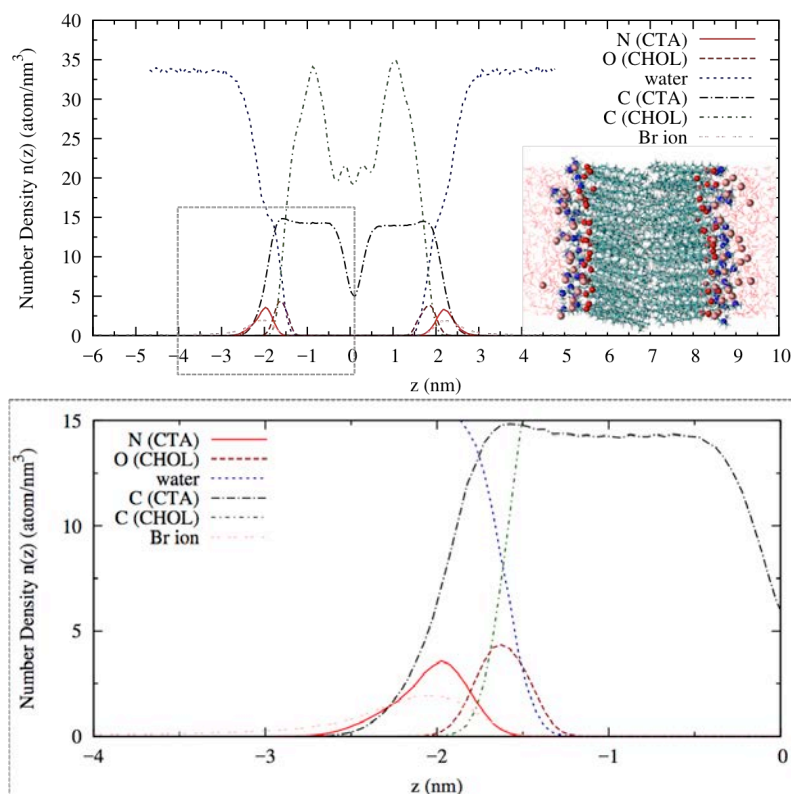


**Figure 3.3:** Average density profile of the Quatsome components; CTAB and cholesterol. It represents the density value vs. the distance in where the zero corresponds to the centre of the box simulation. The interest is focused on those atoms that would appear to have an affinity with the interface. Therefore, the following atoms density profiles were decided to study: the nitrogen atom of the  $\text{CTA}^+$  group, the oxygen atom corresponding to the Chol molecule and also all the corresponding carbon atoms of  $\text{CTA}^+$  and Chol molecule, the oxygen atom of the water and finally the bromide counterion.

As seen in Figure 3.3, the CTAB molecules are arranged into two-layered leaflets with the headgroups in contact with water (red line) and the tails in the interior of the bilayer (black dashed lines). Cholesterol molecules (green lines) accommodate themselves, including the hydroxyl groups (see Figure 3.3) in the hydrophobic region generated by the CTAB tails

to avoid any contact with the water (dark blue dashed-line) medium. Water molecules (dark-blue dashed-line) scarcely penetrate into the bilayer, and the interaction with the membrane components is limited to the solvation of the surfactant's polar headgroups. Regarding the counterions,  $\text{Br}^-$ , they are shown in Figure 3.3, bottom panel. We observed a broad line either in the hydrophobic and hydrophilic region, meaning that a significant quantity of bromide counterions are adsorbed. This will be further studied in Chapter 3 of this thesis. The total bilayer thickness (measured from the peaks in the surfactant headgroup distribution) is about 4.4 nm, and the hydrocarbon region has a thickness about 3.6 nm. These values are in agreement with the average thickness between 4-5 nm, estimated from the cryo-TEM images (see Figure 1.4 in Introduction chapter). As seen in Figure 3.3, the size of this region is enough to accommodate two non-overlapping layers of cholesterol molecules (note the central minima in the density profile of cholesterol molecules). The cholesterol density profile shows a maximum at 1 nm associated to the overlapping of the rigid carbocyclic moieties of the sterol molecules, as represented in the molecular scheme of Figure 3.3. In addition, we have also calculated the thickness of the QS membrane through a homemade-script, that calculates the average distance over the simulation time, using the nitrogen-nitrogen coordinates from the S1 trajectory. At 25 °C we obtain a value of 4.3 nm, slightly smaller, but still in agreement, with the one obtained from the density profile (4.4 nm).

Continuing with the analysis of the Quatsome bilayer at 25 °C, we calculated the equilibrium area per polar headgroup and we obtained a value of 58 Å<sup>2</sup>. This is similar to the ones obtained for certain anionic phospholipids, e.g., values among 53–55 Å<sup>2</sup> were obtained in MD simulations for anionic phosphatidylserine (PS) lipids<sup>21</sup>.

### 3.1.3 ORGANIZATION OF COUNTERIONS

In this section we study the effect of the presence of counterions in the Quatsome components. Firstly we analyze the ion organization at a local level within the bilayer, and

secondly we analyze the impact of the ions in the QS structure at a global level.

As seen in Figure 3.4, the bromide counterions that penetrate inside the bilayer are shared between the CTA<sup>+</sup> headgroup and the -OH group from the cholesterol (Chol). In other words, as  $g(r)$  graph shows, anions not only interact strongly with cationic CTA<sup>+</sup> surfactant, but also with Chol. The  $g(r)$  graph can be found in the mentioned figure. We have computed that 10% of CTA<sup>+</sup> molecules have a Br<sup>-</sup> ion adsorbed on top, and the 72% of the CTA<sup>+</sup> molecules have a Br<sup>-</sup> ion shared with cholesterol (Figure 3.4). For this computation, the first step is to select the ion pair to be studied, in this case Br-N (nitrogen atom from the CTAB). The  $g(r)$  is calculated for the pair, and the distance at the depletion is read (see arrows in Figure 3.4). Then, a homemade script counts the number of bromide ions at the given read distance, and then the percentage is calculated.

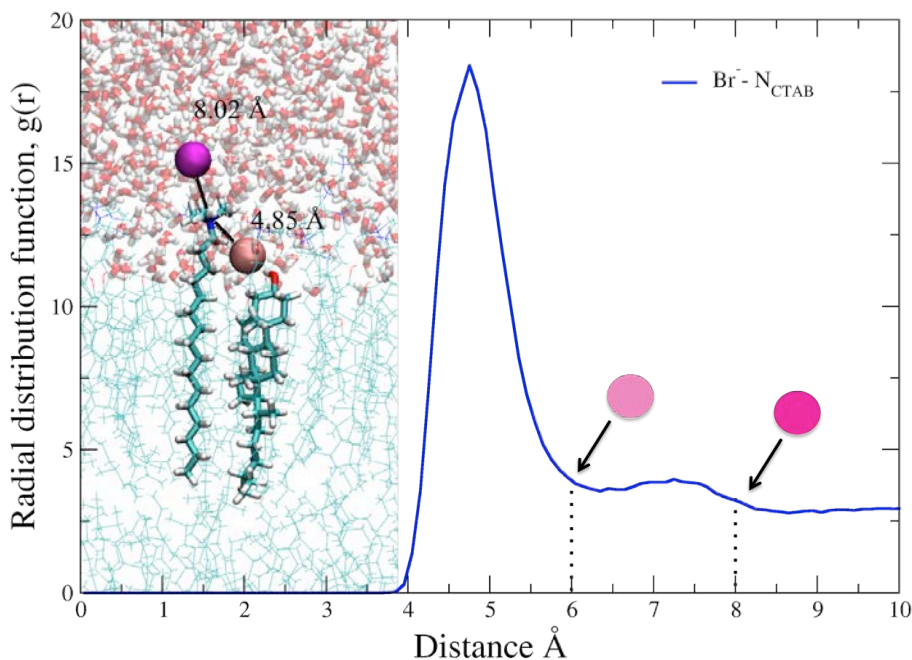


Figure 3.4: Radial distribution function,  $g(r)$ , computed between the bromide anion and the polar headgroup (N atom) of the CTA<sup>+</sup>. Two peaks appear corresponding to two possible locations of bromide atoms coloured in pink and dark-pink. Snapshot image from the MD simulation shows that the first peak of the  $g(r)$  corresponds to when the bromide atom is located between CTA<sup>+</sup> and Chol head groups whereas in the second peak the bromide counterion is located above the CTA<sup>+</sup> molecule.



As said, ions can also have an impact on the QS structure, molecular organization and dynamics of soft systems at global level. The highly hydrated head groups of the molecules constituting the membrane are partly responsible for the interactions between ions and those molecules, by means of the formation of indirect complexes, mediated by water<sup>34</sup>. Complexes like these can significantly affect the properties of the interface itself, altering the molecular dynamics and mechanical properties on the nanoscale<sup>29</sup>. Indeed, recent studies have seen this water-induced phenomena in solid-liquid interfaces<sup>28</sup> and in lipid membranes<sup>34</sup>. Those two cases have cationic ions, which can spontaneously form ordered structures at the surface. Based on our simulations, we have checked for this phenomena in our system, which has a cationic surface-liquid interface interacting with anionic ions. This perspective is something interesting to further study, as ionic nets could play an important role in interfacial phenomena such as charge transfer, crystal growth, nanoscale self-assembly and colloidal stability<sup>34</sup>.

In our simulations we observe that  $\text{Br}^-$  counterions have up to 5 hydrated number (see Figure 3.5-(b)). Structural arrangements of water molecules around the bromide ion are quantified by radial pair distribution function,  $g(r)$ , by the  $\text{Br-O}$ ,  $\text{Br-N}_{CTAB}$ ,  $\text{Br-O}_{Chol}$  radial distribution functions, and the results obtained from our simulations are depicted in Figure 3.5-(d). The  $\text{Br-water}$  and  $\text{Br-O}_{Chol}$  have the same distance, 3.9 Å.

As  $\text{Br}^-$  counterions strongly interact with the oxygen atom of the Chol (proven by our simulations but also experimentally<sup>5</sup>), we observed interesting phenomena in our trajectories.  $\text{Br}^-$  counterions drag the coordinating water inside the QS membrane. In Figure 3.5-(c),  $\text{Br}^-$  counterions coloured in green are the ones able to cross the QS membrane, and the ones colored in yellow are those further than 5 Å apart from the oxygen atom. In that way, it is possible to draw a correlation line between  $\text{Br}^-$  counterions and their waters by hydrogen bonds forming ordered structures as shown in Figure 3.5-(c). In the Figure 3.5-(a) two chains are indicated, in magenta and pink, in order to highlight the ion net, but also because it is observed how  $\text{Br}^-$  counterions can be shared either by two cholesterol

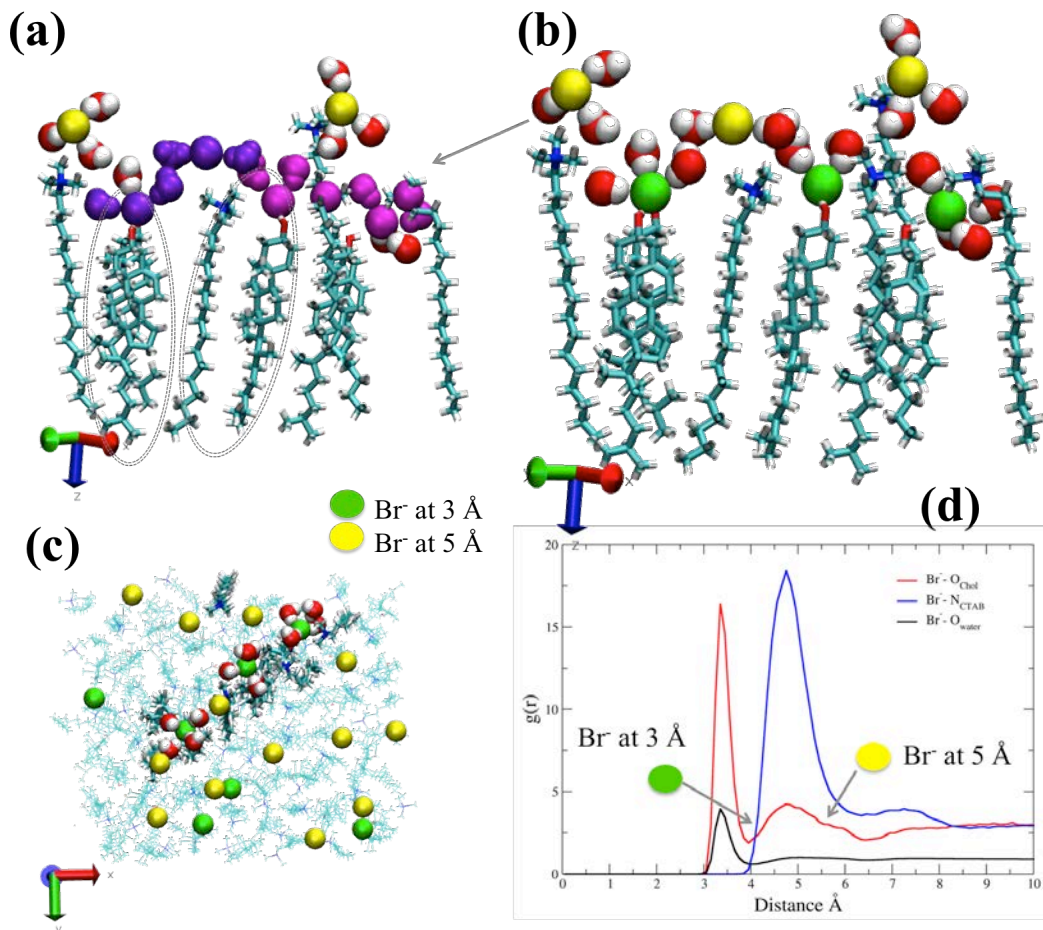


Figure 3.5: (a) Snapshots of the ions at the QS surface-water interface.  $\text{CTA}^+$  and cholesterol molecules are in licorice representation and adsorbed anions are shown as spheres with their van der Waals radii. Bromide ions coloured in green and yellow are the one adsorbed at 3 Å and 5 Å distance from the oxygen atom of the cholesterol. Water molecules at 2.5 Å distance from bromide ions are also represented in van der Waals radii. (b) Is the same as (a) but with the ion nets painted in magenta and pink colours in order to show two different ion-nets formed. (c) Top view of the QS surface highlighting laterally correlated ions that share oxygen atoms in their first coordination shell (green) and second (yellow). (d) Radial pair distribution function of the bromide interactions with cholesterol, CTAB and water molecules.

molecules or by one Chol and one CTAB molecule at the same time.

Finally, it must be mentioned that these water networks appear also without the presence of ions; they are induced by the Cholesterol molecules. This phenomena has been observed in DPPC:Chol bilayer. Results from MD simulations of this bilayer can be found in the Annex, section A.2.1.

### 3.1.4 DIFFUSION COEFFICIENT STUDY

The remaining sections of the analysis at 25 °C are of time-dependent properties, starting by the diffusion coefficient. The diffusion coefficient, also called diffusivity, is an important parameter indicative of the diffusion mobility. It is a physical constant dependent on molecule size and other properties of the diffusing substance as well as on temperature and pressure. In this study, the temperature (298 K) and pressure (1 atm) will be fixed values. The script used to calculate the diffusion coefficient is based on the selection of one atom of interest, and the calculation of the mean square displacement (MSD), whose slope will provide the diffusion coefficient for that particular atom.

The statistical analysis of these trajectories shows that the motion is Brownian, since the mean squared displacement (MSD) in the XY plane follows a straight line with time. The lateral diffusion coefficient  $D$  is also determined by fitting to the Einstein relationship  $MSD(t) = 4Dt$ . Particularizing the expression for the x and y axes, we obtain the following equations:

$$\begin{aligned} \langle x^2 \rangle &= 2D_x \Delta t \\ \langle y^2 \rangle &= 2D_y \Delta t \end{aligned} \tag{3.1}$$

Focus on the simulations run for the systems studied; Quatsomes, relevant results have been obtained. Figure 3.6 shows a Brownian diffusion movement of the atoms selected. It is remarkable that both X and Y directions show a homogeneous movement although atoms are able to explore more regions in Y direction than X direction within the simulation time. This can be explained because the diffusivity in Y direction in QS is one order of magnitude bigger than X direction, which means that the diffusion is faster (see Table 3.2).

Diffusivity is generally described for a given pair of species. For a multi-component system, it is described for each pair of species in the system. The higher the diffusivity (of one substance with respect to another), the faster they diffuse into each other. For the

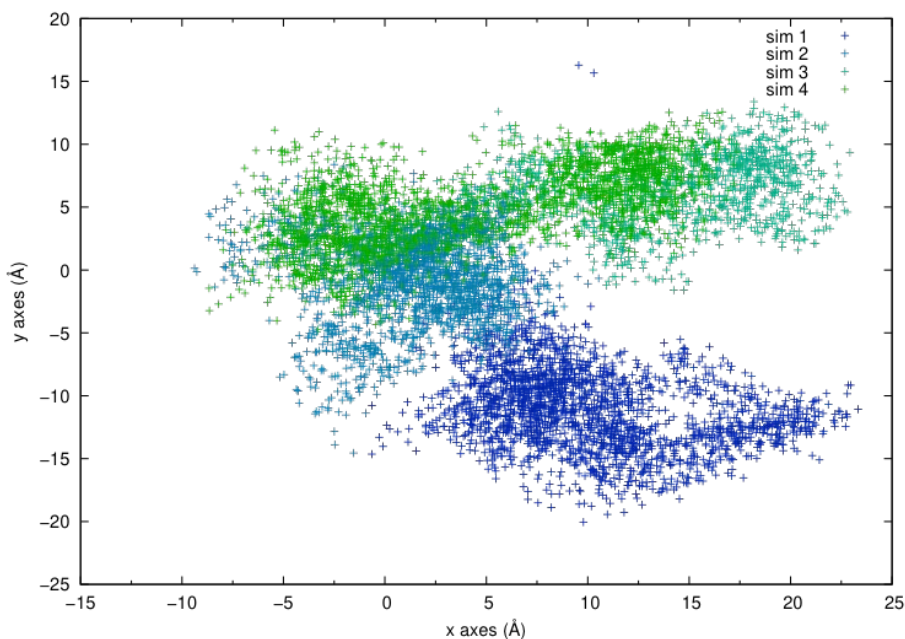


Figure 3.6: Trajectory in X and Y direction of a random nitrogen atom of  $\text{CTA}^+$  molecule (Quatsome). Different colours corresponds to different consecutive simulations. The trajectory starts with: sim 1 (dark-blue), then sim 2 (blue), followed by sim 3 (green) and finally sim 4 (dark-green).

Table 3.2: Diffusion coefficient values of carbon atoms located in in the  $\text{CTA}^+$  molecule's head as a representation of the QS in  $\text{cm}^2/\text{s}$ .

	Diffusion coefficient	C ( $\text{CTA}^+$ )
<b>T=298 K</b>	$D_x$	$4.6 \cdot 10^{-7} \text{ cm}^2/\text{s}$
	$D_y$	$5.2 \cdot 10^{-6} \text{ cm}^2/\text{s}$

study of the diffusion coefficient of QS system it has been selected the C atom of the head of the  $\text{CTA}^+$  molecules. The diffusion coefficient for the study of QS is calculated only in X and Y directions, because our system are conformed as vesicles and to maintain its natural structure, the vesicle cannot diffuse in Z direction (otherwise it would lose its stability).

As we are comparing the diffusion coefficient in liquid phases, it was considered to compare the values of the QS with those of water and phospholipid membranes. For the same temperature and pressure, it is reasonable to think that the value of the density of the molecules in membranes in general would be much higher, and that their mobility would be lower than water, which implies a much lower diffusion coefficient.

Remarkably, we notice that for phospholipids, the value is in the same order of magni-

tude,  $10^{-7}$  cm<sup>2</sup>/s. So, because phospholipid membranes must be in a fluid state for normal cell functioning, it is the structure of fluid bilayers that is relevant to understand the interactions in molecular detail. Based on this, and comparing both diffusion coefficient values and also the orientations of the Cholesterol and CTA<sup>+</sup> tails inside the membrane, it is possible to affirm that QS itself behaves as a fluid membrane.

This result is consistent with the one observed by atom force microscopy, in which the force-separation curves over an area of the supported QS membrane were calculated. All the details of this study can be found in its corresponding work<sup>14</sup>.

In conclusion, both the molecular dynamics simulations run and the calculation of the diffusion coefficient values prove that all the molecules that constitute the QS system have a diffusion movement in an order of magnitude of  $10^{-7}$  cm<sup>2</sup>/s. Thus, the QS system behaves as a fluid membrane, as its diffusion coefficient can be compared to the phospholipid's diffusion coefficient.

### 3.1.5 ORIENTATION OF QUATSOME COMPONENTS

The QS bilayer at 25 °C is shown in Figure 3.7. We show the results for the tilt angle of CTA<sup>+</sup> with respect to time, as well as representative snapshots of the bilayer, showing the tilt of both CTA<sup>+</sup> and Chol molecules. The tilt angle is the angle formed by the direction perpendicular to the surface plane, and the direction determined by the N atom of the CTAB and its centre of masses. For Chol, the tilt was always the same as the one reported for CTA<sup>+</sup> (data shown in Figure A.5 in Annex), so the tilt angles in Figure 3.7 correspond to the tilt of the CTA<sup>+</sup>-Chol synthon. The first remarkable observation is that the symmetry within the bilayer is spontaneously broken, in the sense that the CTA<sup>+</sup> surfactant molecules have different tilts in each leaflet of the bilayer. It is interesting to note that a similar symmetry breaking has been previously observed in MD simulations of other stable vesicles (catanionic surfactant vesicles), see reference<sup>4</sup>, Figure 1. It is also remarkable that bilayer asymmetry is a necessary requisite for systems forming spherical

vesicles in bulk solution<sup>31</sup>, as in the cases of our QS system or the catanionic surfactant mixtures considered in reference<sup>4</sup>.

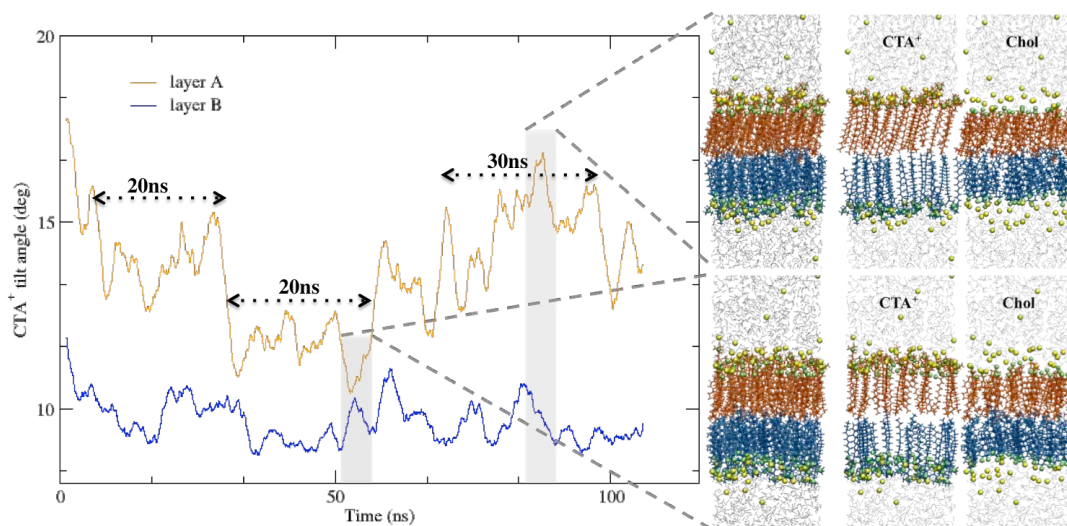


**Figure 3.7:** Results obtained in MD simulations of a QS\_H2O bilayer at 25 °C (no added salt). The left plot shows the tilt angle for CTA<sup>+</sup> molecules (averaged over a leaflet) vs. time during the MD simulations. The data for each leaflet of the bilayer is indicated in a different color. The residence time into different states with different tilt angles are indicated in the figure. Right: representative snapshots of the states indicated in grey in the left plot. For each case we show the full bilayer and to facilitate the visualization we also show partial views with only CTA<sup>+</sup> or only Chol molecules. The molecules at each leaflet are colored different (blue or orange) in correspondence with the left plot. N atoms from the CTA<sup>+</sup> headgroups are indicated as green spheres and Br<sup>-</sup> ions are shown as yellow spheres. The shadow region corresponds to the region occupied by water molecules.

More importantly, not only the average tilt angle is different in each leaflet of the bilayer, but also the behavior of that angle as a function of time. In one of the leaflets, the CTA<sup>+</sup> fluctuates around an average tilt of 10° (Figure 3.7). In the other leaflet, the CTA<sup>+</sup> molecules behave in such a way that they jump between different states, that are defined by a value of the tilt angle, remaining in these states during time intervals of 20-30 ns. The observed states have angle values of ~13° and ~15°. The length of the time intervals are substantial in comparison to the time scale of the simulation.

This simulation results are in line with, and helped to the interpretation of, the following experimental results. An experimental study at nanoscale of a Chol:CTAB QS bilayer was

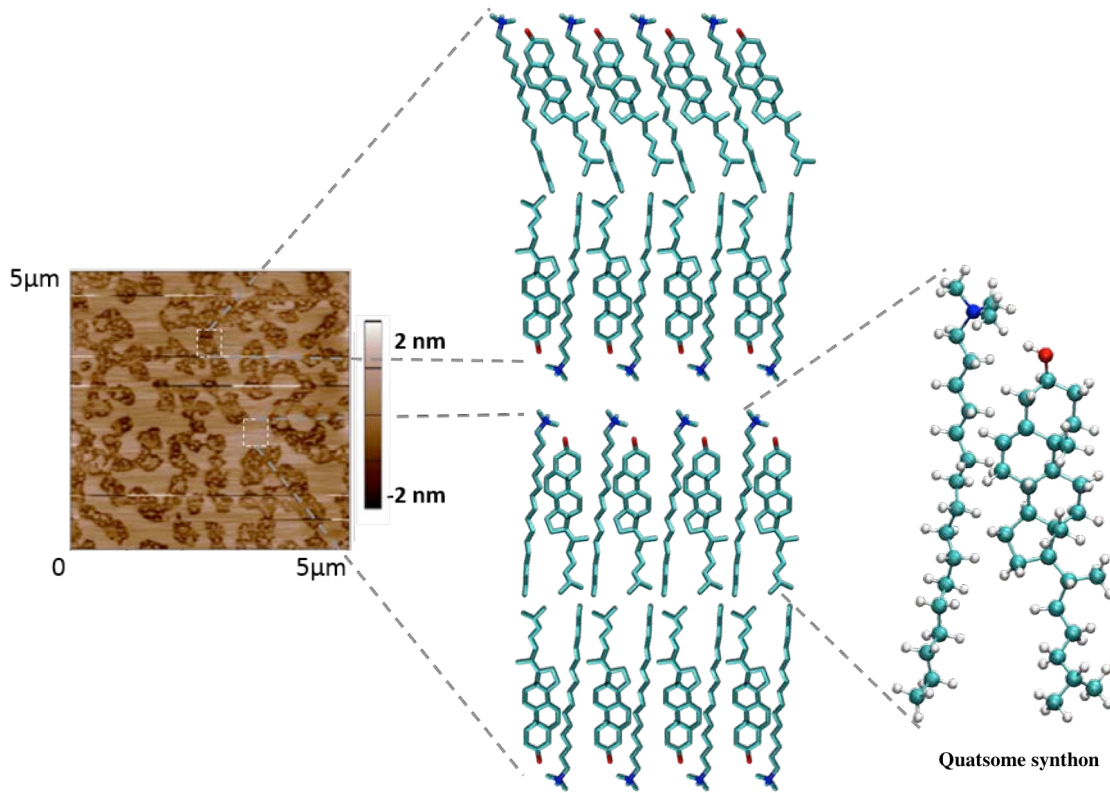


Figure 3.8: Molecular interpretation of the different topographical domains observed in the supported QS membranes by AFM, as domains with different tilt angles for the  $\text{CTA}^+$ -Chol bimolecular synthon. The  $\text{CTA}^+$  and Chol structures are shown in CPK representation. Figure reproduced from ref.<sup>14</sup> with permission from The Royal Society of Chemistry.

performed in collaboration with Dra. Marina I. Giannotti and Dra. Berta Gumí-Audenis from IBEC and Dra. Imma Ratera from ICAMB-CSIC, in order to study its mechanical properties by AFM. A Quatsome membrane was spread over a mica surface for 30 min at room temperature, and it was observed that domains of different thicknesses coexisted as shown in Figure 3.8. We propose a molecular interpretation (see Figure 3.8) for the heterogeneous topography (phase coexistence) observed for the QS membrane. The AFM measurements showed that the different domains of thicknesses were associated with very similar, although discernible, nanomechanical resistance. Based on simulation results on Figure 3.7, we propose that the tilt angle of the synthon of  $\text{CTA}^+$  and Chol is different in the different regions or domains, and thus that the heterogeneities observed are due to different tilt angles, rather than due to different chemical compositions (phase separation).

### 3.1.6 ELASTIC PROPERTIES

The importance of the material properties of QS membranes for its functionalization is well established. Notably, the elastic properties of the membrane, which depend on its composition, can directly influence in the function and its organization<sup>7</sup>. Determining these properties is therefore key for a mechanistic understanding of how the Quatsome system functions. In this section we are going to firstly evaluate the bending rigidity as has generated considerable interest due to the direct implications of bilayer curvature of the Quatsome vesicles and secondly the effect of the tension on the QS bilayer and see how it may affect to the internal structure.

#### BENDING RIGIDITY

Several experimental methods exist to calculate the bending rigidity of lipid bilayers, such as cryo-TEM or small-angle X-ray scattering (SAXS), but it can also be computed from simulations. Thus, we have used a new method that obtains the bending rigidity from MD trajectories by following the microscopic fluctuations of lipid tilts and splays<sup>17</sup>. The algorithm derived from this method is suitable for membranes with binary mixtures of lipids in the liquid ordered and disordered phases. Thus, we have employed it for our system of mixed CTAB/cholesterol, and we have used it also with a DPPC/cholesterol mixed system for comparison purposes.

The strategy used by the algorithm to obtain the bending rigidity is to first calculate the distribution of lipid splay from a well-converged MD simulation trajectories and then extract the bending rigidity modulus from a quadratic fit<sup>17</sup>. For that, it is necessary first to define the head group and tail and the director vector that connects the head and tail groups for the molecules we want to study. For all-atom system, the following set of atoms (in CHARMM36 force-field notations) are used: for the CTA<sup>+</sup> surfactant we use the nitrogen (N) atom and the last carbon atoms (C14, C15, C16) of the molecule as head and tail respectively, and for the director vector we use the three carbon atoms below N (C1, C2,



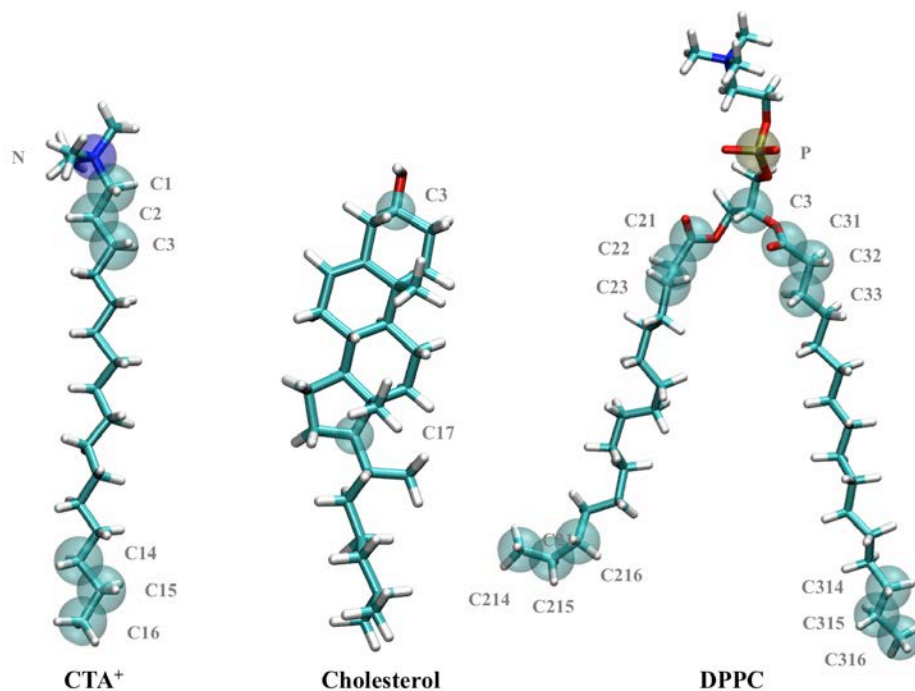


**Figure 3.9: Structures of all-atom CTA<sup>+</sup> (left), cholesterol (center) and DPPC lipid (right) molecules highlighting positions of the atoms (in transparent spheres) used for definition of local director vector (yellow line).**

C3; for the cholesterol molecule, the director vector connects C3 (head group) and C17 (tail) atoms on the ring; for the two-tail DPPC phospholipid, the director vector (C2, C21, C22, C23, C31, C32, C33) connects the center of mass (COM) of the head-groups regions defined by P, to the last three terminal carbon in each lipid tail (C314, C315, C316 C214, C215, C216).

Once the splays have been calculated, their distribution can be obtained and used to determine the bending rigidity using the equation (5) of the section *Theoretical Background* in the work<sup>17</sup>. Firstly, it is required to fix the area per head group. The algorithm then calculates the splay distribution based on the MD trajectories, and then the potential mean force (PMF), for finally computing the bending rigidity value (see Figure 3.10).

In the case of the CTAB/Chol system, the area per polar headgroup is set to  $57 \text{ \AA}^2$ , calculated from the MD trajectories. For the DPPC/Chol, it is  $65 \text{ \AA}^2$ . Plots shown in Figure 3.10 corresponds to the system CTAB/Chol to the last 22 ns of the S1 simulation (see Table

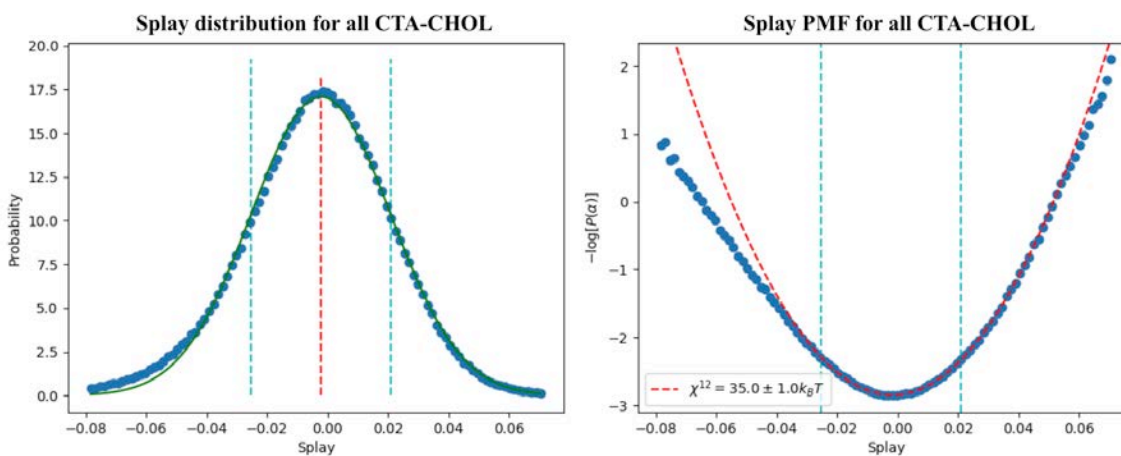


**Figure 3.10:** Figures generated from the algorithm<sup>17</sup>. On the left, the splay distribution and on the right the PMF of the CTA<sup>+</sup> and cholesterol molecules.

3.1). Nevertheless, we calculated the bending rigidity for all the S1 trajectory dividing it in sections, and we calculated the weighted arithmetic mean obtaining a value of  $K_C = 35 k_B T \pm 1$ . We also computed the contribution of CTAB and Chol components to the  $K_C$ , and we estimated a 48% and a 52% by the CTAB and Chol respectively, almost showing the same contribution each. This outstanding result supports the concept of the synthon explained in the introduction; CTAB and Chol act as a unit. The calculations with the DPPC-Chol system threw an unreliable value, so the work by Doktorova et al.<sup>7</sup> was consulted, where the bending rigidity values of 21 phospholipids were obtained from real-space fluctuations (RSF) analysis<sup>16</sup> of the MD trajectories. The obtained values were  $K_C = \sim 15-40 k_B T$ . As it can be seen, our value obtained for the CTAB/Chol system is within that range, which means that the bending rigidity of our system is comparable to that of other phospholipids.

#### AREA EXPANSION MODULUS AND EFFECT OF TENSION

In general, membrane dimensions and mechanical properties (i.e., bilayer thickness, bending and stretching stiffness or membrane tension) can affect the functions of any membrane<sup>24</sup>. As a consequence a large number of techniques including atomic force microscopy imaging and molecular dynamics simulations are employed to get insights about the structure and

mechanical properties of biological membranes<sup>14</sup>. We have considered 15 MD simulations based on S1 simulation and have increased gradually the surface tension of the membrane from initial value  $\gamma = 0$  to  $\gamma = 300$  dyn/cm in order to study some mechanical properties of the Quatsome bilayer. All computational details of simulations performed are given in Table A.3 in Annex.

In the classical elastic model, the membrane response to a given stress is assumed to be linear for small deformations and is characterized by three elastic moduli: the area expansion modulus ( $K_A$ ), the shear modulus ( $\mu$ ), and the bending stiffness (B)<sup>19</sup>. In this study we have evaluated the area expansion modulus  $K_A$  through our simulations. This parameter is defined in the following formula 3.2:

$$K_A^{-1} = \frac{1}{A_o} \left( \frac{\partial A}{\partial \gamma} \right) \quad (3.2)$$

where  $A$  is the area,  $A_o$  the initial area, and  $\gamma$  the applied tension. This formula indicates that the area varies linearly with respect to the tension, by the constant  $A_o/K_A$ . Such constant is in fact the slope of the graph that plots the area per molecule versus the surface tension (in the linear phase), and thus  $K_A$  can be computed as the initial area  $A_o$  divided by the slope.

Figure 3.11 shows precisely that information, and it can be seen how the area per polar head group of the bilayer increases with increasing membrane tension, indicating loosening of packing of the synthon structure in the bilayer. The area per polar head group increased from  $58 \text{ \AA}^2$  to  $61 \text{ \AA}^2$  (total increase of 5.5%) when the membrane tension increased from 0 to 50 dyn/cm, yielding an area expansion modulus ( $K_A$ ) of 1873 dyn/cm; this simulation-based value of  $K_A$  is slightly larger than that of catanionic vesicles (SOS/CTAB)<sup>4</sup> with a value of 1623 dyn/cm and is an order of magnitude smaller than the value from MD simulation of DPPC bilayer<sup>10</sup>,  $130 \pm 60$  dyn/cm, or the experimental value of 241 dyn/cm reported for DOPC bilayer<sup>25</sup>.

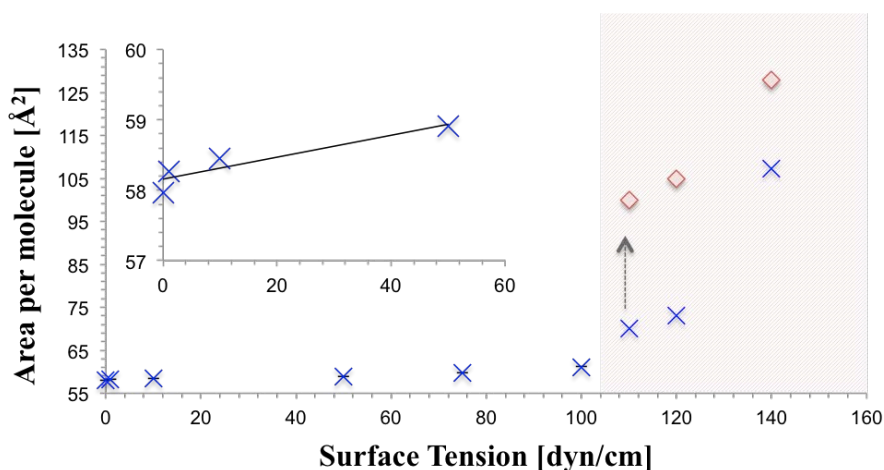


**Figure 3.11:** Time-averaged area per polar head group as function of membrane tension. The coloured area shows the region where the membrane collapses after certain time, which has been indicated by cross-diamond pairs.

This results clearly shows that QS bilayer is more rigid than catanionic vesicles and even than phospholipid ones. This can be explained from the molecular point of view as the cholesterol molecules inside the membrane produces a condensing effect by ordering the fluid phase in the membrane<sup>13,6</sup>. Nevertheless, this characteristic of the cholesterol is related with an increase in the lipid bilayer thickness, as for example in<sup>30</sup>. But, as explained in the introduction<sup>11</sup> and probed in the previous section 3.1, cholesterol is part of the synthon with the CTAB component (in QS bilayer), so it may induce condensing effect leading to more rigidity of the membrane, but not blocking the fluidity of the membrane itself or affecting the physic-chemical properties (i.e. thickness).

For values above 100 dyn/cm, the area per molecule does not stabilize around a value but keeps increasing, until the bilayer collapses. This has been indicated in the graph of Figure 3.11, as the colored area. Besides, a detail of this process can also be seen in Figure 3.12, and in the video linked to the QR code in it.

We also concluded that while the QS membrane is extending its structural and mechanical properties at molecular level change. In general what we observed is that at low values of  $\gamma$  the bilayer exhibits disordered alkyl chain characteristics, indicating that system is in liquid-ordered (Ld) phase. On the contrary, at high values of  $\gamma$  (and before collapsing),

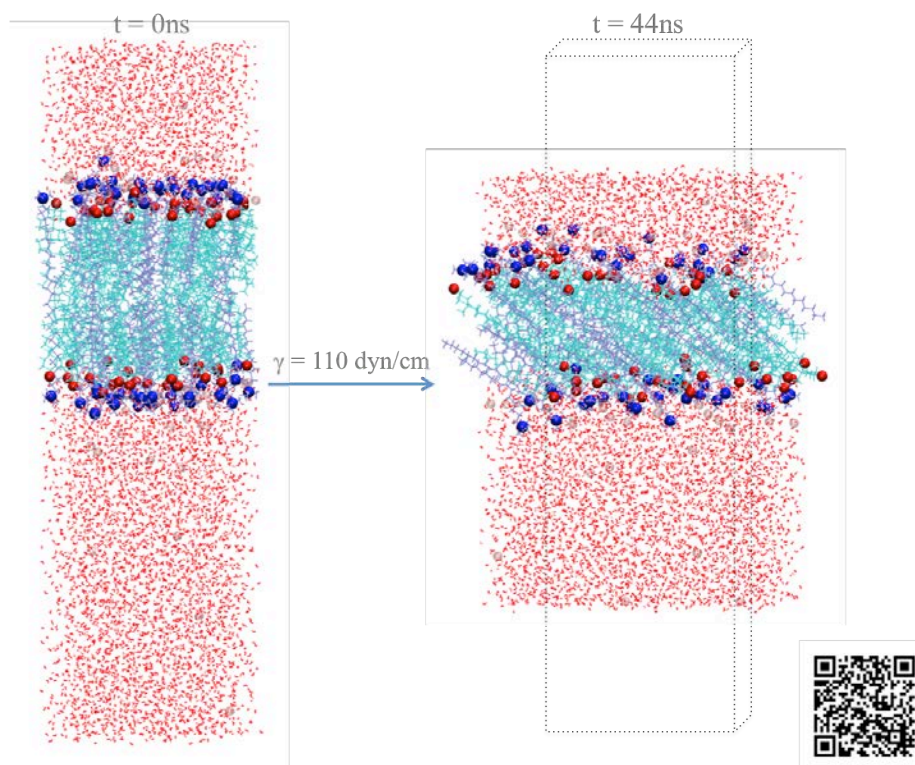


**Figure 3.12:** Snapshots of the simulation of the QS bilayer at  $\gamma = 110\text{ dyn/cm}$ . On the left at 0 ns time in which the bilayer is Ld phase and on the right at 44 ns time is shown the bilayer at S phase.

the bilayer is at gel (S) phase with tilted and ordered alkyl chains. An example of how the tilt angle of the CTA<sup>+</sup> changes within time at  $\gamma = 110\text{ dyn/cm}$  (same simulation as in the Figure 3.12) is shown in Figure A.6 in Annex.

### 3.2 EFFECT OF TEMPERATURE

We performed five more all-atomic MD simulations to study the effect of temperature ( $T$ ) on the QS membrane. This parameter has been selected for study because the literature reports that it has a big effect on the properties of lipid-based bilayers<sup>12</sup>. To this end, we have taken simulation S1 as starting point, and we have extended it another  $\sim 70\text{-}110\text{ ns}$ , varying the temperature. All computational details are the same as those in Table 3.1, with the only difference being that we have considered the following temperatures: 10 °C, 15 °C, 20 °C, 25 °C, 35 °C and 50 °C. Additional details of the simulation are given in Annex,

Table A.2.

We have studied the effect of  $T$  on the thickness and area per molecule. The results are summarized in Table 3.3, we observed no changes regarding the thickness and a small gradual increase in the area per molecule at 50 °C. In Annexes, Figure A.3, we plot the density profiles of the membrane at 10 °C and 50 °C, and we observe that both profiles are almost equal to the one corresponding to 25 °C, concluding that the temperature does not alter the molecular organization of the Quatsome bilayer.

**Table 3.3: Values of area per molecule and thickness vs. temperature.**

<b>T (°C)</b>	<b>Area molec. (Å<sup>2</sup>)</b>	<b>Thickness (nm)</b>
<b>10</b>	57.87	4.3
<b>15</b>	57.69	4.3
<b>20</b>	57.96	4.3
<b>25</b>	57.98	4.3
<b>35</b>	58.43	4.3
<b>50</b>	58.99	4.3

This results are in line with experimental work<sup>12</sup>, where the colloidal structure of the Quatsome was studied, and observed that the morphology does not change upon increasing temperature. This is in contrast with other lipidic systems. As an example, the volumetric thickness of charged membranes, composed of DOPS or DLPS lipids, linearly decreases with the temperature<sup>32</sup>.

Contrary to the case of the thickness and the area per molecule, that have a weak dependence with  $T$ , it has been observed that the the tilt angles of the QS bilayer do have a dependence with the temperature. Recall that the behaviour of this parameter at 25 °C was already studied in the previous section, where different states of tilt angle values over time were observed. In this section, the temperature is varied to analyze its effect over those states.

A first result can be observed in Figure 3.13. The distribution of the angles for 3 different temperatures (15 °C, 25 °C, 50 °C) for both leaflets of the bilayer, shows that the mean angle values do not vary with the temperature, but that one leaflet's distribution has a very

peaked shape, while the other's layer has a more planar shape. This figure also shows that the breaking symmetry phenomena happens at all studied temperatures (above 25 °C as well as below 25 °C).

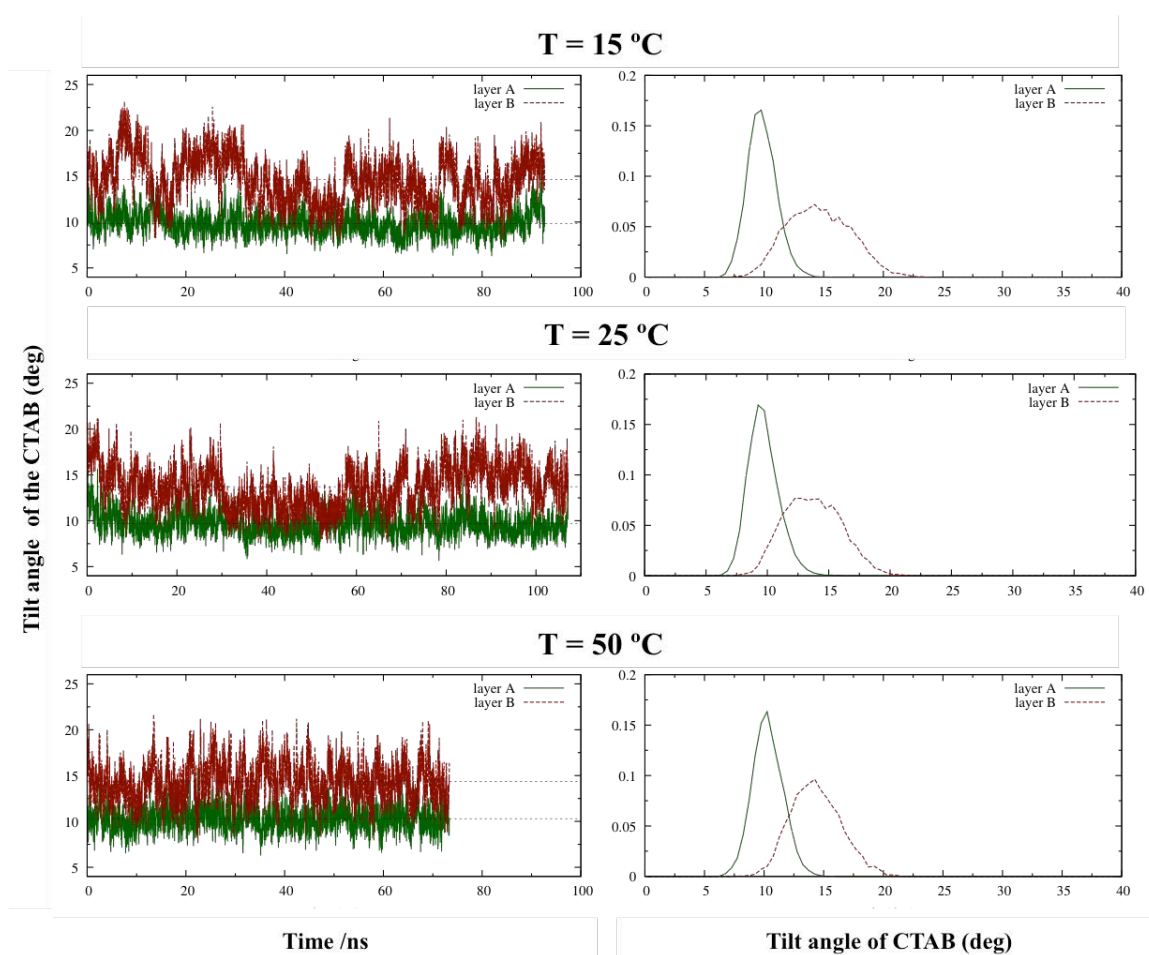


**Figure 3.13:** Comparison of the tilt angle of the  $\text{CTA}^+$  molecules with respect to time and angle distribution and the distribution of the tilt angle of the  $\text{CTA}^+$  molecules at 15 °C, 25 °C and 50 °C.

But then, if these distributions remain constant, where do we observe changes with the temperature? Those changes have been observed in the length of the intervals of the different states where the tilt angle lies. This can be seen in Figure 3.13. Indeed, we can see how, as we increase the temperature (above 25 °C), the lifetime of those states is shorter. And viceversa, as we decrease the temperature (below 25 °C), the length of those intervals is longer. This analysis has been done for all the temperatures considered, and all the

corresponding graphs (angle with respect to time and angle distribution) can be found in the Annexes section, in Figure A.5.

As in the previous section, these simulation results help in the interpretation of experimental work<sup>14</sup>, where it was seen that the QS membrane showed a gradual transition from a heterogeneous to a homogeneous topography upon rising  $T$  (Figure 3.14). Increasing the  $T$  stepwise and leaving the membrane at least for 30 min at each temperature showed that the Quatsome supported (mica) membrane in water turned into a homogeneous phase around  $T = 30\text{ }^{\circ}\text{C}$  (Figure 3.14). From the simulations' point of view, this is due to the tilt angle states changing faster at higher temperatures, as explained in previous paragraph, which has this homogenizing effect (see Figure 3.14).

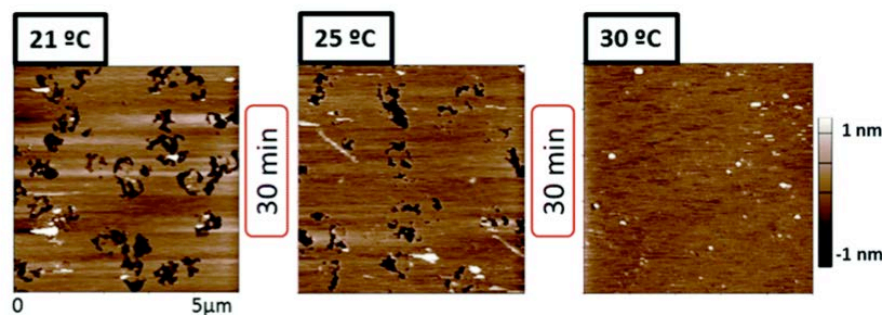


Figure 3.14: AFM topographical images for the QS membrane supported on mica, in ultrapure water. It shows the increase of the experimental temperature. Figure has been adapted from the original on in ref.<sup>14</sup> with permission from The Royal Society of Chemistry.

A deeper quantitative study could be performed by treating the tilt angle with respect to time as time series, and by characterizing those time series by their mean values, Fourier transforms, autocorrelation functions, etc. This way, it would be possible to better quantify the phenomena that are observed qualitatively. Some steps were taken in this direction, but the obtained results were not concluding and a deeper analysis is out of the scope of this thesis.



### 3.3 EFFECT OF ADDITION OF SALT

The effect of ions is of key importance in determining physicochemical properties and functionality of systems like membranes<sup>9</sup>. In spite of the substantial progress achieved in recent years in experimental, theoretical and simulations methods, several effects related to ions still lack a deep physical understanding<sup>18</sup>. A specially big progress has been made related to biological membranes, such as phospholipidic ones, but it is the first time we perform such study for the Quatsome bilayer. An important concept at this point is that of ionic specificity, that refers to the fact that for a wide range of phenomena (surface forces, surface tensions, colloidal stability, etc.) one finds that different ions with the same electrical charge induce different behaviours<sup>6</sup>.

In this section we study the effect of the presence of specific ions in the QS components when 100 mM of NaCl salt is added. As Quatsome is a cationic bilayer, the relevant ions to focus on would be the monovalents Br<sup>-</sup> counterions and Cl<sup>-</sup> ions. For the mentioned purpose, an additional simulation (S2) with added salt was performed starting from the previous simulation, S1. Starting from an equilibrated configuration of the S1 simulation, we added 10 Na<sup>+</sup> and 10 Cl<sup>-</sup> ions (corresponding to ~100 mM) using the ionize plugin of the VMD program. After equilibration and thermalization, we ran a simulation of 131 ns employing the same parameters and conditions as in the S1 case (see Table 3.4).

**Table 3.4: Composition of the systems considered in the MD simulations, including total number of atoms, number of molecules; counterions for the ionic species, the simulation time and the equilibrated size box.**

	<b>Atoms (total)</b>	<b>molec. water/CTAB</b>	<b>Br<sup>-</sup>/Cl<sup>-</sup></b>	<b>Sim time /ns</b>	<b>Size Box</b>
<b>S2</b>	23687	5423/54	54/10	131	226.9nm <sup>3</sup>

Following with the results, the S2 simulation shows that both anions (Br<sup>-</sup> counterions and the Cl<sup>-</sup> anions from the added salt) penetrate in the hydrophilic region of the bilayer. The results for the organization of the anions in both simulations are summarized in Figure 3.15.

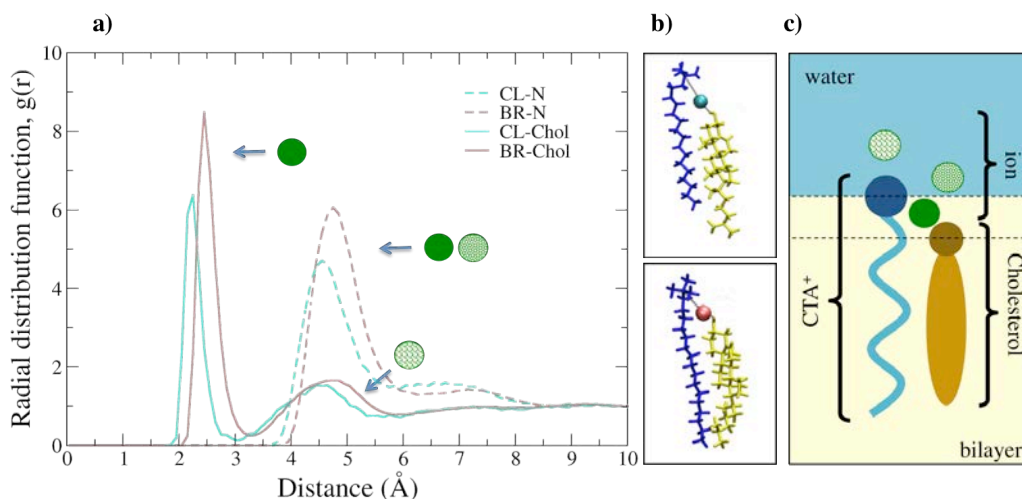


**Figure 3.15:** Interaction of anions with the QS components according to MD simulations at 25 <sup>circ</sup>C. **a)** Radial correlation function  $g(r)$  computed between the anions ( $\text{Br}^-$  or  $\text{Cl}^-$ ) and the polar headgroups (O atom of Chol or N atom of  $\text{CTA}^+$ ) calculated from simulations. **b)** Snapshots of molecular configurations extracted from MD simulations that contribute to the  $g(r)$  function shown in (a).  $\text{CTA}^+$  molecule is shown in blue, Chol molecule in yellow and ions as Van der Waals spheres ( $\text{Cl}^-$  cyan,  $\text{Br}^-$  brown). **c)** Cartoon showing schematically the ionic correlations found in the simulations. A full sphere indicates that the peak corresponds to adsorption of an anion inside the bilayer, shared between  $\text{CTA}^+$  and Chol and a dotted sphere indicates that the peak corresponds to an anion adsorbed on top of a  $\text{CTA}^+$  molecule, as indicated in (a).

As seen in Figure 3.15-(a), the anions that penetrate inside the bilayer are shared between the  $\text{CTA}^+$  headgroup and the -OH group from the cholesterol (Chol). In other words, anions not only interact strongly with cationic  $\text{CTA}^+$  surfactant but also with Chol. It is also worth noting that previous experimental and simulation work on pure Chol monolayers has shown a strong interaction between  $\text{Cl}^-$  and Chol<sup>6</sup>. Here the simulations indicate that the addition of NaCl produces not only an incorporation of  $\text{Cl}^-$  inside the bilayer but also an incorporation of  $\text{Br}^-$ . Recall that in the previous section it was seen in the S1 simulation (where there is no added salt, thus being the  $\text{Br}^-$  counterions the only ions present), that the 10% of  $\text{CTA}^+$  molecules have a  $\text{Br}^-$  ion adsorbed on top, and the 72% of the  $\text{CTA}^+$  molecules have a  $\text{Br}^-$  ion shared with cholesterol (Figure 3.15-(b)). In the simulations with added NaCl (S2), we observe that 8% of  $\text{CTA}^+$  molecules have a  $\text{Br}^-$  adsorbed on top and 2% of  $\text{CTA}^+$  molecules have  $\text{Cl}^-$  anions adsorbed on top, while a 66% have  $\text{Br}^-$  and 9% have  $\text{Cl}^-$  ions shared with Chol (hence a total of 75% of  $\text{CTA}^+$ -Chol synthons share an

anion).

Up to this point we have studied the ions' organization at local level within the bilayer, but we also studied the impact of the ions in the QS structure at global level. Our simulations indicate that the  $\text{Br}^-$  and  $\text{Cl}^-$  ions can form ordered structures when adsorbing at the interface of the QS membrane in water. The attraction between neighbouring ions induces a net formed by the surrounding water molecules.

The local ions' organization results from simulations are in agreement with the experimental results of AFM<sup>14</sup>, in which it has been studied a supported QS membrane with the presence of 100 mM NaCl. In those experiments, the lateral interactions between the molecules of the 2D ordered QS structure were explored by measuring the maximum force the membrane is able to withstand before its rupture (breakthrough force,  $F_b$ ), under the application of an external pressure. Those experiments show an increase in the  $F_b$  after the addition of ions, which is interpreted together with what was seen in the simulations as the ions in the hydrophobic region blocking the lateral mobility of the membrane. This is also seen in other phospholipid bilayers<sup>21,26</sup>.

As it was seen that the temperature had an effect in the tilt angle of the leaflets of the bilayer (as explained in the previous subsection), it is also investigated the possible effect of the added salt in this parameter. Figure 3.16-(b) shows the results of this analysis. Figure 3.16-(a) contains the values of the angles of both leaflets (at 25 °C) with respect to time, while Figure 3.16-(c) has the distributions of those angles for both the cases with and without added salt. In Figure 3.16-(a) we observe again that the tails of the  $\text{CTA}^+$  molecules from the two leaflets have different average tilt angles ( $10^\circ$  and  $14^\circ$  respectively) but that the  $\sim 20$  ns long jumps observed in absence of salt are not observed in presence of added salt. In this case, the fluctuation between different orientations take place at much shorter time scales, of the order of 1 ns or less. In Figure 3.16-(c), we observe that the presence of salt does not affect the breaking symmetry of the bilayer.

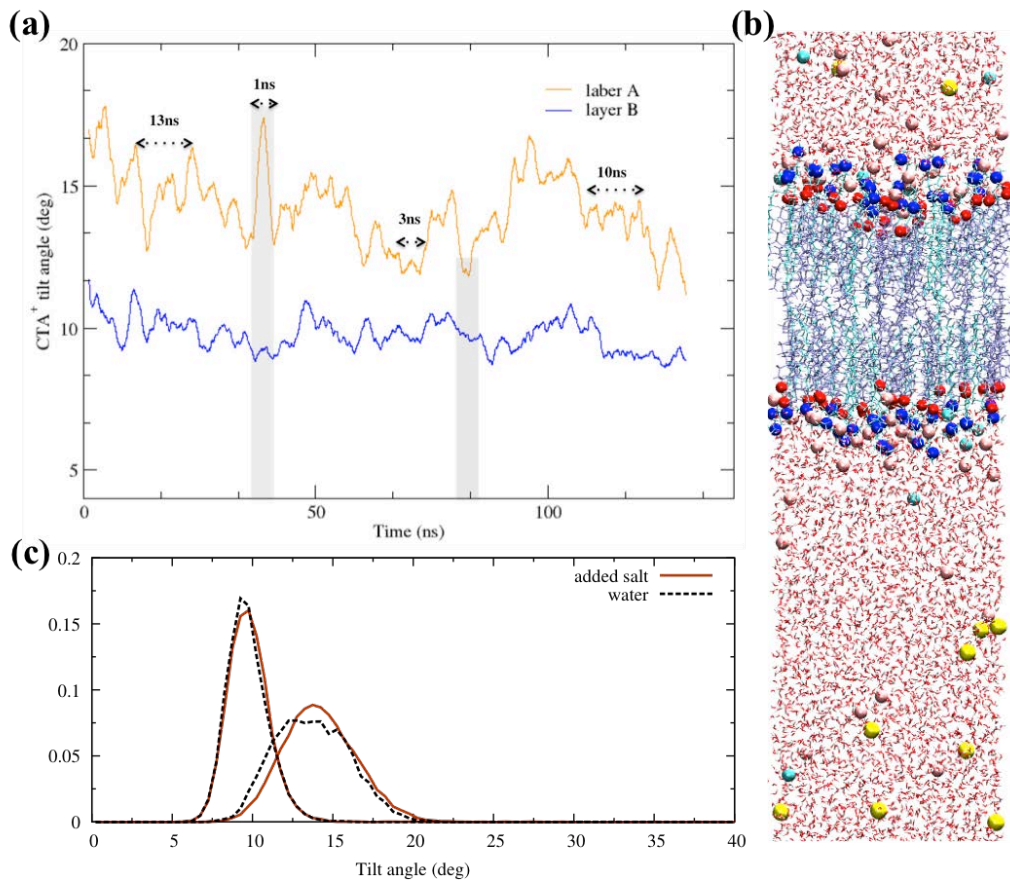


**Figure 3.16:** (a) Shows the tilt angle for CTA<sup>+</sup> molecules (averaged over a leaflet) vs. time during the MD simulations. The data for each leaflet of the bilayer is indicated in a different color as in Figure 3.7. (b) Snapshot of the MD simulations of a QS bilayer at 25 °C with added salt (NaCl) (result from S2 simulation). (c) Distribution of values of tilt angles of CTA<sup>+</sup> molecules for the QS system with water and with added salt (NaCl). Results show similar behavior in both cases pointing out two peaks corresponding to the different orientations described in the main article.

Finally, we performed five more all-atomic MD simulations to show the effect of the temperature ( $T$ ) on the QS membrane with added salt. To this end, we have taken simulation S2 as starting point, and we have extended it another  $\sim 70$ -110 ns, varying the temperature. All computational details are the same as those in Table 3.4, with the only difference being that we have considered the following temperatures: 15 °C, 25 °C, 30 °C, 35 °C, 40 °C and 50 °C, which can be found in Table A.4 in Annexes.

We highlight that we have studied the effect of  $T$  on the thickness and area per molecule, and we observed no changes regarding the thickness and a small gradual increase in the area per molecule at 50 °C (see all values in Table A.5). In Annexes, Figure A.4, we plot the densities profiles of the membrane at 15 °C and 50 °C, and we observe that both profiles are almost equal to the one corresponding to 25 °C, thus the thickness remain constant.

## References

- [1] Cabrera, I., Abasolo, I., Corchero, J. L., Elizondo, E., Gil, P. R., Moreno, E., Faraudo, J., Sala, S., Bueno, D., González-Mira, E., Rivas, M., Melgarejo, M., Pulido, D., Albericio, F., Royo, M., Villaverde, A., García-Parajo, M. F., Schwartz, S., Ventosa, N., & Veciana, J. (2016).  $\alpha$ -Galactosidase-A Loaded-Nanoliposomes with Enhanced Enzymatic Activity and Intracellular Penetration. *Advanced Healthcare Materials*, 5(7), 829–840.
- [2] Cabrera, I., Elizondo, E., Esteban, O., Corchero, J. L., Melgarejo, M., Pulido, D., Córdoba, A., Moreno, E., Unzueta, U., Vazquez, E., Abasolo, I., Schwartz, S., Villaverde, A., Albericio, F., Royo, M., García-Parajo, M. F., Ventosa, N., & Veciana, J. (2013). Multifunctional Nanovesicle-Bioactive Conjugates Prepared by a One-Step Scalable Method Using CO<sub>2</sub>-Expanded Solvents. *Nano Letters*, 13(8), 3766–3774.
- [3] Cansell, F. & Aymonier, C. (2009). Design of functional nanostructured materials using supercritical fluids. *The Journal of Supercritical Fluids*, 47(3), 508–516.
- [4] Chen, C.-h., Tian, C.-a., & Chiu, C.-c. (2017). The Effects of Alkyl Chain Combinations on the Structural and Mechanical Properties of Biomimetic Ion Pair Amphiphile Bilayers. *Bioengineering*, 4(4), 84+.
- [5] D’Angelo, P., Migliorati, V., & Guidoni, L. (2010). Hydration Properties of the Bromide Aqua Ion: the Interplay of First Principle and Classical Molecular Dynamics, and X-ray Absorption Spectroscopy. *Inorganic Chemistry*, 49(9), 4224–4231.
- [6] Del Castillo-Santaella, T., Maldonado-Valderrama, J., Faraudo, J., & Martín-Molina, A. (2016). Specific Ion Effects in Cholesterol Monolayers. *Materials*, 9(5), 340+.
- [7] Doktorova, M., Harries, D., & Khelashvili, G. (2017). Determination of bending rigidity and tilt modulus of lipid membranes from real-space fluctuation analysis of molecular dynamics simulations. *Physical Chemistry Chemical Physics*, 19(25), 16806–16818.
- [8] Elizondo, E., Veciana, J., & Ventosa, N. (2012). Nanostructuring molecular materials as particles and vesicles for drug delivery, using compressed and supercritical fluids. *Nanomedicine*, 7(9), 1391–1408.
- [9] Evans, F. & Wennerström, H. (1991). *The colloidal domain: Where physics, chemistry, biology and technology meet*.

- [10] Feller, S. E., Venable, R. M., & Pastor, R. W. (1997). Computer Simulation of a DPPC Phospholipid Bilayer: Structural Changes as a Function of Molecular Surface Area. *Langmuir*, 13(24), 6555–6561.
- [11] Ferrer-Tasies, L., Moreno-Calvo, E., Cano-Sarabia, M., Aguilera-Arzo, M., Angelova, A., Lesieur, S., Ricart, S., Faraudo, J., Ventosa, N., & Veciana, J. (2013). Quatsomes: Vesicles Formed by Self-Assembly of Sterols and Quaternary Ammonium Surfactants. *Langmuir*, 29(22), 6519–6528.
- [12] Grimaldi, N., Andrade, F., Segovia, N., Ferrer-Tasies, L., Sala, S., Veciana, J., & Ventosa, N. (2016). Lipid-based nanovesicles for nanomedicine. *Chemical Society Reviews*, 45(23), 6520–6545.
- [13] Gumí-Audenis, B., Costa, L., Carlá, F., Comin, F., Sanz, F., & Giannotti, M. (2016). Structure and Nanomechanics of Model Membranes by Atomic Force Microscopy and Spectroscopy: Insights into the Role of Cholesterol and Sphingolipids. *Membranes*, 6(4), 58+.
- [14] Gumí-Audenis, B., Illa Tuset, S., Grimaldi, N., Pasquina, L., Ferrer-Tasies, L., Sanz-Carrasco, F., Veciana, J., Ratera, I., Faraudo, J., Ventosa, N., & Giannotti, M. I. (2018). Insights into the structure and nanomechanics of the Quatsome membrane by force spectroscopy measurements and molecular simulations. *Nanoscale*.
- [15] Jennings, J., Beija, M., Richez, A. P., Cooper, S. D., Mignot, P. E., Thurecht, K. J., Jack, K. S., & Howdle, S. M. (2012). One-Pot Synthesis of Block Copolymers in Supercritical Carbon Dioxide: A Simple Versatile Route to Nanostructured Microparticles. *Journal of the American Chemical Society*, 134(10), 4772–4781.
- [16] Johner, N., Harries, D., & Khelashvili, G. (2014). Curvature and Lipid Packing Modulate the Elastic Properties of Lipid Assemblies: Comparing H II and Lamellar Phases. *The Journal of Physical Chemistry Letters*, 5(23), 4201–4206.
- [17] Johner, N., Harries, D., & Khelashvili, G. (2016). Implementation of a methodology for determining elastic properties of lipid assemblies from molecular dynamics simulations. *BMC Bioinformatics*, 17(1).
- [18] Kunz, W. (2010). Specific ion effects in colloidal and biological systems. *Current Opinion in Colloid & Interface Science*, 15(1-2), 34–39.
- [19] Lenormand, G., Hénon, S., Richert, A., Siméon, J., & Gallet, F. (2001). Direct Measurement of the Area Expansion and Shear Moduli of the Human Red Blood Cell Membrane Skeleton. *Biophysical Journal*, 81(1), 43–56.
- [20] Martín-Molina, A., Rodríguez-Beas, C., & Faraudo, J. (2010). Charge Reversal in Anionic Liposomes: Experimental Demonstration and Molecular Origin. *Physical Review Letters*, 104(16), 168103+.
- [21] Martín-Molina, A., Rodríguez-Beas, C., & Faraudo, J. (2012). Effect of Calcium and Magnesium on Phosphatidylserine Membranes: Experiments and All-Atomic Simulations. *Biophysical Journal*, 102(9), 2095–2103.

- 
- [22] Pasquali, I. & Bettini, R. (2008). Are pharmaceuticals really going supercritical? *International Journal of Pharmaceutics*, 364(2), 176–187.
- [23] Phillips, J. C., Braun, R., Wang, W., Gumbart, J., Tajkhorshid, E., Villa, E., Chipot, C., Skeel, R. D., Kalé, L., & Schulten, K. (2005). Scalable molecular dynamics with NAMD. *Journal of Computational Chemistry*, 26(16), 1781–1802.
- [24] Picas, L., Rico, F., & Scheuring, S. (2012). Direct Measurement of the Mechanical Properties of Lipid Phases in Supported Bilayers. *Biophysical Journal*, 102(1), L01–L03.
- [25] Reddy, A. S., Warshaviak, D. T., & Chachisvilis, M. (2012). Effect of membrane tension on the physical properties of DOPC lipid bilayer membrane. *Biochimica et Biophysica Acta (BBA) - Biomembranes*, 1818(9), 2271–2281.
- [26] Redondo-Morata, L., Giannotti, M. I., & Sanz, F. (2013). Structural impact of cations on lipid bilayer models: Nanomechanical properties by AFM-force spectroscopy. *Molecular Membrane Biology*, 31(1), 17–28.
- [27] Reverchon, E. & Adami, R. (2006). Nanomaterials and supercritical fluids. *The Journal of Supercritical Fluids*, 37(1), 1–22.
- [28] Ricci, M., Spijker, P., & Voitchovsky, K. (2014). Water-induced correlation between single ions imaged at the solid–liquid interface. *Nature Communications*, 5(1).
- [29] Ricci, M., Trewby, W., Cafolla, C., & Voitchovsky, K. (2017). Direct observation of the dynamics of single metal ions at the interface with solids in aqueous solutions. *Scientific Reports*, 7(1).
- [30] Róg, T., Pasenkiewicz-Gierula, M., Vattulainen, I., & Karttunen, M. (2009). Ordering effects of cholesterol and its analogues. *Biochimica et Biophysica Acta (BBA) - Biomembranes*, 1788(1), 97–121.
- [31] Safran, S. A., Pincus, P., & Andelman, D. (1990). Theory of Spontaneous Vesicle Formation in Surfactant Mixtures. *Science*, 248(4953), 354–356.
- [32] Szekely, P., Dvir, T., Asor, R., Resh, R., Steiner, A., Szekely, O., Ginsburg, A., Mosenkis, J., Guralnick, V., Dan, Y., Wolf, T., Tamburu, C., & Raviv, U. (2011). Effect of Temperature on the Structure of Charged Membranes. *The Journal of Physical Chemistry B*, 115(49), 14501–14506.
- [33] Tieleman, D. P., Marrink, S. J., & Berendsen, H. J. C. (1997). A computer perspective of membranes: molecular dynamics studies of lipid bilayer systems. *Biochimica et Biophysica Acta (BBA) - Reviews on Biomembranes*, 1331(3), 235–270.
- [34] Trewby, W., Faraudo, J., & Voitchovskya, K. (2018). Long-lived ionic nano-domains modulate the stiffness of lipid membranes. *Nanoscale (submitted)*.





*I was taught that the way of progress was neither  
swift nor easy.*

Marie Curie

# 4

## CG Simulations:

### Loosing detail to gain insight

In the previous chapter, a physico-chemical characterization of the Quatsome planar bilayer was carried out. All-atomic molecular dynamics simulations were employed to obtain a full atom-level theoretical understanding. However, a bigger picture that encompasses the whole vesicle system is still lacking. Even simple questions such as the existence of asymmetries in the QS membrane are uncertain. At this point, performing simulations of the whole Quatsome vesicle would open up a whole new dimension perspective of the system.

The main goal of this chapter, thus, is to obtain the organization of the full spherical vesicle (maintaining the same proportion 1:1 of chol:ctab components considered in chapter 3). The organization of amphiphilic molecules that self-assemble forming vesicles can lead to thermodynamically stable structures. The theoretical requirements for such stability are well reported in literature<sup>18</sup>, i.e., the presence of a mixed system and the presence of asymmetries inside the membrane. The first one is fulfilled by the Quatsome, and thus investigating the second is the motivation for this chapter. All this makes the QS system very interesting and the results from simulations of the full vesicle very valuable. Nevertheless, the length and time scales needed to study the formation of vesicles and their interactions are far from being feasible in all-atomic (AA) MD simulations. This has motivated the use of MD simulations of coarse-grain (CG) model<sup>14</sup>. CG models focus on essential features, averaging over less important atomistic details.

This chapter verses about the steps taken to be able to simulate the Quatsome vesicle with the CG technique, and its results. The first obstacle came when it was noticed that there was no adequate CG model of one of the components of the Quatsome, the CTAB. The cholesterol model, on the contrary, was available. We proposed a CG CTAB model and performed CG MD simulations in order to check the correctness of such model, as it is explained in a later section. Once this was done, we moved on with the preparation of the Quatsome vesicle simulation, expecting to obtain a spherical vesicle and with the aim of studying the stability, the organization of the components and the potential presence and cause of asymmetries.

#### 4.1 MARTINI MODELS OF CHOLESTEROL AND CTAB

In this section we describe the cholesterol and CTAB Martini models employed in the CG MD simulations, following the methodology described in section 2.3.

The molecule  $C_{27}H_{46}O$  know as Cholesterol ( $(3\beta)$ -cholest-5-en-3-ol) is an sterol, a type of lipid molecule. Cholesterol presents a special challenge for coarse-graining due to its

complicated local structure, see Figure 4.1-(a). The Martini model is based on a four-to-one mapping, i.e., on average four heavy atoms plus associated hydrogens are represented by a single interaction center. But, to represent the geometry of small ring-like fragments or molecules, the general four-to-one mapping approach is too coarse. Ring-like molecules are therefore mapped with a higher resolution of up to two non-hydrogen atoms to one Martini particle<sup>13</sup>.

The first cholesterol model was developed by Marrink et al.<sup>12</sup> in 2007. It was defined by eight particles: six representing the sterol body and two for the short tail. The mapping proposed allowed the planar structured based on 3:1 basis, using special particle set, labeled "S". In early 2014, Daily et al.<sup>4</sup> developed an accurate coarse-grained model for the cholesterol. Using reference atomistic simulations, they systematically modified cholesterol bonded parameters in Martini to improve its performance. In later 2014, with the presentation of the Dry Martini Force Field Model<sup>2</sup>, a modified cholesterol model based on Daily et al.<sup>4</sup> work was used to improve the behaviour of cholesterol in lipid membranes, mainly to prevent the overordering of domains.<sup>2</sup> Therefore, following the same strategy they also implemented the improvements in the cholesterol model in the standard Martini<sup>10</sup>.

Cholesterol has four rigid rings, which Martini has addressed with the smaller type "S" particles, as well as two methyl groups perpendicular to the ring and a branched tail. According to the definition of Martini beads<sup>12</sup>, we have mapped the sterol body as 5 special-apolar beads of type SC<sub>1</sub> and SC<sub>3</sub> and the head group to one SP<sub>1</sub> (polar) bead as shown in Figure 4.1-(b). Finally the alkylic tails were mapped to SC<sub>1</sub> and C<sub>1</sub> beads.

The surfactant  $[\text{N}(\text{CH}_3)_3]^+\text{Br}^-$  known as CTAB (cetrimonium bromide or cetyltrimethylammonium bromide or hexadecyltrimethylammonium bromide, see Figure 4.1-(c), is a quaternary ammonium cationic surfactant, which has a bromide anion as counterion.

There is scarce literature about CTAB coarse-graining<sup>19</sup>, thus we decided to develop our own mapping based on the four-to-one philosophy. Later on, we performed a meticulous study<sup>9</sup> in order to check the predictions of the model and prove that it is a suitable one to

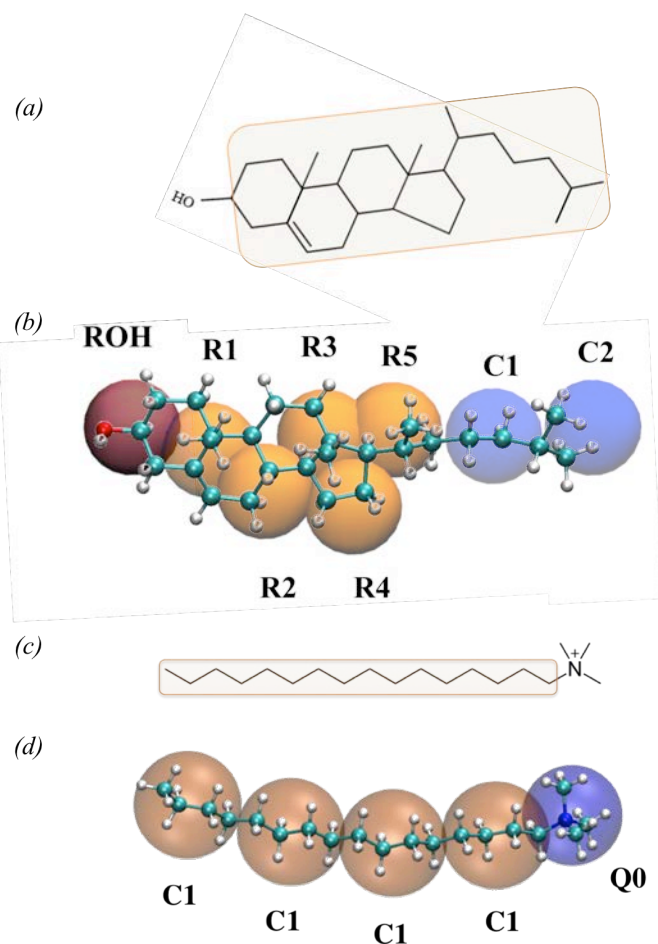


Figure 4.1: (a) and (c) show the structural formula of cholesterol and CTAB, respectively with its hydrophobic tail highlighted. (b) The cholesterol all-atomic structure in CPK representation (oxygen atom from the head group painted in red, hydrogen atoms painted in white and carbon atoms in black). The coarse-grain beads of the Martini model are shown as large spheres named with its type bead. The sterol body of the coarse-grained cholesterol is shown in orange, the hydrophobic part in red and the alkyl tail in blue. (d) Correspondence between the atomistic and coarse-grained (Martini) model of CTA<sup>+</sup>. In the atomistic model, all atoms are shown in CPK representation. The coarse-grain beads of the Martini model are shown as large spheres including all atoms subsumed into the same bead. The hydrophobic beads of type C<sub>1</sub> beads are shown in orange and the hydrophilic charged bead of type Q<sub>0</sub> is shown in blue.

be used for future works.

According to the definition of Martini beads<sup>12</sup>, we have mapped the alkylic tails to 4 hydrophobic beads of type  $C_1$  (the most apolar bead type allowed in Martini, as it is explained in chapter 2, methods) and the headgroup to one  $Q_o$  bead, as shown in Figure 4.1-(d). Using this coarse-grain procedure, we have replaced the atomic model of  $CTA^+$  with 62 atoms by a CG model with only 5 beads. The  $Br^-$  counterion is mapped to a  $Q_a$  bead, which corresponds in Martini to a hydrated anion.

## 4.2 MARTINI MD SIMULATIONS OF CTAB

Once the model has been developed, in this section we present a series of Martini MD simulations with the CG CTAB model. The objective was to compare some basic chemical features of such model with those of the real molecule.

We consider both the explicit solvent Martini force field (W-Martini) and the implicit solvent version of the Martini force field ("dry" Martini, D-Martini) for CTAB. First, we compare the predictions of MD simulations of CTAB between explicit and implicit solvent coarse-grain models and also with all-atomic MD simulations when possible. In particular, we consider the predictions for the potential mean force (PMF) of transfer of CTAB in different situations (water/vacuum interface, water/organic solvent interface and pre-formed CTAB micelle in water). Then, we consider MD simulations of both coarse-grain models for the self-assembly of CTAB in a large system with many micelles, so we are able to observe micelle formation, micelle fusion and surfactant exchange which are events that are rarely observed in all-atomic MD simulations. A summary of all simulations is given in Table 4.1.

Simulations S1-A, S1-M, S2-M and S2-D correspond to a comparison of the different models in the case of a single CTAB molecule adsorbed at an interface. We consider a water/vacuum interface for S1-A and S1-M and water/organic solvent interface in the case of S2-M and S2-D. Simulations S3-A, S3-M and S3-D correspond to the simulation of a single CTAB micelle in water using the three models described in the previous subsection.

**Table 4.1: Summary of simulations performed in this work. We indicate a code for each kind of system and type of model, number of molecules of each type, total number of atoms or CG beads in each simulation, equilibrium size of the system and temperature.**

	System and Model	CTAB molec.	Water molec.	AF molec.	Organic molec.	Total atoms or CG beads	Size	T
S1-A	interface - AA	1	2984	-	-	9015	22 nm <sup>2</sup> × 20 nm	298 K
S1-M	interface - W-Martini	1	724	70	-	800	18 nm <sup>2</sup> × 20 nm	298 K
S2-M	interface - W-Martini	1	3574	397	200	5777	29 nm <sup>2</sup> × 14 nm	303 K
S2-D	interface - D-Martini	1	-	-	200	1806	20 nm <sup>2</sup> × 15 nm	303 K
S3-A	micelle - AA	72	21176	-	-	68064	6 × 13 × 9 nm <sup>3</sup>	298 K
S3-M	micelle - W-Martini	72	14637	1554	-	16723	12 × 13 × 14 nm <sup>3</sup>	298 K
S3-D	micelle - D-Martini	72	-	-	-	432	12.5 × 13.5 × 13 nm <sup>3</sup>	298 K
S4-M	micelles - W-Martini	1000	115000	13000	-	134000	24 × 24 × 32 nm <sup>3</sup>	303 K
S4-D	micelles - D-Martini	1000	-	-	-	6000	30 × 30 × 40 nm <sup>3</sup>	303 K

Finally, in simulations S4-M and S4-D we study the self-assembly of many CTAB molecules in multiple micelles using both Martini forcefields. All MD simulations reported in Table 4.1 were performed using either NAMD<sup>15</sup> or GROMACS<sup>21,1</sup>, as indicated in the following subsections. Snapshots and analysis of the results were obtained using VMD program<sup>8</sup> with home-made analysis scripts, and for the simulations done with GROMACS we also used the analysis tools available with this package<sup>1</sup>.

#### 4.2.1 INTERFACE SIMULATIONS

In simulations S1-A and S1-M, we study the adsorption of CTAB at a water/vacuum interface considering all-atomic (S1-A) and CG Martini model with explicit water (S1-M). The simulation system consists of a single CTA<sup>+</sup> molecule, its Br<sup>-</sup> counterion and a water slab in contact with a large vacuum (see Table 4.1).

In the case of S2-M and S2-D simulations, we have considered CG models (with explicit and implicit solvent respectively) for the adsorption of a CTAB molecule at a water/organic solvent interface. The organic solvent considered here is the same as considered in<sup>22</sup> for the comparison of surfactant adsorption in standard and Dry Martini CG models. Each organic solvent molecule is a linear alkyl chain with 9 Martini CG beads of C<sub>1</sub> type. The simulated system consists of a single CTA<sup>+</sup> molecule, its Br<sup>-</sup> counterion, an organic solvent slab with 200 organic solvent molecules and a water slab (which has explicit water molecules in the

S2-M case and a vacuum in the S2-D case, see Table 4.1).

It should be noted that this choice of the solvent is unrealistic in the sense that 9 CG Martini beads correspond to 36 carbon atoms, so this chain will correspond to hexatriacontane ( $C_{36}H_{74}$ ) which is solid at room conditions (melting point 348 K). Unfortunately, it is not possible to use solvents corresponding to smaller number of Martini CG beads because they do not maintain a stable condensed liquid phase, particularly in the Dry Martini case. It seems that the Martini force field has limitations to model organic solvents, probably because cohesion molecular energies in a real condensed phase are higher than those considered by the simplified Martini and Dry Martini force field. Therefore, we employ here this model for an organic solvent as in previous works<sup>22</sup> only as a technical tool for comparison between standard and Dry Martini models but we should keep in mind that this Martini organic solvent does not really correspond to a model for any real liquid n-alkane.

The MD simulations of these systems (S1-A, S1-M, S2-M and S2-D) were performed using the NAMD 2.12 program<sup>15</sup>. In all cases, we employed a Langevin thermostat to maintain the temperature constant. In simulation S2-M we also employed a Langevin piston to maintain the pressure at 1 atm. The time step was 2 fs in all-atomic MD simulations (S1-A) and 20 fs in CG MD simulations (S1-M, S2-M, S2-D). All other parameters of the simulation were standard for all-atomic or Martini MD simulations with NAMD. The objective of these NPT or NVT simulations was to obtain equilibrated interfaces for subsequent free energy calculations. Due to the small size of the simulated systems, short runs were enough to obtain equilibrium. In the case of the water/vacuum interface, we considered 4 ns for S1-A and 2 ns for S1-M. In the case of the water/organic solvent interface, we used longer times due to the presence of the organic solvent. We considered 10 ns for the explicit water case (S2-M) and 7 ns for the implicit solvent case (S2-D).

Starting from the results of these NVT or NPT MD simulations, we have performed free-energy calculations using the Adaptive Biasing Force (ABF) technique as implemented in NAMD<sup>7</sup>. In these biased MD simulations we obtain the free energy profile (the potential



of mean force, PMF) predicted by each model for the adsorption of the CTAB molecule at the interfaces and its transfer to the different phases. In these simulations, we selected as a generalized "reaction coordinate" the position of the CTAB headgroup in the direction perpendicular to the interface ( $z$  axis) so the origin ( $z = 0$ ) is located at the equilibrium position of the CTAB headgroup at the interface. In the MD-ABF simulations, the CTAB molecule is forced to sample a large interval of values of  $z$ , entering into each of the bulk phases. The force constant employed in the ABF calculation was  $50 \text{ kcal} \cdot \text{mol}^{-1} \cdot \text{\AA}^{-2}$ . PMF of CTAB in each case was obtained with a  $0.1 \text{ \AA}$  resolution. The simulation time for each MD-ABF run (S1-A, S1-M, S2-M and S2-D), is 28, 400, 100 and 800 ns respectively.

In Figure 4.2-(top), we show the PMF associated to the transfer of  $\text{CTA}^+$  to each phase.

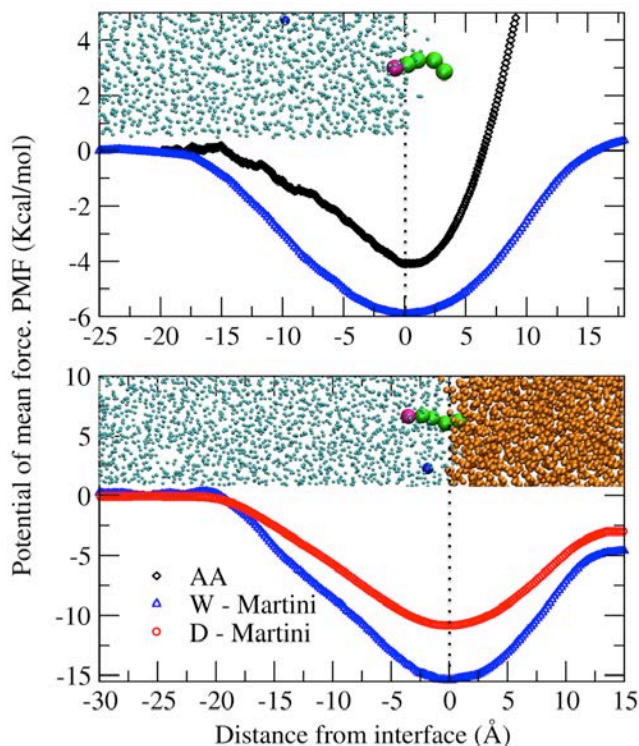


Figure 4.2: Potential of mean force (PMF) of a  $\text{CTA}^+$  surfactant as function of the distance from the interface in two situations: a water slab in contact with vacuum (top panel) and a water slab in contact with an organic solvent slab (bottom panel). The origin of coordinates is taken at the interface, with  $z < 0$  corresponding to the water phase and  $z > 0$  to the vacuum or organic phase. In both cases we include a representative snapshot with the CTAB molecule emphasized ( $\text{CTA}^+$  tail and headgroup are shown in green and pink respectively,  $\text{Br}^-$  is shown in dark-blue). The water slab is always on the left side and the dashed line indicates the interface.

In the all-atomic simulation (S1-A), the transfer of the molecule from the interface to the water phase has a cost of about 4 kcal/mol, whereas in the Martini CG model (S1-M) we obtain a significantly larger value of about 6 kcal/mol. The most important difference between the two models corresponds to the transfer of the molecule from the interface to the vacuum region. In the case of the coarse-grain (S1-M) simulation, the free energy cost of transfer of the molecule from the interface to vacuum is only slightly larger than the cost of transferring the molecule from the interface to the water phase (see Figure 4.2-(top)). However, in the case of the all-atomic simulation (S1-A), this transfer is much more difficult as indicated by the steep increase in the PMF. In the all-atomic simulation, when moving the CTA<sup>+</sup> from the interface, the molecule tries to retain the solvation water of its polar headgroup and deforms the interface (this is, in fact, a realistic feature of the all-atomic simulations). This tendency to retain the solvation water is not observed in the S1-M simulation and it is probably due to the simplicity of the Martini water model and the simplified surfactant-water interactions employed in this case.

In Figure 4.2-(bottom), we compare the PMF for transfer of a single surfactant from the interface to any of the phases using both force fields (S2-M and S2-D simulations). The resulting PMFs have similar shapes but the energies required to transfer the surfactant to the water or the organic phase are higher for simulation S2-M which employs standard (explicit solvent) Martini forcefield. According to the results in Figure 4.2, the standard Martini force field gives larger adsorption free energies for CTAB at interfaces than all-atomic and implicit solvent Martini models. The second simulation (Figure 4.2, bottom) also shows that the preferred location of the surfactant molecule is with its head group at the interface and the tail immersed in the hydrocarbon slab.

It is also interesting to compare the results for both interfaces with the same model (S1-M and S2-M, which employ standard Martini force field). According to Figure 4.2, the adsorption of CTAB to the water/organic solvent interface is substantially more favourable than the adsorption at the water/vacuum interface (6 kcal/mol as compared to 10 kcal/mol).

#### 4.2.2 SINGLE MICELLE SIMULATIONS

In this case, we compare simulations for the three models (all-atomic and CG using standard Martini and Dry Martini) in the case of a pre-assembled micelle of CTAB in water. The all-atomic MD simulations (S3-A) correspond to an extension (a continuation of the MD trajectory) of a previous all-atomic simulation reported in our previous work<sup>5</sup>, in which we consider a pre-formed micelle of 72 CTAB molecules in water. According to the experimental data<sup>16</sup>, this number of surfactants in a micelle corresponds to the average aggregation number found for CTAB concentrations 5-10 mM. Simulation S3-M corresponds to a coarse-grain MD simulation using the Martini model with explicit water. The initial configuration for this simulation was obtained using VMD<sup>8</sup> to convert to coarse-grain the equilibrated all-atomic configuration of the CTAB micelle obtained in S3-A. CG Water and AF beads were added using the Gromacs solvate tool<sup>1</sup>. The initial configuration for S3-D simulation (Dry Martini force field) was obtained by simply removing all water (P4 and AF beads) from an equilibrated S3-M configuration. MD simulations of all these single micelle models (S3-A, S3-M, S3-D) were performed using the NAMD program<sup>15</sup> version 2.9 (as in the original all-atomic study<sup>5</sup>) using a Langevin thermostat to maintain the temperature at 298 K. In S3-A and S3-M simulations we also employ the Langevin piston (NPT simulations) as implemented in NAMD to maintain the pressure at 1 atm. The production run for S3-A, S3-M and S3-D simulations has 65 ns, 47 ns and 1049 ns respectively.

From the simulation results, we have computed the radius of gyration  $R_g$  of the micelles and its principal moments of inertia averaged over all configurations from the equilibrated MD trajectory. The diameter  $D$  of the micelles was computed from the average radius of gyration  $R_g$  with the formula<sup>20</sup>:

$$D = 2\sqrt{\frac{5}{3}}R_g = 2\sqrt{\frac{\frac{5}{3} \mathbf{I}}{\sum_{i=1}^N m_i} \sum_{i=1}^N m_i (\vec{r}_i(t) - \vec{r}_{CM}(t))^2}, \quad (4.1)$$

where  $\vec{r}_i$  and  $m_i$  are the position and mass of the headgroup of each surfactant,  $\vec{r}_{CM}$  is the centre of mass of the  $N$  CTAB molecules and the numerical factor accounts for the geometrical relation between the radius of a sphere and the radius of gyration of a sphere with uniform density. The eccentricity of the micelle was computed from the moments of inertia using the equation<sup>20</sup>:

$$e = 1 - \frac{I_{min}}{I_{av}}, \quad (4.2)$$

where  $I_{min}$  is the minimum principal moment of inertia and  $I_{av}$  is the average of the three principal moments of inertia. We have also computed the degree of ionization  $\alpha$  of the CTAB molecules in the following way. We have first computed the radial distribution function between the  $\text{Br}^-$  ions and the  $\text{CTA}^+$  headgroup<sup>6</sup>. The ions in the first coordination shell of the  $\text{CTA}^+$  headgroup were considered as adsorbed ions so we can obtain the number of adsorbed ions  $N_{ads}$  for all the configurations in the production run. Hence, the degree of ionization  $\alpha$  was computed from the average number of adsorbed ions  $\langle N_{ads} \rangle$  (averaged over all the production run) as:

$$\alpha = 1 - \frac{\langle N_{ads} \rangle}{N_{CTAB}}, \quad (4.3)$$

where  $N_{CTAB}$  is the number of surfactant molecules.

As in the previous subsection, starting from the equilibrium simulations of the micelle systems, we have performed free energy calculations using biased MD simulations with the ABF technique<sup>7</sup>. In these simulations, we selected as a generalized "reaction coordinate" the distance between a selected CTAB headgroup and the centre of the micelle. In the MD-ABF simulations, the selected CTAB molecule is forced to leave the micelle, sampling different values of the radial distance  $r$  from the centre of the micelle until it enters completely the water phase, leaving the micelle. The force constant employed in the calculation was  $10 \text{ kcal} \cdot \text{mol}^{-1} \cdot \text{\AA}^{-2}$ . PMF of CTAB in each case was obtained with a  $0.1 \text{ \AA}$  resolution. The simulation time for each MD-ABF run (S3-A, S3-M, and S3-D), is 48, 36, and 100 ns respectively.

The results of the simulations, including size, shape, and structure of the micelle are summarized in Table 4.2 and in Figure 4.3. In all cases, the pre-assembled micelles were stable during the simulations. In the all-atomic simulation (S3-A), we observe a CTAB molecule leaving the micelle, whereas in the CG simulations all molecules remain in the micelle.

**Table 4.2: Results of single micelle simulations.  $D$  is the diameter of the micelle,  $e$  its eccentricity and  $\alpha$  the degree of ionization of CTAB molecules (see Methods section for details).**

Simulation	D	$e$	$\alpha$
S3-A (all-atomic)	4.79 nm	0.29	0.63
S3-M (Martini)	4.54 nm	0.14	0.78
S3-D (Dry Martini)	4.42 nm	0.12	0.73

We note that all three models predict very similar diameters for the micelles (Table 4.1). The shape of the micelle is almost spherical for CG simulations (see eccentricity  $e$  in Table 4.2) but it has a significant eccentricity in the case of all-atomic simulations (S3-A), indicating a spheroidal shape. This can also be seen in the snapshots shown in Figure 4.3a). In Table 4.2 we also report the degree of ionization  $\alpha$  of the micelle for the three models. The obtained values are very similar, although in the all-atomic (S3-A) simulation we observe a lower ionization (higher condensation of ions) as compared with S3-M and S3-D simulations.

Concerning the structure of the micelles, the three models predict very similar distributions for the hydrocarbon tail inside the micelle (see Figure 4.3), although the all-atomic model predicts a more structured profile with a peak absent in Martini models. The profiles corresponding to polar headgroup and the counterions are very similar in the case of the standard and Dry Martini models. The all-atomic model shows a more broad distribution of headgroup and ions than the Martini models, probably due to the different shape of the micelle (as seen in Table 4.2, the micelle from the all-atomic model has substantially larger eccentricity).

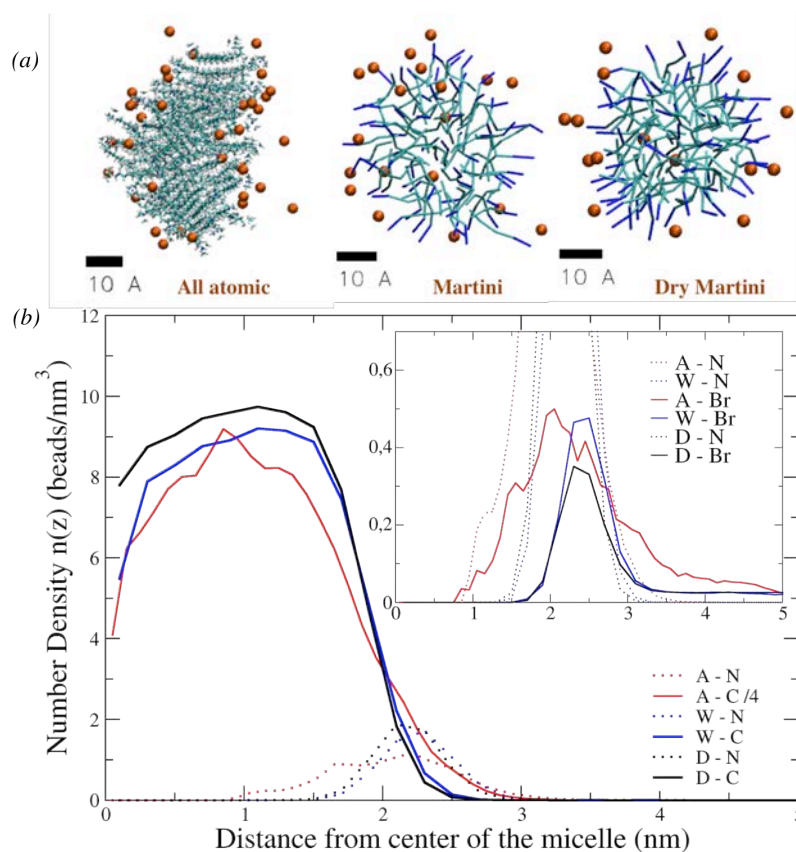


Figure 4.3: (a) Snapshot of CTAB micelle from all-atomic (S3-A), W-Martini (S3-M) and D-Martini (S3-D) simulations. Carbon atoms or beads are colored in cyan with licorice representation and nitrogen and bromide atoms or beads are colored in blue and orange, respectively, with VdW representation. (b) Number density of beads (hydrocarbon tail beads are denoted by C, headgroup beads are denoted by N and ion bead by Br) as function of the distance from centre of the micelle (in the AA case we have divided the atom density between 4 to account for the equivalence between 1 bead to 4 heavy atoms). The inset shows a magnification to show more clearly the location of the headgroup and counterions.

We have also computed (Figure 4.4) the PMF associated to the removal of a single CTAB molecule from the micelle to the water phase. Interestingly, the Dry Martini model predicts a free energy very close to that predicted by the AA model (although the energy profile is a bit more steeper for all-atomic simulations). In contrast, the simulations using the standard Martini force field predict a lower free energy ( $\approx 10$  kcal/mol as compared to  $\approx 13$  kcal/mol).

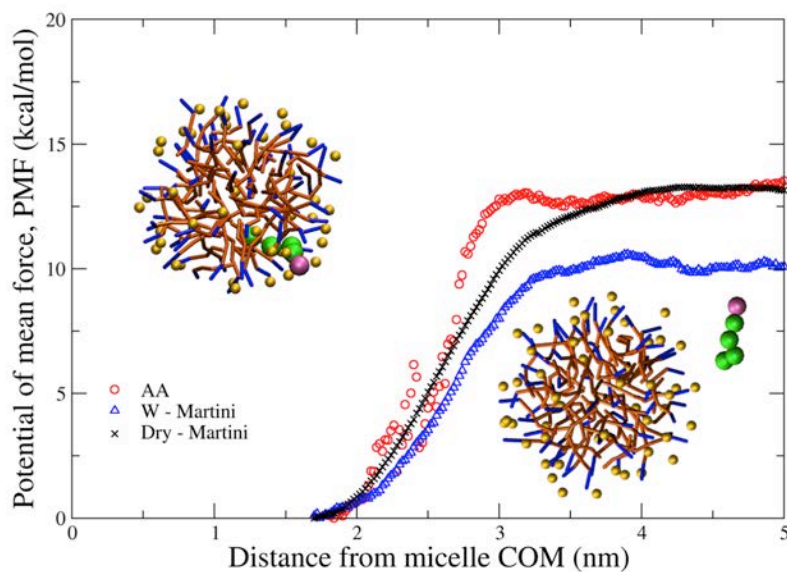


Figure 4.4: Potential of mean force (PMF) of a CTAB surfactant as function of the distance (in nm) between the CTAB headgroup and the centre of mass of a CTAB micelle. We also show two simulation snapshots, corresponding to the situations of CTAB inside the micelle and CTAB extracted from the micelle. The CTAB molecule extracted from the micelle is emphasized (green sphere for the tail and pink for the head group). All other CTAB molecules are shown in bond representation (orange for the tails and blue for the headgroups). Bromide ions are shown as yellow spheres.

#### 4.2.3 SIMULATION OF THE SELF-ASSEMBLY OF MANY MICELLES

Self-assembly of a surfactant solution in multiple micelles is almost impossible to study using all-atomic models due to the large amount of atoms and the long time scales required. In this section, we studied the self-assembly of a large number of CTAB molecules into micelles using both standard and Dry Martini force fields (simulations S4-M and S4-D).

Those MD simulations were performed using GROMACS<sup>1</sup> v5.1.4 and v.2018 respectively. The integration time step was 20 fs and short range coulomb interactions were calculated using a reaction field with a cut off of 1.2 nm and 1.1 nm for Dry Martini and standard Martini respectively. The parameters for the simulations were chosen following the published implementations of both standard<sup>13</sup> and Dry<sup>2</sup> Martini force fields. The non-bonded Lennard-Jones interactions for Dry Martini (S4-D) were shifted at 0.9 nm with

a cut off 1.2 nm, while for standard Martini (S4-M) the Lennard-Jones interactions were modified using potential shift verlet option of GROMACS with a cut off of 1.1 nm.

The NPT ensemble was used for S4-M simulation with explicit solvent, using a Nose-Hoover thermostat and the Parrinello-Rahman barostat (pressure  $P = 1$  bar). The equilibrium size obtained for the simulation cell is reported in Table 4.1. With this equilibrium volume, simulation S4-M correspond to a concentration of CTAB about  $\approx 110$  mM. The NVT ensemble was used for implicit solvent simulations (S4-D), using the Bussi-Donadio-Parrinello thermostat<sup>3</sup>. The size of the simulation box for S4-D (Table 4.1) was chosen as the same employed in the initial conditions of simulation S4-M. In fact, also the initial coordinates of the CTAB molecules were the same, so both simulations started from the same initial conditions. The values for all parameters not detailed above (decay times for the thermostat and barostats...) were those listed as the default values suggested when using Martini forcefield on GROMACS. The number of clusters (micelles) was monitored during the simulation using the *clustsize* tool of GROMACS. These simulations were performed until we observed that the number of clusters remained stable during a substantial time (much larger than the initial time of formation of the clusters). The length of the production run was 334 ns for S4-M and 780 ns for S4-D.

The results are summarized in Figure 4.5 and 4.6. Movies of the simulations, showing the self-assembly process are also available in the QR code in Figure 4.5.

In the case of the standard Martini force field simulation (S4-M), we observe the formation of micelles Figure 4.5-(a). As shown in Figure 4.5-(b), after 200 ns of simulation (see Figure 4.5) the number of micelles as a function of time fluctuates around  $\approx 14$  micelles which corresponds to an average aggregation number of  $\approx 70$  CTAB molecules per micelle. There is of course a distribution of sizes. For example, in the configuration shown in Figure 4.5-(a), we have a few small spherical micelles with only  $\approx 20 - 30$  surfactant molecules and big elongated micelles with  $\approx 140 - 160$  molecules. Unfortunately, with our small number of micelles at equilibrium, we do not have enough statistics to provide an accurate calculation



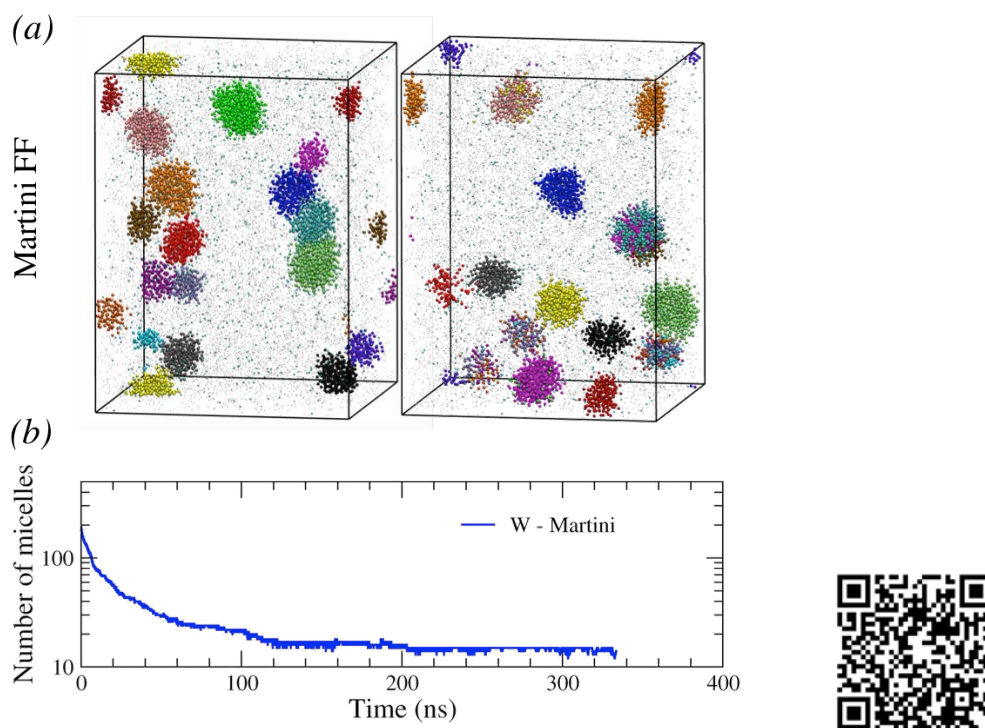


Figure 4.5: (a) Snapshots from self-assembly simulations with Martini force field (S4-M in Table 4.1) at different times:  $t = 260$  ns (left) and  $t = 334$  ns (right). In order to track surfactant exchange and fission and fusion of micelles, we have coloured the surfactant molecules at short times in (a), left panel, according to the micelle to which they belong at that time. In the right panel, corresponding to a later time, we can observe a mixture of colours in individual micelles which indicates exchange of molecules and micelle fission and fusion. In all cases counterions are represented as cyan dots and in water and AF beads are represented as grey dots. (b) Plot of the number of micelles in simulation S4-M as a function of simulation time. The QR code shows the surfactant exchange and fission and fusion of the micelles in (a).

of the size distribution of the micelles.

We also recall that in Figure 4.5-(b) we observe fluctuations in the number of micelles. This is due to fusion and rupture of micelles and exchange of CTAB molecules between the micelles observed during the simulations, as illustrated in Figure 4.5-(a). Once the average number of micelles is stabilized, these processes are still observed in the time scales of the simulation in a way that maintain the average number of micelles. This is what it should be expected in a situation in which the simulations correctly reproduce a thermodynamic equilibrium situation.

As compared with experimental results, the micelles obtained from S4-M simulations have too low aggregation numbers. According to experimental data, the concentration

corresponding to S4-M is above the second micellar concentration of CTAB<sup>11</sup> and elongated micelles with aggregation numbers of  $\approx 150$  are expected.

In the case of the Dry Martini simulation (S4-D), the situation is completely different (see Figure 4.6). At short times ( $\approx 20$  ns), we observe the formation of spherical micelles but at longer times ( $\approx 100 - 200$  ns) these micelles coalesce to give only a few large, elongated micelles (see Figure 4.5). But at even longer times, the micelles fuse giving rise to three large, elongated micelles. These three surviving micelles also aggregate (at  $\approx 500$  ns of simulation), giving rise to a larger structure as seen in Figure 4.6. As seen in the Figure 4.6, the three remaining micelles maintain their identity inside this larger structure, without fusing into a larger micelle. This aggregated state is maintained until the end of the simulation (780 ns). Therefore, the Dry Martini forcefield predicts an unrealistic collapse of the system. This effect has been observed in previous works of a different (anionic) surfactant<sup>22</sup>, in which

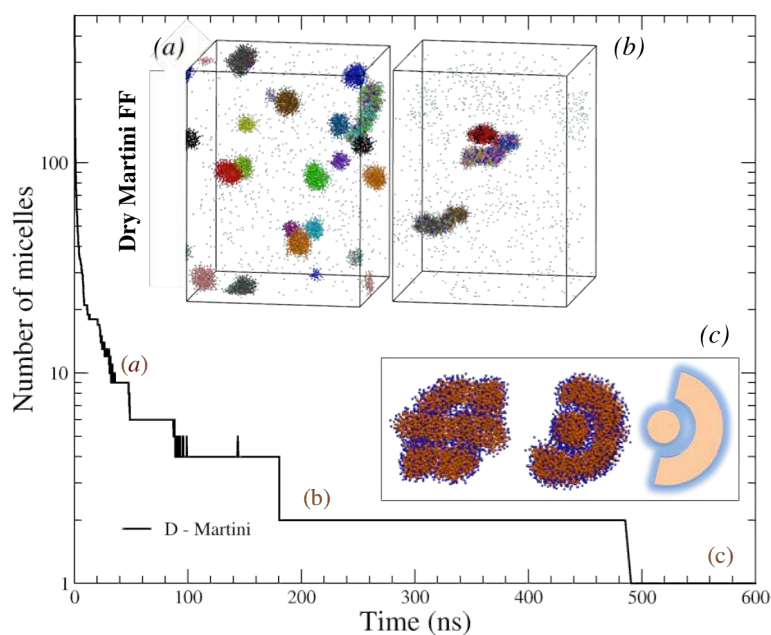


Figure 4.6: Number of micelles as a function of simulation time for the Dry Martini model (D-Martini), simulation S4-D in Table 4.1. The insets (a) and (b) are snapshots corresponding to  $t = 22$  ns and  $t = 180$  ns respectively. In all cases counterions are represented as cyan dots. Inset (c) shows an image of the final structure obtained in the case of Dry Martini S4-D simulations in two different orientations (we also add a cartoon for the sake of clarity). The color codes employed here have the same meaning as in Figure 4.5.

it was proposed a modification of the Dry Martini force field (an artificial increase of the dielectric constant, the use of PME electrostatics and a reparametrization) to correct for the excessive aggregation behaviour. We also tried to implement their modifications in the force field (results not shown) but without success (no improvements in the overall results and a substantial increase of computational time). Also, it is interesting to note that the results presented in the previous subsections indicate that the Dry Martini force field reproduces quite accurately the results from all-atomic MD simulations, including potentials of mean force (see Figure 4.2 and 4.4). At this point, and given the agreement between all-atomic and Dry Martini free energy calculations, we may wonder whether the excess of aggregation predicted by the Dry Martini self-assembly simulations is a problem to be attributed to some intrinsic defect of the Dry Martini model or is a more general problem which will also arise in AA simulations if we had enough computational resources to perform self-assembly simulations with that model.

### 4.3 MARTINI MD SIMULATIONS OF 1:1 CTAB:CHOL; QUATSOME VESICLE

Now that we count with a proper model of cholesterol and CTAB<sup>9</sup>, we are ready to proceed with the main objective of this chapter: to carry out the simulation of the full Quatsome vesicle in order to shed light on the composition and molecular organization in the inner and outer layer of the Quatsome bilayer. Thus, we have performed a theoretical analysis with molecular resolution of a full Quatsome vesicle.

It must be taken into account that this system requires large time and length scales. Thus, we will employ Dry Martini Force Field for our simulations for two main reasons: on one hand it uses implicit solvent, considerably reducing the time and length scales, and on the other hand, it has proven to correctly predict some properties of interest of the CTAB and cholesterol molecules.

Having considered and tried the simulation of the self-assembly of the QS vesicle, due to some limitations it was decided finally to start the simulation with the vesicle already

built, using implicit solvent. In the following subsections, we describe the results of the theoretical analysis, with molecular resolution, of the full Quatsome vesicle.

### 4.3.1 VESICLE BUILD UP

Here we describe in detail the protocols and employed methodologies. The simulated system consists of the Quatsome vesicle made of by a 1:1 ratio of CTAB surfactant and cholesterol molecules using implicit solvent. In our molecular dynamics (MD) simulations, we describe all chemical species (cholesterol, CTA<sup>+</sup> and bromide counterion) using coarse-graining, meaning that we have reduced (in comparison with an all-atom description) the number of degrees of freedom.

The employed force field for the cholesterol and CTAB molecules was the Dry Martini force field<sup>2</sup>. In the case of the cholesterol we employed the model available in the reference<sup>2</sup> and in the case of the CTAB we employed the one in reference<sup>9</sup>.

The build up of the system considers previous experimental and theoretical results available in ref.<sup>5</sup>. Based on those data, we estimated the number of molecules contained in a single vesicle of a Quatsome and its diameter. In this way, the starting point of the simulation of the single Quatsome vesicle is more realistic. The vesicle was constructed using the CHARMMgui tool<sup>17</sup> considering 2054 cholesterol and 2054 2,3-diphenyl-2-cyclopropen-1-one (DPC) as starting configuration. As CTAB molecule is not available in CHARMMgui tool, our strategy was to select a similar surfactant (in terms of number of beads), obtain the system with it and then replace all the DPC molecules for the CTAB ones. Later on, we add the counterions Br<sup>-</sup> using *insert-molecules* tool from GROMACS package. In the end, we obtained as starting point a single vesicle system containing cholesterol and CTA<sup>+</sup> molecules (molar ratio 1:1) and its counterions in implicit solvent. The dimensions of the cubic simulation box are 31.8 nm in the x, y and z-axes. The total number of molecules was 4118 and the simulation box contains a total of 28.756 beads. The initial orientation for the vesicle was completely random and determined by CHARMMgui tool being the initial

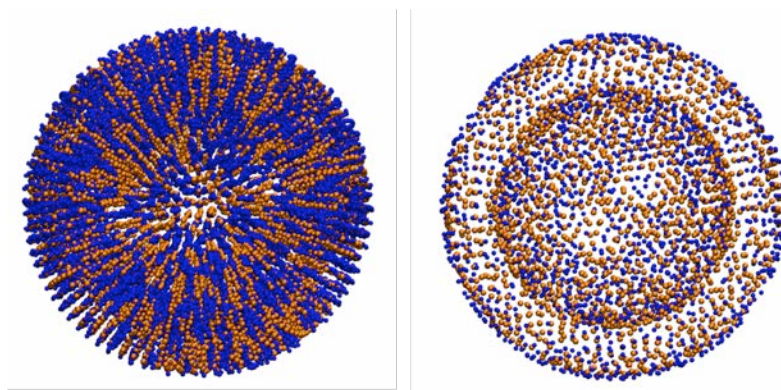


Figure 4.7: Initial configuration of the Quatsome vesicle made of  $\text{CTA}^+$  (blue) and cholesterol (orange). On the left, snapshot of the full structure that shows the random distribution assigned from the CHARMgui tool of both components. On the right, snapshot of the full structure of the vesicle as well, but only pointing out the beads corresponding to the head groups of each component;  $\text{CTA}^+$  in blue and cholesterol in orange. In this way, it is possible to observe the inner and the outer layer limits.

diameter of the vesicle 20 nm. The initial configuration of the system is shown in Figure 4.7.

#### 4.3.2 SIMULATIONS' RESULTS

All the simulations are performed using GROMACS software<sup>21,1</sup> version 2018. The equations of motion were solved with a time step of 20 fs. In all our simulations, the temperature was maintained constant (303 K). The NVT ensemble was used for implicit solvent simulation, using the Bussi-Donadio-Parrinello thermostat<sup>3</sup>. We employed periodic boundary conditions in all directions. The length of the production run was 1001 ns, which is enough time to observe the stability of the vesicle. The first 100 ns corresponded to the adjustment of area per head group of the components, such as it was clearly observed how the layers slightly deform from the initial configuration resulting in a vesicle of smaller diameter than 20 nm (initial fixed value).

The results of the simulation show a stable vesicle with an approximately spherical shape as shown in Figure 4.8-(a). We observe homogeneous distribution of the two components (i.e. segregation or aggregation of any of the components is not observed). The internal structure of the vesicle is a bilayer, as illustrated in Figure 4.8-(b). It is important to

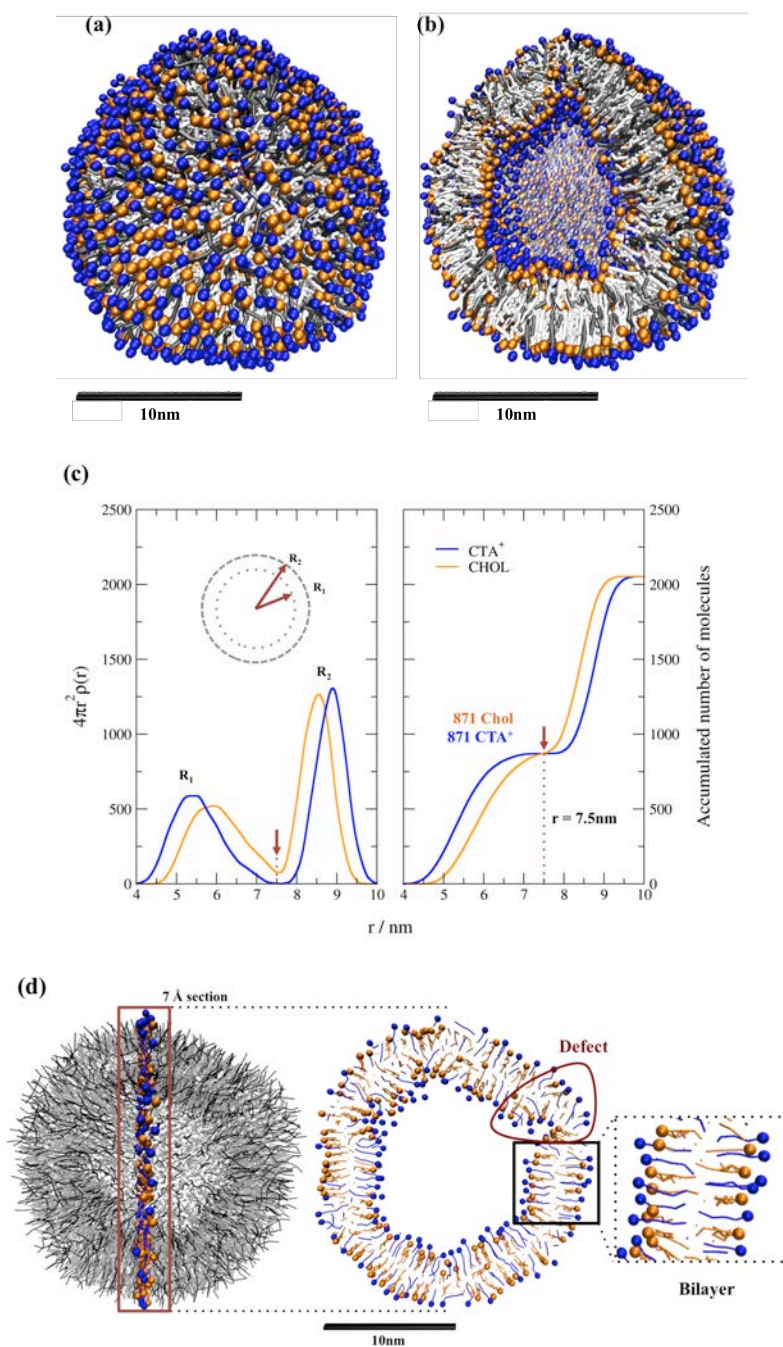


Figure 4.8: Simulation Results. (a) *Loosing detail to gain insight*. Snapshot of an equilibrated (303 K) full Quatsome vesicle and (b) cross section of (a). The head groups of the  $\text{CTA}^+$  and cholesterol molecules are shown as blue and orange balls, respectively. Their tails are shown schematically as cylinders. (c) Radial distribution of vesicle components. Left: radial density profile with  $\rho(r)$  calculated as the number of head group beads per  $\text{nm}^3$ . Right: accumulated (integrated) number of molecules of each component. We also indicate the peaks ( $R_1$  and  $R_2$ ) in the  $\text{CTA}^+$  head group distribution corresponding to the inner and outer radius of the vesicle and its minimum corresponding to the separation between layers. (d) Detailed snapshot showing the internal molecular organization. We select a 7 Å cut of the QS vesicle, showing regions with perfectly ordered planar bilayers (see zoom) and disordered regions.

recall that the vesicle bilayer is in a fluid state, and the components show free mobility of the components within the layers. Molecules are able to diffuse among the layers and they are also able to switch from one layer to another in some cases. In addition, Figure 4.8-(b) clearly shows in a qualitative way how cholesterol is always slightly hidden from the interfaces of the QS surface, a fact that, can be observed both in outer and inner layer of the vesicle. The quantitative analysis of the spatial distribution of the vesicle components (Figure 4.8-(c)) also confirms this more internal localization of cholesterol (see orange line in the figure). The radial distribution of CTA<sup>+</sup> head groups has peaks at radial distances of  $R_1 = 5.2$  nm and  $R_2 = 8.8$  nm (corresponding to the inner and outer layer, respectively). At 7.5 nm we observe a minimum of the distribution of both components, corresponding to the frontier between the two layers. Therefore, taking into account the size of the CTA<sup>+</sup> head group bead (0.47 nm), the diameter of the simulated vesicle can be estimated as  $\sim 18$ -19 nm. This size corresponds to the smaller Quatsomes that have been observed experimentally (see Figure 4.9-(a)).

From Figure 4.8-(c) we estimate a bilayer thickness of 4.07 nm thickness in agreement with the ones calculated in AA simulations<sup>5</sup> and experiments. We have also calculated the accumulated number of molecules as a function of the radial distance average over all equilibrium configurations (Figure 4.8-(c)). We obtain 871 molecules of cholesterol and 871 molecules of CTAB in the inner layer (and correspondingly, we have 1183 molecules of each component in the outer layer). Therefore, an important result is that the molar ratio of the components of the system is 1:1 in both layers. It means that it does exist symmetry of the distribution composition in the Quatsome vesicle.

Looking in detail at Figure 4.8-(c), one can discern planar faces breaking the sphericity of the vesicle itself. In order to analyze in more detail this question, we have selected a 7 Å section of the vesicle and zoomed it in Figure 4.8-(d), in order to qualitatively observe the components' organization inside the vesicle. We observe that the Quatsome system organizes forming regions with planar bilayers and regions with defects, in order to generate

a closed vesicle. It is important to stress that the cholesterol-CTAB synthon is present throughout the whole vesicle, keeping its authentic orientation 1:1 in the planar regions and showing strong deformations in the defect regions. However, we have not observed any segregation of cholesterol or CTAB molecules in the defect region; the molar ratio is maintained. The presence of these facets can also be discerned experimentally, as shown in cryo-TEM images (see Figure 4.9-(b) provided by the group Nanomol.

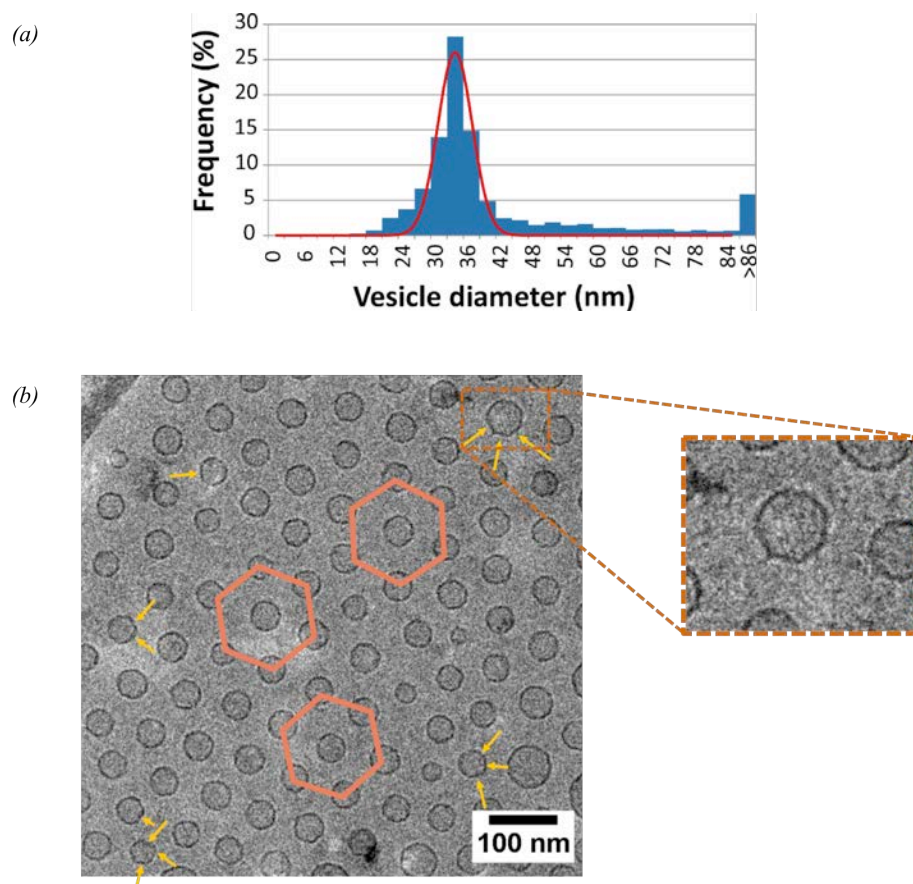


Figure 4.9: (a) Vesicle diameter distribution histogram determined by analyzing cryo-TEM images of 8700 Chol-CTAB Quatsomes prepared by sonication. The experimental vesicle size distribution is adequately fitted by a Gaussian distribution (red line) and shows only small deviations from the equilibrium radius. (b) Cryo-TEM image showing Quatsome unilamellar vesicles. Planar faces observed are pointed with yellow arrows. These results have been provided by Nanomol group (ICMAB-CSIC)



Overall, our calculations suggest that the presence of defects is the responsible for the curvature of the bilayer. It is important to stand out that the synthon is maintaining all around the layers, keeping its authentic 1:1 ratio in the planar regions and completely deformed in the defect regions. We did not observed segregation of cholesterol or CTAB molecules in the defect regions, as the molar ratio is maintained. These results are completely reasonable as an asymmetry is needed in order to induce the spontaneous curvature, otherwise we would have planar bilayers, like discs, and not vesicles. We assume based on our results that we have a geometric asymmetry that induces a spontaneous curvature to the planar layers that once are closed they are stable with time.

## References

- [1] Abraham, M. J., Murtola, T., Schulz, R., Páll, S., Smith, J. C., Hess, B., & Lindahl, E. (2015). GROMACS: High performance molecular simulations through multi-level parallelism from laptops to supercomputers. *SoftwareX*, 1-2, 19–25.
- [2] Arnarez, C., Uusitalo, J. J., Masman, M. F., Ingólfsson, H. I., de Jong, D. H., Melo, M. N., Periole, X., de Vries, A. H., & Marrink, S. J. (2014). Dry Martini, a Coarse-Grained Force Field for Lipid Membrane Simulations with Implicit Solvent. *Journal of Chemical Theory and Computation*, 11(1), 260–275.
- [3] Bussi, G., Donadio, D., & Parrinello, M. (2007). Canonical sampling through velocity rescaling. *The Journal of Chemical Physics*, 126(1), 014101+.
- [4] Daily, M. D., Olsen, B. N., Schlesinger, P. H., Ory, D. S., & Baker, N. A. (2014). Improved Coarse-Grained Modeling of Cholesterol-Containing Lipid Bilayers. *Journal of Chemical Theory and Computation*, 10(5), 2137–2150.
- [5] Ferrer-Tasies, L., Moreno-Calvo, E., Cano-Sarabia, M., Aguilera-Arzo, M., Angelova, A., Lesieur, S., Ricart, S., Faraudo, J., Ventosa, N., & Veciana, J. (2013). Quatsomes: Vesicles Formed by Self-Assembly of Sterols and Quaternary Ammonium Surfactants. *Langmuir*, 29(22), 6519–6528.
- [6] Frenkel, D. & Smit, B. (2001). *Understanding Molecular Simulation*. Orlando, FL, USA: Academic Press, Inc., 2nd edition.
- [7] Hémin, J., Fiorin, G., Chipot, C., & Klein, M. L. (2010). Exploring Multidimensional Free Energy Landscapes Using Time-Dependent Biases on Collective Variables. *Journal of Chemical Theory and Computation*, 6(1), 35–47.
- [8] Humphrey, W., Dalke, A., & Schulten, K. (1996). VMD: Visual molecular dynamics. *Journal of Molecular Graphics*, 14(1), 33–38.
- [9] Illa-Tuset, S., Malaspina, D. C., & Faraudo, J. (2018). Coarse-grained molecular dynamics simulation of the interface behaviour and self-assembly of CTAB cationic surfactants. *Physical Chemistry Chemical Physics*, 20(41), 26422–26430.
- [10] Ingólfsson, H. I., Lopez, C. A., Uusitalo, J. J., de Jong, D. H., Gopal, S. M., Periole, X., & Marrink, S. J. (2014). The power of coarse graining in biomolecular simulations. *Wiley Interdisciplinary Reviews: Computational Molecular Science*, 4(3), 225–248.

- [11] Magnus Bergström, L. (2016). Second CMC in surfactant micellar systems. *Current Opinion in Colloid & Interface Science*, 22, 46–50.
- [12] Marrink, S. J., Risselada, H. J., Yefimov, S., Tieleman, D. P., & de Vries, A. H. (2007). The MARTINI Force Field: Coarse Grained Model for Biomolecular Simulations. *The Journal of Physical Chemistry B*, 111(27), 7812–7824.
- [13] Marrink, S. J. & Tieleman, D. P. (2013). Perspective on the Martini model. *Chemical Society Reviews*, 42(16), 6801–6822.
- [14] Noid, W. G. (2013). Perspective: Coarse-grained models for biomolecular systems. *The Journal of Chemical Physics*, 139(9), 090901+.
- [15] Phillips, J. C., Braun, R., Wang, W., Gumbart, J., Tajkhorshid, E., Villa, E., Chipot, C., Skeel, R. D., Kalé, L., & Schulten, K. (2005). Scalable molecular dynamics with NAMD. *Journal of Computational Chemistry*, 26(16), 1781–1802.
- [16] Pisárčik, M., Devínsky, F., & Pupák, M. (2015). Determination of micelle aggregation numbers of alkyltrimethylammonium bromide and sodium dodecyl sulfate surfactants using time-resolved fluorescence quenching. *Open Chemistry*, 13(1).
- [17] Qi, Y., Ingólfsson, H. I., Cheng, X., Lee, J., Marrink, S. J., & Im, W. (2015). CHARMM-GUI Martini Maker for Coarse-Grained Simulations with the Martini Force Field. *Journal of Chemical Theory and Computation*, 11(9), 4486–4494.
- [18] Safran, S. A., Pincus, P., & Andelman, D. (1990). Theory of Spontaneous Vesicle Formation in Surfactant Mixtures. *Science*, 248(4953), 354–356.
- [19] Sangwai, A. V. & Sureshkumar, R. (2011). Coarse-Grained Molecular Dynamics Simulations of the Sphere to Rod Transition in Surfactant Micelles. *Langmuir*, 27(11), 6628–6638.
- [20] Storm, S., Jakobtorweihen, S., Smirnova, I., & Panagiotopoulos, A. Z. (2013). Molecular Dynamics Simulation of SDS and CTAB Micellization and Prediction of Partition Equilibria with COSMOmic. *Langmuir*, 29(37), 11582–11592.
- [21] Van Der Spoel, D., Lindahl, E., Hess, B., Groenhof, G., Mark, A. E., & Berendsen, H. J. C. (2005). GROMACS: Fast, flexible, and free. *Journal of Computational Chemistry*, 26(16), 1701–1718.
- [22] Wang, S. & Larson, R. G. (2015). Coarse-Grained Molecular Dynamics Simulation of Self-Assembly and Surface Adsorption of Ionic Surfactants Using an Implicit Water Model. *Langmuir*, 31(4), 1262–1271.

*Science, for me, gives a partial explanation for life. In so far as it goes, it is based on fact, experience and experiment.*

Rosalind Franklin

# 5

## Quatsomes with hydrophilic dyes

In the previous chapters, we have studied the Quatsome from a theoretical point of view with respect to its supramolecular organization. At this point, and thanks to some important findings like the thermodynamical stability of the system, we are in a position to investigate potential usages.

Vesicles like the Quatsome are very promising nanocarriers due to its structure and functionalizable surface. In this chapter, we are going to study this capacity, using the Quatsome as an approach for nanostructuring fluorescent probes. Fluorescent probes are molecules that absorb light of a specific wavelength and emit light of a different (typically

longer) wavelength, a process known as fluorescence, and are used mainly to study biological samples. The molecules, also known as fluorophores, can be attached to a nanocarrier structure and act as a marker for analysis with fluorescence microscopy, i.e. bioimaging<sup>20</sup>. Considering the positive charged surface of the QS membrane we propose using the Quat-some vesicle for nanostructuring hydrophilic dyes in aqueous media, in particular using the fluorescein molecule (see Figure 5.1).

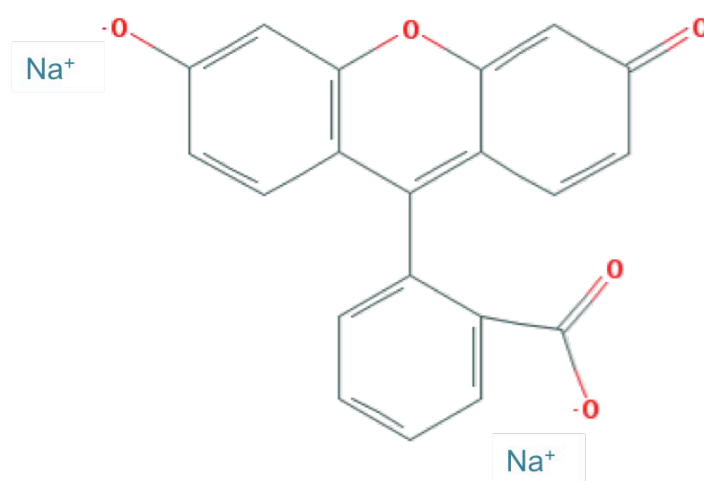


**Figure 5.1: Fluorescein dianion chemical structure. It is an organic dye that emits intense green fluorescence in the presence of alkaline solutions.**

The fluorescein dye has been studied for several decades now, and it is one of the most used fluorescent probes due to the modest brightness, large absorption in the visible range and easy chemical modification for labelling of biomolecules<sup>22,16</sup>. As an example, absorption and fluorescence spectra of fluorescein in cetyltrimethylammonium chloride (CTAC) micelles have been obtained, and it was found that fluorescein was solubilized at the inner border of the Stern region<sup>4</sup> of the CTAC<sup>11</sup>. This case is relevant for the present chapter, as our QS system contains CTAB molecules, and thus the behaviour described in the mentioned work can be taken as a guide.

However, literature reports several phenomena about the fluorescein molecule that can constitute a drawback for our purposes. i.e., photobleaching during prolonged illumination,

which makes them incapable of continuous observation and long-term imaging for studies of living cells<sup>26</sup> or the ability for self-association in solution. In particular, this last phenomena mentioned is called aggregation and affect the photophysical properties of dyes. For this reason, the nature and consequences of the aggregation phenomena<sup>15,6</sup> of fluorescein dyes are introduced here.

Aggregation is a common phenomenon observed in xanthene<sup>24,1</sup> dyes in aqueous solution, and fluorescein belongs to that family. Despite this phenomenon, xanthene dyes have variety of technical applications like being the building blocks for sensor construction<sup>5</sup>. The aggregation mainly comes in the form of dimers, except at high concentrations in solvents with a high dielectric constant. Coulombic forces counteract the attraction between charged dyes, but a solvent with a high dielectric constant, such as water will lower this repulsion. Self-aggregation is not a phenomena limited to dyes, i.e., hydrogen-bonding causes aggregation in carboxylic acids<sup>14</sup> (Figure 5.1 shows that the fluorescein molecule has a carboxylic group). The strength of the aggregation between the two dye molecules depends on the nature of the dye, the solvent (the presence of hydroxyl groups in the solvent molecules plays an important role in promoting aggregation whereas the present of the glycerol prevents it), concentration<sup>24</sup> and the coordination with metal-ions<sup>7,26</sup>. The aggregation phenomena of fluorescein molecules in water solvent has been well studied from both an experimental<sup>24</sup> and theoretical point of view, concluding that fluorescein aggregates in water forming symmetric structures that are stabilized by  $\pi - \pi$  edge-to-face interactions<sup>6</sup>.

An increase in fluorescein concentration produces changes in the electronic absorption and emission spectra. These changes have been attributed to dimer but also trimer formation<sup>15</sup>. Rohatgi<sup>18</sup> and Arbeloa<sup>15</sup> proposed feasible dimer and trimer structures in terms of distances between the monomers' centres of mass. Analysis of changes in the absorption spectrum with respect to dye concentration allows to obtain the equilibrium constant for the association process and to derive the absorption and occasionally the emission spectrum of the aggregates. For head-to-tail dimers (J-type)<sup>10</sup>, the transition to higher energy

excited state is forbidden and the spectrum shows a single band red-shifted with respect to the monomer.

At the same time, this results in self-quenched fluorescence<sup>9,3</sup>. Fluorescence quenching refers to any process that decreases the fluorescence intensity of a sample. However, this process is reversible, as the quenching-causative molecular interactions can be controlled, for instance by functionalizing<sup>22</sup> the fluorophore or encapsulating<sup>17</sup> it to produce increased electrostatic repulsion and water solubility.

The usage of the QS decorated with fluorescein is proposed as a solution to minimize the self-aggregation and the fluorescence quenching. As said, those photophysical properties of small-molecule fluorophores like fluorescein may not remain stable with time, and a strategy to avoid that is to trap the dye into a nanostructure to minimize quenching.

In this chapter not only we propose the Quatsome system as an optimized nanostructure, but also we will carry out a study of the nature of the binding of fluorescein to the system, because experimental results have proved the quenching of the dye-loaded QS system. This suggests a binding consisting of a electrostatic interaction, but deeper understanding is needed to truly explain such result. At the same time, the importance of electrostatic and/or hydrophobic interactions on the aggregation process will be studied.

Sodium fluorescein is highly soluble in water, so that in solution it is fully dissociated in two sodium ions and a fluorescein molecule, which are in equilibrium between the anionic and dianionic state<sup>21,6</sup>. That last state is the one we are interested in. In this work, we modelled the Fluorescein dianion ( $\text{Fl}^{2-}$ ) from scratch, and we performed our study in water alone and in water in contact with a catanionic membrane (Quatsome), in order to understand the electrostatic and/or hydrophobic interactions on the aggregation process. All-atomic molecular dynamics (MD) simulations provide deep structural detail of the inter- and intra-molecular interactions.

## 5.1 MODEL AND FORCE FIELD FOR FLUORESCHEIN DIANION

The fluorescein molecule has been used frequently at the experimental level. However, this is not the case at the theoretical level, and a valid model of the fluorescein dianion molecule was not found in the literature. For this reason, it was necessary to develop our own model and force field compatible with CHARMM. The followed strategy to obtain the fluorescein dianion ( $\text{Fl}^{2-}$ ) parameter set is explained in this section. We started by generating a first set of parameters using the automated CHARMM Force Field tool CGenFF program, available for online use<sup>25</sup>, for the neutral fluorescein molecule ( $\text{Fl}^0$ ), for fluorescein anion molecule ( $\text{Fl}^{-}$ ) by removing the H atom of the carboxyl group and finally for the fluorescein dianion molecule ( $\text{Fl}^{2-}$ ) by removing the H atoms from the hydroxyl and carboxyl group (removed from atoms O1 and O5, respectively, as shown in Figure 5.2).

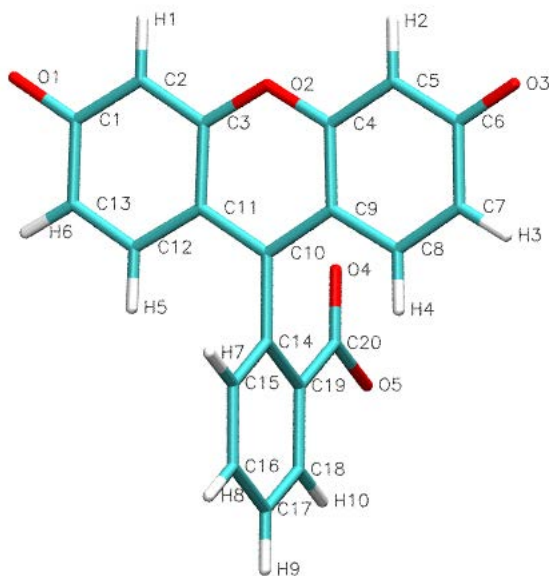


**Figure 5.2: Fluorescein dianion structure with atomic number scheme.**

Some of the parameters obtained using this procedure showed high penalty values in some areas within the molecule structure, for the three different protonate states (see Figure 5.3). Those areas with high penalties were very similar in the three molecules. As explained



in the methodology, in chapter 2, to have a value with a penalty means that some checks are required and one good strategy could be to follow the CHARMM philosophy methodology<sup>27</sup>.

Following the CHARMM philosophy means that the fluorescein molecule is divided into well known fragments (see Figure 5.3) and the molecular topologies of those fragments are recalculated again. In that way, as shown in the figure, some fragments like the bencenol and bencenal have good parameter sets (meaning no penalties), while others like the anthracene do have penalties. Thus, we will focus in optimizing those last ones, as it will be explained in a later paragraph.

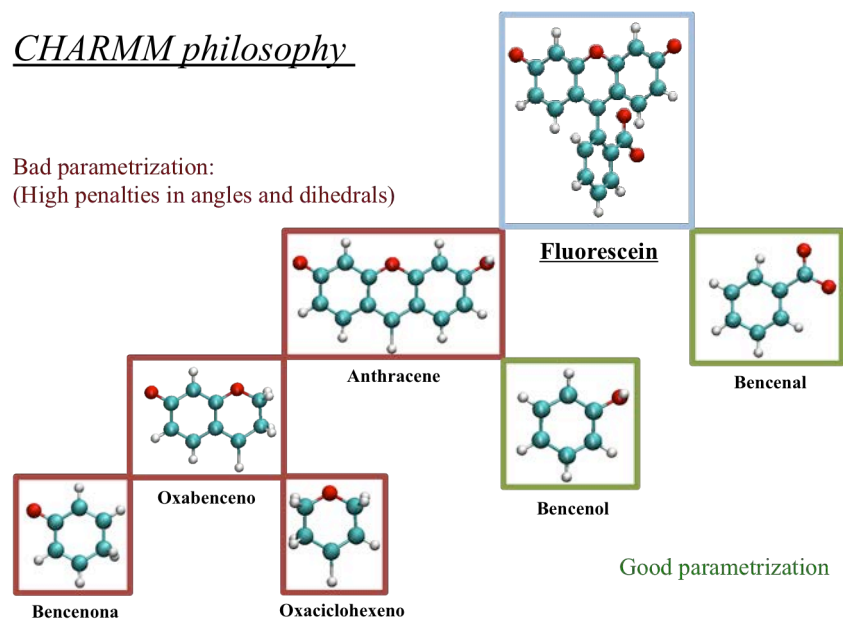


**Figure 5.3:** Scheme of the fluorescein molecule (blue outline) partition into well known molecules like: bencenal and anthracene following the CHARMM philosophy methodology. Molecules with red outline show high penalties in their molecular topology while the ones with green outline do not. All molecules' structures are represented in CPK showing the oxygen atoms in red, the hydrogen atoms in white and the carbon atoms in cyan.

Additionally, the values obtained for  $\text{Fl}^{1-}$  (CGenFF) were compared to those in Swiss-Param<sup>28</sup> server for the same fluorescein structure. The server derives data from the Merck Molecular Force Field (MMFF)<sup>12</sup>, which is fully compatible with CHARMM all-atomic force field. Minimum differences (in the order of  $10^{-2}$ ) were observed between the values of both parameter sets, except for the dihedral from ether to ketone group and carboxyl

group (deprotonate area).

Furthermore, the structure was optimized and the vibrational frequencies were calculated for the fluorescein molecule and for the three different protonate states. This was done with Gaussian09 program<sup>8</sup>, starting from the neutral structure and iteratively using the results from one step in the following one, ending with the di-deprotonated structure. The calculations were performed using density functional theory DFT with RM062X functional and the 6-311+G(d,p) basis set. The calculation was performed in the presence of a solvent (water) using specific keyword of Gaussian. It was observed that the vibrational frequencies of both molecules;  $\text{Fl}^{1-}$  and  $\text{Fl}^{2-}$ , were nearly the same.

Having explained all the previous, the summary is threefold: firstly, the molecular topology obtained from the CGenFF force field for  $\text{Fl}^{1-}$  and  $\text{Fl}^{2-}$  have similar penalties, secondly the model of the  $\text{Fl}^{1-}$  observed in SwissParam is very close to the  $\text{Fl}^{1-}$  from CGenFF, and thirdly the geometry optimization from Gaussian is almost the same for  $\text{Fl}^{1-}$  and  $\text{Fl}^{2-}$ . For these reasons, we select the parameter set from the  $\text{Fl}^{2-}$  (CGenFF) molecule as a starting point for the modelling of the fluorescein dianion molecule. As shown, there is a good agreement between parameter sets of  $\text{Fl}^{1-}$  and  $\text{Fl}^{2-}$  molecules, as the only difference is the deprotonation of the hydroxyl group between both structures.

In order to go further with the validation of the  $\text{Fl}^{2-}$  (CGenFF) parameter set, the quantum mechanics (QM) energies were compared to the energies of the molecular mechanics (MM) force field for the geometries from  $\text{Fl}^{2-}$  (CGenFF) and  $\text{Fl}^{2-}$  (Gaussian), and the force field parameters of the dihedral angles were adjusted to obtain an optimal fit of the MM energies to the QM energies, according to a rigid potential energy scan (PES) procedure at the same theoretical level as the  $\text{Fl}^{2-}$  geometry optimization by Gaussian. The dihedral angle potential is mostly used to constrain the rotation around a bond. We considered all the dihedral angles that needed a check, those to which penalties had been associated (ten in total). For that, we calculated the potential of the dihedral that describes the torsional and bonded interactions by MM and QM. As it is a rigid framework where carbon atoms

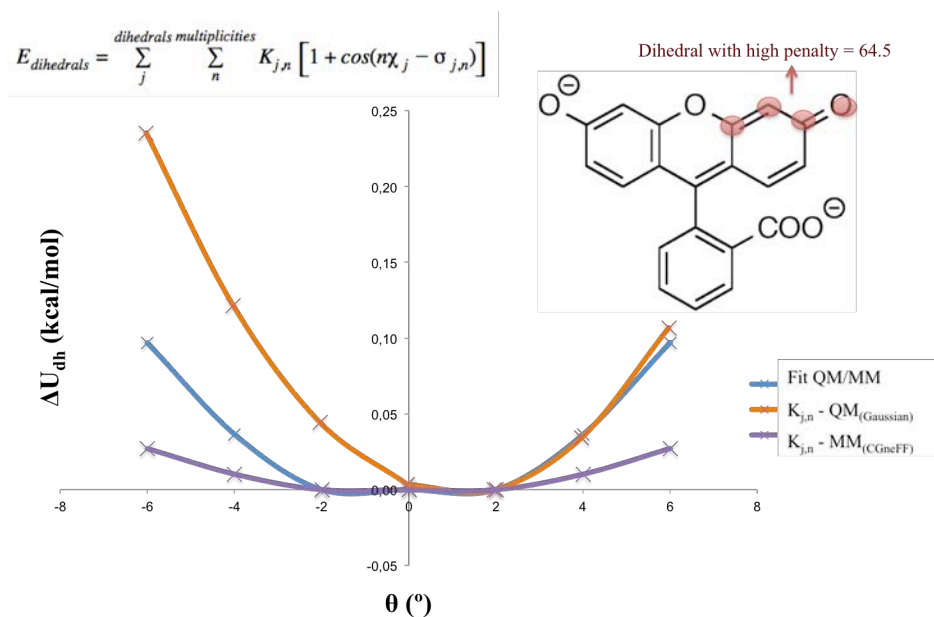


**Figure 5.4:** Dihedral PESs for the fluorescein dianion model compound. Orange line represents QM data and the purple lines for MM data. The blue one refers to fit in between QM/MM data.

are  $sp^2$  hybridized, which prefers planar configuration and prevents the dihedral angle to deviate above  $180^\circ$ , we got a range from  $-40^\circ$  to  $40^\circ$  with an increment of 2 degrees. Then, we compared the force constant,  $K_{j,n}$  between MM and QM. For MM, the constant is obtained from the expression in Equation 2.6 in chapter 2 (which has been repeated in Figure 5.4), and for QM the constant is obtained from PES procedure. Afterwards, we manually adjusted the force constant value, searching for a value in between those thrown by MM and QM, in order to improve the parameters of the dihedral angles. Figure 5.4 shows an example of the described process, among the 10 that were performed.

Finally, charges were computed for the optimized geometry of  $\text{Fl}^{2-}$  (Gaussian) using the Merz-Kollman charge model<sup>13</sup>. All the parameters used for the fluorescein dianion molecule model are available in this repository: [https://bitbucket.org/icmab\\_soft\\_matter\\_theory/fluorescein/src/master/](https://bitbucket.org/icmab_soft_matter_theory/fluorescein/src/master/). We point out that the build-up of the force field has been done manually, in comparison with the automated case of SwissParam, by merging all the information obtained and described before, and it is ready to be used.

## 5.2 MOLECULAR DYNAMICS SIMULATION OF FLUORESCEIN IN WATER

The previously developed model has been employed for studying the behaviour of the fluorescein both in water and in the Quatsome bilayer. Molecular dynamics simulations have been performed in both environments, and in this section we start by those in water.

Some general computational details: we performed AA-MD simulations using NAMD 2.11 software; the equations of motion were solved using a time step of 2 fs and structures were saved every 10 ps; electrostatic interactions were computed using the PME method with usual settings in NAMD (1 Å resolution, updated each 2 time steps); Lennard-Jones interactions were truncated at 1.2 nm employing a switching function starting at 1.0 nm; periodic boundary conditions were employed in all directions, temperature was kept constant at 298 K using a Langevin thermostat with a relaxation time of 1 ps and a pressure of 1 atm was imposed using the isotropic Nosé-Hoover-Langevin piston implemented in NAMD (oscillation period of 100 fs and decay time of 50 fs).

Simulations have been carried out by loading different quantities of dye molecules; using the fluorescein dianion model and force field described in the previous section. And we have solvated them in a cubic box with TIP3P water molecules so the fluorescein molecules are free to translate and rotate. The size of simulation the box was adjusted in order to have always the same water concentration with the aim of seeing the concentration effect in the behaviour of the dyes. Details of the simulations are described in Table 5.1.

**Table 5.1: Computational details of the systems considered in the MD simulations, including number of fluorescein molecules, counterions and waters molecules, total number of atoms, simulation time and the simulation box size.**

	Fl <sup>2-</sup>	Na <sup>+</sup>	Water molec.	Atoms (total)	Sim time /ns	Box size /nm <sup>3</sup>
Flu_1	1	2	6974	20959	49.95	206
Flu_2	2	4	7064	21356	48.77	211
Flu_3	3	6	9398	28305	46.80	279
Flu_4	4	8	7071	24361	49.78	209
Flu_9	9	18	6878	20967	50.11	205
Flu_27	27	54	6912	21761	49.62	210

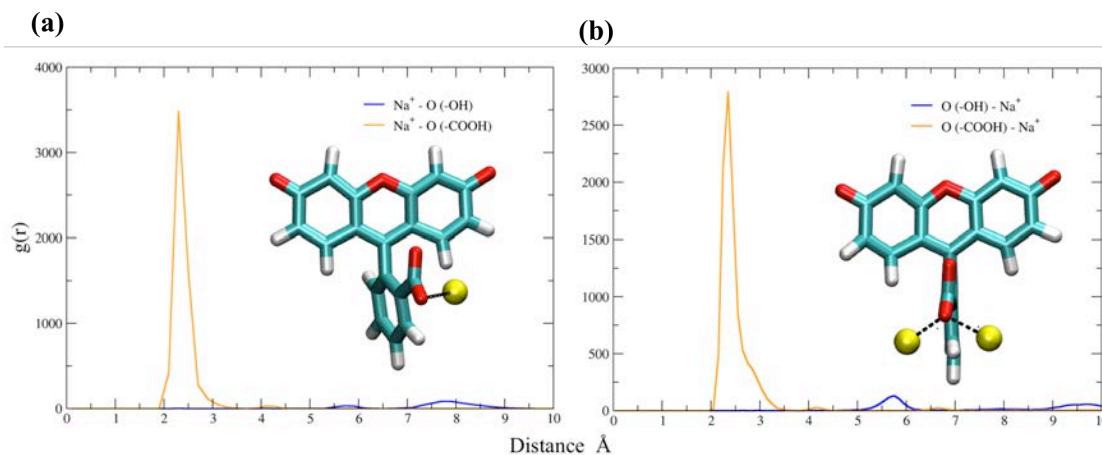


Figure 5.5: Snapshots (a) and (b) from simulation Flu\_1 and Flu\_2, respectively, show fluorescein dianion molecule with one and two respectively sodium atoms and it is marked the average distance once the interaction between the counterion and the oxygen atom of the carboxyl group is made. Fluorescein molecules are represented in Licoride and sodium atoms are represented as yellow spheres. (a) and (c) show the radial distribution function  $g(r)$  describing the probability of finding an oxygen from the carboxyl group (-COOH, orange line) and hydroxyl group (-OH, blue line) from fluorescein molecules and sodium counterion pair at distance  $r = 3 \text{ \AA}$ .

We started simulating a single fluorescein dianion with their two counterions (sodium atoms) and simulating 50 ns the dynamics of this dye solvated in water. Despite free movement behaviour was expected, we clearly observed that a sodium atom was quickly attached to the carboxyl group ( $-\text{COO}^-$ ) balancing one of the negative charges of the fluorescein molecule, whereas the other counterion kept fluctuating free far apart from the dye. In Figure 5.5-(a) it is shown how the sodium atom (yellow sphere) interacts with the carboxyl group with an average distance of  $2.5 \text{ \AA}$ , as it can be seen in the  $g(r)$  graph of the figure. Analyzing the other simulations containing multiple fluorescein molecules we observed exactly the same behaviour described. When focusing on the simulation with two dyes (Flu\_2) we observe that after some time one of the fluorescein molecules had two counterions attached instead of one, in this case the  $g(r)$  graph showing an average distance of  $2.5 \text{ \AA}$  and  $2.7 \text{ \AA}$  with respect to the carboxyl group, as shown in Figure 5.5-(b). Both molecules fluctuated between being far and close, but remaining unaggregated in time, having one or two counterions attached.

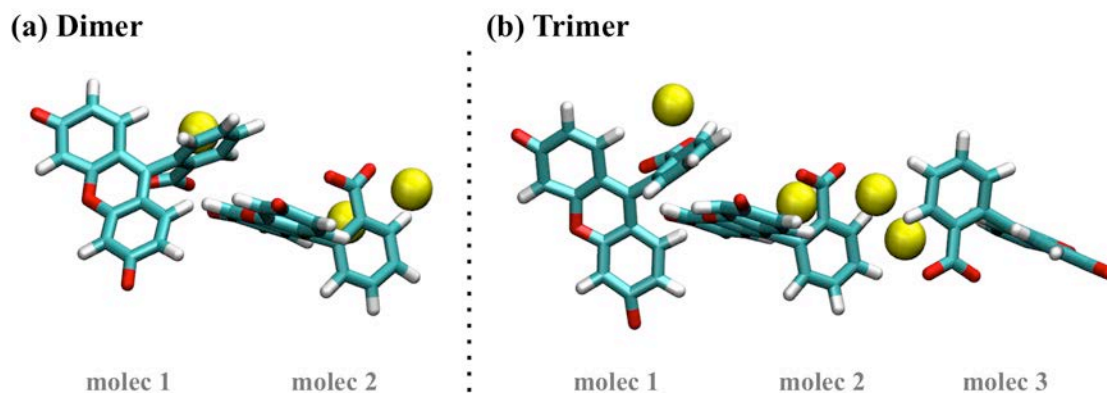
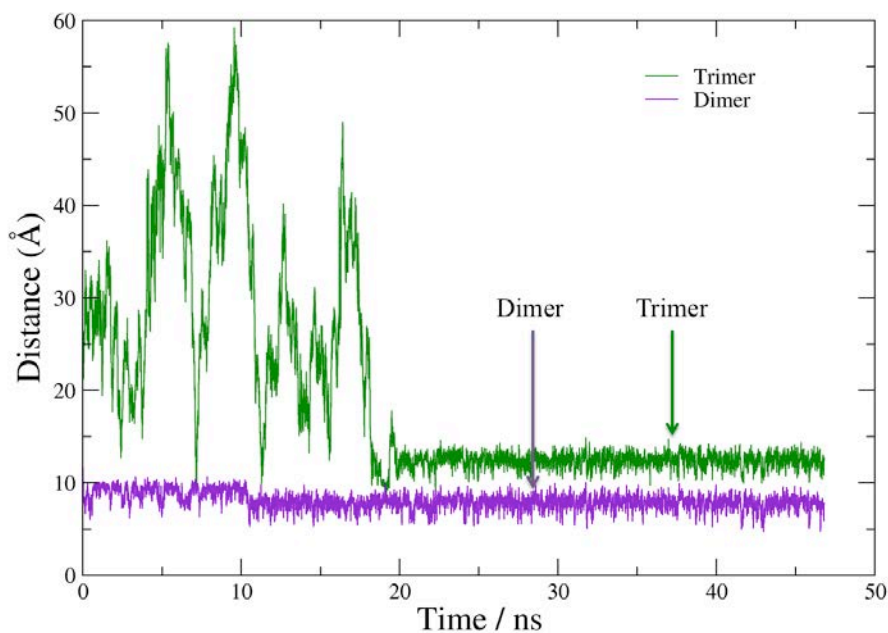


Figure 5.6: Snapshots of the dimer (a) and trimer (a) geometry from the simulation Flu\_3. Fluorescein molecules are represented in licorice and sodium atoms are represented as yellow spheres.

Simulations Flu\_3 and Flu\_4 confirmed the tendency of fluorescein molecules to form dimers and trimers. In order to understand the dimer and trimer geometry we qualitatively studied the different orientations with the MD trajectories and quantified the dimer and trimer life time. In simulation Flu\_3 the dimerization occurs at the beginning of the simulation with  $\pi - \pi$  interactions. Let us have two molecules that we name molecule 1 and molecule 2. The interactions involve on one hand the ring with the carboxyl group of molecule 1 and on the other hand the ring with the hydroxyl group of molecule 2 (see in Figure 5.6-(a)). This result is in agreement with literature, as explained in the introduction of this chapter, thus proving that our fluorescein force field (developed in the section 5.1) models the features of the fluorescein in water successfully. On the contrary, an unexpected result is the fact that the  $\pi - \pi$  interaction also involves one sodium counterion condensed in the carboxyl part of one of the molecules of the dimer. It is also observed that, the non-bonded carboxyl part of the molecule 2 of the dimer has almost all the time two counterions attached. After 20 ns of simulation a trimer is formed and remains stable. What we observe is that the third molecule (molecule 3) is attached to the dimer forming symmetric image and adding another counterion to the trimer (see Figure 5.6-(b)). Same behaviour is observed at simulation Flu\_4, in which we can have two dimers or one trimer and a single fluorescein molecule in water interacting in the same way as described in simulation Flu\_3. This let us

conclude that sodium counterions are playing a key roll in the aggregation of the fluorescein molecules in water leading a solid stability of the aggregates once formed.

The analysis of the spontaneous formation and decomposition of the dimer and trimer was done based on the whole trajectory of the simulation Flu\_3. The life time of the dimer and trimer was calculated by the evolution of the distance between the centres of mass of the involved molecules. In Figure 5.7, it can be observed that the formation of the dimer aggregate takes place at the beginning of the simulation and at 20 ns approximately the presence of trimers is observed. The average distance between the centre of mass of the dimer and trimer are 7.8 Å and 17.2 Å, respectively.



**Figure 5.7:** This graph shows the distance between centers of masses of fluorescein molecules involved in the dimer and trimer formation, with respect to time. The green line corresponds to the trimer and the magenta line to the dimer.

Finally, in simulations Flu\_9 and Flu\_27 it is observed that the dyes tend to quickly aggregate forming more than one aggregate. In the case of Flu\_9 simulation, a main aggregate, and another smaller one were observed, and in the case of Flu\_27 simulation, a big aggregate and two smaller ones were observed. However both of them have in common that the aggregates oriented following a pattern: edge to face  $\pi - \pi$  interactions or by ion

condensation as shown in Figure 5.8.

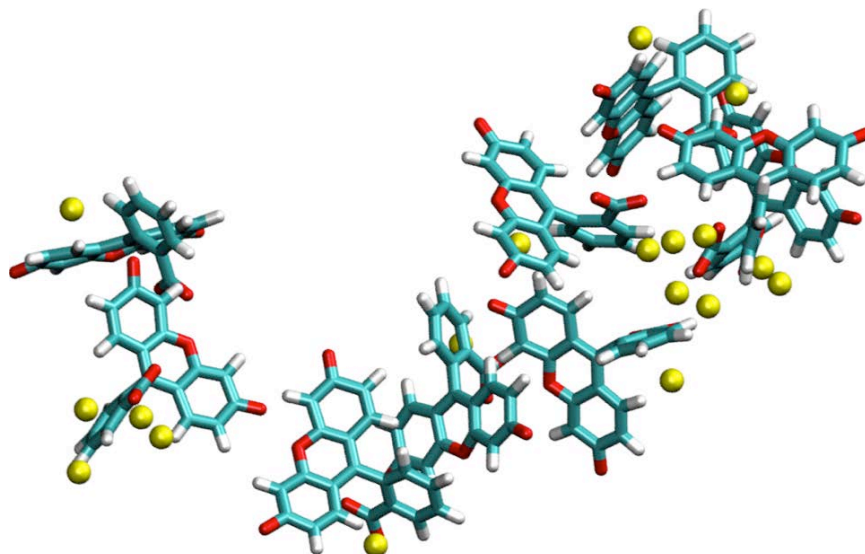


**Figure 5.8:** Snapshot from MD simulation Flu\_9, showing a big aggregate of fluorescein molecules and the sodium counterions in between.

### 5.3 FLUORESCEIN IN QUATSOME BILAYER

For the simulations of the fluorescein in the Quatsome bilayer, we employ the same computational details described in the section 5.2 of fluorescein in water, with the only difference we control the pressure with the anisotropic Nosé-Hoover-Langevin piston implemented in NAMD (instead of isotropic). We impose a pressure of 1 atm in the direction perpendicular to the QS bilayer and a zero surface tension, as in the previous simulation of QS bilayer (see chapter 3).

We performed 4 different simulations, with the compositions given in Table 5.2. Simulations S1, S2, S3 and S4 correspond to one or multiple fluorescein dyes adsorbed into a Quatsome bilayer ( $15.7 \text{ nm}^2$  patch) made of 27 CTAB surfactant and 27 cholesterol molecules (each leaflet). These simulation systems were built as described in S1 simulation of chapter 3, section 3.2, and we used the resulting configuration as the starting point. Then, we manually added four different loadings of fluorescein dyes, with two counterions per one



fluorescein molecule, in the water phase. Finally we performed an energy minimization of the whole QS-dye systems.

**Table 5.2: Computational details of the systems considered in the MD simulations, including number of atoms, number of fluorescein, water and CTAB molecules, fluorescein and CTAB ratio and simulation time and the simulation box size.**

	Atoms (total)	molec. $\text{Fl}^{2-}$ /water/CTAB	$\text{Fl}^{2-}$ /CTAB	Sim time /ns
<b>S1</b>	25708	1/6091/54	1:54	110
<b>S2</b>	27037	4/6497/54	1:13.5	120
<b>S3</b>	26794	10/6342/54	1:5.4	110
<b>S4</b>	30268	28/7278/54	1:1.9	90

Once the initial configurations were prepared, we performed AA-MD simulations. In all the cases, we first performed equilibration simulations of 1 ns in the NPT ensemble. After these simulations, we performed further equilibration simulations using the NPT ensemble maintaining the QS bilayer at zero tension, 298 K and 1 atm, in order to emulate the conditions found in a vesicle<sup>19</sup>. In all the cases, we performed long production simulations for 110 ns, 120 ns, 110 ns and 90 ns for S1, S2, S3 and S4 simulations respectively.

In S1 simulation, only 1.5 ns were required for the adsorption of the  $\text{Fl}^{2-}$  molecule within QS surface. In this case, the attractive interaction between the vesicle and the dianion is strong enough to hold the  $\text{Fl}^{2-}$  tightly close to the surface of QS during the whole calculation time (110 ns). By analyzing radial distribution function,  $g(r)$ , between the two negative oxygen atoms (O1 and O5 atoms, see Figure 5.1) of  $\text{Fl}^{2-}$  and the N atom of the CTAB, information on the orientation of fluorescein dye on Quatsome surface can be extracted. As shown in Figure 5.9,  $\text{Fl}^{2-}$  can stay in two possible orientations. In the most probable orientation (probability of 66%), the oxygen atom from the deprotonated  $-\text{OH}$  group of the  $\text{Fl}^{2-}$  molecule is in contact with the positively charged headgroup of CTAB. On the other orientation (34% probability), the  $\text{Fl}^{2-}$  molecule is in contact with the CTAB headgroup through its carboxylic group.

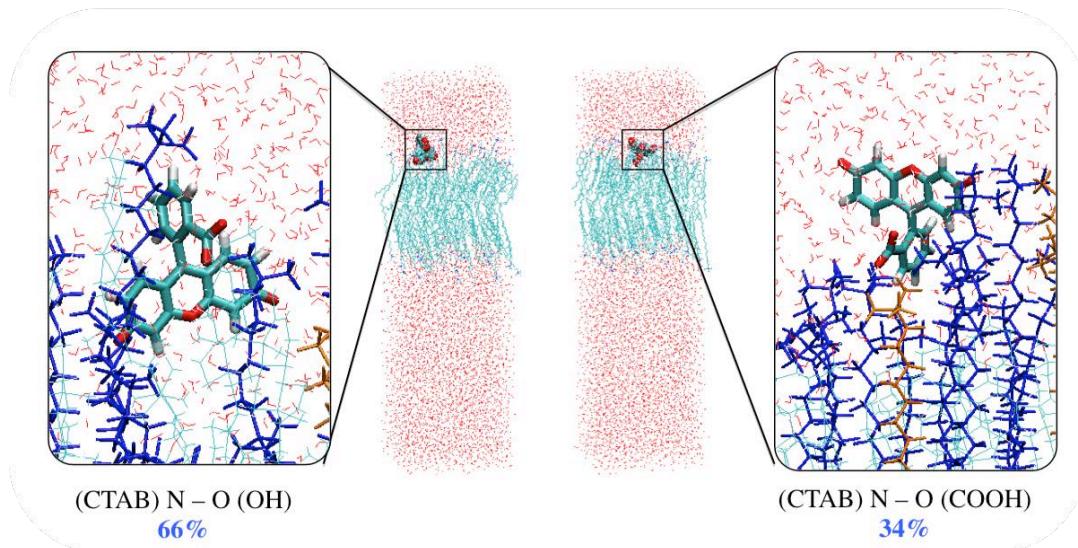


**Figure 5.9:** Snapshots of the large simulation box making emphasis on a single FI molecule orientation when is attached to the QS surface. Water is shown in red and QS in light blue. Two orientations can occur, when hydroxyl and carboxyl groups from  $\text{FI}^{2-}$  are closed to nitrogen atoms from  $\text{CTA}^+$  from QS.

Simulations S2, S3 and S4 show fluorescein adsorption into the QS surface, although the time required for the adsorption to happen increases with the fluorescein concentration. S2 simulations that contains 4 fluorescein molecules, some of them absorbed more quickly than some in S4 simulations (that contains 27 fluorescein molecules). This means that there is a competition between two driving forces, one towards forming  $\text{FI}^{2-}$  aggregates in water and other towards making  $\text{FI}^{2-}$  interact with the QS surface. Importantly enough, it is also observed that always at least one fluorescein molecule gets adsorbed into the QS surface, and that this interaction happens in the few initial nanoseconds of the simulation. This is a crucial result, as it means that there will always be emission from the QS-dye loaded system, although the efficiency will be low. Representative snapshots of S2, S3 and S4 simulations at a random instant are shown in Figure 5.10 and the main results are listed below.

When there are one or more  $\text{FI}^{2-}$  molecules attached to the surface of the vesicle three situations arise, all of them are shown in Figure 5.11. Figure 5.11-(c) shows the case where there is a monomer fluctuating within the QS surface without interacting with any other fluorescein molecule. Figure 5.11-(a) and (b) present the interaction between two fluorescein

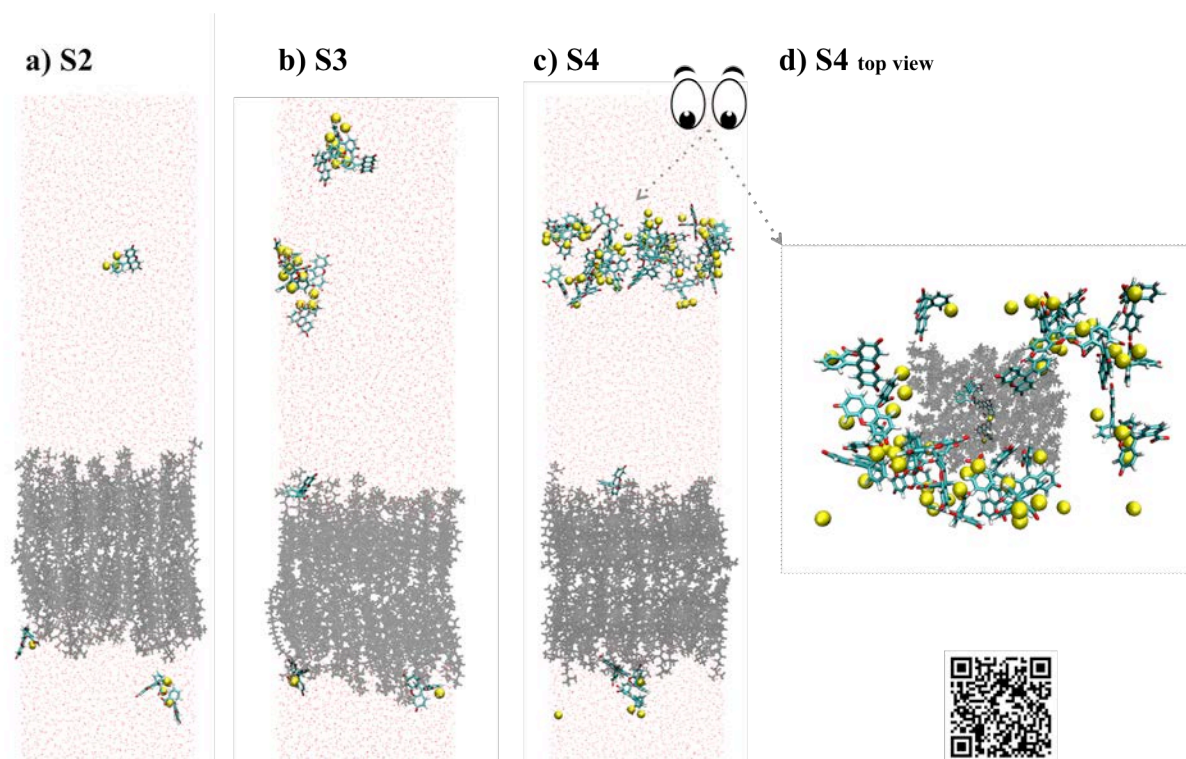


**Figure 5.10:** Snapshot of S2, S3 and S4 simulation at the final instant of the simulation. Quatsome membrane is painted in black, fluorescein molecules in cyan and sodium counterions in yellow spheres. (d) corresponds to a snapshot of the S4 simulation from the top view in order to show the big aggregate is form far away from the QS surface. QR code is added in order to show a movie of S4 simulation.

molecules forming a dimer that can orientate in two ways. Figure 5.11-(c) shows the case where the fluorescein is forming a trimer. In either case, strong fluctuations in the position of the molecules are observed throughout the simulation time. This is due to the fact that the interaction is of electrostatic nature. In the trajectories, it is observed how molecules move towards the QS surface, deposit on it and then fly away. However, as mentioned before, at least one  $\text{Fl}^{2-}$  is always attached to the QS surface. This is a really interesting result, that is in agreement with experimental results from the QS-dye system (more details and discussion are shown in a latter section of the chapter), because fluorescent emission is always observed in the QS-fluorescein system, regardless of the concentration of the dye. However, note also that these results show the weak electrostatic interaction between the anionic fluorescein dye and the positive surface of the Quatsome.

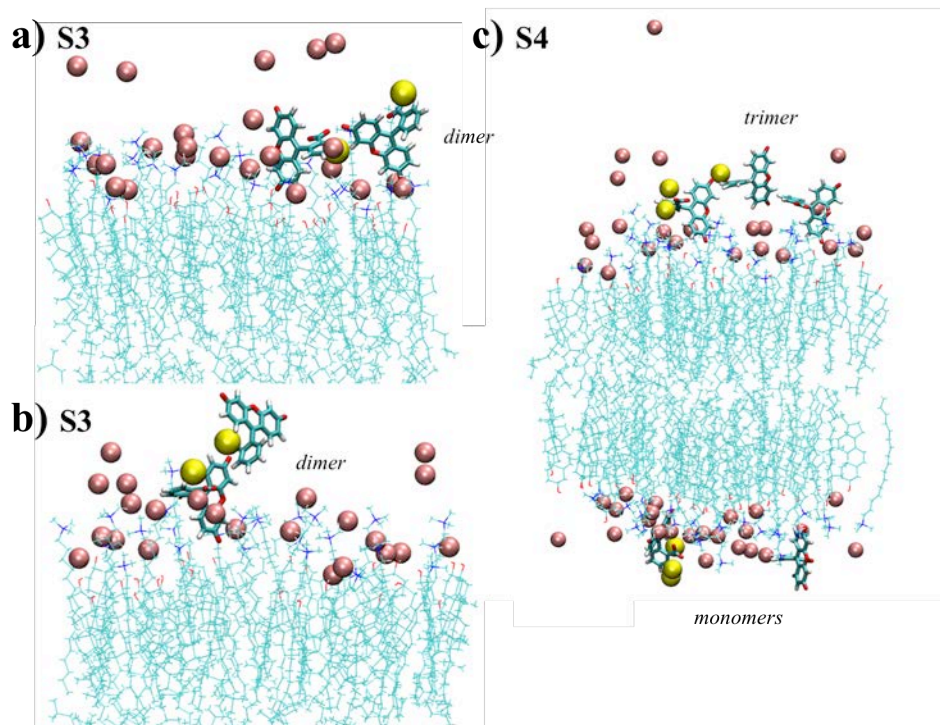


**Figure 5.11:** (a)-Snapshot of a layer of the QS membrane in which two fluorescein dianion dyes are interacting between them forming a dimer and also interacting electrostatically with the QS surface. (b)-Snapshot of a dimer absorbed into the membrane, but with only one of the fluorescein molecules interacting electrostatically with the QS. (c)-Snapshot of both layers of the QS membrane in which we observed a trimer absorbed in one interface (top) and two monomers absorbed in the other interface (bottom). Pink spheres are the  $\text{Br}^-$  counterions of the CTAB molecules. (a) and (b) Snapshots are taken from S3 simulation whereas (c) snapshots corresponds to S4 simulation.

Molecules that do not interact with the surface form aggregates in water. The size of such aggregates increases with the  $\text{Fl}^{2-}/\text{CTAB}$  ratio (see Table 5.2), as shown in simulations S3 and S4 of Figure 5.10 and 5.11. In S2 simulation, only one molecule is attached to the QS surface during all the simulation time, since the other three fluctuate in water without forming aggregates. In S3 and S4 simulations, at least one molecule is attached on the QS surface and the others form aggregates.

To understand clearly the interaction between fluorescein dianion molecule and QS bilayer, we also studied the possibility of formation of hydrogen bonds. Therefore, by using the Hydrogen Bonds plug-in in VMD program we counted the number of hydrogen bonds formed throughout a given trajectory. In the first place, it was observed that there is no hydrogen bond formation between the whole  $\text{CTA}^+$  molecules and both oxygen atoms from

hydroxyl and carboxyl group of the  $\text{Fl}^{2-}$  molecule, and neither with cholesterol. However, hydrogen bond formation was observed between water and both oxygen atoms from hydroxyl and carboxyl group of the  $\text{Fl}^{2-}$  molecule (see Figure 5.12).

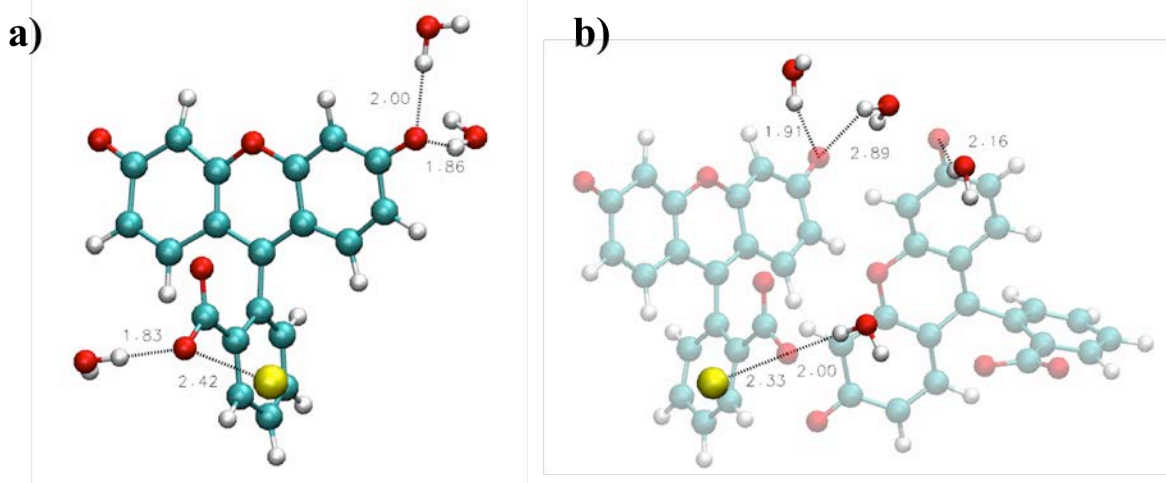


**Figure 5.12:** (a)-(b) snapshots of the fluorescein monomer and dimer, respectively showing the hydrogen bonds with water molecules but also the interaction with the sodium counterion.

Based on results, we concluded that fluorescein dianion molecule forms hydrogen bonds when surrounded in water molecules but not when attached to QS surface. Water molecules would be the responsible for the hydrogen-bond formation, decreasing the electrostatic repulsion between the dianions<sup>15</sup> or positive QS surface. In addition, it has been also demonstrated the interaction between the oxygen from the carboxyl group of the fluorescein ( $-\text{COOH}$ ) molecule and sodium counterions (see Figure 5.12-(a)), showing same behaviour as in fluorescein molecules in water solvent only (section 5.2). We conclude that the sodium counterions have as well a contribution in the weakness of the electrostatic interaction between the fluorescein molecules and QS vesicles. Hence, from MD simulation run, we can affirm that it will exist a clear competition between the electrostatic interaction that bonds the fluorescein molecules to QS surface, to its counterions and the hydrogen bond interaction that allows fluorescein molecules to fluctuate in water by forming aggregates.

## 5.4 ANALYSIS OF EXPERIMENTAL RESULTS

In this section, we analyze relevant experimental results about the Quatsome and the fluorescein molecule to our own theoretical work. All the experimental details are reported in Dr. Antonio Ardizzone PhD thesis<sup>2</sup>, in Nanomol group (ICMAB-CSIC).

The compressed CO<sub>2</sub> methodology, DELOS-SUSP, was used for the preparation for the plain Quatsomes. A detailed description of such process is given in Annex, Figure A.1. The preparation of the Quatsomes decorated with Fl<sup>2-</sup> was done as follows: 1 μM solution of Fl<sup>2-</sup> in MilliQ water is prepared, in which the pH is modified at 9 (by addition of NaOH) in order to have the fluorescein in dianionic state. Several vials with different concentrations of the Quatsomes were prepared, and the Fl<sup>2-</sup> solution was added to each vial, thus obtaining samples with the same concentration of Fl<sup>2-</sup> but different concentration of QS. Samples were incubated at room temperature under gentle stirring for 30 minutes. Notice that the strategy followed by the experimentalists to study the effect of the concentration on the properties of the system were the opposite to our own strategy; while in our simulations we fixed the QS concentration and change the dye concentration, the experimental cases are done the other way around. Both strategies are complementary and the obtained results can be compared. In simulations S1-S4, it must be taken into account that the two leaflets of QS are exposed to the interaction with the dyes, whereas in the experiments only the external leaflet is accessible to the fluorescein. As an example, the simulation S2 (Table 5.2) corresponds to an equivalent experimental situation of 4 fluorescein molecules interacting with 54 CTAB molecules, an experimental ratio of 2:27 between fluorescein and CTAB.

It was observed that purification of QS-Fl<sup>2-</sup> by diafiltration induced a release of Fl<sup>2-</sup> molecules from the QS surface. Series of washing cycles with fresh MilliQ water were done achieving a complete removal of all the fluorescein molecules decorating the QS surface, proving the weak electrostatic interaction between the anionic dye and the positive surface of the Quatsomes. This is completely in agreement with our simulations, which clearly show the equilibrium state between Fl<sup>2-</sup> molecules bounded to QS surface and Fl<sup>2-</sup> molecules

unbounded, freely diffusing in water.

It was possible to measure the presence of unbounded dye molecules in QS-FI<sup>2-</sup> samples by using centrifugal filters (Centricon, Merck Millipore with 100 kDa cut off). Presence of non-attached FI<sup>2-</sup> molecules was verified for samples that had less concentration of QS. Simulation S1 corresponds to the experimental sample with the highest loading without detecting the presence of unbounded FI<sup>2-</sup> molecules. The other three simulations (S2, S3 and S4), correspond to experiments with higher FI<sup>2-</sup> loadings on Quatsomes, in which the presence of unbounded fluorescein has been detected (see FI-QS-5, FI-QS-6 and FI-QS-7 samples of Figure 5.13). This is in agreement with our simulations' results, where unbounded fluorescein can be seen, as in the trajectories of simulations S2, S3 and S4.

No relevant variations of the QS average sizes have been noticed after the addition of fluorescein. Measurements done with DLS technique shows 70 nm of mean size, which is maintained over 2 months, except in the case of the experiment with the highest amount of FI<sup>2-</sup>/QS ratio. This suggests the aggregation of material; the membrane components together with fluorescein aggregates. This has also been observed in our simulations S2, S3 and S4.

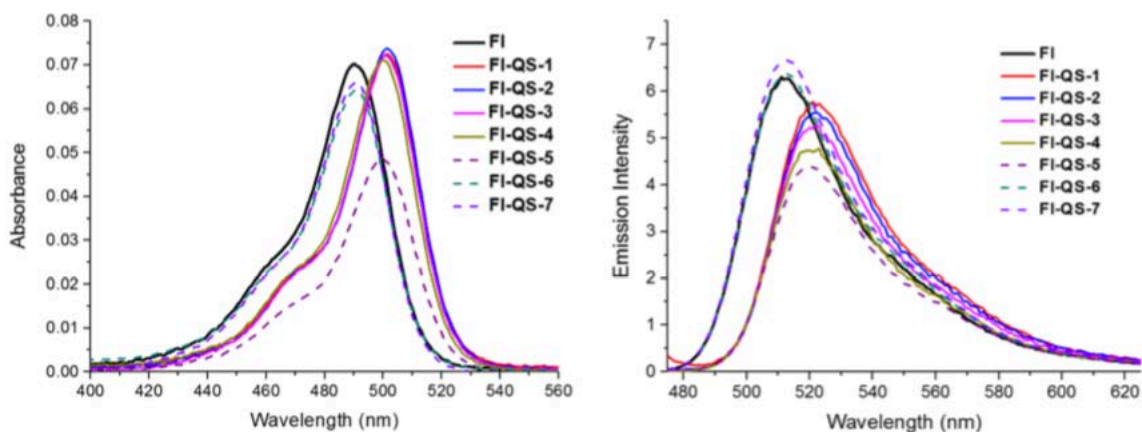


Figure 5.13: UV-vis absorption (left) and emission normalized by absorbance at  $\lambda$  (right) of FI<sup>2-</sup> and FI<sup>2-</sup> - decorated Quatsomes at different loadings. The code used to name the samples is made of three parts: the first one refers to the fluorescein dye (FI, in this case), the second one refers to the Quatsome vesicle (QS) and finally, the last one, is a number associated to the dye loading, as in this case from 1 to 7 at increasing loading.

The structuration of the QS has been evaluated by comparing the photophysical properties of the QS decorated with  $\text{Fl}^{2-}$  and  $\text{Fl}^{2-}$  in a water solution at  $\text{pH} = 9$ . The UV-vis absorption and emission spectras of the QS decorated with  $\text{Fl}^{2-}$  are shown in Figure 5.13. The results show coherence with other works reported in literature about the interaction of the fluorescein with CTAB micelles<sup>22</sup>. Both absorption and emission of QS decorated with  $\text{Fl}^{2-}$  are red-shifted, probably due to the excited state of the probe when interacting with CTAB. As a consequence of the increased loading of fluorophores, self-quenching of the emission is noticed, as shown by the decrease of emission intensity (Figure 5.13).

Nevertheless, the re-organization over a vesicle can have a positive effect on the photostability of a dye. Photodegradation of fluorescein occurs via an interaction of the fluorophore in the ground state with oxygen in the singlet state<sup>23</sup>. For these reason, the photostability of the  $\text{Fl}^{2-}$  in water has been compared to that of QS decorated with  $\text{Fl}^{2-}$ . The evolution of the measured fluorescence is shown in Figure 5.14.

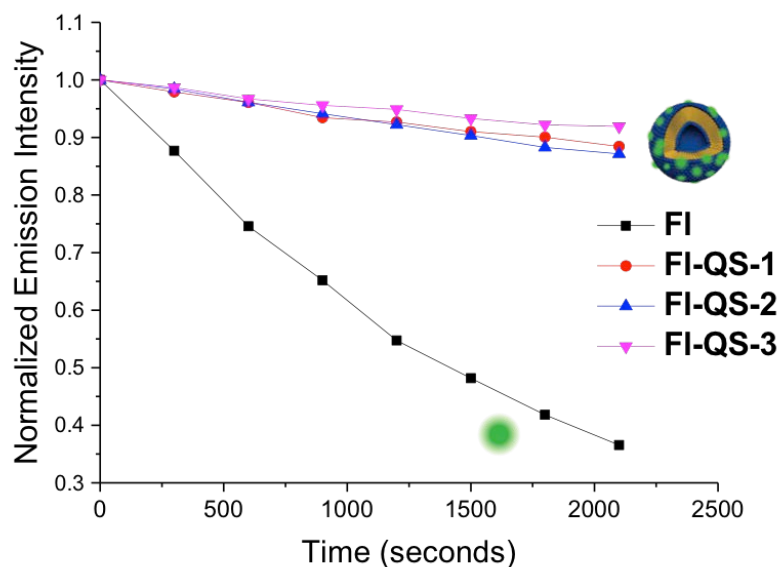


Figure 5.14: Variation of measured fluorescence of the free  $\text{Fl}^{2-}$  (black line) and  $\text{Fl}^{2-}$  - QS at different irradiation times. The fluorescence intensity has been normalized by the value before starting the irradiation.



Only the samples with lower  $\text{Fl}^{2-}$  contents were monitored in order to exclude any possible contribution of free  $\text{Fl}^{2-}$  in water to the observed emission. Emission of free  $\text{Fl}^{2-}$  decreases more than 60% after 40 minutes of irradiation, while it decreases less than 15% when it is decorating the QS surface. This result can be explained by the fact that the fluorescein is an hydrophilic dye that forms hydrogen bonds with the hydrogen of the water, as it has been shown in a previous section. The fact that the dye interacts electrostatically with the surface of the Quatome implies that the fluorescein is protected from forming hydrogen bonds easily, limiting the photodegradation of the dye and making therefore fluorescein more photostable when attached to QS<sup>17</sup>.

Based on our theoretical work supported with experiments, we conclude that the strategy to nanostructure the anionic fluorescein dye on the surface of QS in basic water (taking advantage of the cationic head of the CTAB molecules of QS) was a good initial strategy to functionalize the surface of our vesicle. Nevertheless, the weak interaction between the anionic dye of the fluorophores and the QS compromises the integrity and suitability of the fluorescent organic vesicles for applications with imaging purposes. All this suggests the search for other strategies for the nanostructuration like considering dyes with a different nature, for instance hydrophobic dyes.

## References

- [1] Al Haddabi, B., Al Lawati, H. A. J., & Suliman, F. O. (2016). An enhanced cerium(IV)–rhodamine 6G chemiluminescence system using guest–host interactions in a lab-on-a-chip platform for estimating the total phenolic content in food samples. *Talanta*, 150, 399–406.
- [2] Ardizzone, A. (2017). *New fluorescent nanovesicles, by self-assembly of organic fluorophores, sterols and surfactants, as probes for bioimaging*. PhD thesis, Institut de Ciència de Materials de Barcelona (ICMAB-CSIC).
- [3] Bozkurt, E., Bayraktutan, T., Acar, M., & Toprak, M. (2013). Spectroscopic studies on the interaction of fluorescein and safranin T in PC liposomes. *Spectrochimica Acta Part A: Molecular and Biomolecular Spectroscopy*, 101, 31–35.
- [4] Buurma, N. J., Serena, P., Blandamer, M. J., & Engberts, J. B. F. N. (2004). The Nature of the Micellar Stern Region As Studied by Reaction Kinetics. 2 †,1. *The Journal of Organic Chemistry*, 69(11), 3899–3906.
- [5] Carter, K. P., Young, A. M., & Palmer, A. E. (2014). Fluorescent Sensors for Measuring Metal Ions in Living Systems. *Chemical Reviews*, 114(8), 4564–4601.
- [6] Casalini, T., Salvalaglio, M., Perale, G., Masi, M., & Cavallotti, C. (2011). Diffusion and Aggregation of Sodium Fluorescein in Aqueous Solutions. *The Journal of Physical Chemistry B*, 115(44), 12896–12904.
- [7] Chitta, R. K. & Gross, M. L. (2004). Electrospray Ionization-Mass Spectrometry and Tandem Mass Spectrometry Reveal Self-Association and Metal-Ion Binding of Hydrophobic Peptides: A Study of the Gramicidin Dimer. *Biophysical Journal*, 86(1), 473–479.
- [8] Frisch (2009). *Gaussian 09*. Gaussian, Inc., Wallingford CT.
- [9] Gehlen, M. H. & De Schryver, F. C. (1993). Time-resolved fluorescence quenching in micellar assemblies. *Chemical Reviews*, 93(1), 199–221.
- [10] Goftar, M. K., Moradi, N., & Kor, N. M. (2004). Spectroscopic studies on aggregation phenomena of dyes. *European Journal of Experimental Biology*, 4(2), 72–81.
- [11] Hadjianestis, J. & Nikokavouras, J. (1993). Luminol chemiluminescence in micellar media II: Energy transfer to fluorescein. *Journal of Photochemistry and Photobiology A: Chemistry*, 69(3), 337–343.

- [12] Halgren, T. A. (1996). Merck molecular force field. I. Basis, form, scope, parameterization, and performance of MMFF94. *Journal of Computational Chemistry*, 17(5-6), 490–519.
- [13] Hu, H., Lu, Z., & Yang, W. (2007). Fitting Molecular Electrostatic Potentials from Quantum Mechanical Calculations. *Journal of Chemical Theory and Computation*, 3(3), 1004–1013.
- [14] Lippert, E. (1975). Hydrogen Bonding. Von M. D. Joesten und L. J. Schaad. Marcel Dekker, Inc., New York 1974. 1. Aufl., VI, 622 S., \$ 45.—. *Angewandte Chemie*, 87(17), 637.
- [15] López Arbeloa, I. (1983). Aggregation of halofluorescein dyes. *Dyes and Pigments*, 4(3), 213–220.
- [16] Munkholm, C., Parkinson, D. R., & Walt, D. R. (1990). Intramolecular fluorescence self-quenching of fluoresceinamine. *Journal of the American Chemical Society*, 112(7), 2608–2612.
- [17] Reisch, A. & Klymchenko, A. S. (2016). Fluorescent Polymer Nanoparticles Based on Dyes: Seeking Brighter Tools for Bioimaging. *Small*, 12(15), 1968–1992.
- [18] Rohatgi, K. K. & Singhal, G. S. (1962). Determination of Average Molar Absorptivity for Self-Absorption of Fluorescent Radiation in Fluorescein Solution. *Analytical Chemistry*, 34(13), 1702–1706.
- [19] Safran, S. A., Pincus, P., & Andelman, D. (1990). Theory of Spontaneous Vesicle Formation in Surfactant Mixtures. *Science*, 248(4953), 354–356.
- [20] Shao, Q. & Xing, B. (2010). Photoactive molecules for applications in molecular imaging and cell biology. *Chemical Society Reviews*, 39(8), 2835–2846.
- [21] Sjöback, R., Nygren, J., & Kubista, M. (1995). Absorption and fluorescence properties of fluorescein. *Spectrochimica Acta Part A: Molecular and Biomolecular Spectroscopy*, 51(6), L7–L21.
- [22] Song, A., Zhang, J., Zhang, M., Shen, T., & Tang, J. (2000). Spectral properties and structure of fluorescein and its alkyl derivatives in micelles. *Colloids and Surfaces A: Physicochemical and Engineering Aspects*, 167(3), 253–262.
- [23] Song, L., van Gijlswijk, R. P. M., Young, I. T., & Tanke, H. J. (1997). Influence of fluorochrome labeling density on the photobleaching kinetics of fluorescein in microscopy. *Cytometry*, 27(3), 213–223.
- [24] Valdes-Aguilera, O. & Neckers, D. C. (2002). Aggregation phenomena in xanthene dyes. *Accounts of Chemical Research*, 22(5), 171–177.
- [25] Vanommeslaeghe, K., Hatcher, E., Acharya, C., Kundu, S., Zhong, S., Shim, J., Darian, E., Guvench, O., Lopes, P., Vorobyov, I., & Mackerell, A. D. (2009). CHARMM general force field: A force field for drug-like molecules compatible with the CHARMM

- all-atom additive biological force fields. *Journal of Computational Chemistry*, 31(4), NA.
- [26] Zhang, J., Cheng, F., Li, J., Zhu, J.-J., & Lu, Y. (2016). Fluorescent nanoprobe for sensing and imaging of metal ions: Recent advances and future perspectives. *Nano Today*, 11(3), 309–329.
- [27] Zhu, X., Lopes, P. E. M., & MacKerell, A. D. (2012). Recent developments and applications of the CHARMM force fields. *Wiley Interdisciplinary Reviews: Computational Molecular Science*, 2(1), 167–185.
- [28] Zoete, V., Cuendet, M. A., Grosdidier, A., & Michielin, O. (2011). SwissParam: A fast force field generation tool for small organic molecules. *Journal of Computational Chemistry*, 32(11), 2359–2368.



*All sorts of things can happen when you're open  
to new ideas and playing around with things.*

Stephanie Kwolek

# 6

## Quatsomes with hydrophobic dyes

Chapter 5 verses about the first attempt of this work to functionalize the Quatsome system, by using it as a scaffold for fluorescein molecules (in that case a hydrophilic fluorescent dye). Not having found an optimal result with respect to the initial objective (the simulations have shown that fluorescein molecules tend to aggregate), chapter 6 explores other widely used fluorescent probes as candidates, the hydrophobic family of carbocyanine dyes.

The desirable properties of good fluorescent probes for microscopy are brightness and high photostability and capacity of site-specific labeling and showing bio-compatibility. Carbocyanine dyes are highly fluorescent, although they may suffer poor solubility in aqueous

media, limiting their use for bioapplications<sup>14,18</sup>. Loading these dyes into a non-fluorescent nanocarrier as the Quatsome, arranged as fluorescent organic system, offers an interesting strategy to bring these organic dyes into aqueous media. The goal of this chapter is to study the interactions of the elements of the QS-dye system, to see if the desirable physical properties of the Quatsome and the desirable optical properties of the dyes are altered. Similar studies have used small unilamellar vesicles (SUVs), e.g., liposomes, with sizes of 100 nm, as supramolecular nanostructures<sup>20</sup>. However, there is a strong interest towards new vesicular formulations, made by nonlipid components, able to overcome the intrinsic instability of liposomes that hinders their biomedical applications<sup>9</sup>.

Carbocyanine molecules are lipophilic fluorophores with long alkyl chains, which can be integrated into QS membrane exploiting hydrophobic interactions between the chains of the dyes and the hydrophobic compartment of the double-layer membrane. The general cyanine structure consist of two nitrogen atoms (one of which is positively charged) linked by a conjugated chain of carbons. Specifically, we use two water-insoluble carbocyanine dyes with two 18-carbons aliphatic chains; 1,1 -dioctadecyl-3,3,3 ,3 -tetramethylindocarbocyanine perchlorate (DiI) and 1,1 -dioctadecyl-3,3,3 ,3 -tetramethylindodi-carbocyanine perchlorate (DiD) (see their chemical structure in Figure 6.1)<sup>27,29</sup>.

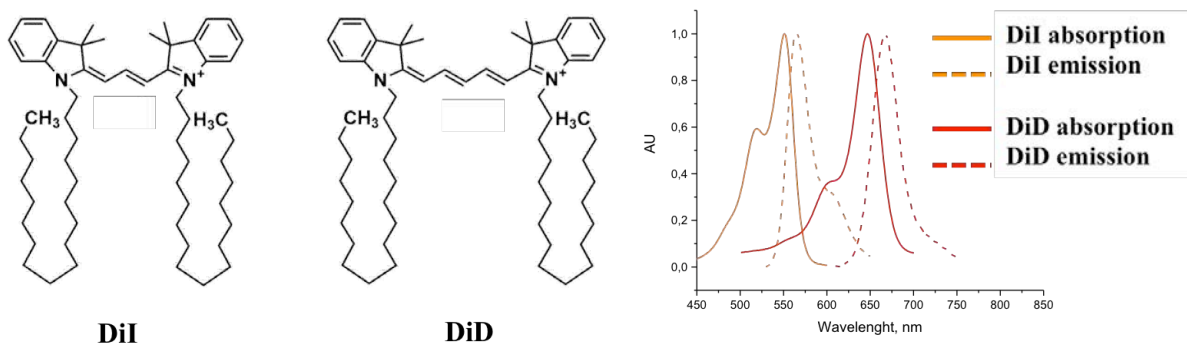


**Figure 6.1:** Schematic representation of chemical structure of DiI and DiD dye and normalized UV-vis absorption and emission spectra of DiI (yellow) and DiD (red). Experimental data is done by Dr. Ardizzone<sup>2</sup> in Nanomol group.

Since fluorescence techniques only indirectly probe the dynamics of the native dye-loaded Quatsome components, there exists a need to precisely determine the dynamics and interactions of the elements of the system and water, at the atomic level<sup>10</sup>. Moreover, no structural studies (X-ray crystallography or NMR) have been reported on Quatsome bilayers containing DiI or DiD. In this line, all-atomic MD simulations can provide this information, giving insight about the fidelity of the probe to QS fluidity and the extent to which the probe perturbs the bilayer, and providing the first detailed predictions of DiI and DiD dye location in a QS bilayer<sup>3</sup>.

Our AA-MD results are supported by experiments including the synthesis (comparing different methodologies) and the characterization of the system, as well as stochastic optical reconstruction microscopy (STORM), an innovative superresolution microscopy technique<sup>30</sup>, in order to explore the potential of the dye-loaded QS for biological imaging.

## 6.1 MODEL AND FORCE FIELD OF CARBOCYANINE DYES

Cyanine family is well studied both experimentally and theoretically in literature since decades ago. Nevertheless, we were interested in finding a suitable model and force field for DiI (Cy3) and DiD (Cy5) carbocyanines compatible with CHARMM for our purpose, and for that we utilize the follow strategy based on DFT electronic structure calculations. In the case of DiI dye; first of all, its molecular structure was designed using GaussView program, which is a part of the Gaussian09 software package<sup>7</sup>. After that, the geometry of the molecule was optimized employing the Gaussian09 program. Quantum mechanics (QM) calculations were performed using density functional theory (DFT) with RM062X functional and 6-311+G(d,p) basis set and also taking into account the presence of water solvent for the optimization geometry. After geometry optimization, a first guess for the force field parameters was obtained using the optimized structure in the CGenFF program<sup>28</sup> available as a web server. The force field parameters for the carboxyl chains  $[-\text{CH}_2-\text{CH}_3]_{18}$  were available but some of the parameters obtained by analogy for the cyanine part of



the DiI molecule had high penalties, indicating the need for re-parametrization. These parameters with high penalties were substituted by the parameters proposed in ref<sup>22,23</sup> for dyes (Cy3 dye parameter set in that reference). The parameters were obtained and validated by using MM methods and QM calculations to compute the potential surface energies, as detailed in the mentioned reference. Partial charges on DiI molecule were obtained using the charge partitioning Merz-Kollman (MK) method<sup>11</sup>. The DiI molecule has a net charge of +1e and it is distributed as shown in Figure 6.2. There is an small asymmetry in the charge distribution between the two indole rings of the head group (0.47e - 0.67e). The

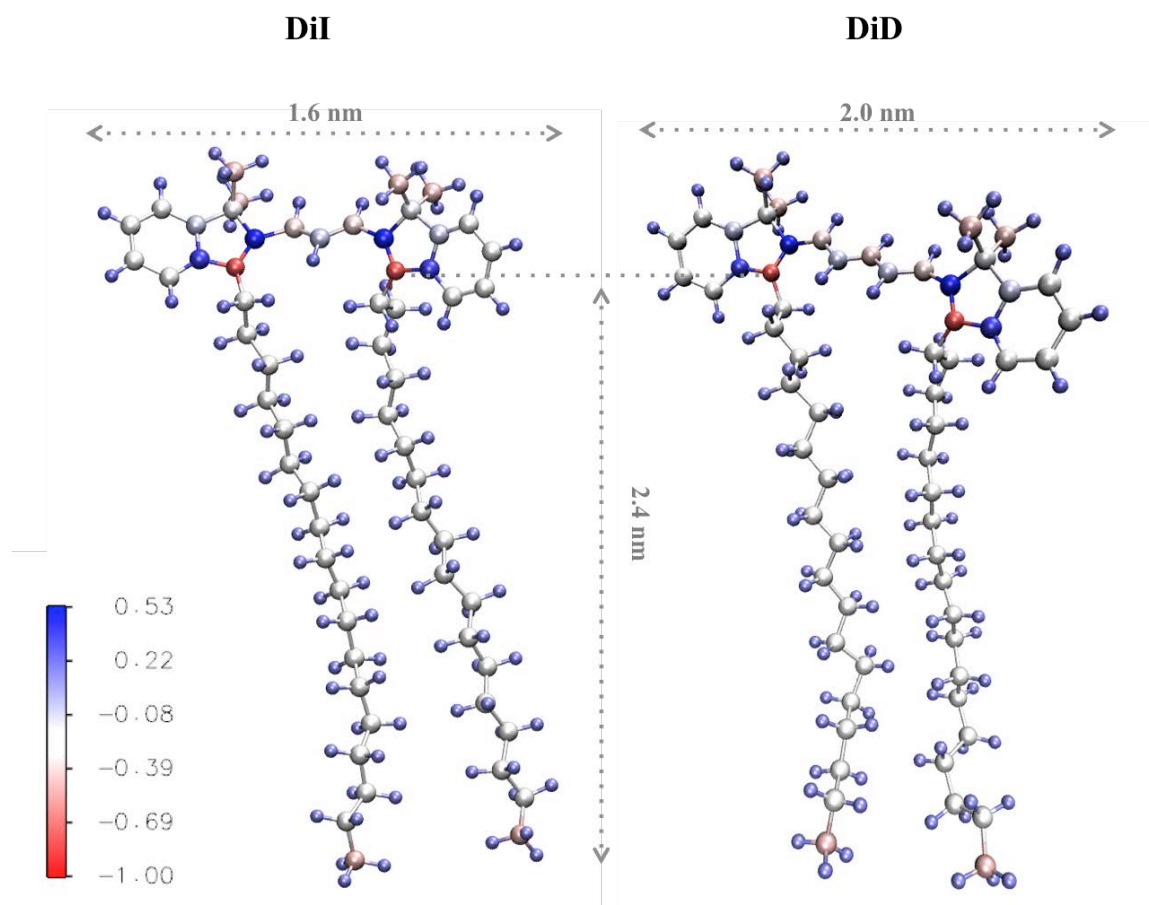


**Figure 6.2:** Simulation snapshots of the DiI (left) and DiD (right) dyes using CPK representation. The color scheme corresponds to the partial charge (in e units) as indicated in the color ruler. Distance corresponding to nitrogen atom of the headgroup of the dye and the last carbon atom of the tail has a value of  $\sim 2.4$  Å and the corresponding distance for the length of the head group of the DiI ( $n = 1$ ) and DiD ( $n = 2$ ) dyes are 1.6 Å and 2.0 Å, respectively.

chromophore bridge has a small charge of  $-0.122e$ .

In the case of DiD dye, we took advantage of the already developed model for the DiI, as the two dyes just differ in the number of ethylene groups in the chromophoric part, with  $n = 1$  for DiI and  $n = 2$  for DiD. We followed the same steps to design and optimize the molecule and we obtained the corresponding force field. The DiD molecule also has a net charge of  $+1e$ , and the charge distribution is given in Figure 6.2. Unlike in the case of the DiI, in the DiD the head group charge distribution obtained from DFT calculations using the MK method is almost symmetric. The indole rings have a charge of  $0.48e$  and  $0.49e$ . The chromophore bridge has a charge of  $-0.127e$ , similar to that of the DiI.

Input files containing all the employed parameters for the DiI and DiD dyes are available in this repository: [https://bitbucket.org/icmab\\_soft\\_matter\\_theory/carbocyanine-dyes/src/master/](https://bitbucket.org/icmab_soft_matter_theory/carbocyanine-dyes/src/master/)

## 6.2 MOLECULAR DYNAMICS SIMULATIONS OF CARBOCYANINE DYES

Once the model of the carbocyanine dyes is ready to be used, in this section we carry out AA-MD simulations of the QS system with the dyes. There are three subsections: In the first one, two different starting relative positions of the dye with respect to the Quatsome are studied. In the second, the behaviour of a single dye at the Quatsome bilayer is analyzed. And in the third, the interactions between two dyes in the QS are studied. Finally, a subsection of experimental results is included.

All the simulations employ the same parameters of the force field (partial charges and bond, angle and dihedral equilibrium values and force constants) for the DiI and DiD dyes, which are those described in section 6.1. The QS membrane and water were modeled as in chapters 3 and 5.

All the simulations have the same computational details: MD simulations were performed using NAMD 2.11 software. The equations of motion were solved using a time step of 2 fs. Electrostatic interactions were computed using the PME method with usual settings

in NAMD (1 Å resolution, updated each 2 time steps). Lennard-Jones interactions were truncated at 1.2 nm employing a switching function starting at 1.0 nm. Periodic boundary conditions were employed in all directions. Temperature was kept constant at 298 K using a Langevin thermostat with a relaxation time of 1 ps. Pressure of 1 atm was imposed using the anisotropic Nosé-Hoover-Langevin piston implemented in NAMD (oscillation period of 100 fs and decay time of 50 fs).

The equilibrated Quatsome bilayer employed in all the simulations of this chapter is the same as the one in Chapter 3. This is, the Quatsome (QS) bilayer is formed of a patch of 15.7 nm<sup>2</sup> (containing 54 CTAB and 54 cholesterol molecules) simulated in water.

### 6.2.1 SIMULATIONS ABOUT THE STARTING POSITION

In this section we started by simulating the DiI dye and the Quatsome bilayer separated in water, expecting an interaction by hydrophobic effect.

**Table 6.1: Composition of the systems considered in the MD simulations, including total number of atoms, ratio of the components of the system (DiI dye, water and CTAB molecules), total simulation time and size box after equilibration.**

	Atoms (total)	Num. Molec. dye/water/CTAB	Sim time	Size Box
<b>S1</b>	26946	1/6463/54	12 ns	25.7 nm <sup>2</sup> x 15.1 nm
<b>S2</b>	26946	1/6463/54	90 ns	18.1 nm <sup>2</sup> x 14.3 nm

S1 simulation (see Table 6.1) was built up with the aim of illustrating the trajectory of a single DiI located far away from the Quatsome membrane in water. Additionally, a chloride atom was added in order to balance the positive charge induced by the DiI dye. It was performed a simulation of 10 ns of NPT ensemble, and it was find out that the DiI molecule was not attracted towards the QS membrane, even though it is an hydrophobic molecule. In order to force the interaction between the dye and the QS we run 1 ns of steered molecular dynamics (SMD) simulation, which allows to apply an external force to the molecule to move it in a desired direction. For that, a force of 1573.77 pN was applied on the DiI's centre of mass, forcing it to move towards the QS surface in z direction only.

Then, we run 1 ns of NPT ensemble with superficial tension equal to zero, expecting the DiI dye to enter inside the membrane. However, we found that the molecule automatically bounced from the QS surface moving in the opposite direction, staying in the water (see Figure 6.3). Analyzing the simulation results, we concluded that the DiI molecule is not able to enter inside the QS membrane. We discarded repeating the simulation for the DiD dye, as we assume that the results would be the same.

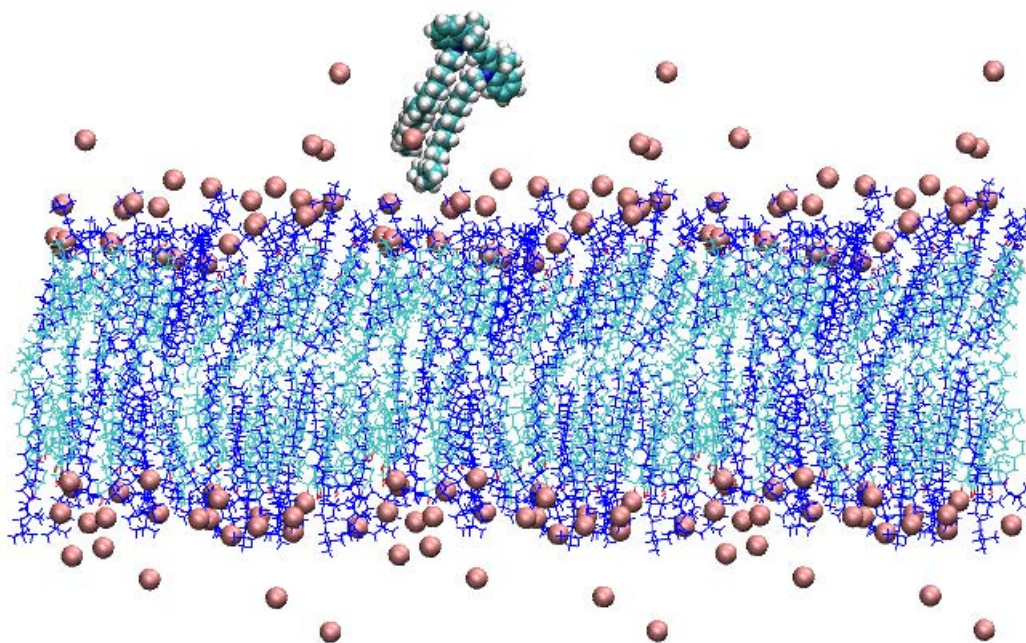


**Figure 6.3:** Simulation snapshot of the QS membrane with DiI dye outside (S1 simulation). It is possible to observe the orientation of the dye (Van der Waals radii representation) with its tails orientated towards the QS surface. CTA<sup>+</sup> molecules are painted in cyan and cholesterol molecules in blue. Bromide counterions of the CTAB are shown as pink spheres.

Based on the previous result, we changed the strategy and considered a starting point where the DiI molecule was inside the QS membrane. Firstly, we manually introduced a DiI molecule inside one of the layers of the QS bilayer, between CTA<sup>+</sup> and cholesterol molecules. But also, we added a chloride atom in order to balance the positive charge induced by the DiI dye (S2 simulations, see computational details in Table 6.1). We needed to run a 10 ps minimization in order to avoid the overlap between the QS components and

the DiI dye. Then, 90 ns of simulation were run, using NPT ensemble with surface tension equal to zero. The results show that the dye remains inside the QS membrane stable along simulation time, not deforming the membrane. Figure 6.4 shows the DiI molecule inside the QS membrane.

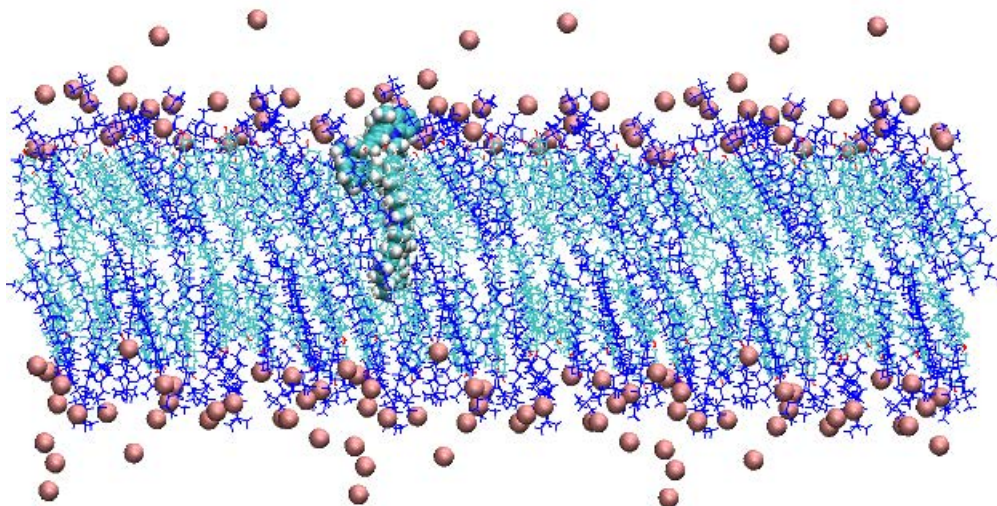


**Figure 6.4:** Simulation snapshot of of the QS membrane with DiI dye inside (S2 simulation). It is possible to observe the orientation of the dye (Van der Waals radii representation) inside the QS membrane.  $\text{CTA}^+$  molecules are painted in cyan and cholesterol molecules in blue. Bromide counterions of the CTAB are shown as pink spheres.

Previous experimental work<sup>2</sup> proves that the preparation method plays an important role in the spectroscopic properties of the DiI and DiD dye, as aggregation states of the fluorophores inside the QS membrane can occur. Methods such as incubation or ultrasonication, in which DiI and DiD dyes are loaded after QS synthesis, are less efficient than DELOS-SUSP methods, in which the QS-dye system is synthesized at the same time. It has been demonstrated experimentally that DELOS-SUSP methodology leads to the best compromise between distribution of the dye over the membrane of QS and morphology of the vesicles.

Both simulations (S1 and S2) can be compared with both types of experimental preparation methods. On one hand, the first simulation, S1, takes as starting point the DiI molecule outside the membrane, as incubation or ultrasonication methods do, and it is

shown that the DiI molecule does not enter the QS membrane, staying in the water. On the other hand, S2, with the starting point of the DiI molecule inside the QS membrane, corresponds to the DELOS-SUSP method, and better results in terms of stability of the dye inside the QS membrane are obtained.

We conclude that, despite it was expected to see how a single dye would be incorporated inside the QS membrane avoiding the water molecules due to its hydrophobicity, simulations did not show that. The reason is that the preparation method plays an important role for the incorporation of the dyes inside the QS membrane. Nevertheless, simulations demonstrated that once the hydrophobic dye is incorporated inside the QS membrane, it remains stable without exiting. This is required for the system to have good fluorescent emission, as expected.

### 6.2.2 SINGLE DYE (DI I OR DI D) AT QUATSOME BILAYER

All simulations described in this section are built-up and minimized exactly in the same way as simulation S2 (previous section). We considered a QS patch with a single dye molecule (DiI or DiD) in water. Simulation S3 is the one with DiI dye and S4 is the one with DiD dye. Computational details are described below in Table 6.2.

**Table 6.2: Composition of the systems considered in the MD simulations, including total number of atoms, number of molecules; molecules of dyes; S3-DiI and S4-DiD, water and CTAB, the simulation times and the equilibrated size box.**

	<b>Atoms (total)</b>	<b>molec. dye/water/CTAB</b>	<b>Sim. time</b>	<b>Size Box</b>
<b>S3</b>	26946	1/6463/54	310 ns	258 nm <sup>3</sup>
<b>S4</b>	26848	1/6429/54	310 ns	257 nm <sup>3</sup>

In both cases, we first performed 1 ns of equilibration simulations using NPT ensemble and then we performed larger equilibration simulations (80 ns for QS-DiI and 100 ns for QS-DiD) using the NPT ensemble maintaining the QS bilayer at zero tension. After the equilibration simulations, we performed production simulations for 230 ns and 210 ns for S3 and S4 simulations respectively. In the case of S3 simulation, the equilibrated size of

the simulation box for S3 was 43.96 Å and 41.03 Å in the XY plane and 143.13 Å for the vertical (Z) direction. And, in the case of S4, we had 45.20 Å and 41.23 Å in the XY plane and 137.97 Å in the vertical (Z) direction.

The first result observed while looking at the long trajectories is that both dyes are stable inside the QS bilayer. They stay in one layer during all the simulation time, no flip-flop is observed at the studied timescale. Moreover, the dye became a part of the leaflet, maintaining the stability and fluidity of it, and the bilayer showed no change or deformation due to the incorporation of the dye molecule. It can be concluded from the simulations that the model employed for DiI and DiD dyes and Quatsome correctly predicts the experimental observation that the dyes are stable inside QS membrane<sup>2</sup>.

In Figure 6.5, we show snapshots from the simulations and the average atomic density profiles. Both DiD and DiI dyes have their carbocyanine groups in contact with water, with their nitrogen atoms located in the hydrophilic region of the QS bilayer (i.e., inside

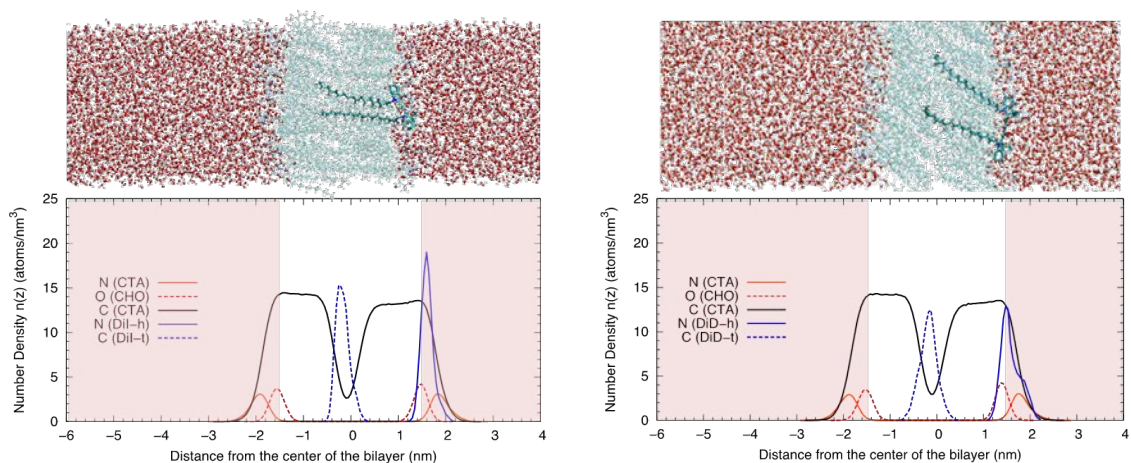


**Figure 6.5: Results from MD simulations for hydrophobic dyes in Quatsomes: (a) DiI and (b) DiD.** For each dye, we show a representative snapshot and the average atomic density profiles of selected atoms in the direction perpendicular to the QS bilayer. In the snapshots, CTAB molecules, water molecules and the dye molecule (emphasized) are shown in CPK representation. Cholesterol molecules and ions are not shown for clarity. The atomic density profiles indicate the location of two characteristic dye atoms (N from the carbocyanines and terminal C from the alkyl chain), the location of the hydrophobic core (C atoms from CTAB) and the hydrophilic headgroup region (defined by oxygen atoms from cholesterol -OH and nitrogen atoms from CTAB). The atomic density for dye atoms is multiplied by a factor of 100 to help identification of the peaks. The region occupied with water is indicated with a shadow to help interpretation of atomic density profiles.

the QS region delimited by the head groups of the CTAB surfactants and the -OH groups of the cholesterol molecules). Density profiles of both dyes are almost identical and results obtained are representative due to the large amount of collected data, which leads to stable statistics. The hydrophobic area is well defined within 3 nm zone (Fig. 6.5, white area).

Regarding the molecular organization of the QS-dye system (see Figure 6.5), the aliphatic chains in both carbocyanines dyes are immersed inside the hydrophobic layer of the QS, as expected, and the head groups formed by two quinoline and the chromophore part are located in the QS surface-water interface. Looking at the graph from right to left, the atoms that show more affinity towards water are ranked as nitrogen atoms from CTAB-head, nitrogen atoms from dye-head, oxygen atom from Chol-head and carbon atoms from dye and CTAB-tail. It is worth mentioning that, sometimes, during the simulation trajectory the head group of the dye tilted with respect to the QS surface. Then, one of the two quinoline groups of each carbocyanine remained more exposed to water, while the other one was immersed in the bilayer. Regardless of the location of the dyes in the QS, we point out that they oriented in parallel with the water-surface interface (this has been already observed in simulation S3). This is in contrast with the study of the DiI inside the DPPC lipid bilayer, where the dyes appear hidden below the head groups of the phospholipids<sup>10</sup>. This behaviour of dyes at DPPC bilayers can lead to instabilities in the long term, as the dyes are far from the water-surface interface.

As shown in Figure 6.5, the presence of a dye may affect the two leaflets of the QS bilayer, as the dye length is larger than one of the QS leaflets. Distance between the density peaks corresponding to carbocyanine nitrogen atoms and the terminal carbon atom of the aliphatic chains is around  $\sim 2.4$  nm, compared with the 3.4 nm size of the hydrophobic bilayer of the QS (see Figure 6.2).

We noticed that loading a single DiI or DiD molecules in the membrane did not change the thickness of the bilayer (measured from the peaks of the nitrogen-nitrogen atom distance from CTAB distribution), as we obtained a value of 4.17 nm (almost similar value as



QS membrane alone calculated in Chapter 3, 4.3 nm). This result is again in contrast with the MD simulations work<sup>10</sup> that studied DiI loaded in DPPC lipid bilayer. They calculated a thickness of 4.22 nm of the membrane alone, but observed an increase of thickness when adding the dye. These absolute thickness changes correspond to increases of 5.2%. Despite the fact that loading dyes inside the QS leaflets could make us expect instabilities on the membrane, the results show the contrary, with dyes perfectly incorporated and interdigitated between QS components.

Concerning the orientation of the dyes at the water/QS interface, in Figure 6.6, we report

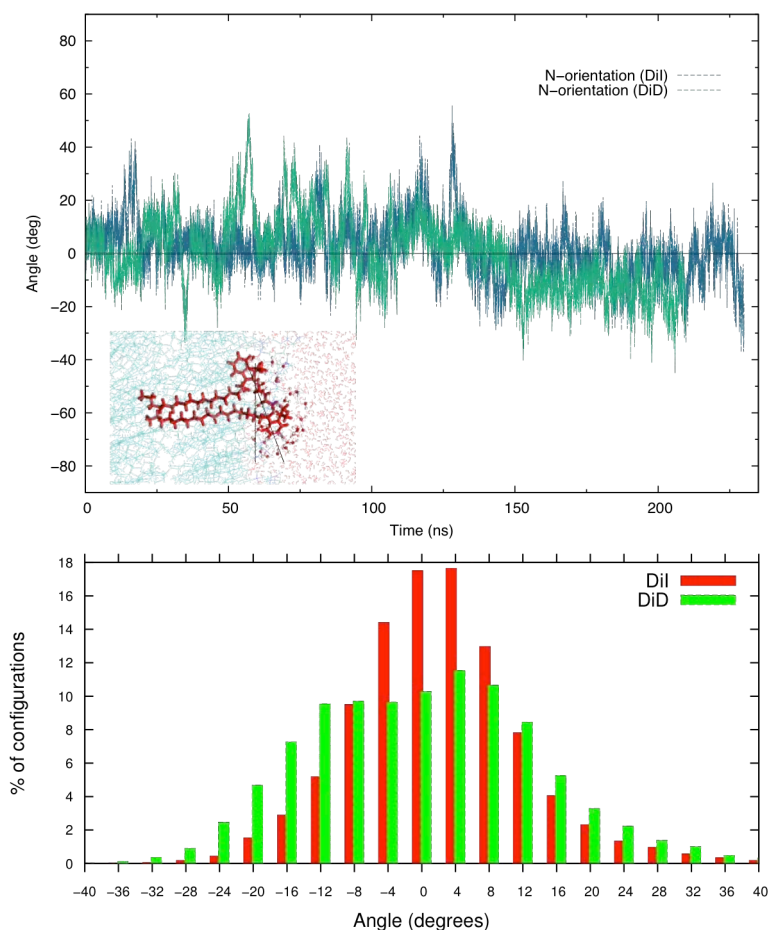


**Figure 6.6:** Top panel: Angle between carbocyanine groups of DiI or DiD and the water/QS interface as a function of time during MD simulations, sampled each 10 ps. Inset: snapshot of observed orientation of a dye molecule in MD simulations illustrating the definition of the angle. Bottom panel: Histogram of angles in the configurations obtained in the top panel (% of configurations with given angles, each 4°).

the angle between carbocyanine groups of DiI or DiD dye and the water/QS interface as a function of time during the MD simulations. We report the observed time series during the production runs and the statistics derived from the time series. The average (equilibrium) angle is  $1.88^\circ$  in the case of DiI dye and  $0.14^\circ$  in the case of DiD dye (see Figure 6.6). The slightly larger value for the DiI dye can be explained by the charge distribution asymmetry in the head group of that molecule, as it has been explained in the previous section. In average the carbocyanine group can be considered parallel to the interface. However, clear fluctuations are observed in Figure 6.6 with substantial deviations from the average angle. These fluctuations are more frequent in the case of DiD dye (Figure 6.6). On the contrary, the DiI chromophore angle in a DPPC phospholipid bilayer was  $\sim 13^\circ$  with respect to the bilayer normal<sup>10</sup>.

For both dyes we observe a substantial mobility in the QS membrane. In Figure 6.7 we report the lateral (in the bilayer plane, XY plane) motion of the DiI and DiD dyes in the QS bilayer. In order to characterize the motion of the dyes, we have selected the central carbon atom of the carbocyanine. The trajectory followed by this particular atom is shown for the full production run in the top panels of Figures 6.7 for DiI and DiD dyes, respectively. The statistical analysis of these trajectories shows that the motion is Brownian, since the mean squared displacement (MSD) in the XY plane follows a straight line with time. If we compare both trajectories we notice, on one hand, that the DiI dye has more mobility inside the membrane than DiD dye, as it is able to explore a bigger surface within the same time. On the other hand, the DiD dye, which has a longer chromophore part, seems to diffuse with a preferred direction and this can lead to slow movement and exploration within the membrane in comparison with the DiI dye.

The lateral diffusion coefficient  $D$  is also determined in Figure 6.7 (values obtained for that case are given in  $\text{\AA}^2 \text{ps}^{-1}$ ) by fitting to the Einstein relationship  $\text{MSD}(t) = 4Dt$ . We calculated diffusion coefficient values for DiD and DiI dyes but also for Quatsome (CTA<sup>+</sup> component). In this case, we compare the diffusion coefficient of the CTA<sup>+</sup> with and without

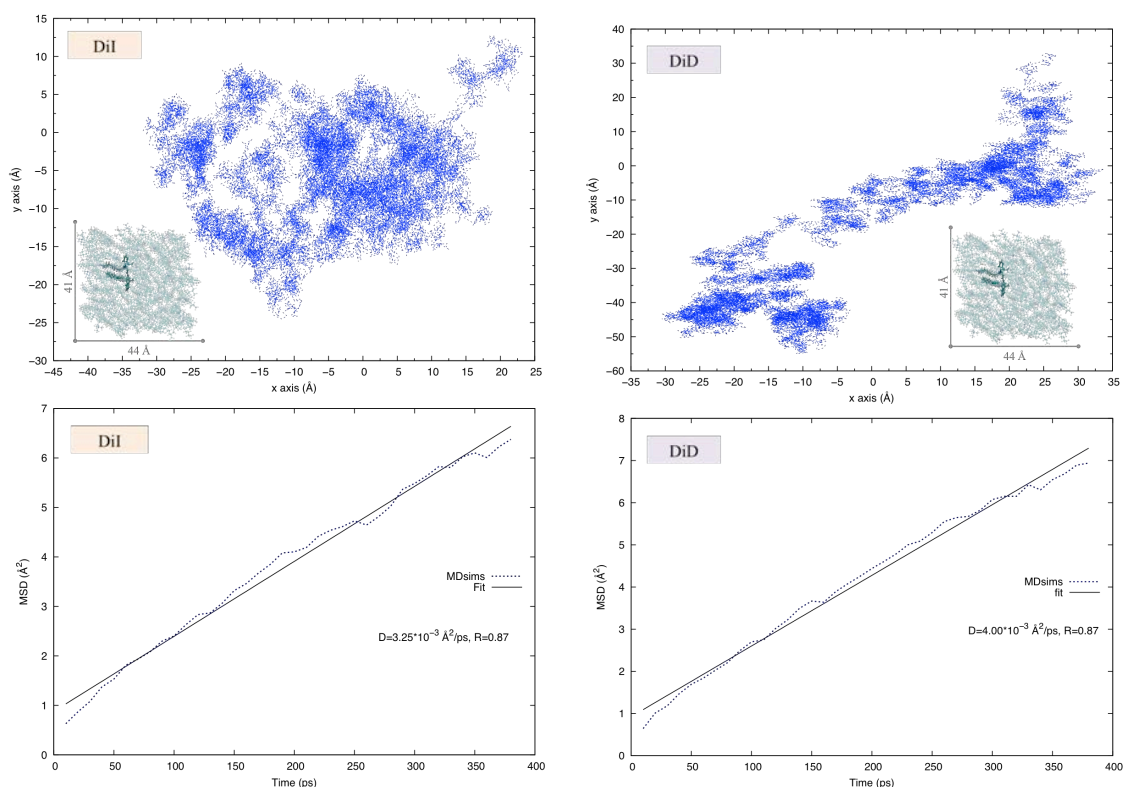


**Figure 6.7:** Top: Lateral diffusion of DiI and DiD dyes in the XY plane (the plane of the QS bilayer) during MD simulations of dyes in QS bilayers. Top panels: Trajectory of DiI and DiD (top), indicating the X,Y position of the central carbon of the carbocyanine each 10 ps during a 160 ns MD simulation. Bottom: MSD of the trajectory calculated over the trajectory of the top panel, averaged over blocks of 400 ps. We also show a linear fit of the MSD and the results of the fitting, which gives the lateral diffusion coefficient according to Einstein relation.

the presence of a dye inside the membrane. Finally we compare them with phospholipid molecules in a lipid bilayer and water.

Note that the diffusion coefficients are calculated averaging only the bilayer planar directions (X and Y), otherwise the vesicle would lose its stability. As seen in the Table 6.3, values of diffusion coefficient are in the order of  $10^{-11}$  m<sup>2</sup>/s, diffusing much slower than water molecules. Remarkably, we notice that the order of magnitude of the diffusion coefficient of a phospholipid lipid bilayer<sup>1</sup> is the same,  $10^{-11}$  m<sup>2</sup>/s, i.e. the value of the diffusion coefficient of DPPC is  $1.07 \times 10^{-11}$  m<sup>2</sup>/s and the DiI dye inside it is  $9.7 \times 10^{-12}$  m<sup>2</sup>/s<sup>10</sup>. Based on the fluid mosaic model<sup>21</sup>, phospholipid membranes must be in a fluid state for normal cell functioning. Thus, by comparing the given diffusion coefficients, one can affirm that QS

itself behaves as a fluid membrane, as phospholipids in liposomes. The fact that dyes are loaded in it does not change its diffusion and fluidity properties.

**Table 6.3: Diffusion coefficient values for the dyes, Quatsome (CTA<sup>+</sup>), water and phospholipid molecule in m<sup>2</sup>/s. The selected atom for the calculation of the diffusion coefficient for QS and water molecules are a hydrogen atom of the methyl group located on the bottom of the CTA<sup>+</sup> tail in the QS and the oxygen atom of a random water molecule selected, respectively.**

	Diffusion coefficient (m <sup>2</sup> s <sup>-1</sup> )
<b>DiI</b>	3.2 x 10 <sup>-11</sup>
<b>DiD</b>	4 x 10 <sup>-11</sup>
<b>CTA<sup>+</sup></b> (dye inside QS)	2.3 x 10 <sup>-11</sup>
<b>CTA<sup>+</sup></b> (no dye inside QS)	2.27 x 10 <sup>-11</sup>
<b>Phospholipid</b> <sup>1</sup>	1 x 10 <sup>-11</sup>
<b>water</b> <sup>15</sup> (TIP3P)	5 x 10 <sup>-9</sup>

### 6.2.3 DYE-DYE INTERACTION

In order to study the dye-dye interaction inside the QS membrane, we followed the strategy described below. Firstly, to build up a system made of a Quatsome membrane loaded with two DiI molecules or two DiD molecules, we took simulations S3 and S4 respectively, duplicated them and merged the result, giving simulations S5 and S6 respectively. In the case of S7 simulation, we merged simulations S3 and S4, and added two more patches of Quatsome membrane, to have the case of one DiI and one DiD molecule. In all cases it was required to run a 10 ps minimization in order to avoid the overlap between the QS components. Then, ~40 ns of simulation were run, using NPT ensemble with surface tension equal to zero. All the computational details are described in Table 6.4.

**Table 6.4: Composition of the systems considered in the MD simulations, including total number of atoms, ratio of the components of the system and simulation time.**

	Atoms (total)	Num. Molec. dyes/water/CTAB	Sim. Time	Size Box
<b>S5</b>	53892	2/12926/108	41.5 ns	32.2 nm <sup>2</sup> x 16 nm
<b>S6</b>	53696	2/12858/108	40.5 ns	32.1 nm <sup>2</sup> x 16 nm
<b>S7</b>	101248	2/23778/216	40.6 ns	91.2 nm <sup>2</sup> x 16 nm

## SIMULATIONS WITH TWO IDENTICAL DYES: DiI-DiI AND DiD-DiD

For both the DiI-DiI and DiD-DiD dye cases, both pairs are perfectly incorporated and interdigitated between QS components. Furthermore, they do not aggregate. Note that DiI dyes in DPPC phospholipid bilayer<sup>10</sup> also do not aggregate. This result is really important, because dye aggregation and interactions with QS could strongly limit their utility, substantially modifying the linear and nonlinear optical properties of the dyes<sup>8,4</sup>.

Results from DiI-DiI pair (S5 simulation) show that both dyes remain inside the QS membrane stable along simulation time, not deforming the membrane or aggregating between them. The calculated thickness (measured from the peaks of the nitrogen-nitrogen atom distance from CTAB distribution) did not change, as we obtained a value of 4.17 nm (same value as single dye at the QS (Figure 6.5)). From the density profile we also observed that the orientation of the bilayer components did not change when adding the two dyes. They show the same behaviour as in the case of a single dye. In Figure 6.8-(a), the DiI molecules inside the QS membrane are shown. As observed there, both dyes are located and oriented as expected, being the head groups at the water-surface interface and the tails completely immerse in the hydrophobic region of the membrane. Both dyes are not aggregated or close enough to interact with each other. As the interest of this simulation was to study the possible interaction between dyes within the membrane and such interaction does not happen, results of the behaviour of each individual dye are not commented because they are the same as those in simulation S3. Finally, we calculated the distance between both dyes as a function of time. Figure 6.8-(a) shows the distribution of distance of the central carbon atoms of both dyes, presenting a wide distribution, practically uniform between 4.2 - 4.7 nm.

Very similar results are obtained for the DiD-DiD pair (S6 simulation) inside the QS membrane. We observed stability of the whole system during time, and no interaction nor aggregation of both dyes. Thus, as explained before, the results of the behaviour of individual dyes are analogous to those in simulation S4. Nevertheless, the thickness of the

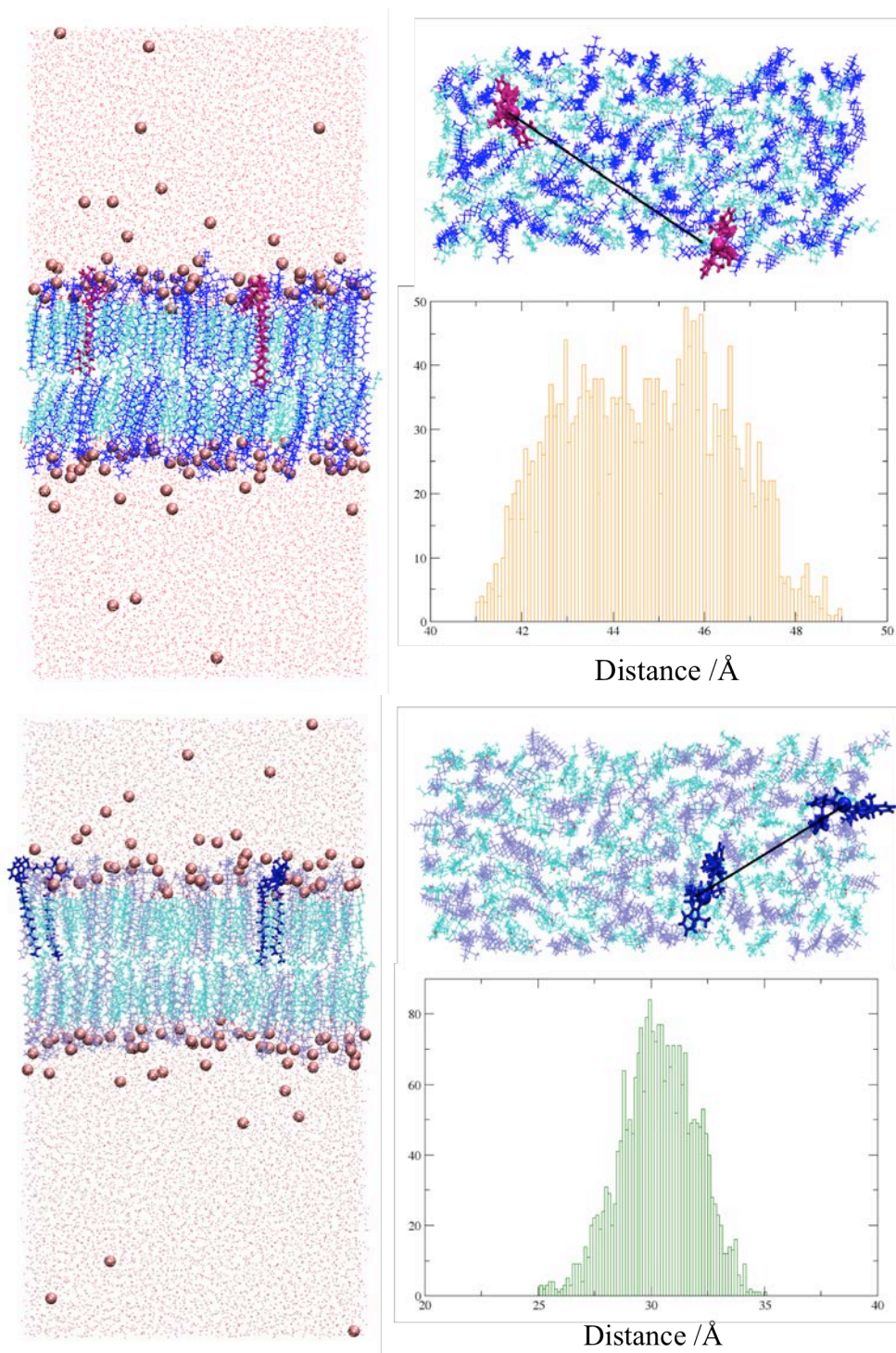


Figure 6.8: Two snapshots of the Quatsome membrane (front and top view) showing both components CTA<sup>+</sup> and cholesterol in blue and cyan, respectively for (a) panel and grey and cyan for (b) panel. Bromide counterions are represented in pink spheres and the two DII and DID dyes are in licorice representation in magenta and dark-blue colour, respectively. The distribution of the distance of the bond of the center of mass of the chromophore part of the dyes is plotted in both cases.

membrane slightly increased to a value of 4.26 nm, and the distance distribution obtained is a bit different. As shown in Figure 6.8-(b), a Gaussian distribution is obtained, with a peak at  $\sim 3$  nm.

We concluded that the relatively long carbon alkyl chain of the DiI or DiD dyes are permitted, energetically, to cross the center of the bilayer and extend into the opposite leaflet (see Figure 6.8). Stable location of dyes in one leaflet is caused by the chromophore's and the QS surface's positive charge, as no tendency to flip to the opposite leaflet is observed.

### SIMULATION WITH DII-DID DYES

In the case of the DiI-DiD pair, the thickness value is 4.32 nm, in comparison to the QS membrane alone (4.3 nm value calculated in Chapter 3). It is a consistent result as we do not observe any deformation of the membrane. However, we do see aggregation between dyes.

It must be highlighted that at the beginning of the simulation run both dyes were separated, located at a random point inside the QS membrane, and after equilibration they moved towards each other. Once being close, they remained in that relative position until the end of the simulation, diffusing together through the Quatsome membrane, as shown in Figure 6.9.

This figure shows two favourable and most probable configurations when dyes are aggregated. Tails appear always together, but the head groups can be either attracted or repelled. With the word attracted we refer to the fact that the headgroups are interacting, appearing together. And with the word repelled we refer to the fact that the headgroups are not interacting, appearing separated. This is due to their positive charge distributed in the head group. Figure 6.9-(b) shows the attracted case and 6.9-(a) the repelled case. The pair distance showed a typical equilibrated value of  $\sim 8.9$  Å, although we observed values of  $\sim 12$  Å corresponding to the case when head groups are repelling. The zoomed snapshots

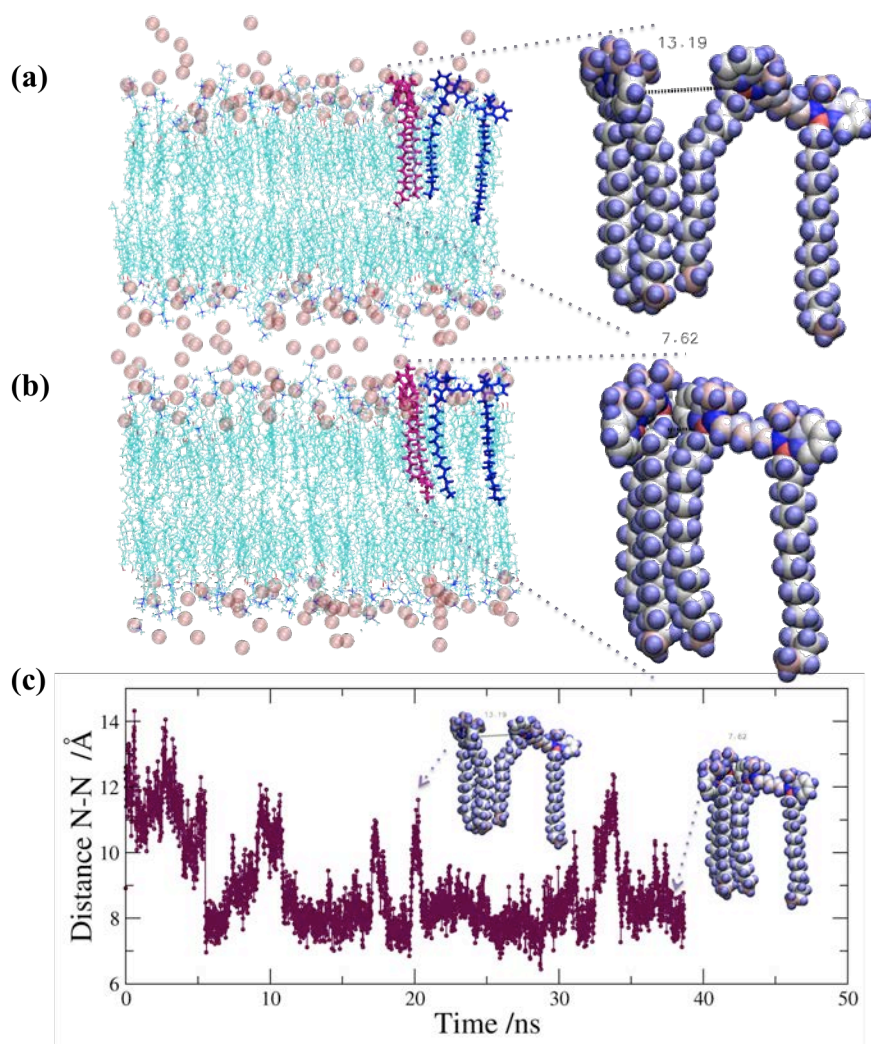


**Figure 6.9:** Two examples of the DiI-DiD pair orientation inside the QS bilayer. Snapshots of the QS membrane with both dyes inside; DiI (pink) and DiD (blue), with a zoomed image next to it. Both zoomed snapshots of the dyes are in Van der Waals radii representation showing their charge distribution. Also, two graphs are associated in each orientation panel in order to show the distance between the N-N (charged) between both head groups of the dyes.

in the figure not only show the configuration of the dyes but its charge distribution (charge scheme is the same as in Figure 6.2). We show also the bond distance of the N-N of both dyes with respect to time.

In order to calculate how strong this interaction is, we calculated the PMF between each dyes, considering the nitrogen-nitrogen atom distance from CTAB as generalized coordinates. Figure 6.10 shows that big force (up to  $\sim 25$  kcal/mol) is needed to separate both



dyes' head groups more than  $\sim 16$  Å and tails show resistance to being separated.

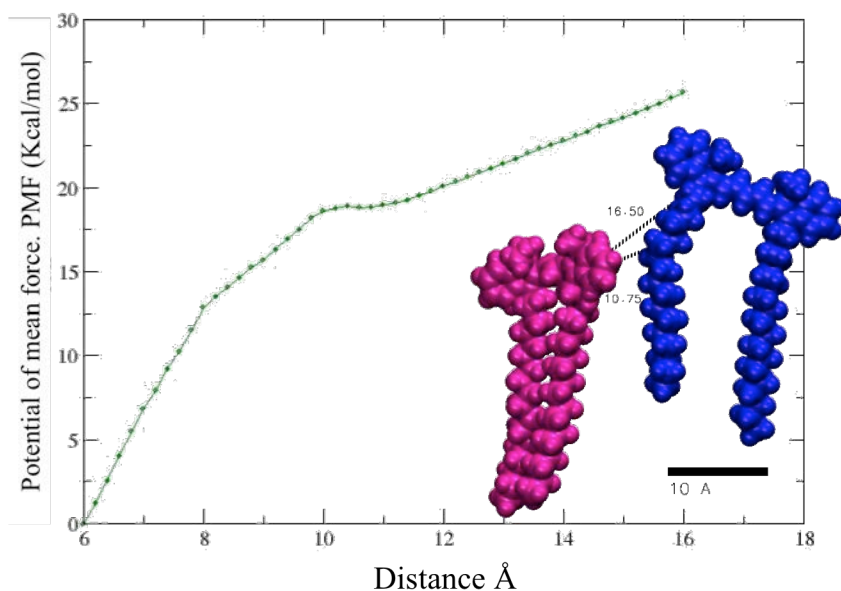


**Figure 6.10:** PMF between N-N bond of both dyes. Molecules are in Van der Waals radii representation and painted in blue and pink for the DiD and DiI dye, respectively.

The fact that both dyes with different length in the chromophore part are interacting or aggregating, can have an impact regarding the optical properties of the dyes. When two dyes are close enough to each other they can exchange energy by RET (Fluorescent Energy Transfer)<sup>13,12</sup>, and the emission can occur from one of many independently moving (or oriented) molecules. These process occurs without emission of a real photon, exchanging a virtual photon, as a result of dipole-dipole interaction between the donor and acceptor. In our case with the DiI dye is the donor and the DiD dye is the acceptor.

This phenomenon is interesting due to its potential for designing multicolor fluorescent nanoparticles for bioimaging, for instance to visualize specific targets from complex living cells<sup>17,6,16</sup>. Nevertheless, the exact mechanism of these phenomena (RET) is under investigation, as it is unclear how both donor-acceptor dyes interact for this emission to occur. A theory developed by Painelli et al.<sup>24</sup> predicts that the dye that acts as donor is excited, in which the positive charge is located in one of the nitrogen atoms of the head group obtaining two degenerate states, and the dye that acts as acceptor is in its ground state, having the

positive charge located in the center of mass of the chromophore part<sup>26,25</sup>.

Thus, according to this theory, in order to understand if energy transfer phenomena occurs in our system, the distance between donor-acceptor seems critical. For this reason we have computed that value during our simulations, shown in Figures 6.8 and 6.9. Thus, the theory suggests that the distance between chromophores should be calculated between one nitrogen atom of the head group and the center of mass of the chromophore part. We have considered both nitrogen atoms and results are plotted in Figure 6.11. Both nitrogen atoms (N1 and N2) have an average distance of 1.3 nm to the center of mass of the chromophore part, obtaining equal values but different distributions of distance with time. This average distance is almost the double of the that one calculated for the N-N bond distance (0.89 nm), as shown in Figure 6.11.

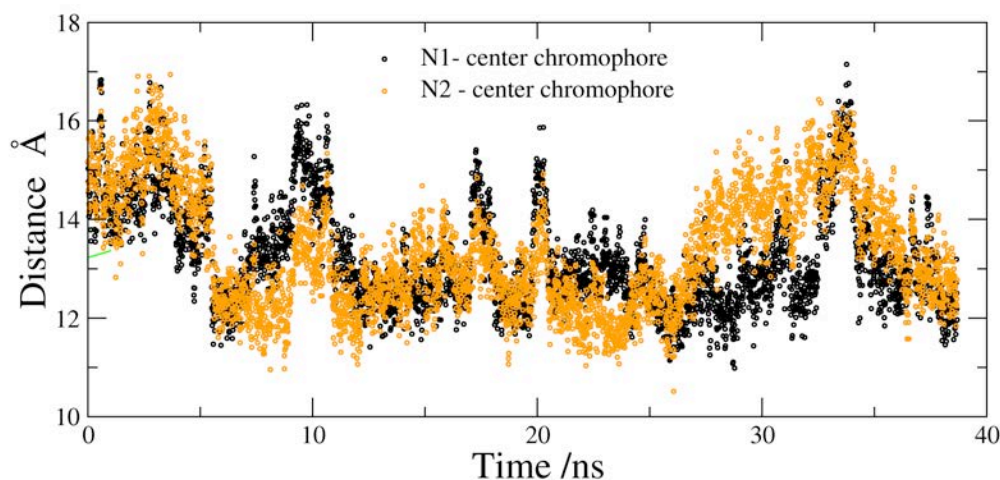


**Figure 6.11:** Distance of the nitrogen atom of the DiI dye (donor) and center of mass of the chromophore part of the DiD dye (acceptor) with time. As DiI dye presents two nitrogen atoms in its head group, it has been considered both possible bonds with the DiD (donor).

#### 6.2.4 EXPERIMENTAL RESULTS

The results of our MD simulations are supported by experiments developed in collaboration with Nanomol group (ICMAB-CSIC) and Dr. Lorenzo Albertazzi at the Institut de Bioenginyeria de Catalunya (IBEC). Those experiments include the synthesis, in which

different methodologies for the preparation of the Quatsome system loaded with dyes are considered, the characterization of the system, and a technique called stochastic optical reconstruction microscopy (STORM, an innovative super-resolution microscopy technique<sup>30</sup>). All this experimental work has been done with the aim of exploring the potential of the dye-loaded QS for biological imaging.

All the experimental results reported and discussed in ref.<sup>2</sup> show that, taking advantage of the non-covalent interaction between the aliphatic chains of the dyes (the carbocyanines) and the hydrophobic compartment of Quatsomes bilayer, it is possible to solubilize DiI and DiD hydrophobic dyes with long alkyl chains in water, by incorporating them into Quatsomes (Figure 6.12-B). Dye-loaded QS can be prepared in a one-step method using compressed CO<sub>2</sub>, DELOS-SUSP<sup>5</sup> method (Figure 6.12-A), showing several advantages over conventional routes for the preparation of functionalized vesicles like sonication (Figure 6.12-C).

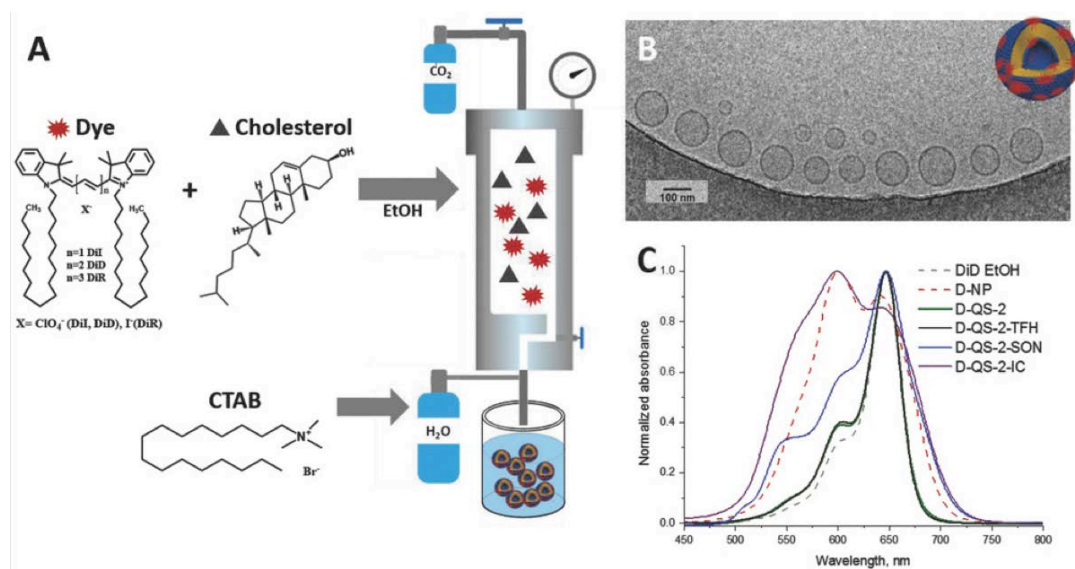


Figure 6.12: A) Schematic representation of the DELOS-SUSP method for the preparation of QS loaded with dyes (DiI and DiD), B) Cryo-TEM image of DiD-QS and C) absorption spectra of DiD in ethanol solvent (EtOH) and DiD-QS prepared by different methods; thin film hydration (TFH), sonication (SON) and incubation (IC) Note: 'D-QS-2' is the code used by the experimentalist, for a specific loading of the DiD dye in the QS bilayer. Figure adapted from ref.<sup>3</sup> with permission from the Wiley-VCH.

The absorption spectra of DiD-loaded QS obtained by DELOS-SUSP and by thin film hydration (THF) are very similar to the spectra of solvated DiD in ethanol solvent, showing a narrow band with well-determined vibronic structure. In Figure 6.12, all the other samples show a broad spectrum with the appearance of intense features on the blue wing of the band, pointing to the formation of H-aggregates<sup>19</sup>. The similarity of spectra of DiD-loaded QS prepared by DELOS-SUSP and TFH methods suggests that the dye molecules are well dispersed as isolated species inside the QS membrane.

DiD-loaded QS are colloiddally stable during months, with no appreciable changes in size distributions, nor in absorption or emission spectra over a 2 month period (Figure 6.13). In terms of size particle, despite samples with DiI are bigger than samples of QS without DiI dye, they are stable, their size not changing. Polydispersity index (Pdi) changes exactly the same in both samples (with and without dye) after 2 months. Similarly, the variation of the  $\zeta$ -potential after 2 months is more or less the same for both samples; both values decrease, probably due to the dilution of big particles. Values are reported in Table 6.5.

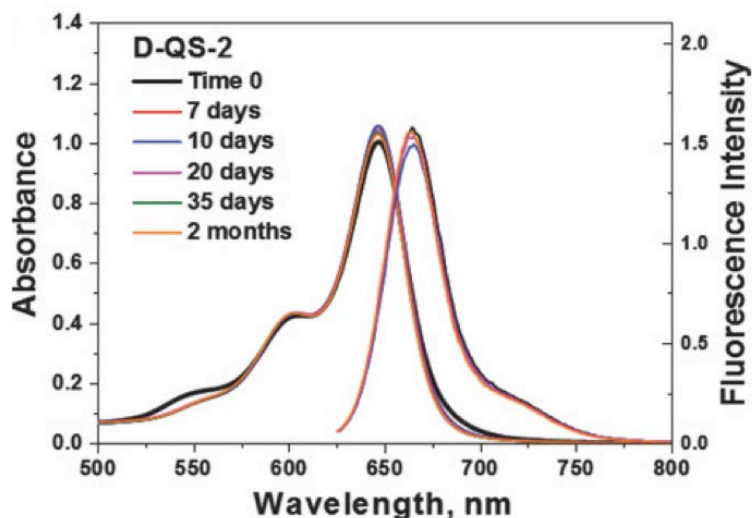


Figure 6.13: A) Stability of the DiD-QS sample in water evaluated by UV-Vis absorption and emission spectra ( $\lambda_{exc} = 610$  nm) monitored over 2 months. Figure reproduced from ref.<sup>3</sup> with permission from the Wiley-VCH.

**Table 6.5: Size and Z-potential of Quatsome samples with and without DiI dye.**

	Z-average (d.nm)		Pdi		Z-potential	
	0 days	2 months	0 days	2 months	0 days	2 months
<b>QS</b>	77.23	77.61 ± 29	0.457	0.414	93.5	88.9 ± 7.8
<b>QS-DiI</b>	95.53	95.77 ± 33	0.136	0.14	43.6	36.7 ± 5.1

Within this context, it was possible to explore the potential of dye-loaded QS for imaging. In particular, we demonstrated that thanks to their colloidal and photochemical stability and to the photophysical properties, they can be used as probes for STORM superresolution microscopy.

The analysis of the images at molecular level provided quantitative information about the size of the vesicles and a rough estimation of the number of dyes localized in each vesicle (see Figure 6.14-A). The size distribution obtained by analyzing the STORM images (Figure 6.14-B) reveals that the mean size of resolved Quatsomes (6137 in total) is around 99 nm, the mode is around 85 nm and very few vesicles have sizes higher than 200 nm. Comparing these values with the sizes of the vesicles detected by the cryo-TEM images, Quatsomes appear a bit smaller under the electron microscope.

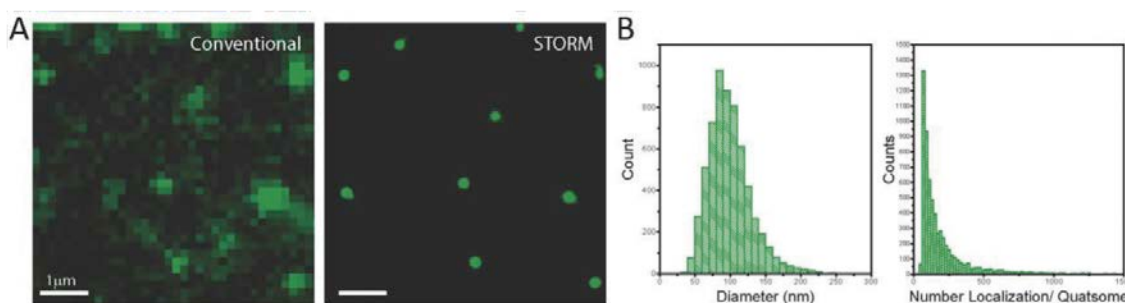


**Figure 6.14: A)** Images of DiI-loaded QS obtained by conventional wide-field microscopy and STORM ( $\lambda_{exc} = 561$  nm). **B)** Distribution of size and number of localizations per QS extrapolated from STORM images.

As a closure for this chapter, we want to point out that all the presented results lead us to the conclusion that all-atomic MD simulations are a feasible method to determine precise dye locations in QS bilayer. This information cannot be determined by means of experimental tests. Our simulation results are also consistent with the experimentally-observed enhancement of fluorescence of DiI and DiD dyes upon incorporation into membranes. Overall, it has been shown that a family of non-water fluorophores, the carbocyanines (DiI and DiD), can be stabilized in aqueous media by means of their incorporation inside the Quatsome membrane, obtaining a potential class of nanostructured systems with excellent optical and colloidal properties.



# References

- [1] Almeida, P. F. F. & Vaz, W. L. C. (1995). Chapter 6 - Lateral Diffusion in Membranes. In R. Lipowsky & E. Sackmann (Eds.), *Handbook of Biological Physics* (pp. 367–373). Amsterdam: Elsevier Science.
- [2] Ardizzone, A. (2017). *New fluorescent nanovesicles, by self-assembly of organic fluorophores, sterols and surfactants, as probes for bioimaging*. PhD thesis, Institut de Ciència de Materials de Barcelona (ICMAB-CSIC).
- [3] Ardizzone, A., Kurhuzenkau, S., Illa-Tuset, S., Faraudo, J., Bondar, M., Hagan, D., Van Stryland, E. W., Painelli, A., Sissa, C., Feiner, N., Albertazzi, L., Veciana, J., & Ventosa, N. (2018). Nanostructuring Lipophilic Dyes in Water Using Stable Vesicles, Quasomes, as Scaffolds and Their Use as Probes for Bioimaging. *Small*, 14(16), 1703851+.
- [4] Bangbelu, A., Wang, J., & Leszczynski, J. (2010). TDDFT Study of the Optical Properties of Cy5 and Its Derivatives. *The Journal of Physical Chemistry A*, 114(10), 3551–3555.
- [5] Cano-Sarabia, M., Ventosa, N., Sala, S., Patiño, C., Arranz, R., & Veciana, J. (2008). Preparation of Uniform Rich Cholesterol Unilamellar Nanovesicles Using CO<sub>2</sub>-Expanded Solvents. *Langmuir*, 24(6), 2433–2437.
- [6] Clapp, A. R., Medintz, I. L., Mauro, J. M., Fisher, B. R., Bawendi, M. G., & Matoussi, H. (2004). Fluorescence Resonance Energy Transfer Between Quantum Dot Donors and Dye-Labeled Protein Acceptors. *J. Am. Chem. Soc.*, 126(1), 301–310.
- [7] Frisch (2009). *Gaussian 09*. Gaussian, Inc., Wallingford CT.
- [8] Giesecking, R. L., Mukhopadhyay, S., Shiring, S. B., Risko, C., & Brédas, J.-L. (2014). Impact of Bulk Aggregation on the Electronic Structure of Streptocyanines: Implications for the Solid-State Nonlinear Optical Properties and All-Optical Switching Applications. *The Journal of Physical Chemistry C*, 118(41), 23575–23585.
- [9] Grimaldi, N., Andrade, F., Segovia, N., Ferrer-Tasies, L., Sala, S., Veciana, J., & Ventosa, N. (2016). Lipid-based nanovesicles for nanomedicine. *Chemical Society Reviews*, 45(23), 6520–6545.
- [10] Gullapalli, R. R., Demirel, M. C., & Butler, P. J. (2008). Molecular dynamics simulations of DiI-C18(3) in a DPPC lipid bilayer. *Physical Chemistry Chemical Physics*, 10(24), 3548–3560.



- [11] Hu, H., Lu, Z., & Yang, W. (2007). Fitting Molecular Electrostatic Potentials from Quantum Mechanical Calculations. *Journal of Chemical Theory and Computation*, 3(3), 1004–1013.
- [12] Jovin, T. M. & Arndt-Jovin, D. J. (1989). *FRET Microscopy: Digital Imaging of Fluorescence Resonance Energy Transfer. Application in Cell Biology*, (pp. 99–117). Elsevier.
- [13] Lakowicz, J. R. (2006). *Principles of Fluorescence Spectroscopy*. University of Maryland School of Medicine: Springer.
- [14] Li, Q., Liu, L., Liu, J.-W., Jiang, J.-H., Yu, R.-Q., & Chu, X. (2014). Nanomaterial-based fluorescent probes for live-cell imaging. *TrAC Trends in Analytical Chemistry*, 58, 130–144.
- [15] Mark, P. & Nilsson, L. (2001). Structure and Dynamics of the TIP3P, SPC, and SPC/E Water Models at 298 K. *The Journal of Physical Chemistry A*, 105(43), 9954–9960.
- [16] McDonald, T. O., Martin, P., Patterson, J. P., Smith, D., Giardiello, M., Marcello, M., See, V., O'Reilly, R. K., Owen, A., & Rannard, S. (2012). Multicomponent Organic Nanoparticles for Fluorescence Studies in Biological Systems. *Advanced Functional Materials*, 22(12), 2469–2478.
- [17] Medintz, I. L., Clapp, A. R., Mattoussi, H., Goldman, E. R., Fisher, B., & Mauro, J. M. (2003). Self-assembled nanoscale biosensors based on quantum dot FRET donors. *Nature Materials*, 2(9), 630–638.
- [18] Menon, J. U., Jadeja, P., Tambe, P., Vu, K., Yuan, B., & Nguyen, K. T. (2013). Nanomaterials for Photo-Based Diagnostic and Therapeutic Applications. *Theranostics*, 3(3), 152–166.
- [19] Monopoli, M. P., Åberg, C., Salvati, A., & Dawson, K. A. (2012). Biomolecular coronas provide the biological identity of nanosized materials. *Nature Nanotechnology*, 7(12), 779–786.
- [20] Sercombe, L., Veerati, T., Moheimani, F., Wu, S. Y., Sood, A. K., & Hua, S. (2015). Advances and Challenges of Liposome Assisted Drug Delivery. *Frontiers in Pharmacology*, 6.
- [21] Singer, S. J. & Nicolson, G. L. (1972). The Fluid Mosaic Model of the Structure of Cell Membranes. *Science*, 175(4023), 720–731.
- [22] Spiriti, J., Binder, J. K., Levitus, M., & van der Vaart, A. (2011). Cy3-DNA Stacking Interactions Strongly Depend on the Identity of the Terminal Basepair. *Biophysical Journal*, 100(4), 1049–1057.
- [23] Spiriti, J. M. (2011). *Applications of adaptive umbrella sampling in biomolecular simulation*. PhD thesis, Arizona State University, Tempe, Arizona.

- 
- [24] Terenziani, F., Painelli, A., Katan, C., Charlot, M., & Blanchard-Desce, M. (2006). Charge Instability in Quadrupolar Chromophores: Symmetry Breaking and Solvatochromism. *Journal of the American Chemical Society*, 128(49), 15742–15755.
- [25] Terenziani, F., Przhonska, O. V., Webster, S., Padilha, L. A., Slominsky, Y. L., Davydenko, I. G., Gerasov, A. O., Kovtun, Y. P., Shandura, M. P., Kachkovski, A. D., Hagan, D. J., Van Stryland, E. W., & Painelli, A. (2010). Essential-State Model for Polymethine Dyes: Symmetry Breaking and Optical Spectra. *The Journal of Physical Chemistry Letters*, 1(12), 1800–1804.
- [26] Terenziani, F., Sissa, C., & Painelli, A. (2008). Symmetry Breaking in Octupolar Chromophores: Solvatochromism and Electroabsorption. *The Journal of Physical Chemistry B*, 112(16), 5079–5087.
- [27] Texier, I., Goutayer, M., Da Silva, A., Guyon, L., Djaker, N., Josserand, V., Neumann, E., Bibette, J., & Vinet, F. (2009). Cyanine-loaded lipid nanoparticles for improved in vivo fluorescence imaging. *Journal of Biomedical Optics*, 14(5), 054005+.
- [28] Vanommeslaeghe, K., Hatcher, E., Acharya, C., Kundu, S., Zhong, S., Shim, J., Darian, E., Guvench, O., Lopes, P., Vorobyov, I., & Mackerell, A. D. (2009). CHARMM general force field: A force field for drug-like molecules compatible with the CHARMM all-atom additive biological force fields. *Journal of Computational Chemistry*, 31(4), NA.
- [29] Wagh, A., Qian, S. Y., & Law, B. (2012). Development of Biocompatible Polymeric Nanoparticles for in Vivo NIR and FRET Imaging. *Bioconjugate Chemistry*, 23(5), 981–992.
- [30] Zhuang, X. (2009). Nano-imaging with STORM. *Nature Photonics*, 3(7), 365–367.

*Sciences provide an understanding of a universal experience, Arts are a universal understanding of a personal experience... they are both a part of us and a manifestation of the same thing... the arts and sciences are avatars of human creativity*

Mae Jemison

# 7

## Conclusions and Perspectives

### 7.1 GENERAL CONCLUSIONS

In this PhD thesis, we have investigated the Quatsome vesicular system via MD simulations, with the aim of getting a detailed insight about this system and its interactions with other organic molecules, like dyes, at an atomistic and molecular level. Along this research, we have developed the sought deep understanding about the physico-chemical properties of the Quatsome, as well as important insight about its applicability for imaging. We have presented the conclusions of our results in each chapter, but we want to summarize here the most important ones.

In the beginning, we considered a planar bilayer of a novel system, made of surfactant (CTAB) and sterol (Chol) molecules: the Quatsome. Previous atomistic simulations of this system had revealed the synergy between the CTA<sup>+</sup> (of CTAB) and the cholesterol molecules, making them self-assemble into bimolecular amphiphiles (called synthons), and then into bilayers. By all-atomic simulations, we obtained the most relevant physicochemical properties of the system, at the maximum spatial resolution. The observed molecular organization of the components explains the robustness and stability of the system, as it remains stable under variations, for example the presence of tension or salt, or the increase in temperature. We have observed the existence of asymmetries in the tilt angle of the components of the bilayer, which has also been seen in other cationic systems as well as in experimental AFM measurements of the QS. We believe that this phenomenon could be related to the spontaneous curvature of the bilayers of thermodynamically stable vesicles.

We developed a Martini coarse-grained force field for the CTAB<sup>6</sup>. We simulated a full Quatsome vesicle via coarse-grained simulations (for the first time to the best of our knowledge). From the results we conclude that the presence of defects in the bilayer is the responsible for the curvature in it. This is in line with the theory, that requires an asymmetry for the existence of spontaneous curvature. Without such asymmetry, we would expect to see disc-shaped bilayers instead of vesicles.

In the second part of the thesis, we have investigated the interaction of the Quatsome with dyes. We developed a force field for the fluorescein molecule, and based on the MD simulations using such force field, we conclude that the strategy to nanostructure the anionic fluorescein dye on the surface of the QS in water (taking advantage of the cationic head of the CTAB molecules) is a good initial strategy to functionalize the surface of our vesicle. Despite the existence of electrostatic interaction between fluorescein molecules and Quatsome surface, there is a competition between such attraction and the tendency of fluorescein

to aggregate in water, resulting in very few dye molecules attaching to the QS surface. This compromises the integrity and suitability of the resulting fluorescent organic vesicles for applications with imaging purposes. All this suggests that the search of other strategies for nanostructuring of dyes is required, for instance considering dyes of hydrophobic nature. The MD simulations reported in chapter 6 show that a family of non-water soluble fluorophores, the carbocyanines (DiI and DiD), can be stabilized in aqueous media by incorporating them to the Quatsome, obtaining a potential class of nanostructured systems with excellent optical and colloidal properties. Our simulation results are consistent with the experimentally-observed enhancement of the incorporation of DiI and DiD into membranes. In addition, we want to highlight that MD simulations are a suitable method to determine precise dye positioning in the Quatsome bilayer, and that this information is not reachable by means of experimental tests.

By all the previously explained, we consider that the initial goal of the thesis, to deepen the overall understanding of the Quatsome vesicular system and some of its applications, has been fulfilled.

### 7.2 PERSPECTIVES AND ONGOING WORK

The present thesis has opened many perspectives for future work. In fact, we started a preliminary exploration of several possible extensions of the present work in the following directions. A summary is explained: the self-assembly mechanism for Quatsome vesicle formation and the possibility of changing the Quatsome components, using other surfactant or other sterol.

### 7.2.1 SELF-ASSEMBLY OF QUATSOME VESICLE

In chapter 4 of this thesis we performed a simulation where we obtained a stable full Quatsome vesicle. Furthermore, it has been experimentally proven (by Nanomol group) that when CTAB and cholesterol molecules are dispersed in aqueous solution, they tend to spontaneously self-assemble into vesicles of various sizes, due to their hydrophobic and hydrophilic segments. This two facts encouraged us to simulate the self-assembly process, to obtain more information of the stabilization mechanism. For that, we performed coarse-grain MD simulations with CTAB and cholesterol molecules randomly distributed in aqueous media (1:1 ratio and employing the same computational details as in chapter 4), to see if the system would evolve towards the formation of a vesicle. Preliminary results are shown in Figure 7.1 and 7.2.

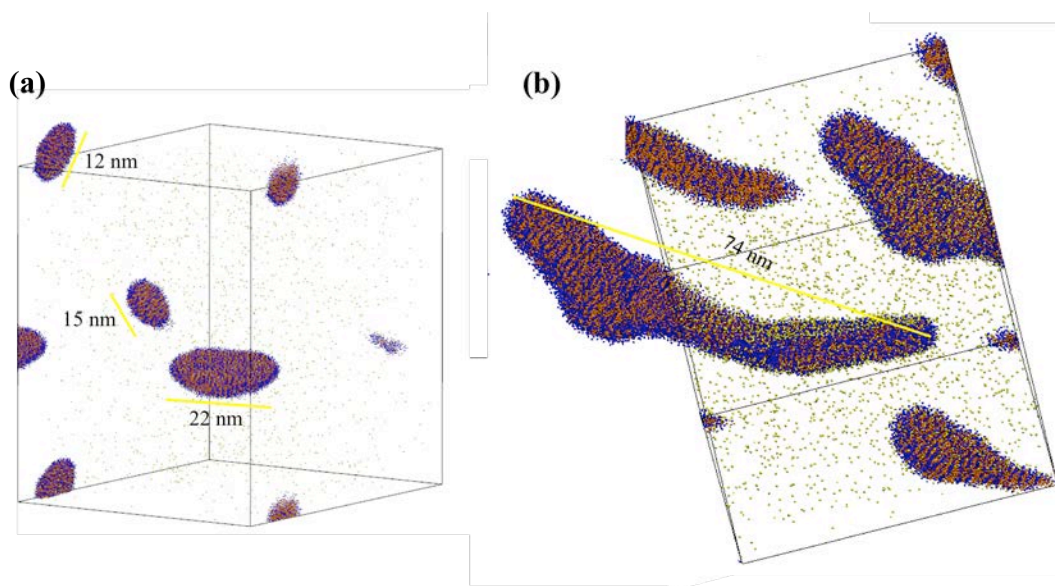


**Figure 7.1:** (a)-(b) Simulation snapshot of the final equilibrated configuration of the system. Box size for (a) 65x78x78 nm and (b) 44x42x42 nm. CTAB molecules are colored in blue, cholesterol molecules in orange and bromide ion in yellow. Boundary conditions applied for the to reconstruct the images.

Firstly, we considered the same number of CTAB and Chol molecules (2197 each component) as in the simulation of a full QS vesicle (chapter 4). After 9  $\mu$ s of simulation time, we obtained 3 disk-like micelles with a diameter size ranging in  $\sim$ 12-22 nm as shown in

Figure 7.1-(a). After longer simulation time, we concluded that the system had reached an equilibrium state or the dynamics of the system were too slow. Thus, we decided to increase the concentration of the same system, by considering a simulation box of 32x33x36 nm, but the system reached a planar bilayer patch connected to itself due to the boundary conditions, so we discarded it. Secondly, we doubled the number of component molecules, so we made up a system of 4123 CTAB and 4123 cholesterol molecules. In this case, we obtained a final configuration after 603 ns, in which all the molecules were together forming a long deformed bilayer, with certain curvature and a length of of 74 nm (see Figure 7.1-(b)). Finally, we increased the number of QS components up to 8748 of CTAB and 8748 of cholesterol molecules. We obtained similar results as in the previous case, a final meta-stable state in which all molecules were together forming irregular shapes with curvature (see Figure 7.2-(c)).

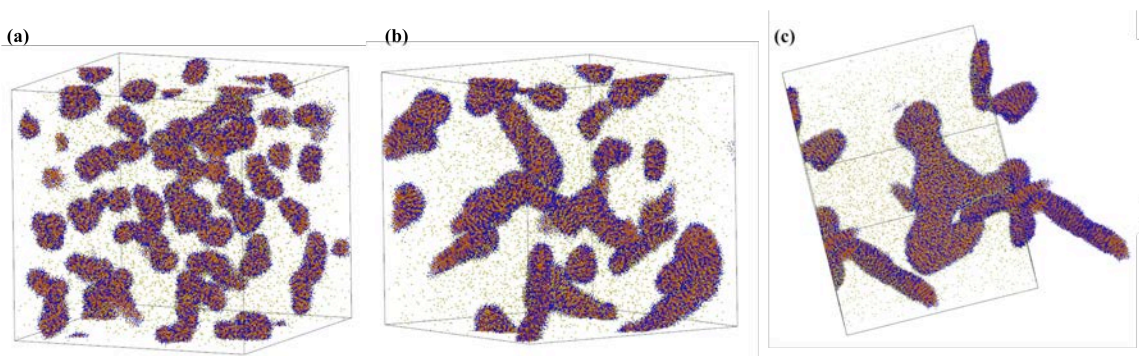


**Figure 7.2:** Simulation snapshots of the formation of the big-assemble made of CTAB and Chol molecules in a cubic box of 54x54x54 nm. Image (c) boundary conditions applied for the to reconstruct the images.

All run simulations have in common that, spontaneously, the components of the QS preferred to interdigitate forming those unilamellar structures, rather than aggregate forming micelles of CTAB or cholesterol crystals. Also, as shown in the Figure 7.2, from the MD trajectories we observed how CTAB and cholesterol molecules rapidly assembled into small mixed micelles and then they started fusing into elongated micelles. Those micelles started fusing between them too, reaching a final state in which all the molecules considered for the simulated system were assembled into a big structure with a non-defined morphology.

As far as we have observed in the CG-MD trajectories, the system is in a meta-stable state. A certain curvature is observed, but there is no clear indication that the bilayer will close into a vesicle. There are three most probable possibilities: the first one is that the vesiculation leads to a thermodynamically stable vesicle<sup>4</sup>. In that case, our simulations would still be in an early stage of the process, and more simulation time would be required to see the vesiculation. The second possibility is that the formation process leads to a kinetically stable vesicle<sup>3</sup>, so the bilayer in our simulations would be in an energy well, and some extra energy would be needed for the vesicle closure. The third scenario would be related to the limitations of coarse-grained method or the employed component models<sup>6</sup>.

About the mentioned limitations, it is well known that Martini coarse-grained simulations<sup>8</sup> reproduce well the  $\Delta G$  energy value. However, the model can consider contributions on  $\Delta G$  that should be in the  $\Delta H$ . Thus it induces to generate configurations with lower entropy, and that is why the solvent in Martini can crystallize and we have to consider adding anti-freezing water molecules to overcome this problem. As the entropy of the system is a fixed value due to the CG approximations, one thing that can be done is to increase the temperature of the system.

As we did not reach a proper vesicles as final structures from our simulations, we considered increasing the temperature in order to increase the entropy of the system. We

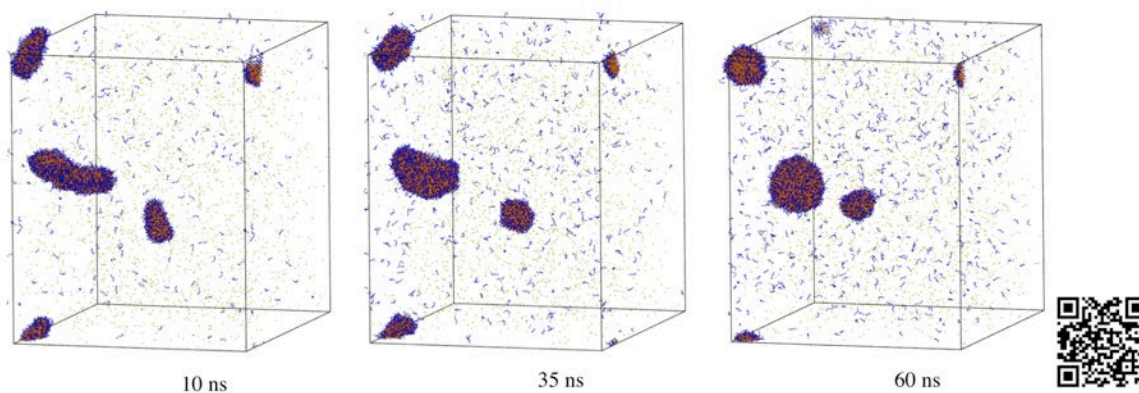


**Figure 7.3:** Simulation snapshots of the self-assembly of the Quatsome vesicles from a disk-like micelles configuration. Temperature of the system 503.15 K. The QR code shows the vesiculation of the Quatsome vesicles.



considered the last configuration of the first case of study, the one corresponding to Figure 7.1-(a) and raised the temperature from 298 K up to 503.15 K. Automatically, we observed how the system relaxes and some CTAB molecules evaporates. The three disk-like micelles evolve to spherical vesicles as expected (see Figure 7.3).

We compare the lamellar-to-vesicle transformation process of the Quatsome system to a pre-equilibrated POPC bilayer (361 lipids per leaflet)<sup>1</sup>. This simulation started from a regular planar equilibrated bilayer conformation, and then considered a bigger simulation box, so that the bilayer would not be in contact with itself (through the simulation box limits), with the aim of observing a lamellar-to-vesicle transformation process (as shown in Figure 7.3). Whereas in our case, we start from a disk-like micelles configurations. Lipid headgroups rapidly replaced the lipid tails exposed at the edges of the bilayer patch to form a bicellar intermediate (snapshot at  $t = 10$  ns). A rather fast closure of the bicelle followed ( $t = 60, 70$  ns) to form a small vesicle ( $t = 100$  ns). We observed the same behaviour with the Quatsome system but with less simulation time as shown in Figure 7.3. This process of vesicle formation is identical to that described for standard Martini<sup>7</sup>.

Although there are no concluding results yet, the gathered evidence so far leads us

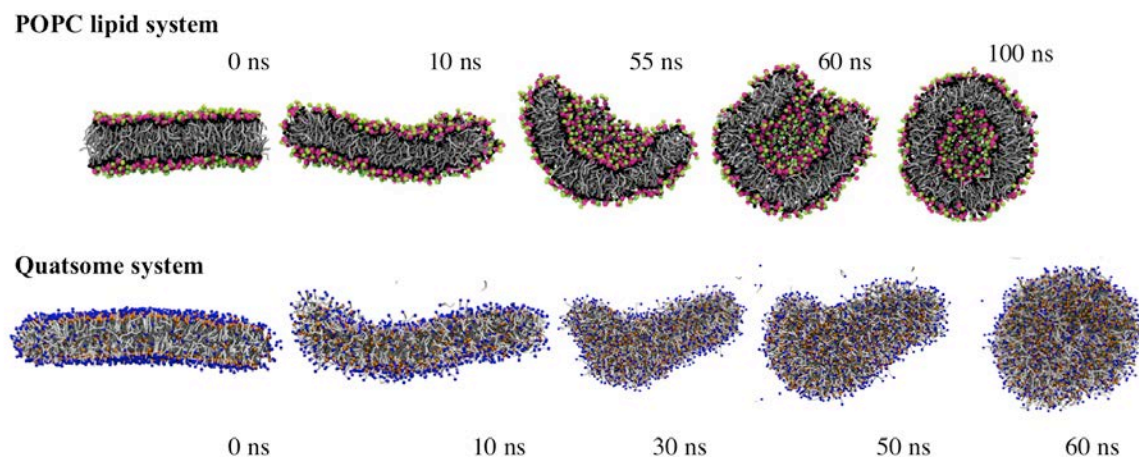


**Figure 7.4:** Lamellar-to-vesicle transition for POPC lipid and Quatsome system. Figure of the POPC lipid system is adapted from ref.<sup>1</sup> with permission from The American Chemical Society, whereas the snapshots from the transition of the Quatsome system are from our MD simulations.

think that we are in the first scenario: a vesiculation process that leads to thermodynamically stable Quatsome vesicles. Preliminary experimental evidences obtained by Nanomol group (Dra. Mariana Kober, Dra. Lidia Ferrer-Tassies and Dra. Nora Ventosa) are the following. Quatsomes can be obtained following different preparation routes. It seems that size distributions, vesicle morphology and  $\zeta$ -potential, are practically identical when QS were prepared using ultrasounds (US) and the depressurization of a CO<sub>2</sub>-expanded liquid (DELOS-SUSP). Also, the Quatsome formation is reversible, meaning that QS rupture and re-formation can be controlled by varying the volume fraction of ethanol in the dispersant. Finally, Quatsomes are stable in time. For QS dispersed in water the temporal stability is truly remarkable. Evidence from our MD simulations remarks the stability of the QS bilayer, both in a planar bilayer and in a vesicle shape. We have seen asymmetries in the leaflets and the QS synthon is maintained during the full vesicle simulation.

This ongoing work is one of the most interesting perspectives of this thesis and intense work is being done.

### 7.3 CHANGING THE SURFACTANT: MKC

For applications involving intravenous administration, the CTAB is not a suitable surfactant due to its toxicity<sup>10</sup>. In order to be able to use Quatsomes for this type of applications, an interesting option is being considered. In particular, we started to explore the case of vesicles made of tetradecyldimethylbenzylammonium chloride (MKC) surfactant and cholesterol (see Figure 7.5-(a)).

Experiments done by Nanomol group (Guillem Vargas and Dr. Nora Ventosa), showed that the presence of salt in solution (NaCl) is essential to achieve stable vesicles made of Chol/MKC, but also that an excess of salt makes the vesicles unstable. Hence, these cationic vesicles can exist only in a certain, appropriate range of salt concentration ( $\sim$ 100-300 mM of NaCl, see Figure 7.5-(b)). At 0 mM of NaCl, unstable elements of more than one population (vesicles and tubular structures) were obtained, and above 300 mM of NaCl, precipitation

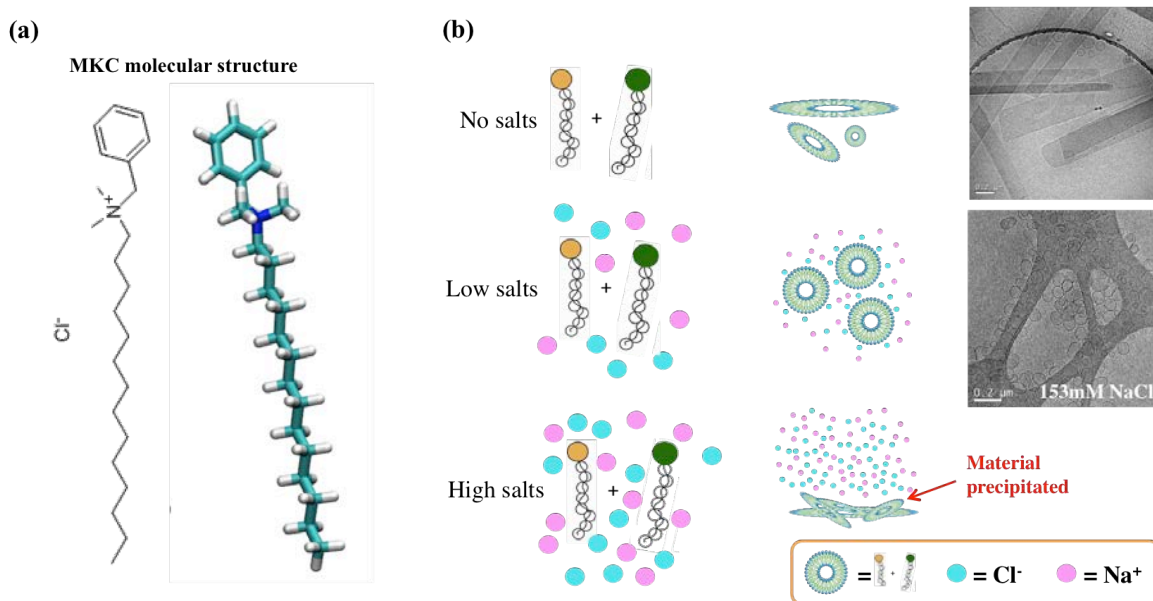


**Figure 7.5:** (a) Chemical structure of the MKC molecule. (b) Experimental scheme of the Chol/MKC 1:1 vesicle formation as function of the salt concentration (no salts, low salts and high salts). Cryo-TEM images are provided by Nanomol group.

and lack of formation of unilamellar vesicles was observed. On the contrary, in the case of Chol/CTAB system, Quatsome vesicles were already formed in pure water and are stable in several salt concentrations.

In order to understand this effect, we performed a series of atomistic MD simulations with the Chol/MKC system in water and in presence of NaCl salt at different concentrations. High-level DFT quantum mechanics calculations were used for the parameterization of the force fields employed in our MD simulations.

We built up a Chol/MKC 1:1 planar membrane at 0, 100 and 500 mM of NaCl added salt. Observing the dynamic trajectories we saw that all the three cases behave as a fluid membrane. At concentrations of 100 mM of NaCl our simulations show the formation of stable bilayers, whereas at concentrations of 0 or 500 mM of NaCl the bilayer structure is no longer stable (see Figure 7.6).

As seen in Figure 7.6-(b), when 100 mM NaCl is added, we obtain an interdigitated bilayer with a thickness (nitrogen-nitrogen atom distance) of 3.5 nm (smaller than the thick-

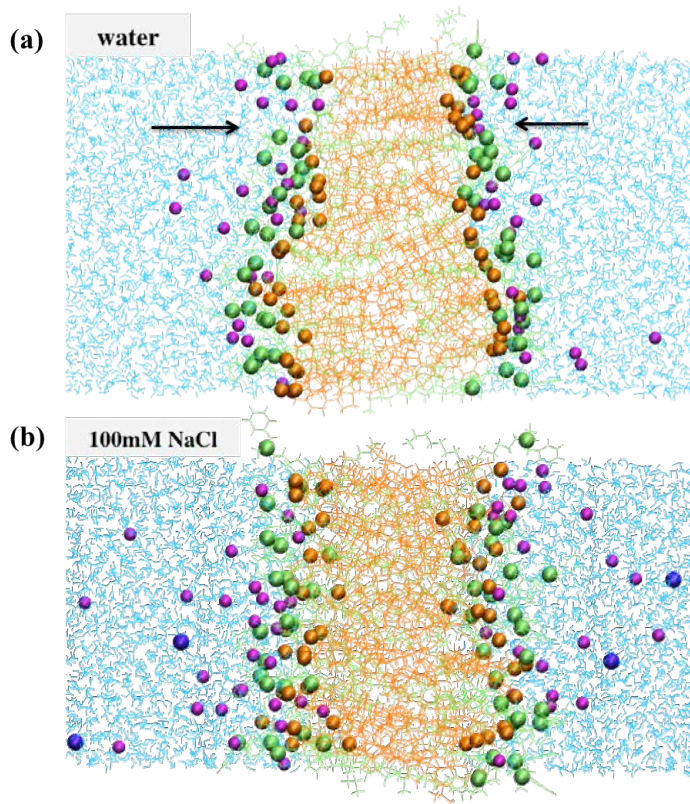
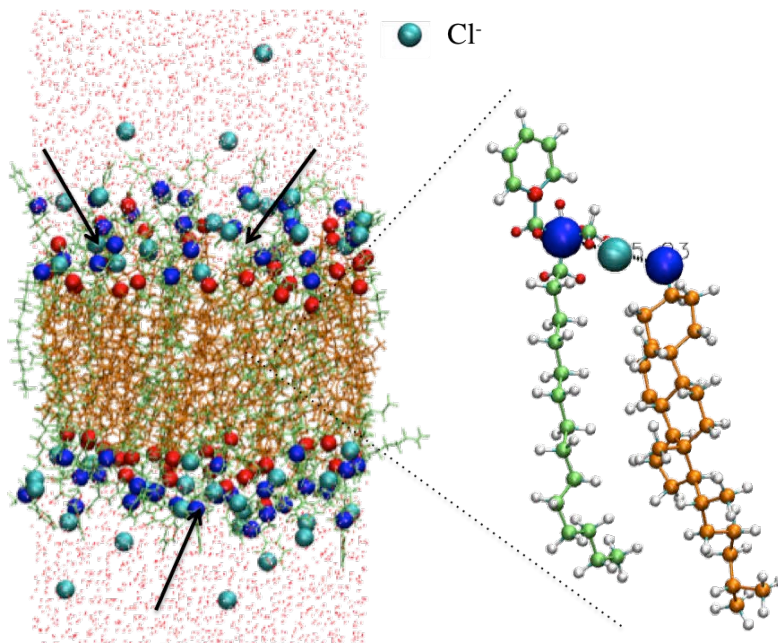


Figure 7.6: (a) and (b) Simulation snapshot of the Chol/MKC 1:1 bilayer in water (0 mM of added NaCl) and in water with 100 mM of added NaCl, respectively. MKC and Chol molecules are represented in green and orange respectively and nitrogen atom of MKC and oxygen atom of Chol are green and orange spheres. Chloride and sodium ions are represented in magenta and dark-blue spheres. Water molecules are coloured in blue.

ness of the Quatsome bilayer, 4.3 nm). When no salt is added, we observe a membrane formed by coexisting structures of monolayers (see black arrows in Figure 7.6-(a)) and bilayers. Another relevant result is that MKC and cholesterol do not form a synthon, as CTAB and cholesterol do. The interactions between the head groups that are responsible of the formation of the synthon are in this case (Chol/MKC) weak, and that structure is not formed.

These results suggest that the molecular organization of the MKC and Chol does not lead to the formation of a robust bilayer as CTAB/Chol does, but taking into account the experimental results (Figure 7.5), it must be concluded that an external factor is stabilizing the Chol/MKC bilayer: the  $\text{Cl}^-$  ions.

Thus, we studied the interaction of the  $\text{Cl}^-$  added ions with the MKC and Chol components. Our simulations predicted that anions not only adsorb onto the membrane surface but also that some of them penetrate in the membrane structure, being an integral part of this cationic vesicle (see Figure 7.7).



**Figure 7.7:** Simulation snapshot of the Chol/MKC bilayer 1:1 with 100 mM added NaCl salt. MKC surfactant and cholesterol molecules are coloured in green and orange, respectively. Headgroups of the each components are represented in spheres, blue for MKC and red for cholesterol. Chloride ions are represented in cyan spheres.

This perspective clearly shows that, depending on the desired application, the vesicles can be tuned (in this case changing the components). In that sense, the CTAB/Chol Quat-some is a starting point, but can be modified to adapt to the necessities. This constitutes a promising working line, as it has been shown in the particular case of the Chol/MKC system.

## 7.4 CHANGING THE STEROL: CHOLESTEROL WITH A VINYL SULPHONE GROUP

Following a similar strategy to the one in the previous section, here a change of the sterol is investigated. We have studied the substitution of cholesterol by functionalized cholesterol with a vinyl sulphone (VS) group, the cholest-5-ene,3-[2-(ethenylsulfonyl)etoxy], obtaining a bilayer made of CTAB and Chol-VS components at 1:1 ratio. Even though Chol-VS is not an ionic molecule its atomic structure is based on a defined polar head and non-polar chain (see Figure 7.8-(a) where the Chol-VS is shown). AA-MD simulations were performed to have a molecular picture of the interaction between Chol-VS and CTAB.

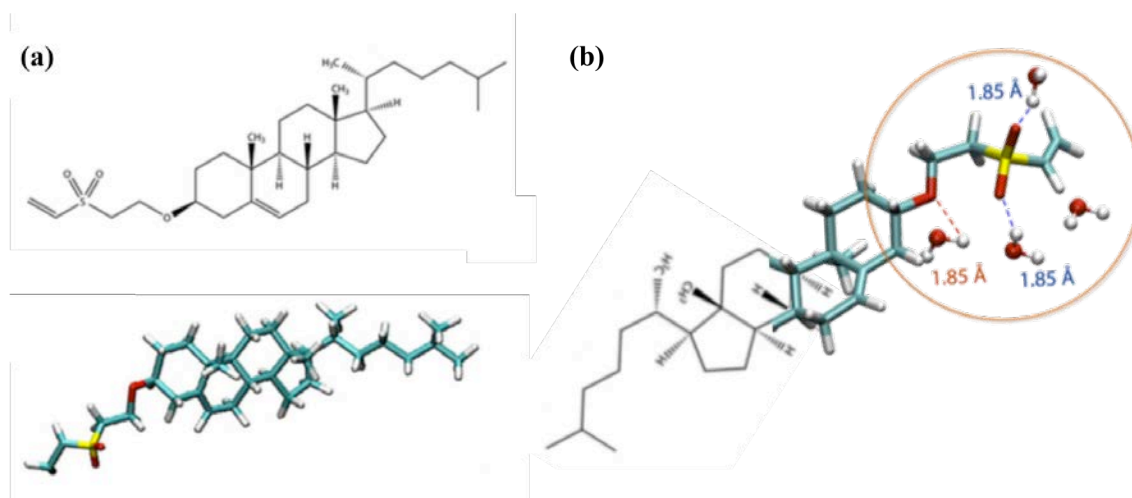


Figure 7.8: (a) Molecular structure and atomistic structure with bonds-only format of Chol-VS molecule. (b) Hydrogen bond interactions between oxygen atoms of Chol-VS molecule and hydrogen atoms contained in water. The peak at 1.85 Å corresponds to the exact tabulated value where hydrogen bonds occur<sup>9</sup>.

Employing the Chol-VS model from ref.<sup>5</sup>, we performed MD simulations that show that Chol-VS is amphiphilic, unlike the cholesterol molecule, which is hydrophobic. Its headgroups are able to form several hydrogen bonds with water, as shown in Figure 7.8-(b).

Once the amphiphilic character of the Chol-VS had been demonstrated, we studied the interaction between the CTAB and Chol-VS, using the same strategy as in work<sup>2</sup>. MD simulations were carried out considering a single molecule of CTAB and Chol-VS in water.

Analyzing the simulations it was observed that almost all the time both the hydrophilic part and the alkyl chain of both molecules were bonded, being the S-N bond (sulphur atom of the Chol-VS molecule with the nitrogen atom of the CTAB) distance 5-6 Å in average. In fewer times, the alkyl chains would separate, giving rise to another conformation, with a tail to tail distance of  $\sim 24$  Å. We concluded that the Chol-VS/CTAB association will be much weaker in comparison with that of the Chol/CTAB (Quatsome).

In order to predict the geometry of the self-assembled structure, we use the packing parameter concept (described in chapter 1). The corresponding parameters are given in table 7.1, where they can be compared to those of the components of the Quatsome. With the packing parameter equal to 0.54, CTAB and Chol-VS will pack forming a cylinder vesicle, as this value is near to the limit of infinite cylinder but within the range of vesicles.

**Table 7.1: Packing parameter values of cholesterol, CTAB and Chol-VS. Note:  $l_c$  is the length of the hydrocarbon chain,  $v$  is the volume of the hydrocarbon chain and  $a_o$  is the optimal cross-sectional area per headgroup at the polar hydrocarbon/water interface of the assembly. The packing parameter is calculated by  $p = v/(a_o \cdot l_c)$ .**

Molecule	$v$ /nm <sup>3</sup>	$l_c$ /nm	$a_o$ /Å <sup>2</sup>	$p=v/(a_o \cdot l_c)$
<b>Cholesterol</b>	0.40	1.73	19.00	1.22
<b>CTAB</b>	0.544	1.93	64.00	0.42
<b>Chol-VS</b>	0.40	1.73	37.28	0.62
<b>Chol/CTAB synthon</b>	0.94	1.73	64.00	0.85
<b>Chol-VS/CTAB synthon</b>	0.94	1.73	101.28	0.54

To study the interaction between Chol-VS and CTAB, a new simulation was performed, considering a multiple system of molecules of CTAB and molecules of Chol-VS in water. Figure 7.9 shows a snapshot of this simulation on it is clearly visible that mixed systems of CTAB and Chol-VS in water cause the formation of tubular structures, where the hydrophobic parts of both molecules are orientated inside these tubular assemblies, and the hydrophilic heads of Chol-VS and CTAB are in contact with water.

The formation of these tubular structures using Chol-VS and CTAB agrees with the ribbon-like structures observed experimentally (see Figure 7.10). These experiments were performed by the Nanomol group (ICMAB-CSIC). This association between Chol-VS/CTAB

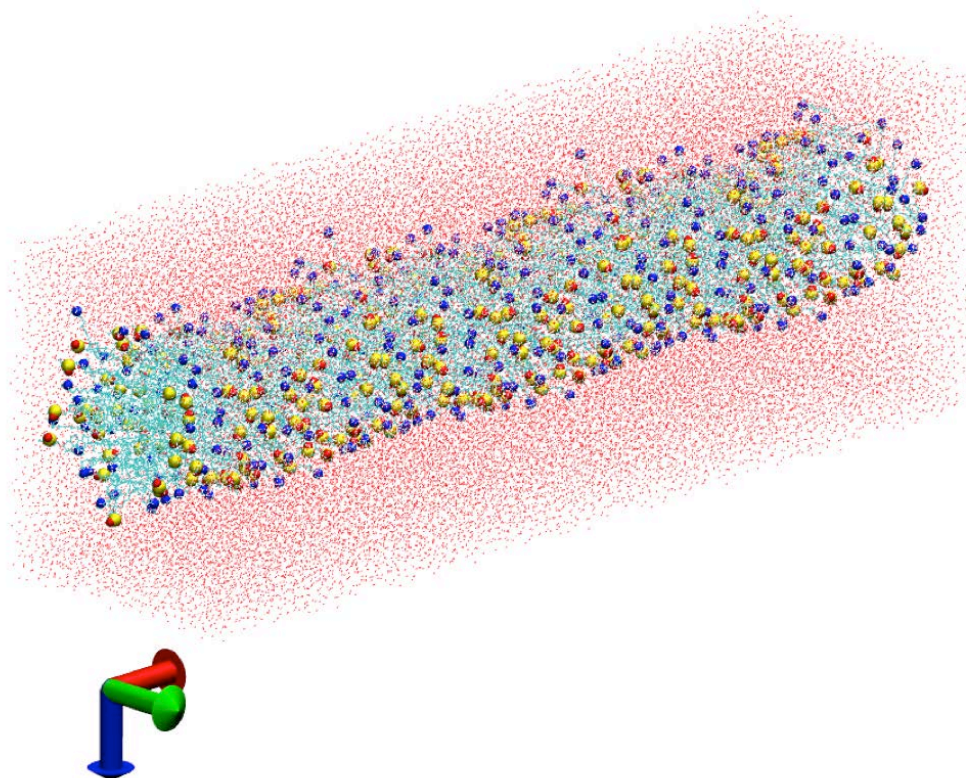


**Figure 7.9:** Simulation snapshot with boundary conditions applied in X direction. It shows how the Chol-VS/CTAB molecules in water form a nanoribbon.

is very different from that observed in the case of Chol/CTAB<sup>2</sup>. In the case of Chol/CTAB system, the cholesterol molecule is wrapped with the CTAB surfactant, which behaves as a second hydrophobic tail for CTAB. On the contrary, in the Chol-VS/CTAB case, the two molecules are together in parallel, head to head most of the time. These changes in the interaction cause a decrease in the packing parameter and consequently, the formed assemble tend to be tubular structures (Figure 7.10 and 7.9).

Experimental and theoretical studies revealed the formation of elongated structures. According to the studied packing parameter for the Chol-VS/CTAB system, mixtures of Chol-VS and CTAB molecules in water induces to sphere-to-cylindrical transition of CTAB micelles; and these cylindrical micelles probably direct the growth of the nanoribbons observed experimentally Figure 7.10 and with the simulations Figure 7.9.



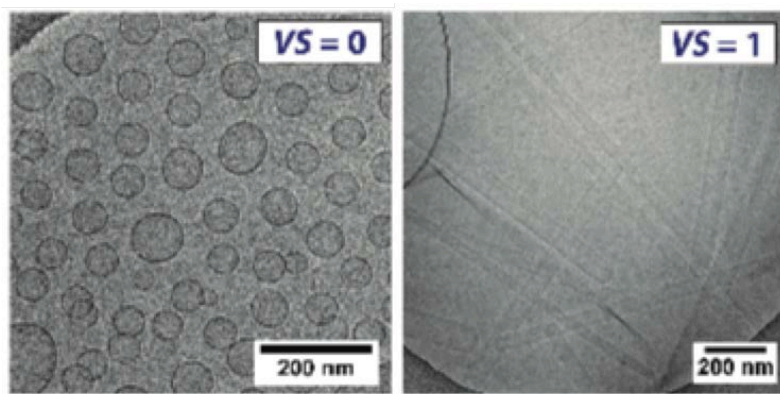


Figure 7.10: Cryo-TEM image corresponding to  $VS = 0$  is the mixed containing Chol:CTAB and the one corresponding to  $VS = 1$  is the Chol-VS/CTAB mixture. Images courtesy of Dra. Lidia Ferrer-Tasies (Nanomol group).

This last study clearly shows that the knowledge of the packing parameter allows us to tune the shape of the vesicles. By employing different components (in this case Chol-VS) that give rise to the desired packing parameter, we obtain the corresponding desired geometry. This constitutes also a very interesting line of work, which can be further explored with other sterols or modified cholesterol molecules.

## References

- [1] Arnarez, C., Uusitalo, J. J., Masman, M. F., Ingólfsson, H. I., de Jong, D. H., Melo, M. N., Periole, X., de Vries, A. H., & Marrink, S. J. (2014). Dry Martini, a Coarse-Grained Force Field for Lipid Membrane Simulations with Implicit Solvent. *Journal of Chemical Theory and Computation*, 11(1), 260–275.
- [2] Ferrer-Tasies, L., Moreno-Calvo, E., Cano-Sarabia, M., Aguilera-Arzo, M., Angelova, A., Lesieur, S., Ricart, S., Faraudo, J., Ventosa, N., & Veciana, J. (2013). Quatsomes: Vesicles Formed by Self-Assembly of Sterols and Quaternary Ammonium Surfactants. *Langmuir*, 29(22), 6519–6528.
- [3] Guida, V. (2010). Thermodynamics and kinetics of vesicles formation processes. *Advances in Colloid and Interface Science*, 161(1-2), 77–88.
- [4] Huang, C., Quinn, D., Sadovsky, Y., Suresh, S., & Hsia, K. J. (2017). Formation and size distribution of self-assembled vesicles. *Proceedings of the National Academy of Sciences*, 114(11), 2910–2915.
- [5] Illa-Tuset, S. & Faraudo, J. (2014). Atomistic simulation of amphiphilic molecules. Application to functionalized cholesterol. Master’s thesis, IQS School of Engineering, Via Augusta, 390, 08017 Barcelona.
- [6] Illa-Tuset, S., Malaspina, D. C., & Faraudo, J. (2018). Coarse-grained molecular dynamics simulation of the interface behaviour and self-assembly of CTAB cationic surfactants. *Physical Chemistry Chemical Physics*.
- [7] Marrink, S. J., Risselada, H. J., Yefimov, S., Tieleman, D. P., & de Vries, A. H. (2007). The MARTINI Force Field: Coarse Grained Model for Biomolecular Simulations. *The Journal of Physical Chemistry B*, 111(27), 7812–7824.
- [8] Marrink, S. J. & Tieleman, D. P. (2013). Perspective on the Martini model. *Chemical Society Reviews*, 42(16), 6801–6822.
- [9] Minch, M. J. (1999). An Introduction to Hydrogen Bonding (Jeffrey, George A.). *J. Chem. Educ.*, 76(6), 759+.
- [10] Okahara, A., Tanioka, H., Takada, K., & Kawazu, K. (2013). Ocular Toxicity of Benzalkonium Chloride Homologs Compared with Their Mixtures. *Journal of Toxicologic Pathology*, 26(4), 343–349.



*I always have a basic plot outline, but I like to leave some things to be decided while I write.*

J. K. Rowling



## Annex

In this annex, supplementary information about the research carried out in this thesis can be found. It contains information that helps readers understand the thesis or it provides essential background on the research process. However, this information is too long or detailed to fit into the main text. Such information has been divided into sections corresponding to each chapter.

## A.1 CHAPTER 2 ANNEX: METHODS

### A.1.1 PREPARATION OF THE QUATSOMES BY THE DELOS-SUSP METHOD AND A DESCRIPTION OF THE EQUIPMENT

Depressurization of an Expanded Organic Solution-Suspension (DELOS-SUSP) method is a compressed fluid (CFs)-based procedure for the production of multifunctional small unilamellar vesicles (SUVs). In the last 25 years, several CFs-based methodologies for the preparation of nanostructured materials have been developed<sup>15,22,27</sup>. CFs exist as gas at normal conditions of pressure (P) and temperature (T), but can be converted into liquids or supercritical fluids increasing P. Concerning the production of nanomaterials, the solvation capacity of a CFs (both in the liquid or supercritical phase) is one of the most important parameters. It can indeed be tuned by pressure changes, which propagate more quickly than temperature and composition variations. In this way, a fine control over the morphology of materials at the microscopic scale can be achieved, opposite to most of conventional processing techniques<sup>8,3</sup>. CO<sub>2</sub> is the most used compressed fluid in this sense, thanks to its low critical pressure ( $P_c = 74$  bar) and temperature ( $T_c = 31$  °C), which allow working at mild conditions, with low production cost and reduced damage to the processed molecules. In addition to that, it is non-flammable, non-toxic, inexpensive and non-polluting, all properties that have made it a green-substitute to conventional organic solvents for the preparation of nanomaterials.

DELOS-SUSP method allows the one-step preparation of multifunctional CTAB-cholesterol nanovesicles among other formulations including nanovesicles-bioactive hybrids<sup>2,1</sup>. A scheme of the DELOS-SUSP process for the formation of multifunctional nanovesicles is shown in Figure A.1.

In few words, a solution of the membrane Quatsome components and the non-water soluble compounds (e.g. cholesterol and non-water soluble dyes) in an organic solvent (in this case ethanol) is loaded into a high-pressure autoclave, at the working temperature (Figure

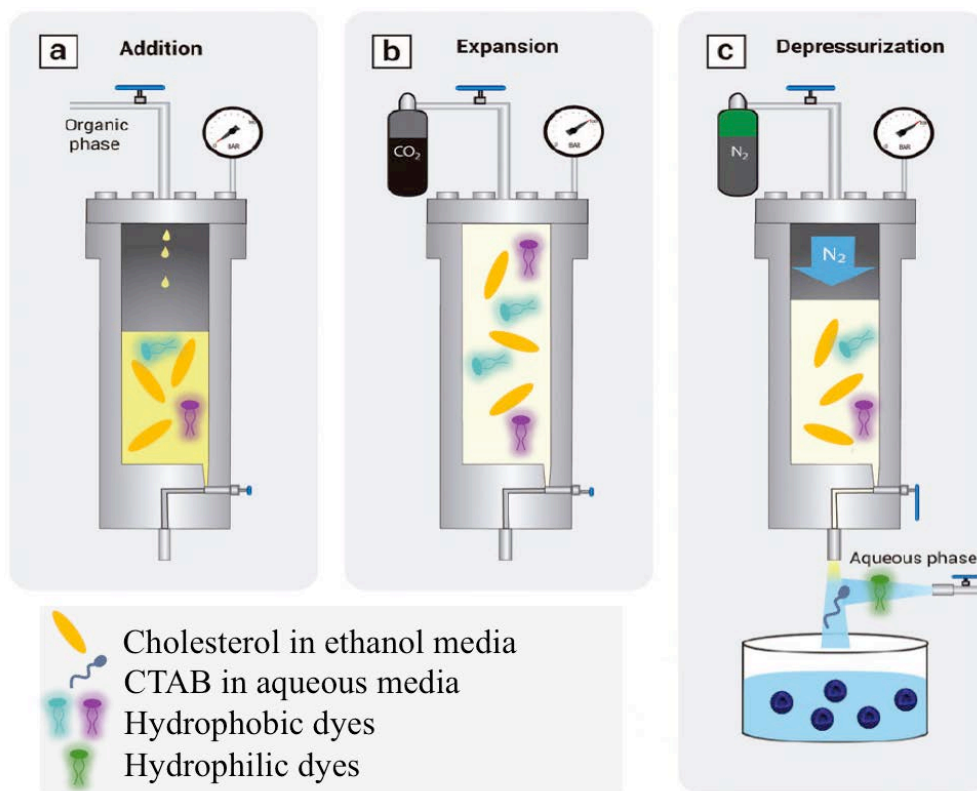


Figure A.1: Schematic representation of the DELOS-SUSP process. Patent. EP1843836; US7754777; CA2566760.

A.1). The reactor is then pressurized by addition of compressed CO<sub>2</sub> until reaching the working pressure (10 MPa), in order to obtain a CO<sub>2</sub>-expanded solution of the compounds. Finally, in the last stage, the vesicular structures are formed by depressurizing the CO<sub>2</sub>-expanded solution over an aqueous phase, which contains the surfactant (e.g. CTAB) and water-soluble dyes to be encapsulated (Figure A.1). In the final step, N<sub>2</sub> at the working pressure is added to the reactor to keep constant the pressure inside the autoclave during the depressurization. As effect of the depressurization, the CO<sub>2</sub>-expanded solution experiences an abrupt and homogeneous temperature decrease (induced by the evaporation of CO<sub>2</sub>) which likely is the cause of the high structural homogeneity in terms of composition, size and morphology of the obtained vesicles. Thanks to this, no further post-processing steps, generally required with the conventional methods of vesicles production, are necessary in order to reduce and homogenize the size of the formed vesicles.

## A.2 CHAPTER 3 ANNEX: CHARACTERIZATION OF THE QS BILAYER

### A.2.1 MD SIMULATION OF DPPC/CHOL BILAYER

One of the analysis of the section 3.1.3 (organization of counterions) was based on the organization at global level of the Quatsome bilayer in water (without added salt). We observed how bromide ions were able to penetrate up to the hydrophobic part of the membrane forming a ion-water network. In order to compare with liposome systems, we repeated the procedure but considering DPPC lipid instead of CTAB surfactant resulting on a DPPC:Chol (60:40) bilayer in water. All computational details of this simulation are reported in the work<sup>1</sup> with the only difference that we extended the simulation time up to 40 ns. A description of the system simulated is described in Table A.1.

**Table A.1: Composition of the systems considered in the MD simulations, including total number of atoms, number of molecules; water, DPPC and Chol molecules, the simulation time, the area per polar head group and the thickness (nitrogen-nitrogen atom distance).**

Atoms	molec. water/DPPC/Chol	Sim time	Area (headgroup)	Thickness
127031	28973/230/138	40 ns	75.5 Å <sup>2</sup>	4.9 nm

The main results are that although in this lipid bilayer we do not have Br<sup>-</sup> counterions, we do observed how water molecules are able to form hydrogen bounds with oxygen atom of the phospholipid (green spheres in the figure) crossing the membrane surface (see Figure A.2 and form ordered structures (black lines). It is concluded thus, the DPPC:Chol bilayer has similar behaviour as the Quatsome bilayer.

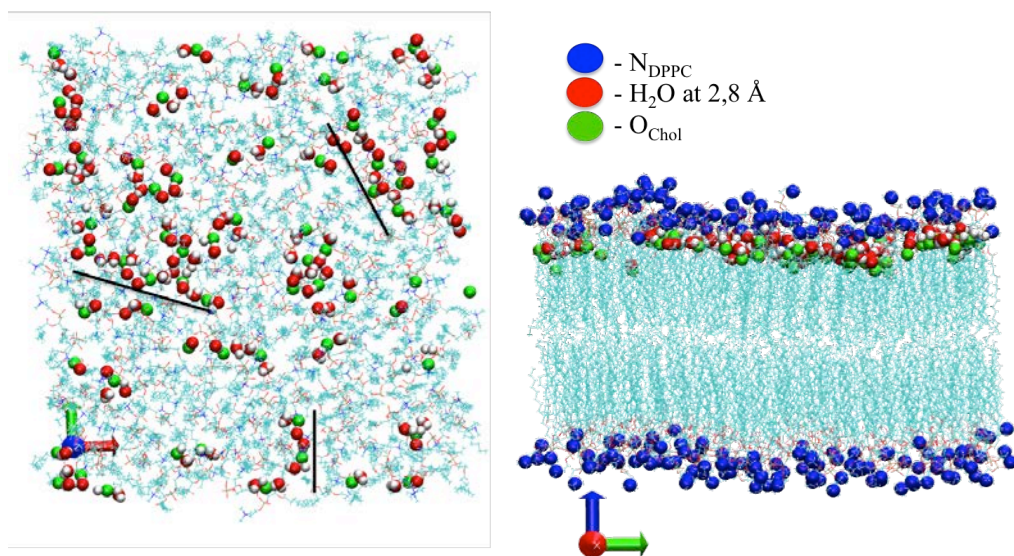


Figure A.2: On the left, top view of the DPPC/Chol surface highlighting laterally correlated water that share oxygen atoms in their first coordination shell (green). On the right, snapshots of the ions at the DPPC/Chol surface-water interface. DPPC and cholesterol molecules are in licorice representation. Nitrogen atoms from the DPPC head group (in blue) and oxygen atoms (in green) from the cholesterol are represented in Van der Waals radii. Water molecules at 2.5 Å distance from oxygen atom of the cholesterol (green) are also represented in Van der Waals radii.

### A.2.2 COMPUTATIONAL DETAILS OF THE ALL AA-MD SIMULATION PERFORMED

All computational details of the 6 simulations performed in order to study the **effect of temperature** (section 3.2) on the Quatsome bilayer are shown in Table A.2.

Table A.2: Composition of the systems considered in the MD simulations, including total number of atoms, number of molecules; water and CTAB molecules, the simulation time and the equilibrated size box.

	T /°C	Atoms (total)	molecules water/CTAB	Sim time /ns	Size Box
S1	10	23727	5443/54	88.21	226.5 nm <sup>3</sup>
	15	23727	5443/54	71.14	226.5 nm <sup>3</sup>
	20	23727	5443/54	72.15	226.5 nm <sup>3</sup>
	25	23727	5443/54	107.14	226.5 nm <sup>3</sup>
	35	23727	5443/54	72.48	226.5 nm <sup>3</sup>
	50	23727	5443/54	73.35	226.5 nm <sup>3</sup>



All computational details of the 16 simulations performed in order to study the **effect of tension** (section 3.3) on the Quatsome bilayer are shown in Table A.3.

**Table A.3: Surface tension values study for the S1 simulation, as a function of area of the bilayer and the simulation time.**

S1 simulation T = 25 °C			
$\gamma$ /dyn/cm	Area /nm <sup>2</sup>	err $\pm$	Sim. time /ns
0	57.96	0	107.00
1	58.26	0.010	22.45
10	58.45	0.033	22.40
20	58.66	0.012	20.00
35	59.19	0.015	20.00
50	58.91	0.048	33.90
75	60.01	0.013	37.97
100	61.34	0.021	70.96
110	70.03 - 100*	-	35.43
120	73.06 - 84*	-	8.80
140	107.20 - 130*	-	8.99
150	85*	-	3.04
160	103*	-	1.52
180	85*	-	0.85
200	73*	-	0.49
300	72*	-	0.22

\* values after collapse

In order to clarify how the effect of tension study was carried out, here is a summary. We gradually increased the surface tension ( $\gamma$ ) from the equilibrated point of the S1 simulation. For values of  $\gamma$  of 1, 10, 20, 35 dyn/cm We run  $\sim 20$ ns in order to let the simulation box adjust the volume (indeed the area). As we kept increasing the surface tension ( $\gamma$  being 50, 75 or 100 dyn/cm) we run for more time the simulation in order to ensure we reach an equilibrium state, and thus a constant area. 110 dyn/cm was the turning point at which we observed the membrane and the simulation collapse after some time (as explained in the main text of the thesis, section 3.3). In Table A.3 we show for  $\gamma = 110, 120$  and 140 dyn/cm two values, the value just before collapse and the value after collapse. And for  $\gamma > 140$  dyn/cm, we observed that the area drastically changed in few ns and the system collapsed.

All computational details of the 16 simulations performed in order to study the **effect of ions** (section 3.5.1) on the Quatsome bilayer are shown in Table A.4.

**Table A.4:** Composition of the systems considered in the MD simulations, including total number of atoms, number of molecules; water, CTAB and  $\text{Cl}^-$  molecules, the simulation time and the equilibrated size box.

	T /°C	Atoms (total)	water/CTAB/ $\text{Cl}^-$	Sim time /ns	Size Box
	15	23687	5423/54/10	66.92	226.9 nm <sup>3</sup>
<b>S2</b>	25	23687	5423/54/10	131.06	226.9 nm <sup>3</sup>
	30	23687	5423/54/10	60.00	226.9 nm <sup>3</sup>
	35	23687	5423/54/10	65.89	226.9 nm <sup>3</sup>
	40	23687	5423/54/10	65.86	226.9 nm <sup>3</sup>
	50	23687	5423/54/10	60.00	226.9 nm <sup>3</sup>

### A.2.3 FURTHER DETAILS OF THE EFFECT OF T AND ADDED SALT ON THE CHARACTERIZATION OF THE QS BILAYER

As mentioned in the section 3.2 of thesis, we studied the effect of T on the thickness and area per molecule, and we observed no changes regarding the thickness. We did the same study at different T for the QS bilayer with added salt (S2 simulations). Down below we show the densities profiles of the membrane at 10 °C, 25 °C and 50 °C for QS system in water (see Figure A.3) and for QS system added salt (see Figure A.4).

Also we have summarized all the values of the thickness and the area per polar head group as function of T for S1 and S2 simulations performed in section 3.2 and 3.5 respectively. Values are shown in Table A.5.

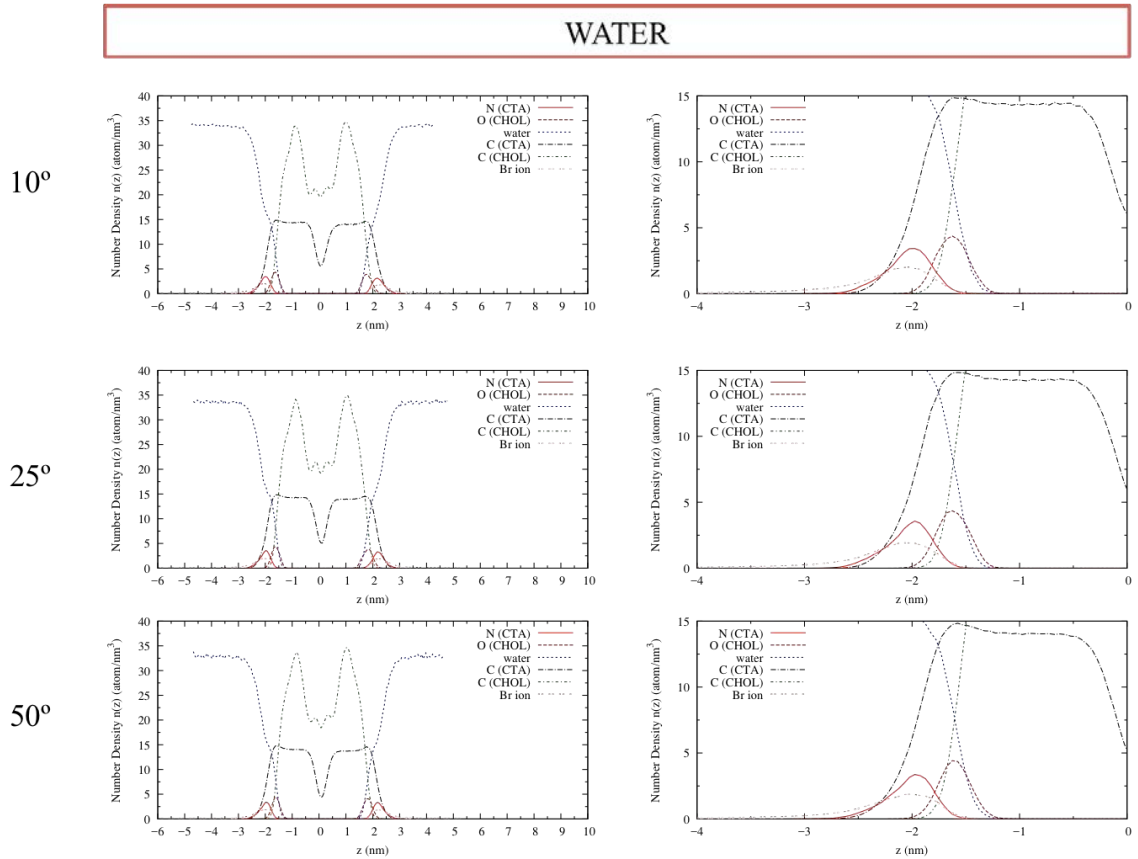
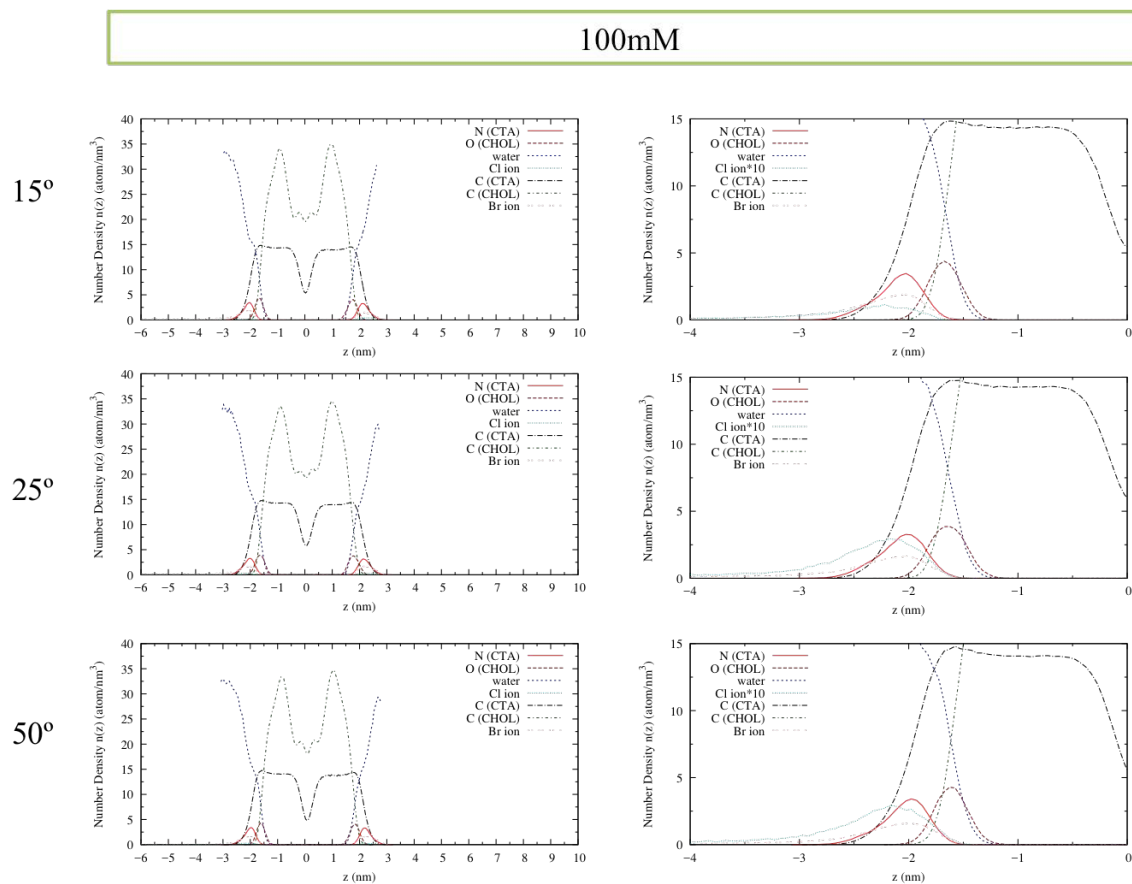


Figure A.3: Density profiles at 10 °C, 25 °C and 50 °C for the QS bilayer in water.

Table A.5: Area per polar head group and thickness of the S1 simulation (water) and S2 simulation (ions) at different temperatures.

Temperature /°C	Area per polar head group /Å <sup>2</sup>		Thickness /nm	
	Sim_H2O	Sim_PBS	Sim_H2O	Sim_PBS
10	57.87	—	4.26	—
15	57.69	57.90	4.27	4.27
20	57.96	—	4.27	—
25	57.98	57.96	4.28	4.28
30	—	58.16	—	4.27
35	58.44	58.24	4.27	4.29
40	—	58.50	—	4.28
50	58.99	58.68	4.27	4.29

In addition and following the characterization of the QS bilayer, in the chapter 3 section 3.2, we observed a breaking symmetry within the two layers of the membrane. We observed



**Figure A.4:** Density profiles at 15 °C, 25 °C and 50 °C for the QS bilayer in water with 100 mM added NaCl salt.

as well, how the tilt angle changes with temperature. In the following Figure A.5, we report all the tilt angles of the CTAB at all the temperature studied (see Table A.2) with time. It is shown how one of the layers (red) fluctuates more than the other one (green) within time but also how those fluctuation are getting softer when temperature is increased. Temperatures above 25 °C show less jumps than the ones below 25 °C. It is also shown for all T, the tilt distribution of the CTA<sup>+</sup> layers and a values of the tilt average for each layer and representative punctual tilt values.

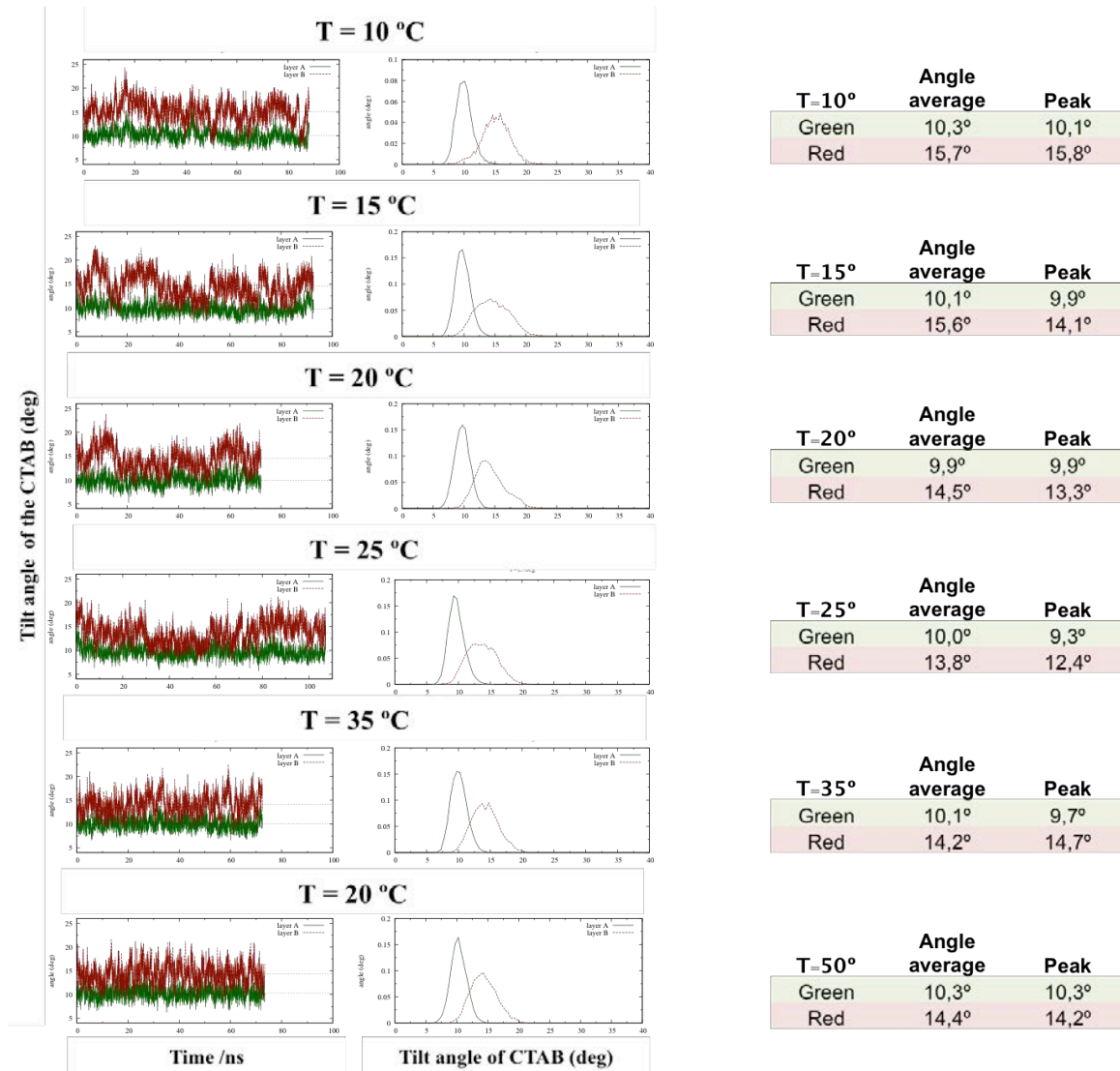


Figure A.5: The panel shows; Variation of the tilt angle of the CTAB<sup>+</sup> for both leaflets with time, the tilt angle distribution and the tilt average values for all T simulated based on S1 simulation.

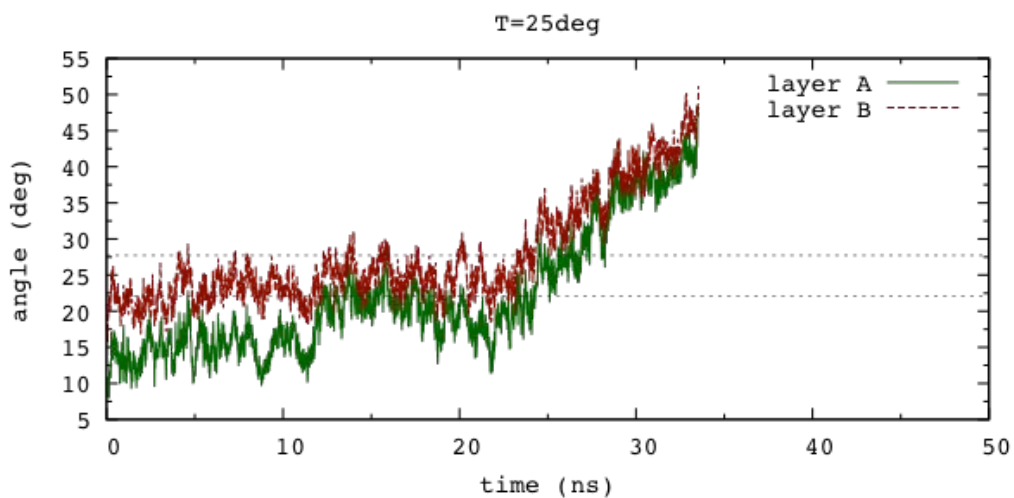


Figure A.6: Variation of the tilt angle of the CTA<sup>+</sup> for both leaflets with time at the moment when a tension of 100 dyn/cm is applied on the QS bilayer.

Regarding how tilt angle is affecting by different parameters, in section 3.3 we mention how the membrane collapse at certain values of  $\gamma$  and thus, how the tilt angle of the CTA<sup>+</sup> change within the trajectory. Down below, it is shown and example at  $\gamma = 100$  dyn/cm (Figure A.6).



# Nomenclature

<b>AA</b>	All-atomic
<b>AFM</b>	Atomic force microscopy
<b>CG</b>	Coarse-grain
<b>CHARMM</b>	Chemistry at Harvard Macromolecular Mechanics
<b>Chol</b>	Cholesterol molecule
<b>CTA+ or CTA CTAB</b>	Cetrimonium bromide surfactant
<b>DFT</b>	Density functional theory
<b>DiI</b>	1,1'-Dioctadecyl-3,3',3'-Tetramethylindocarbocyanine Perchlorate
<b>DiD</b>	1,1'-Dioctadecyl-3,3',3'-Tetramethylindodicarbocyanine Perchlorate
<b>DPPC</b>	Dipalmitoylphosphatidylcholine phospholipid
<b>DOPC</b>	Dipalmitoylphosphatidylcholine phospholipid



<b>CGenFF</b>	CHARMM general force field
<b><math>g(\mathbf{r})</math></b>	Radial distribution function
<b>MD</b>	Molecular dynamics
<b>MK</b>	Merz-Kollman method
<b>MKC</b>	Tetradecyldimethylbenzylammonium chloride surfactant
<b>MM</b>	Molecular mechanics
<b>MSD</b>	Mean squared displacement
<b>PES</b>	Potential energy surface
<b>PMF</b>	Potential of Mean Force
<b>QM</b>	Quantum mechanics
<b>QS</b>	Quatsome
<b>STORM</b>	Stochastic Optical Reconstruction Microscopy
<b>VMD</b>	Visual Molecular Dynamics
<b>SUVs</b>	Small unilamellar vesicles

# Scientific Contributions

## Publications

- "Insights into the structure and nanomechanics of the Quatsome membrane by force spectroscopy measurements and molecular simulations", Berta Gumí-Audenis, **Sílvia Illa-Tuset**, Natascia Grimaldi, Laia Pasquina-Lemonche, Lidia Ferrer-Tasies, Fausto Sanz, Jaume Veciana, Imma Ratera, Jordi Faraudo, Nora Ventosa and Marina I. Giannotti, **Nanoscale**, 2018, *10*, 23001-2301
- "Coarse-grained molecular dynamics simulation of the interface behaviour and self-assembly of CTAB cationic surfactants", **Sílvia Illa-Tuset**, David C. Malaspina and Jordi Faraudo, **Phys. Chem. Chem. Phys.**, 2018, *20*, 26422-26430
- "Nanostructuring Lipophilic Dyes in Water Using Stable Vesicles, Quatsomes, as Scaffolds and Their Use as Probes for Bioimaging", Antonio Ardizzone, Siarhei Kurhuzenkau, **Sílvia Illa-Tuset**, Jordi Faraudo, Mykhailo Bondar, David Hagan, Eric W. Van Stryland, Anna Painelli, Cristina Sissa, Natalia Feiner, Lorenzo Albertazzi, Jaume Veciana, Nora Ventosa, **Small**, 2018, *14*, 1703851

## Attendance to conference and schools

### 2018

- Attendance and Poster presentation at Hermes Summer School in London (UK).

### 2017

- Oral presentation at JPhD Congress in Barcelona (Spain).
- Attendance and Poster presentation at Martini Workshop in Groningen (The Netherlands).
- Attendance at Schrodinger Workshop in Barcelona (Spain).
- Oral presentation at MATBIO Congress in Barcelona (Spain).

### 2016

- Introduction to Gaussian: Theory and Practice course lead by SCUBE Scientific Software Solutions Ltd. (total course hours 40) in Chennai (India)
- Oral presentation and Training in super resolution microscopy, materials for 2PM and REACH regulations (total course hours 8), organized by ITN Nano2fun, in Bordeaux (France)
- Oral presentation and Training in nanofabrication (total course hours 8), organized by ITN Nano2fun, in Hannover (Germany)

### 2015

- Attendance at Light on Molecular Functional Materials Congress in Bangalore (India).
- Oral presentation and Training in communicating science (total course hours 8), organized by ITN Nano2fun in Bangalore (India).
- Oral presentation and Training in professional conduct and career planning and doctors at industry (total course hours 12), organized by ITN Nano2fun in Barcelona (Spain).

